Understanding the Effect of Seasonal Variability on the Structure of Ice Shelves and Meltwater Plumes

Christopher MacMackin

Trinity College

University of Oxford

A thesis submitted for the degree of

Doctor of Philosophy

Michaelmas 2018

Acknowledgements

This thesis would not have been written without the help and support of many people. First and foremost, I would like to thank my supervisor, Prof. Andrew Wells, for his valuable advice and editing, in addition to how welcoming and accessible he has been throughout my degree.

I'd also like to extend my gratitude to my viva examiners, Dr. Adrian Jenkins and Prof. Laure Zanna. Similarly, Profs. David Marshall and Ray Pierrehumbert are to be thanked for their helpful feedback during my transfer and confirmation of status vivas.

My thanks to Laura Cimoli, for providing me with background information on how freshwater input affects global ocean circulation, and to Prof. Ian Hewitt for his helpful conversations about my work. I also thank Prof. Peter Read in his capacity as my college advisor.

A doctorate is a long and expensive endeavour and mine would not have been possible without the generous support of the Clarendon Fund and Caryll Birkett. In addition, thank you to the Atmospheric, Oceanic, and Planetary Physics department for nominating me for the former and Trinity College for selecting me to receive the latter funding.

As they often go under-appreciated, a thank you goes out to all of the ancillary staff at the university, department, and Trinity College, including administrators, technicians, cooks, and cleaners. It is your dedication that keeps Oxford functioning.

I would like to thank the many incredible friends I have made in Oxford through my department and the Trinity College graduate community. Without your support and companionship I would doubtless have broken down under the pressure of my degree. In particular, I would like to thank John Kenny, Nick Holgate, Cosima Gillhammer, and Matt Brown.

Finally, I would like to thank my family for their unwavering backing throughout my doctorate, from application to submission. In particular, my parents Bill and Patti MacMackin have my eternal gratitude for the patience and understanding they provided during our weakly chats. My love and appreciation also goes out to my grandmother, Norma Boyles, for her doting support, even though my studies have taken me much further from her than she would have liked. It is only with the backing of incredible people such as yourselves that I have been able to achieve what I have.

Abstract

Ice shelves are important to the climate system as they control the release of fresh water from ice sheets into the ocean, with consequences for sea level rise and ocean dynamics. Channels modifying basal melt rates and structural integrity have been observed inscribed in the undersides of some ice shelves. Observations indicate that some channels run in a transverse to ice flow and it has been suggested that these form due to seasonal variations in ocean properties.

This thesis analyses the effect of seasonal variability on ice shelves and meltwater plumes in the underlying ocean. A linear perturbation analysis on vertically integrated ice and plume models showed that seasonal forcing of subglacial discharge or ice flux can generate small ripples melted into the base of the ice shelf. These ripples did not develop into overdeepened channels, but the ripples caused by ice flux appear similar to basal terraces observed underneath some ice shelves. Code was developed to run 1-D nonlinear simulations with the vertically-integrated equations, producing similar results to the linear case. However, runs neglecting hydrostatic pressure gradients exhibited a feedback causing ice flux-generated ripples to grow into small proto-channels. A horizontally-integrated plume model was derived, incorporating the Coriolis force and transverse plume flow into a 1-D model which agreed well with a 3-D ocean simulation. Coupling this horizontally-integrated plume with a co-evolving ice shelf prevented proto-channels from forming. It appears unlikely that subglacial discharge or ice flux variations can give rise to observed transverse channels.

A new approach was developed to predict the evolution of internal radar reflectors observed within ice shelves, using vertically-integrated models of ice flow. It is hoped this approach might have applications for inverse modelling and data assimilation.

Contents

1

Ice Shelves and the Ocean

Contents

1.1 Ice Shelves in the Climate System

There are many forms of ice which play distinct and interacting roles in the climate system. Sea ice forms from freezing the salty water of the ocean and is thus quite different from glaciers, which form from compaction of freshwater snow (see, e.g., Cuffey and Paterson, 2010, , for a broad overview of glaciers). Icebergs originate from the fragmentation of glaciers into the ocean. Glaciers on the continental scale are often called *ice sheets*. If an ice sheet meets the ocean then it may form a *tide-water glacier*, meaning that the ice presents a nearly vertical face to the water.

These formations are common in the fjords of Greenland. Alternatively, it may form an ice-shelf, where the ice sheet becomes buoyant at a *grounding line* and floats on the ocean. In this case, the ice will thin until it eventually reaches a calving front, where icebergs break off. The bottom of an ice shelf presents a sloping, rather than vertical, interface to the ocean. Ice sheets and shelves have been of recent interest due to their potential to cause dramatic sea level rise as they melt in response to global warming (e.g. Shepherd, Ivins, et al., 2012; DeConto and Pollard, 2016).

As they are already floating near hydrostatic equilibrium, the melting of ice shelves does not directly contribute to sea level rise, except to a small degree due to the resulting salinity and temperature changes in the ocean (Jenkins and Holland, 2007). They also contain relatively little mass compared to ice sheets. However, the melting of ice shelves is still of importance to understanding global sea levels, as 80% of Antarctica's grounded ice sheets reach the ocean by flowing through an ice shelf (Pritchard et al., 2012) and the geometry of an ice shelf can impact their flow. As such, the ice lost due to melting of ice shelves does ultimately represent a loss of mass from the Antarctic ice sheet and basal melting of ice shelves is important when determining Antarctic mass balance and resulting sea level rise. Jacobs, Helmer, et al. (1992) provided an early example of a mass balance study which accounts for basal melting, using a combination of observational data and modelling. They found that Antarctica had a negative mass balance (net loss of ice) and that basal melting from ice shelves was an important contributor to mass loss; were there no basal melting then the mass balance would have been positive. However, the uncertainty in this estimate was substantial, and the results could also be considered consistent with Antarctica being in a steady state. According to this estimate, melting was a relatively minor process, with about five times more ice mass lost from Antarctica due to iceberg calving. A more recent paper (Rignot and Steffen, 2008) which analysed the mass balance of the ice shelf in front of the Petermann Glacier in Greenland found that 80% of this ice shelf's mass is removed by basal melting before calving can occur. From an extensive survey of Antarctic ice shelves, Rignot, Jacobs, et al. (2013) found that proportions of calving to melting vary greatly around the continent, with no appreciable basal melting in some areas and mass loss almost entirely due to melting in others. Overall, basal melting was found to be the largest mass-loss process in Antarctica.

Many ice shelves also act to buttress ice sheets, restraining their flow into the ocean and offsetting the *marine ice sheet instability* (Weertman, 1974; Schoof, 2007, 2012; Alley, Anandakrishnan, et al., 2015). Marine ice sheets (those which are grounded with bases below sea level) will have certain equilibrium grounding line positions where the outflowing ice flux is equal to the rate of accumulation of mass on the sheet. If the ground slopes down into the ocean then a perturbation of the grounding line inland would result in the overlying ice being thinner and hence there being a smaller flux through it. As such, the grounded ice would thicken and no longer be buoyant, causing the grounding line to advance back to its original position. Similarly if the grounding line were perturbed towards the ocean, then the overlying ice would be thicker and the flux through it greater, causing the grounded ice to thin and become buoyant. Thus, the grounding line would return to the equilibrium position and this is a stable equilibrium. By a similar argument, if the ice sheet were on ground sloping down away from the ocean, then any perturbation to an equilibrium grounding line position would cause runaway advance or retreat.

Buttressing arises due to friction between the edges of ice shelves and the adjacent ground. Often this is modelled as a no-slip condition (e.g. Dupont and Alley, 2006; Goldberg et al., 2009; Sergienko, 2013), although it may also be parameterised (e.g. Dupont and Alley, 2005) or treated as a drag force (e.g. Gagliardini et al., 2010; Sergienko, 2013). This friction causes a shear stress within the ice shelf, resisting the flow. As such, it can reduce the speed with which ice enters the ocean and, in some situations, act to stabilise the equilibrium position of the grounding line (Dupont and Alley, 2005; Goldberg et al., 2009). In certain cases, buttressing may even cause the grounding line to advance, increasing the volume of ice above sea level (Goldberg et al., 2009). Reduction of the length or thickness of an ice shelf would decrease the magnitude of the buttressing due to reduced contact area for friction on the sidewalls. This would potentially allow for greater mass loss from ice sheets (due to greater ice flux across the grounding line) and for grounding line retreat, depending on the geometry of the ice shelf and ocean bed. It has been shown that identical levels of ice thinning occurring at different locations on an ice shelf can result in dramatically different levels of increased ice flux crossing the grounding line (Reese et al., 2018). Ice shelves are particularly sensitive to thinning near the grounding line, active ice streams, and shear margins. If this results in grounding line retreat then there can be significant sea level rise, as previously grounded ice begins to float. It is believed that, upon becoming unstable, the grounding line can shift position very rapidly on geological timescales (on the order of hundreds of years). With sufficient ocean warming, it may be possible for grounding line retreat to destabilise the entire West Antarctic Ice Sheet (see review of observational and modelling evidence by Alley, Anandakrishnan, et al., 2015).

In addition to grounded ice sheets, ice shelf melting can impact the oceans. It has been suggested that fresh ice-shelf melt water has acted to increase the stability of stratification in the upper layers of the ocean around Antarctica, inhibiting convective transfer of heat from lower layers (e.g. Bintanja et al., 2013; Williams G. D. et al., 2016). This would result in cooler surface waters and would mean that more sea ice could form, potentially explaining the increased volumes of sea ice observed around Antarctica, even in the face of climate change (e.g. Bintanja et al., 2013). However, some other simulations, using historical records of mass loss from Antarctica, found that the increase in sea ice formation which results is small and insufficient to counteract expected ice loss due to climate change (e.g. Swart and Fyfe, 2013).

Ocean freshening around the poles may also affect global ocean dynamics. An early simulation by Manabe and Stouffer (1995) indicated that a ten year spike in runoff from Greenland would cause a sudden decrease in the strength of the Atlantic Meridional Overturning Circulation (AMOC), resulting in reduced heat transport and cooling of the north Atlantic. However, over a period of a few centuries, the AMOC gradually increased back to its original strength. Most research on this subject (e.g. Vellinga and Wood, 2002; Weijer et al., 2012; Hu et al., 2013; Jackson et al., 2015) has focused on the impact of freshening around Greenland. Although much uncertainty remains, it appears that some reduction in the AMOC is expected to result from increased fresh water fluxes and this may reduce the warming from the greenhouse effect in northern Europe. It may also alter precipitation and reduce the productivity of vegetation. Less work has been done on freshening around Antarctica and results have been contradictory, with some suggesting that it would reduce the AMOC and other suggesting that it may strengthen it (e.g. Swingedouw et al., 2009; Hu et al., 2013, and references therein). Such divergent results may be due to the fact that freshening in the Southern Ocean can result in three different feedback mechanisms: the freshening causing the Atlantic pycnocline to deepen and Antarctic Bottom Water production to decrease, enhancing the North Atlantic Deep Water (NADW) cell within the AMOC; the spread of fresh water into the North Atlantic, tending to weaken the NADW cell; and increased winds in the southern hemisphere due to increased temperature gradients from changes in global ocean circulation caused by the input of the fresh water. The second of these would tend to weaken the AMOC, while the other two tend to strengthen it, and they all act on different time scales, causing complex interactions (Swingedouw et al., 2009, and references therein). Furthermore, their overall effect seems to depend on the existing state of the AMOC, making interpretation of paleo-data and different models challenging.

Ice shelves also calve icebergs, which act as distributed sources of fresh water and sinks of heat in the oceans. As such, they can affect ocean stratification, sea ice formation, and deep water formation (e.g. Jongma et al., 2009). Ice sheets also impact global energy balance and atmospheric circulation. Loss of ice shelves and, through them, ice sheets would alter the Earth's albedo, providing a feedback on warming (e.g. Budd et al., 1998). On multi-century timescales, the melting of an ice shelf or sheet will change the planet's topography, with consequences for atmospheric dynamics such as changes to precipitation patterns and altered stationary wave patterns (Roe and Lindzen, 2001). Similar processes as those affecting ice shelves may be important in the dynamics of a past Snowball Earth (e.g. Goodman and Pierrehumbert, 2003) or for icy moons elsewhere in the solar system (e.g. Hurford and Brunt, 2014).

Given the many roles which ice shelves play in the climate system, it is important to understand their stability against melting and mechanical failure. Channels have been observed melted into the base of ice shelves, which are of interest as they may affect the stability of the ice. The formation of channels running parallel to the direction of ice flow is thought to be well understood, but less clear is the origin of channels observed running in the transverse direction. This thesis seeks to evaluate the suggestion that seasonal forcing could give rise to the initial perturbations which grow into transverse channels, using a mix of analytic and numerical modelling techniques.

The next section of this chapter will discuss the properties of ice shelves and the nearby oceans, particularly as they relate to melting. In § 1.3, the topography of the basal surface of ice shelves is discussed, focusing on the channels which have been observed etched into the bottom of many shelves. The equations typically used to model ice shelves and their associated meltwater plumes are presented in § 1.4. The chapter ends with the formulation of the research question for this thesis and gives an outline of the remainder of the dissertation.

1.2 Properties of Ice Shelves and the Adjacent Ocean

Ice shelves (see diagram in figure 1.1) originate at a *grounding line*, which is the location where an ice sheet becomes sufficiently thin to float on the ocean in approximate hydrostatic equilibrium, although stresses near the grounding line may cause it to deviate from this to some degree (Schoof and Hewitt, 2013). An ice shelf will then progressively thin by a combination of basal and surface ablation and viscous stretching until it reaches a *calving front*, where icebergs break off. Ice shelves can reach sizes of order 100 km in length and tens (Greenland) to hundreds (Antarctica) of kilometres wide (Wilson et al., 2017; Rignot, Jacobs, et al., 2013). They range from hundreds of metres to over a kilometre thick at the grounding

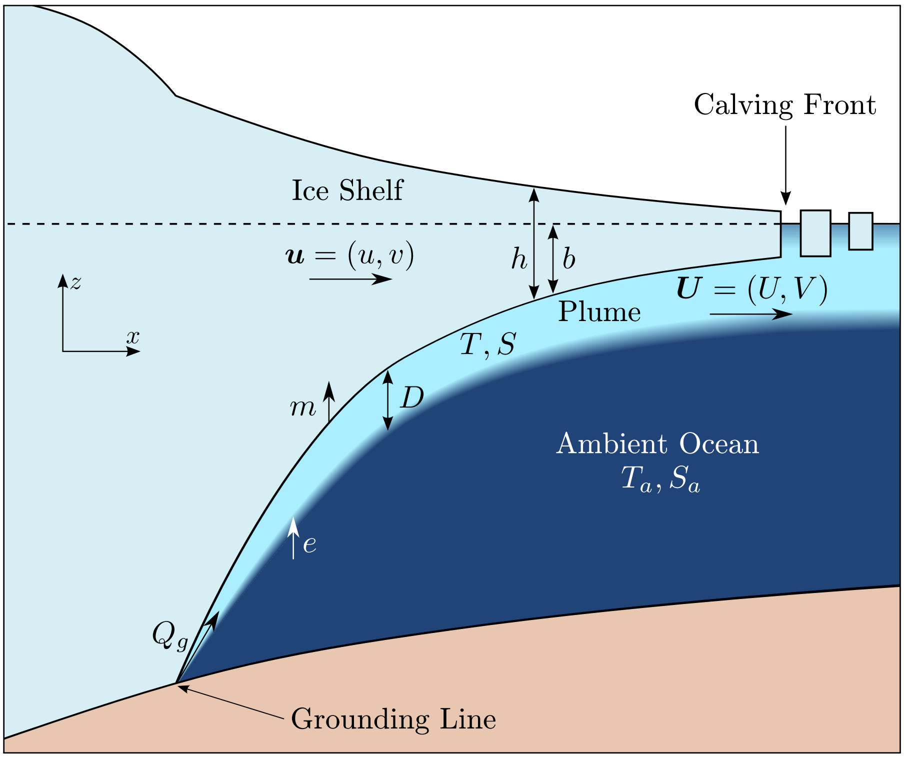

Figure 1.1: A simplified diagram of an ice shelf and plume. The symbols on the diagram are used in § 1.4. The ice flow has a vertically integrated velocity $\boldsymbol{u}$, with longitudinal and transverse components u and v, respectively. h is the thickness of the ice shelf, while b is the depth of its lower surface below sea level. Subglacial discharge at the grounding line, with volume flux Q_g, feeds a plume of thickness D flowing underneath the ice shelf with vertically integrated velocity $\vec{U}$. This velocity also has longitudinal, U, and transverse, V, components. The plume has a temperature, T, and salinity, S, which drive melting m at the base of the ice shelf. The plume is further fed by turbulent entrainment, e, of the ambient ocean water. This water has its own temperature and salinity: T_a and S_a, respectively.

line, tapering down to a few tens or hundreds of metres at the calving front (Cuffey and Paterson, 2010). Ice shelf meltwater is relatively fresh and thus buoyant in the saline seawater, causing it to flow up the sloped underside of the ice shelf in a plume, as first modelled by MacAyeal (1985) and Jenkins (1991). The ocean water in the ice shelf cavity underneath the plume is warmer than the melting point of ice and hence provides a source of heat for the melting. The shear between the plume and the ambient ocean causes warm seawater to be entrained into the plume, providing more heat with which to drive further melting. The salt from the ocean water acts to depress the melting point of the ice (Woods, 1992), also promoting melt. Subglacial discharge (meltwater which accumulates underneath the ice sheet and flows out through the grounding line) can act to initiate the plume. While ablation can also occur on the upper surface of an ice shelf, the process described above tends to be the dominant source of mass loss (e.g. Rignot and Steffen, 2008).

1.2.1 Basal Melting

As described above, heat and salt from the ocean cause melting on the lower surface of ice shelves. Melt rates on the order of $1\,\mathrm{m\,yr^{-1}}$ have been reported on the Ronne Ice Shelf (Jenkins, Corr, et al., 2006) and appear to be typical for Antarctica (Rignot, Jacobs, et al., 2013). The three remaining Greenland ice shelves tend to have melt rates which are an order of magnitude larger (e.g. Rignot and Jacobs, 2002; Rignot and Steffen, 2008; Wilson et al., 2017). High melt rates ($\gtrsim 10\,\mathrm{m\,yr^{-1}}$) have also been observed on some Antarctic ice shelves adjacent to relatively warm ocean water, such as Pine Island Glacier (e.g. Jacobs, Jenkins, Giulivi, et al., 2011; Stanton et al., 2013; Dutrieux, Vaughan, et al., 2013). Basal melt makes up over half of mass lost by Antarctic ice shelves, considerably more than previously thought, and is particularly important for those ice shelves in contact with warm water in Western Antarctica, as illustrated in figure 1.2 (Rignot, Jacobs, et al., 2013). A wide variety of factors influence the magnitude and distribution of melt, as reviewed below.

Observations and results from a three dimensional ocean model with a static ice sheet show that melt is the most rapid in regions of large basal slope, as this is where warm ambient water is most rapidly entrained (Dutrieux, Stewart, et al., 2014; Little, Gnanadesikan, et al., 2009). Because basal slope is highest near the grounding line and high pressures at these depths reduce the melting point of ice, the fastest melting tends to occur here (e.g. Rignot and Steffen, 2008; Dutrieux, Vaughan, et al., 2013; Wilson et al., 2017). The majority of the melting happens over the next few tens of kilometres, as the heat of the plume is used. Under the remainder of the shelf, relatively little melting occurs and most of the heat carried in the plume will be advected away (Little, Gnanadesikan, et al., 2009). While ice-shelf shape would seem to affect the melt rate, the state of the ice shelf and the plume are tightly coupled in all but the lowest-melt settings (Sergienko et al., 2013), making

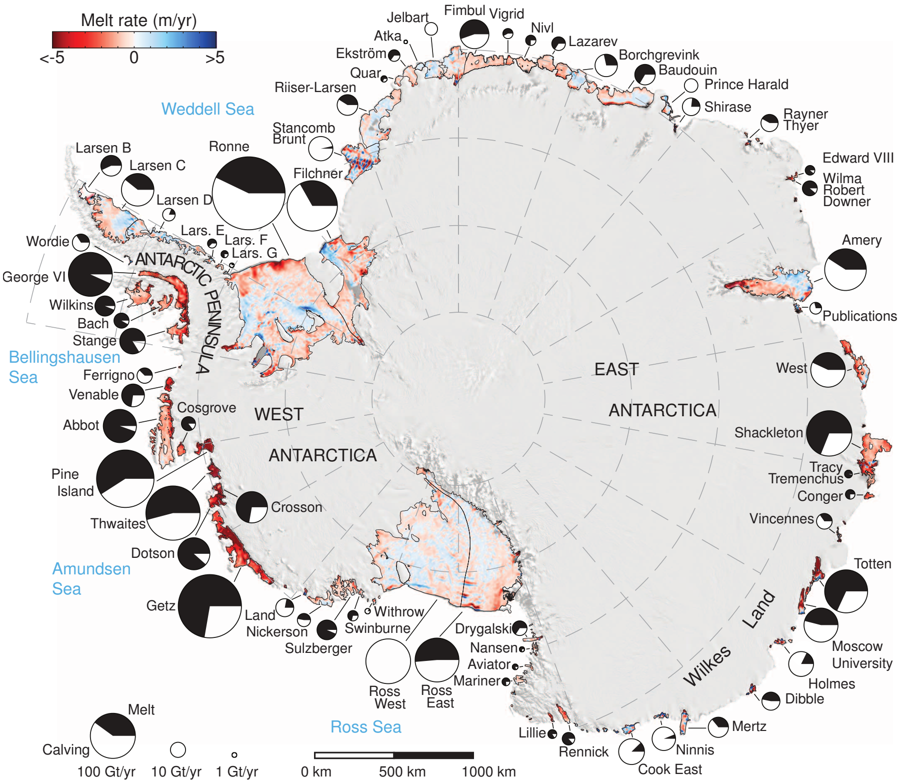

Figure 1.2: Pie charts show the fraction of mass loss in each named ice shelf around the Antarctic coast due to basal melting (black) compared to that due to calving (white). Colours indicate melt rates under each ice shelf. *(Image source: Rignot, Jacobs, et al., 2013)*

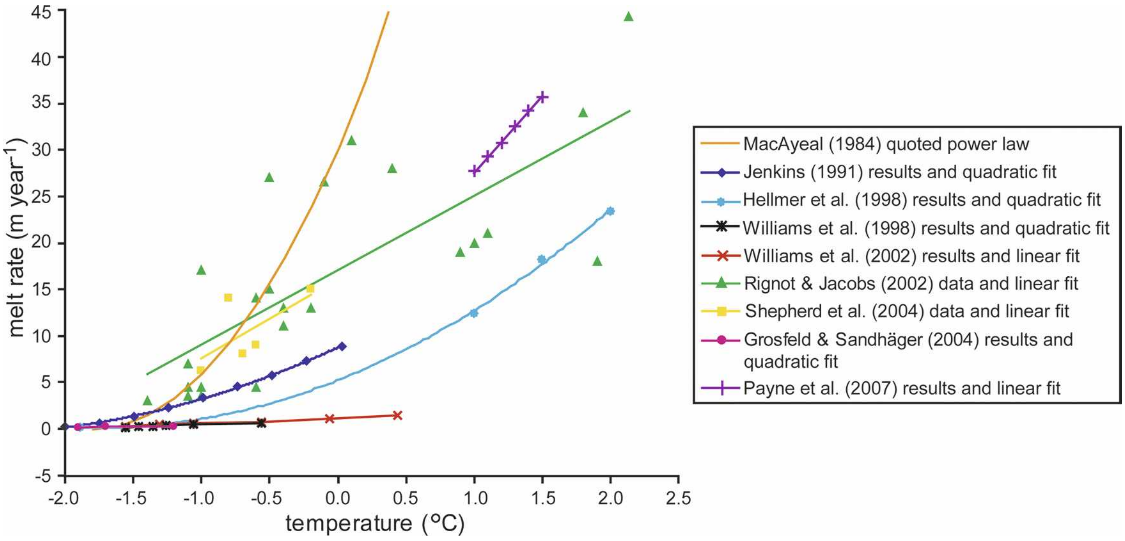

Figure 1.3: The results of various studies relating ice shelf melt rates to ocean temperatures near the ice shelf. The studies of Rignot and Jacobs (2002) and Shepherd, Wingham, et al. (2004) were observational, while the remainder were modelling studies. *(Plot source: Holland et al., 2008)*

it difficult to untangle cause and effect and meaning that uncoupled simulations, such as that of Little, Gnanadesikan, et al. (2009), must be viewed with caution.

As would be expected, the melt rate underneath ice shelves appears to increase with the difference between the melting point of ice and the ocean temperature. However, there is little agreement between studies on the functional dependence of melt rate on temperature, as can be seen in figure 1.3 (Holland, Thomas, et al., 2008). Observational data from within ice shelf cavities is sparse. While indicating a positive trend between melt and temperature, it is noisy (Rignot and Jacobs, 2002; Shepherd, Wingham, et al., 2004). Jenkins (2011) and Walker, Holland, et al. (2013) both used similar one dimensional vertically integrated plume models (see § 1.4.2) to evaluate the dependence of melt rate on temperature. The former found a linear relationship in the immediate vicinity of the grounding line, where subglacial discharge is the main source of buoyancy, while there was an unspecified nonlinear relationship elsewhere. Walker, Holland, et al. (2013) found a power law dependence between the maximum melt rate and temperature. An earlier suite of two dimensional plume simulations found what also appeared to be a linear relationship, although this was over a much smaller range of temperatures (Payne et al., 2007). Gladish et al. (2012) and Sergienko (2013) also performed two dimensional plume simulations coupled to an evolving ice shelf and found that melt rates increased with ocean temperature. Interestingly, Gladish et al. (2012) found that lowering the temperature below a certain threshold resulted in a drastic reorganisation of melting leading to increased melting overall. However, these simulations were subject to numerical difficulties, so it is unclear whether this is a realisable physical effect.

Using a fully three dimensional general circulation model (GCM), Holland et al. (2008) found a quadratic relationship between melt rate and temperature. Given the complexity of the model used, the quadratic curve fit the data with a remarkable degree of accuracy. By simplifying the equations, Holland et al. (2008) identified that the melt rate was determined by the product of the temperature difference between the ocean and the melting point and the velocity at which the plume moved beneath the ice shelf. In regions where meltwater was the dominant source of buoyancy, Jenkins (2011) also found that the melt rate was a product of plume temperature and velocity, the latter itself a function of temperature. While Jenkins did not investigate any further, Holland et al. (2008) found that the plume velocity varied linearly with temperature: higher temperatures resulted in greater melting of the ice shelf, with the resulting fresh water lowering the plume density and increasing its buoyancy. Under the prevailing geostrophic balance, increased buoyancy led to faster across-shelf flow. The exact value of the coefficients in the quadratic were found to depend on the shape of the ice shelf and the basal topography. While this was the first study to identify a quadratic relationship rather than a linear fit or other power law, Holland et al. (2008) found that the data could be fit with a reasonable degree of accuracy by a power law similar to those used in most other studies, and that most of those studies finding linear results were looking at too small a range of temperatures to be able to identify nonlinear behaviour. It should be noted that the simplicity of the relationship between melt rate and temperature found here may, in part, be due to the parameterisations used to describe thermal transfer, which are linear with the plume velocity. Some simulations, such as those by Sergienko (2013), used a more complicated relationship, although this would not necessarily have a large impact on the results. A later 3-D study using a nonlinear parameterisation and a different scheme for vertical discretisation reproduced these results (Gwyther, Cougnon, et al., 2016), suggesting the linear thermal transfer was not a determining factor.

Changing the distribution of water temperature can also alter melting. Sergienko et al. (2013) found that, beneath ice shelves where the bottom layer of water was already relatively warm, allowing the warm water to impinge into shallower depths resulted in a greater increase in melting than did increasing the temperature of the deep water. However, beneath ice shelves where the water was initially colder, the opposite was found. In both settings, the melt rate increased with the thickness of the ice shelf, as thicker ice penetrates into deeper water with higher pressure, where the melting temperature is thus lower.

Another parameter which can influence the melt rate of ice shelves in models is subglacial discharge. Jenkins (2011) found that melt rates scaled with the cube root of the discharge rate. Gladish et al. (2012) recorded a linear change in melt rate with subglacial discharge, up to the threshold at which the ice shelf became unstable. Note that while ocean temperature could only plausibly vary by a few degrees, plausible subglacial discharge rates span several orders of magnitude, so this mechanism could potentially greatly influence the melt rate.

In addition to parameters which might vary naturally, the melt rate depends on parameters which are intrinsically constant but poorly constrained. For example, Millgate et al. (2013) report changes to melt rate depending on the eddy viscosity used to parameterise turbulence, with increased viscosity generally leading to higher melt rates. Similarly, a plume model found that melting increases with basal drag (Walker, Holland, et al., 2013). However, this is only true when entrainment depends on basal drag—otherwise the resulting decrease in plume velocity due to drag leads to decreased melting. Similar experiments run with a fully 3-D ocean model also showed melt increasing with drag but found that, in warm cavities, there was a maximum drag coefficient beyond which the melt rate plateaued (Gwyther, Galton-Fenzi, et al., 2015). Finally, a very weak negative correlation between ocean salinity and melting has been noted by Payne et al. (2007).

None of the above analysis accounts for tidal mixing, in which the velocity of the ocean imparted by tidal forcing would alter the entrainment and turbulent salt and heat transfer rates. This would be expected to be most significant near the grounding line, where in-flowing water would be moving the fastest and there is minimal vertical mixing required. A simplified 1-D model used by Holland (2008) indicated that there would only be a significant zone of tidal mixing (where the plume model would break down) underneath an ice shelf with a shallow basal slope, in cold water. A study using a full ocean circulation model for the Larsen C Ice Shelf, however, found that tidal effects were significant (Mueller et al., 2012). Without tidal mixing, melt was strongest at the grounding line, while with it the melt was concentrated around two peninsulas at the grounding line and in a region in north-east of the shelf, near the calving front. However, in all simulations this ice shelf had a very small melt rate ($\lesssim 0.5\,\mathrm{m\,s^{-1}}$), suggesting that perhaps these effects would not be so significant in a more rapidly melting ice shelf where tidal forces would be small compared to buoyancy and plume dynamics would thus dominate the flow. (Gwyther, Cougnon, et al., 2016) also found that the inclusion of tidal forcing changed the distribution of melt, as well as increasing the rate slightly. In this case simulations were run in a cavity with idealised geometry. However, here the melt became more concentrated near the grounding line, eastern boundary, and calving front. Changes to the melt rate and pattern were much more dramatic for cold cavities with low non-tidal melt rates, as postulated above.

Because the melting point of ice decreases with increasing pressure (and hence increasing depth), water which is at or above the freezing point at the grounding line will become super-cooled as it rises in the plume, assuming it experiences no external heating. In the super-cooled regions, ice crystals form in suspension (so-called *frazil ice*), which, once large enough, precipitate onto the ice shelf bottom forming marine ice (e.g. Bombosch and Jenkins, 1995; Smedsrud and Jenkins, 2004). This behaviour, in which ice is melted near the grounding line and refrozen closer to the calving front, is called an *ice pump* (Lewis and Perkin, 1986). However, this does not occur for ice shelves with shallow grounding lines or in contact with warmer ocean water. This report focuses on ice shelves meeting the latter criteria and, as such, ice pump behaviour is ignored hereafter.

In summary, many factors are important to determining the basal melt rates of ice shelves. There is a positive correlation between melting and ocean temperature, although the form of this dependence remains unclear and it may depend on the dynamical balance in a particular cavity. The most vigorous melting tends to occur near the grounding line, where the ice is deepest in the ocean, hence having the lowest pressure-dependent melting point and being in contact with the warmest water. The shape of the ice shelf affects the melt rate, meaning that the ice and ocean are tightly coupled systems. Melt rates have also been shown to depend on subglacial discharge, eddy viscosity, and turbulent drag.

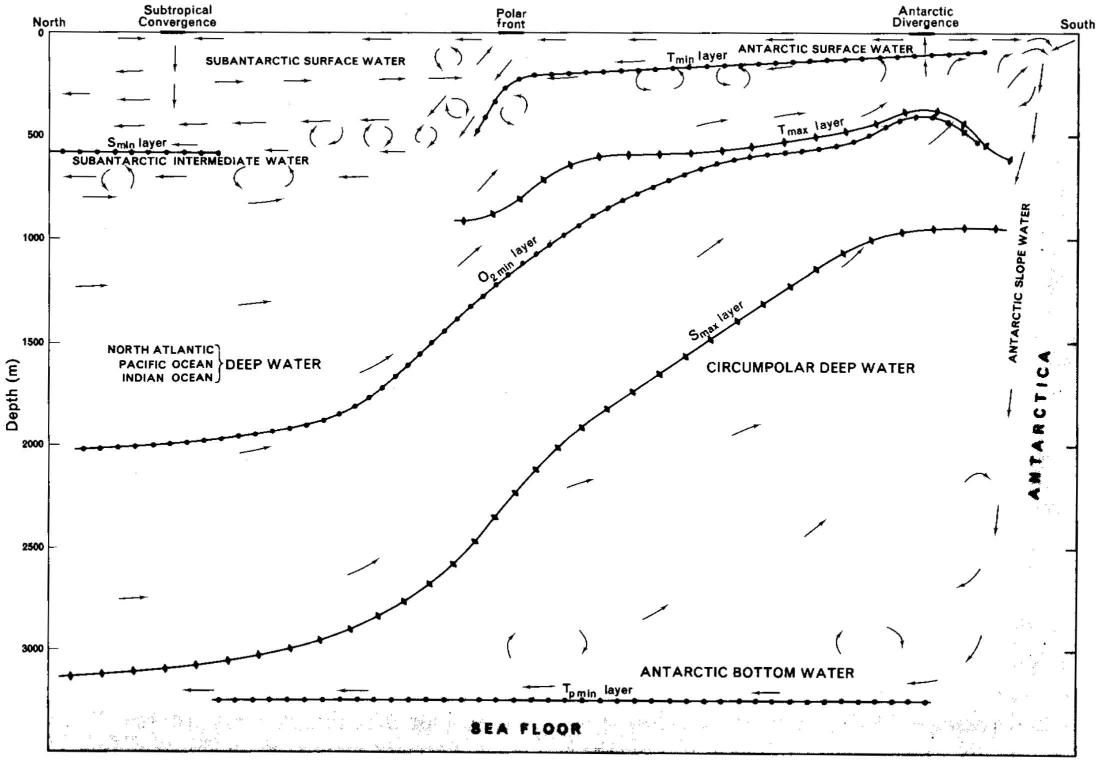

Figure 1.4: A simplified diagram of the water masses present around Antarctica. *(Image source: Foldvik and Gammelsrød, 1988)*

1.2.2 Ocean Properties

As much of the melting of ice shelves is driven by the ocean, it is important to understand ocean properties near them. The Southern Ocean consists of cold, relatively fresh Antarctic Surface Water (AASW, flowing away from the pole) and warmer, saline Circumpolar Deep Water (CDW, flowing towards the pole), with other deep water masses (originating in the Atlantic, Pacific, or Indian oceans) filling the space in between, as shown in figure 1.4 (Foldvik and Gammelsrød, 1988). Beneath all of this lies a flow of very cold Antarctic Bottom Water at the sea floor (Foldvik and Gammelsrød, 1988). Water on the continental shelf around Antarctica tends to be stratified in two layers: AASW and somewhat warmer bottom water, separated by a thermocline (e.g. Jacobs, Hellmer, et al., 1996; Smith et al., 1999; Nicholls and Østerhus, 2004; Jacobs, Jenkins, Hellmer, et al., 2012). Around most of Antarctica the lower layer remains relatively cold however, often with potential temperatures of $-2°$ C. In these cold areas, the mass of water below the upper mixed layer is formed by High Salinity Shelf Water (HSSW), produced during sea ice formation, which can then flow into the cavity beneath ice shelves (Nicholls and Østerhus, 2004). Along with super-cooled ice shelf melt water (Ice Shelf Water, ISW), which can be dense enough to sink beneath the AASW too, the HSSW could also flow over the ledge of the continental shelf (Foldvik and Gammelsrød, 1988; Nicholls and Østerhus, 2004). In the Amundsen and Bellingshausen Seas (West Antarctica), bottom potential temperatures can reach over $1°$ C (Schmidtko et al., 2014).

In the West Antarctic seas, where the most vigorously melting ice shelves are present, the bottom layer of the ocean has been found to have similar properties to the Circumpolar Deep Water (CDW) found in the Antarctic Circumpolar Current, or ACC (Jacobs, Hellmer, et al., 1996; Jacobs, Jenkins, Hellmer, et al., 2012). The upper layer of CDW is modified by partially mixing with the AASW. The warm modified CDW will diffuse some heat into the water above, explaining why even the surface temperatures in the Amundsen and Bellingshausen seas are warmer than elsewhere around Antarctica (Smith et al., 1999; Jacobs, Jenkins, Hellmer, et al., 2012). Smith et al. (1999) observed that the upper 100–200 m of the ocean in this region consists of AASW with relatively low salinity and temperatures near freezing. During the summer, solar radiation and melting of sea ice warms and freshens the upper 20–30 m of water, while mixing from storms results in the creation of several distinct layers. During the autumn and winter, as warming stops and storms increase, the surface layer eventually becomes well-mixed again. It also cools considerably during these months, forming Winter Water (Costa et al., 2008).

Observations have indicated that CDW flows onto the continental shelf near West Antarctica through a series of channels (Klinck et al., 2004; Arneborg et al., 2012; Wåhlin et al., 2013; Assmann et al., 2013). This finding has also been replicated in modelling studies (Thoma et al., 2008; Dinniman et al., 2012; Assmann et al., 2013; Nakayama et al., 2014). However, there is disagreement over the exact mechanism responsible. Some studies (e.g. Klinck et al., 2004; Jacobs, Jenkins, Hellmer, et al., 2012; Walker, Jenkins, et al., 2013) suggest that the ACC is diverted by basal topography to flow onto the continental shelf. Others (e.g. Thoma et al., 2008; Dinniman et al., 2012) suggest that transport is driven by wind forcing. There is also debate over the degree of variability in this flow. Those modellers who found that transport of CDW was driven by winds indicated that there was significant seasonal variability. Klinck et al. (2004) suggest that CDW is carried onto the shelf in distinct intrusion events. There are some hints of seasonal variability in the observations of Wåhlin et al. (2013), although the observational period was too short to be conclusive. These variations in inflow had the effect of raising the thermocline on the continental shelf at certain times of year. However, other observations suggest that CDW transport is fairly steady (Arneborg et al., 2012; Walker, Jenkins, et al., 2013), and a combined observational and computational study by Assmann et al. (2013) showed that 70% of the heat transport is due to persistent inflow. A high-resolution simulation run by St-Laurent et al. (2015) suggested that heat loss through polynyas was a key driver of seasonal variability in ocean heat content and ice shelf melting in the Amundsen Sea. However, Jenkins, Dutrieux, Jacobs, Steig, et al. (2016) noted that seasonal wind patterns also affect such surface processes, these surface processes could not explain observed warming at depth, and that observed variations in heat were compatible with the results of Thoma et al. (2008). Despite some issues, Jenkins, Dutrieux, Jacobs, Steig, et al. (2016) concluded that the work of Thoma et al. (2008) still represents a plausible mechanism for forcing the movement of warm water onto the continental shelf. A set of mooring-based observations noted seasonal variation of heat transport onto the continental shelf and found that it correlated well with Ekman pumping due to sea ice drag (Kim et al., 2017). The strength of this pumping depended on ice extent and seasonality was thus due to variations in the size of polyanas rather than wind strength. It has also been suggested that surface heat flux processes may explain seasonal variations in ocean temperature at shallower depths, while altered ocean flow patterns (likely driven by local wind conditions) explain deeper and interannual variability (Webber Benjamin G. M. et al., 2017). Clearly, considerable uncertainty remains regarding the nature of warming events in the Amundsen Sea.

It is the ocean conditions in the cavities underneath ice shelves which affect their melting and not those in front of them. In particular, the most vigorous melting occurs at the grounding line, at the extreme end of the cavity. As such, understanding the transport of CDW onto the continental shelf is insufficient; its transport into the sub-ice shelf cavity is also important. This is not necessarily strait-forward to estimate, with Dinniman et al. (2012) finding that there were complex interactions between melt rates, CDW flux, and westerly winds, which made understanding the impact of a single factor difficult. Time scales for ventilating the cavities beneath ice shelves are also important. These tend to be interannual (Jenkins, Holland, et al., 2004; Mueller et al., 2012), suggesting that seasonal variations in the ocean in front of the ice shelf may have little direct impact on seasonality of melt at the grounding line. More recent work by Holland (2017) showed that even if variation occur on a timescale shorter than the ventilation period, they can still produce some change in melting, although this is smaller than would be expected based solely on the magnitude of temperature change at the calving front. Ventilation tends to occur more quickly for warm-cavity ice shelves, so in these cases seasonal variability at the front can still have some significant effect near the grounding line. Shallower ice shelves, such as George VI Ice Shelf, appear to be more affected by changes in the ocean driven by surface processes (Holland et al., 2010). Highly local factors, such as bathymetry, can also be important. An example of this would be Pine Island Glacier, in the cavity of which there is a prominent ridge. Autosub3 observations show that, while CDW penetrates well into the cavity in front of the ridge, it has trouble accessing behind the ridge (Jenkins, Dutrieux, Jacobs, McPhail, et al., 2010; Dutrieux, De Rydt, et al., 2014). However, fast, turbulent flow of water over the ridge has resulted in higher melt rates in the ice above it, widening the gap and making it easier for CDW to access the posterior cavity (Jenkins, Dutrieux, Jacobs, McPhail, et al., 2010).

In contrast to Antarctica, access of water from the continental shelf to ice shelves around Greenland is mediated by the presence of fjords (see Straneo and Cenedese, 2015, and references therein for a broad review of fjord properties). Much like the shelf water outside of them, water in fjords tends to consist of a cold, relatively fresh upper layer of polar origin and a warmer, more saline lower layer of Atlantic origin. There is also at least one layer modified by fresh glacial meltwater, at the surface or between the Atlantic and polar water. Some of the circulation within fjords may be the result of these buoyancy-driven flows. More important, however, are the intermediary flows, driven by density variations outside of the fjord. Such variations can arise from up- or down-welling caused by wind or from advection of density anomalies past the mouth of the fjord. If the fjord is sufficiently wide, then this circulation will be geostrophic. This mechanism would be able to flush the upper to mid-depth fjord water in a time scale of about two months. The deepest fjord water is often separated from the ocean by a sill and fed by dense water which flows over the sill and entrains shallower fjord water. Less is known about the circulation of this water, which would be in closest contact with an ice shelf grounding line; studies estimate renewal time scales ranging from months to decades (Straneo and Cenedese, 2015, and references therein).

To summarise, oceans near ice shelves tend to be stratified into two layers, with a cold, relatively fresh layer sitting atop a warmer, more saline one. Around most of Antarctica, the bottom layer consists of cold HSSW, but in the Amundsen and Bellingshausen Seas it is made up of warmer CDW which has intruded onto the continental shelf. The rate at which CDW crosses onto the shelf may vary seasonally, but this remains uncertain. The ocean around Greenland is similarly stratified, but warm water must intrude into a fjord before it can reach an ice shelf. In all cases, the ocean water must move from the calving front to the grounding line of an ice shelf, a process for which the timescale is thought to be interannual for the larger shelves.

1.2.3 Basal Hydrology and Subglacial Discharge

Glaciers in Greenland have been observed to accelerate during the summer, increasing in speed by over 100% in some cases (e.g. Zwally et al., 2002; Joughin et al., 2008; Bartholomew et al., 2010). This acceleration correlates with increased surface melt in many cases. It is believed that summer-time surface melt was able to make its way to the glacier base via cracks and moulins, where it lubricated basal sliding and caused accelerated ice flow into the ocean (Zwally et al., 2002; Das et al., 2008; Bartholomew et al., 2010). It is expected that the subglacial drainage system would be modified in response to this increased volume flux with the potential to further affect basal sliding, as discussed by Schoof and Hewitt (2013). Of particular interest her is that this meltwater can enter the ocean at the base of a tidewater glacier or ice shelf, providing the source of subglacial discharge. This discharge will vary seasonally and is strongest during the summer (Straneo and Cenedese, 2015). Less is known about subglacial hydrology in Antarctica, but there is evidence suggesting that some channels on ice shelves connect to drainage channels beneath the upstream ice sheet (e.g., Le Brocq et al., 2013). Combined satellite and modelling data also indicate that outflow from subglacial lakes varies over time (Carter and Fricker, 2012). This could drive oscillations in subglacial discharge and ice velocity for Antarctic ice shelves as well.

1.3 Basal Topography

Observational surveys have revealed the existence of extensive networks of channels on the undersides of some ice shelves. Channels are variations in basal depth of ice shelves, reaching up to a few hundred metres in height and typically a few kilometres in width (e.g. Rignot and Steffen, 2008; Vaughan et al., 2012). Narrower and shallower channels have also been observed (Langley et al., 2014; Drews, 2015). Channels have been most extensively studied in the ice shelves associated with the Petermann Glacier (Rignot and Steffen, 2008; Dutrieux, Stewart, et al., 2014) and Pine Island Glacier (Payne et al., 2007; Mankoff et al., 2012; Vaughan et al., 2012; Dutrieux, Stewart, et al., 2014). However, they appear to be widespread and have also been observed under the Amery Ice shelf (Fricker et al., 2009), Filchner-Ronne Ice Shelf (Le Brocq et al., 2013), Fimbul Ice Shelf (Langley et al., 2014), Roi Baudouin Ice Shelf (Drews, 2015), Ross Ice Shelf (Marsh et al., 2016), Nansen Ice Shelf (Dow et al., 2018), and various other areas around Antarctica (Alley, Scambos, et al., 2016). A map of locations of channels in ice shelves can be found in figure 1.5

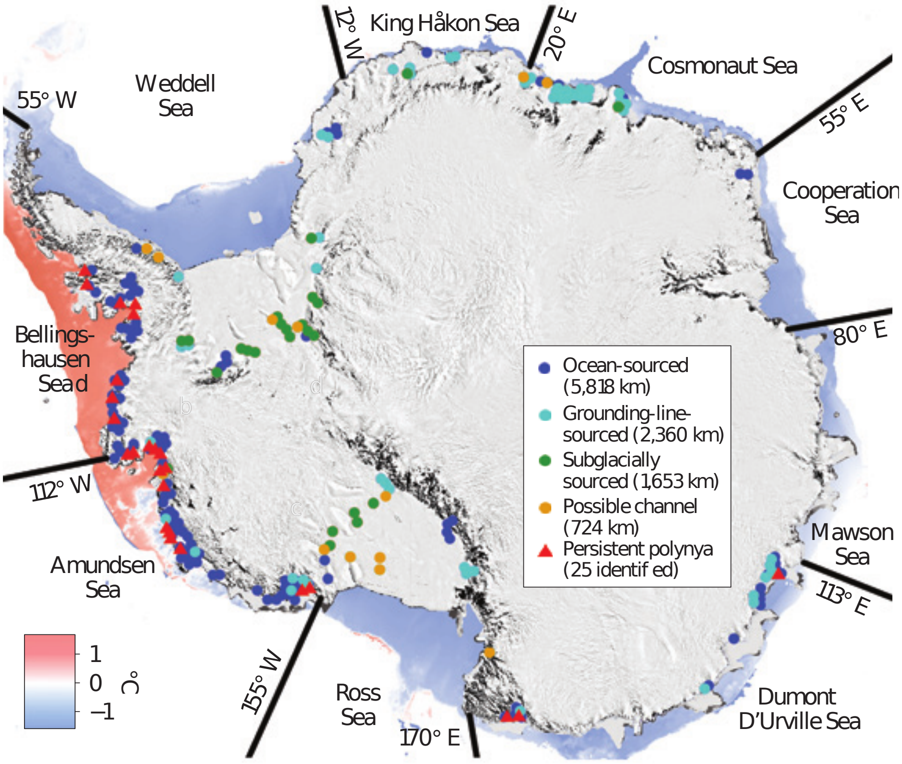

Figure 1.5: Locations of channels in ice shelves around Antarctica. These are classified according to where they are initiated (see legend, which also gives the total length observed). Each dot represents 50 km of channel. Colour around the continent indicates ocean temperatures at depths shallower than 1500 m. *(Image source: Alley, Scambos, et al., 2016)*

(Alley, Scambos, et al., 2016). The basal topography can be measured using airborne radar (e.g. Vaughan et al., 2012; Le Brocq et al., 2013; Alley, Scambos, et al., 2016), satellite-based radar (e.g. Rignot and Steffen, 2008) or imagery (e.g. Alley, Scambos, et al., 2016), surface altimetry coupled with assumptions of hydrostatic equilibrium (e.g. Payne et al., 2007; Bindschadler, Vaughan, et al., 2011; Alley, Scambos, et al., 2016; Gourmelen et al., 2017; Dow et al., 2018), ground-based radar (e.g. Dutrieux, Stewart, et al., 2014), and autonomous underwater vehicles using sonar (e.g. Vaughan et al., 2012; Dutrieux, Stewart, et al., 2014).

Using satellite imagery and altimetry data, in addition to airborne radar data, Alley, Scambos, et al. (2016) identified three categories of channels: those beginning away from the grounding line (hereafter, *ocean sourced*), those beginning at the grounding line where sources of subglacial discharge are believed to occur (hereafter, *subglacially sourced*), and those beginning at the grounding line away from suspected sources of subglacial discharge (hereafter, *grounding line sourced*). Ocean and subglacially sourced channels were found to deepen along the flow. All channel types tended to have steeper western walls, presumably as a result of Coriolis forces steering flow and heat transfer in the ocean beneath the channel. Channels were found to be most common on ice shelves exposed to warm oceans, such as those in Western Antarctica (Alley, Scambos, et al., 2016), but have also been observed under ice shelves where the ocean is only slightly warmer than the freezing point (Langley et al., 2014). In addition to the types of channels described above, Fricker et al. (2009) and Dow et al. (2018) identified channels on the Amery and Nansen Ice Shelves (respectively) which form in the suture zones where ice streams join. Dow et al. (2018) suggest that in, the case of the channel on Nansen Ice Shelf, this is due to one of the ice streams being thicker than the other, causing a large basal gradient in the suture zone. This gradient promotes plume flow and hence basal melting.

Observations by Dutrieux, Stewart, et al. (2014) have revealed that channels beneath Petermann and Pine Island Glacier (PIG) ice shelves do not have smooth sides. Instead they consist of flat terraces ranging from tens to hundreds of metres across, joined by steep slopes with elevation changes of 20–40 m. It was also noted that the melting rate remained fairly constant across each terrace but would jump between them.

Both Vaughan et al. (2012) and Dutrieux, Stewart, et al. (2014) found indications of crevasses above the vertices of channels in the Pine Island ice shelf. The former measured the crevasses to have widths of 50–100 m and heights of at least 30 m and as much as 210 m, while the latter measured widths of about 200 m. Ridges were observed on the surface of the ice shelf between channels and were found to feature extensive surface crevasses (Vaughan et al., 2012). A linear-elastic thin beam model was proposed to explain the formation of these crevasses. The region of the ice shelf in which channels form would no longer be in hydrostatic equilibrium with the ocean and, as such, the surface above the channels would tend to sag, forming the aforementioned ridges on the surface between channels. This would cause compression of the ice above the channels and extension of ice on the ridges. The mechanical stress from the extension would cause crevasses to form. Similarly, on the base of the ice shelf, compression would occur between the channels and extension at the channels' apexes, causing crevasses to form at the latter. Vaughan et al. (2012) tested this hypothesis numerically using a finite element model, which produced the expected patterns of stress, although it was not sophisticated enough to be able to model the actual fracture process. Such a process would weaken ice shelves and could lead to their disintegration. Additionally, crevasses capable of fracturing the ice shelf have been observed running transverse to channels (Dow et al., 2018). These are thought to form in regions where the ice is thinnest (e.g., due to channels) and is laterally constrained, preventing longitudinal cracks from developing. The indentations between ridges have been found to funnel surface melt-water into rivers on the Nansen and Petermann Ice Shelves (Dow et al., 2018).

Stanton et al. (2013) found that melt occurred at the apex of a channel in the PIG ice shelf but hardly at all on the keel. However, Dutrieux, Stewart, et al. (2014) found a more complicated relationship, with melt being highest at apexes near the grounding line and highest at the keels farther away. The locations where Stanton et al. (2013) took their data fell in the region where Dutrieux, Stewart, et al. (2014) found melting to be most pronounced on the keels. However, while Stanton et al. (2013) measured the melt rate by drilling through the ice, Dutrieux, Stewart, et al. (2014) calculated it from the mass balance, suggesting that more weight should be given to the direct measurements of the former. Using ice-penetrating radar to measure ice thickness around a channel on the Ross ice Shelf over several weeks, Marsh et al. (2016) also found the melt to be highest at the channel apex.

Various numerical studies have shown that the melt-water plume from the ice shelf tends to be directed along the channels. This result is robust across a range of modelling approaches: linear stability analysis (Dallaston et al., 2015), ocean plume models with a static ice shelf Payne et al., 2007; Millgate et al., 2013, and coupled ice shelf/ocean plume models (Gladish et al., 2012; Sergienko, 2013). Such channelised flow would increase entrainment within channels, transferring more heat from the ambient ocean to the ice shelf and thus causing increased melt and deepening the channel. Channelisation of warm water is supported by the observation of persistent polynyas in front of the PIG ice shelf corresponding to the positions of channels (Mankoff et al., 2012). Thus, if some perturbation initiates a channel, this channelisation feedback effect would allow it to grow. Multiple studies have established that variability in the underlying topography at the grounding line can provide such a perturbation (Gladish et al., 2012; Sergienko, 2013; Dallaston et al., 2015).

In a highly simplified linear perturbation analysis, it was found that variation in subglacial discharge along the grounding line can also cause channelisation (Dallaston et al., 2015). In this case, the increased flux of melt-water in some regions along the grounding line cause increased melting in those areas, creating the beginnings of a channel. The meltwater flow channelisation feedback then acts to grow the channel along the length of the ice shelf. This is in keeping with observations which found that basal channels on the Filchner-Ronne ice shelf (Le Brocq et al., 2013), along with many others (Alley, Scambos, et al., 2016), were aligned with the predicted locations for outflow of subglacial discharge. On the Ross Ice Shelf, melt rates are strongest just behind the starting location of a channel (Marsh et al., 2016). This, coupled with a nearby system of draining lakes on the surface of the ice, led Marsh et al. to conclude that this channel was also initiated by subglacial discharge.

Sergienko (2013) demonstrated that shear stress at the shelf boundaries can cause spontaneous channelisation, even without variations in basal topography or subglacial discharge at the grounding line. The shear stress causes a laterally nonuniform basal profile for the ice shelf, which is then exaggerated via the melt-driven feedback. This causes further stress in the shelf, resulting in the warping of its interior and the formation of channels. Like Vaughan et al. (2012), Sergienko (2013) found that the stress caused by channels in ice shelves was sufficient to cause the ice to fracture and form crevasses. This, combined with the fact that channels can drastically thin the ice shelves at their apex (Rignot and Steffen, 2008) and can feature higher melting rates than the surrounding ice (Gourmelen et al., 2017), suggests that channels could encourage the breakup of ice shelves. Furthermore, the surface rivers observed above channels by Dow et al. (2018) could further thin the ice shelf through erosion and, when they flow into a crevasse (as on Nansen Ice shelf), enlarge cracks through hydrofracture.

On the other hand, running simulations of a Petermann-like ice sheet, Gladish et al. (2012) and Millgate et al. (2013) found that increasing the number of channels in an ice shelf of fixed size, and hence decreasing the width of the channels, tends to decrease the overall melt rate. This was because the channel keels tended to impede large scale geostrophic flow over the full extent of the ice shelf, causing the plume to move more slowly and thus be less effective at transferring heat from the ambient ocean. While this was not analysed, the results of simulations of a PIG-like ice shelf by Sergienko (2013) are broadly in agreement, as average melt rates in shelves featuring channels are similar to or smaller than those without. This was true even in cases where the Coriolis forces were neglected, potentially indicating that geostrophic balance is not the only mechanism responsible for this effect. The tendency of channels to reduce overall melt rates may act to preserve ice shelves. As a result of these contrasting impacts on fracture and melt, the net effect of channels on ice shelf stability remains unclear. Nonetheless, if ice shelf stability is assessed only from the area-averaged melt rate and fails to account for the potentially higher melt within channels then ice shelf stability will be overestimated (e.g. Gourmelen et al., 2017).

There may be a preferred scale for channel formation: Dallaston et al. (2015) found that steeper slopes, caused by narrower channels, amplify the channelisation effect, while narrower channels tend to be smoothed out by modelled eddy diffusivity. These two mechanisms interact to cause a channel width for which there is optimal growth.

The numerical models of ice shelves discussed above have all made the assumption that the ice is floating in hydrostatic equilibrium with the ocean. There is no reason to think this is necessarily true around channels, where bridging stresses could be significant. Drews (2015) used a fully 3-D Stokes model of the ice to test whether

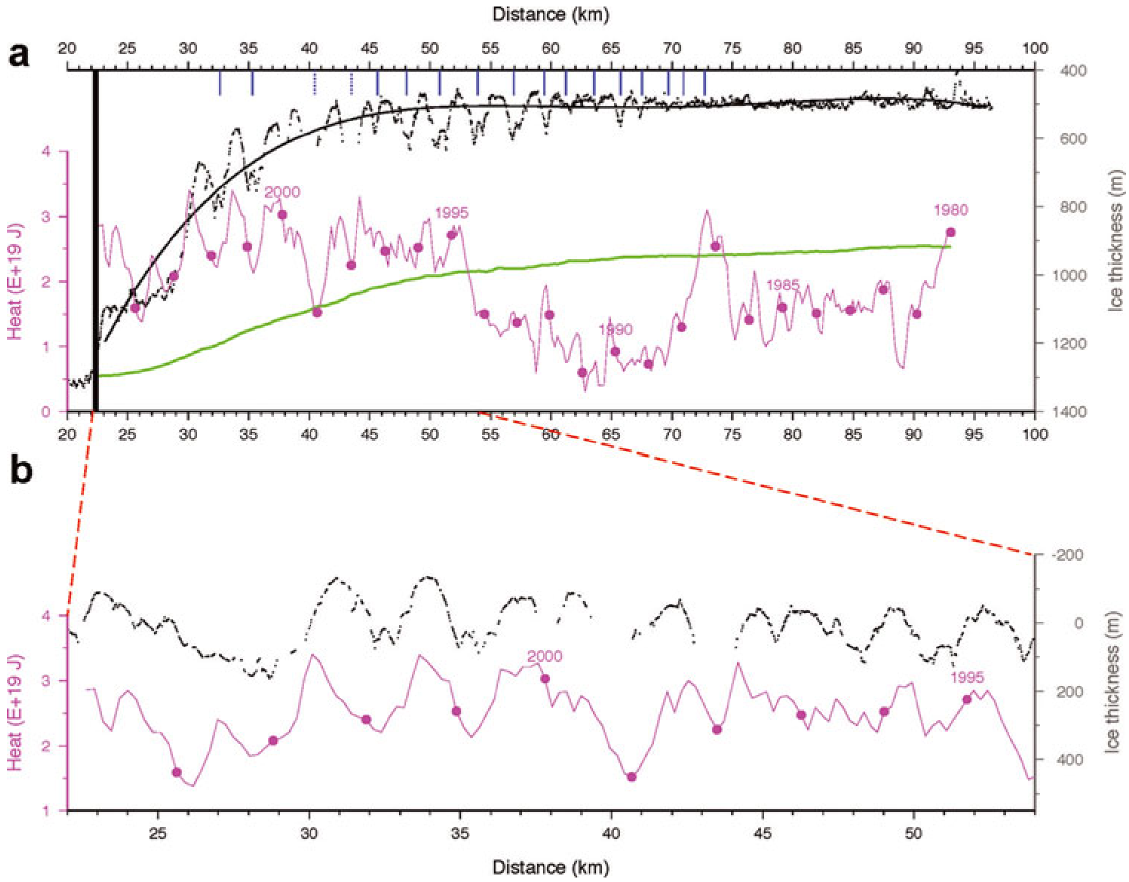

Figure 1.6: (a) The thickness (black dots) of the Pine Island Glacier ice shelf along a transect running parallel to the direction of flow. A five term polynomial (thick black line) was fit to these data. Also shown (mauve lines) is the heat content in front of the ice shelf at the time each portion of ice was estimated to have crossed the grounding line, determined from the simulation of Thoma et al. (2008). Mauve dots correspond to January of the year with which they are labelled. The green curve is thickness the ice shelf would have had were there no basal melt. (b) An inset from the previous panel, with detrended thickness data. *(Plot source: Bindschadler, Vaughan, et al., 2011)*

or not this was the case. Prescribing a basal melt rate, it was found that only very narrow channels deviated substantially from hydrostatic equilibrium; for the conditions in this study, the ratio of channel width to depth had to be less than 5. This condition is not met for the vast majority of channels which have been studied, although Drews (2015) observed such narrow channels in the Roi Baudouin Ice Shelf.

In addition to channels running in the direction of the ice flow, Bindschadler, Vaughan, et al. (2011) identified wave-like basal oscillations in one segment of the PIG ice shelf, the keels of which run perpendicular to the flow (see figure 1.6). The size of these voids was found to correlate with estimates for the ocean heat content in front of the ice shelf in the year that the ice in question crossed the grounding line and the spacing was consistent with ice advection over an annual period. Ocean heat data were taken from a simulation run by Thoma et al. (2008), which calculated ocean circulation in the Amundsen Sea and deep Southern Ocean, forced with historical surface temperature and pressure data. Heat content would reach a maximum during the late austral summer or, in some years, in the early austral winter. The minimum occurred more regularly, in austral midwinter.

Bindschadler, Vaughan, et al. (2011) suggested that the voids seen in the ice shelf profile arose from a warmer ocean at certain times of year, which expanded basal crevasses near the grounding line where melting is most intense. In effect, these crevasses would be acting as initial perturbations which would then be expanded via the meltwater feedback, as in longitudinal channels. Bindschadler, Vaughan, et al. (2011) felt that the oceans would contain sufficient heat at any time of year to expand a crevasses, suggesting that the warm water in some way caused crevasses to form. This could occur if the warmer water caused higher melt rates and lower friction, leading to acceleration of the ice sheet's motion with the resulting stress causing the ice to fracture. Alternatively, warmer water has been shown to result, counter-intuitively, in colder internal temperatures of the ice, which would make it more brittle and liable to form crevasses (Sergienko et al., 2013). Changing water temperature could drive variable melt, but modelling results indicate that water temperatures within the cavity tend to vary on a timescale that is longer than one year (Holland, 2017).

However, stress from shelf boundaries has also been shown to result in channels running at an angle to the direction of flow (Sergienko, 2013), which may render the earlier explanation unnecessary. Furthermore, the results of Thoma et al. (2008) have been called into question by some observations. Walker, Jenkins, et al. (2013) found that transport of CDW onto the continental shelf was primarily the result of an undercurrent, driven by the Antarctic Slope Front, which there is no reason to expect to vary over the year. While this does not preclude seasonal variations due to wind forcing, it suggests they may be less important than thought by Thoma et al. (2008), as discussed earlier in § 1.2.2.

There have been some limited additional observations of transverse channels. A single one, several hundred metres across, was observed under the Fimbul ice shelf (Langley et al., 2014). A mooring observed that the ocean water was running parallel to the channel, although it is unclear whether this is due to channelisation or the direction of flow across the entire ice shelf. There are some indications of transverse ripples under the floating ice tongue of Ryder Glacier and oscillations in the melt rate under the 79 North Glacier's ice tongue, both in Greenland (Wilson et al., 2017). These features are a few kilometres in width and a few tens of metres in height, but are rather indistinct. Two transverse channels appear to have formed in a fully 3-D Stokes flow simulation of an ice shelf, qualitatively similar to that of Pine Island Glacier, coupled to a fully 3-D ocean model (Asay-Davis et al., 2016). The width and spacing of these channels were at least an order of magnitude larger than what was observed by Bindschadler, Nowicki, et al. (2013), although the depth is comparable. The mechanism leading to the formation of these channels has not been explored.

On the Larsen C ice shelf, transverse crevasses have been observed (McGrath, Steffen, Scambos, et al., 2012; McGrath, Steffen, Rajaram, et al., 2012; Luckman et al., 2012). Whereas a channel is formed from melting of the ice shelf, a crevasse is formed from the ice fracturing under stress and tend to be narrower. However, a narrow channel could easily be mistaken for a wide crevasse or vice-versa. In particular, the shape of the crevasse studied by McGrath, Steffen, Rajaram, et al. (2012) appears very channel-like: approximately a kilometre in width, 200 m in height, and with fairly smooth corners. However, McGrath, Steffen, Scambos, et al. (2012) observed crevasses with sharp corners; were melting to play a significant role in their evolution, one might expect such features to have been smoothed out. These crevasses are a few hundred metres in width and on the order of 100 m high, much smaller than the features seen by Bindschadler, Vaughan, et al. (2011). Despite this, McGrath, Steffen, Scambos, et al. (2012) referred to the features of Bindschadler, Vaughan, et al. (2011) as crevasses, rather than channels. The mechanisms of melting and fracture are not mutually exclusive; Vaughan et al. (2012) found that crevasses would often form at the apex of channels under Pine Island Glacier. It is also possible that crevasses would serve to initiate melt-driven channel growth, as suggested by Bindschadler, Vaughan, et al. (2011). The crevasses observed by McGrath, Steffen, Scambos, et al. (2012) and Luckman et al. (2012) were spaced periodically. However, the timescales for the periodicity calculated from ice flow range from interannual to decadal, depending on the location. This suggests that the annual spacing seen by Bindschadler, Vaughan, et al. (2011) may just be a coincidence.

In summary, there is clear evidence of variations of ice thickness with periodic spacing. The spacing between these features on Pine Island Glacier agreed with annual ice advection, but indicated longer advective time scales elsewhere. These observations may arise due to either crevassing, melt, or some feedback between the two. Further research into the plausibility of seasonal mechanisms for channel formation is required to properly evaluate this.

1.4 Ice and Ocean Fluid Dynamics

There are multiple approaches to modelling ice and the ocean, of varying complexity. Glaciers can be modelled as three dimensional systems using the Stokes equation for viscous flow (c.f. Schoof and Hewitt, 2013). While this is the most accurate approach, it is computationally expensive to solve and is therefore seldom used. For this reason, simplifying assumptions are usually adopted to allow the ice equations to be vertically integrated to become a 2-D system, known as the *shallow shelf* model when applied to an ice shelf (Morland and Shoemaker, 1982). This is the model used for all calculations in this thesis and its derivation is discussed in § 1.4.1.

Similarly, the ocean in the cavity beneath the glacier can be modelled as a fully 3-D fluid. This can be achieved by running an existing ocean simulation code in the cavity (e.g. Millgate et al., 2013; Jordan et al., 2018), but is also computationally expensive. As such, simplified models are often adopted. At the other end of the complexity spectrum are empirically tuned parameterisations which calculate the melt rate as a function of properties such as ocean temperature, basal depth, basal slope, and/or distance from the grounding line (e.g. Walker, Dupont, et al., 2008; Little, Goldberg, et al., 2012). While efficient, this approach can not capture feedback between the ice shelf shape and ocean flow. As such, models of intermediate complexity are often used. Jenkins (2016) proposed a 1-D model, assuming variation only in the direction perpendicular to the base of the ice, which was able to separate the boundary current into a superposition of geostrophic flow and friction-dominated flow adjacent to the ice, similar to an Ekman layer. However, this required choosing an arbitrary assumption in order to impose gradients in the direction parallel to ice-ocean interface, such as prescribing an entrainment velocity (leading to divergence) or a thermal driving gradient. Without such assumptions, only trivial steady-state results could be produced. Plume models have also been widely used, in which the equations describing the ocean are vertically integrated to reduce them to a 2-D system (e.g. Jenkins, 1991). Such a model is used in this thesis and presented in § 1.4.2.

1.4.1 Shallow Shelf Model

Although usually thought of as a solid, on large scales ice can be modelled as a highly viscous non-Newtonian fluid. It is treated as incompressible, so that

$$\nabla \cdot \vec{u} = 0, \tag{1.1}$$

where $\vec{u} = (u, v, w)$ is the ice velocity field. Stress (σ_{ij}) is decomposed into isotropic (corresponding to pressure, p) and deviatoric (τ_{ij}) components, according to $\sigma_{ij} = -p\delta_{ij} + \tau_{ij}$. The deviatoric stress is expressed as

$$\tau_{ij} = 2\eta D_{ij}, \quad D_{ij} = \frac{1}{2}\left(\frac{\partial u_i}{\partial x_j} + \frac{\partial u_j}{\partial x_i}\right), \tag{1.2}$$

where η is the viscosity, D_{ij} is the strain rate, and $x_i = (x, y, z)$ represent the two horizontal and the vertical coordinates, with x and y often chosen so as to align parallel and perpendicular to the direction of ice flow, respectively. The viscosity is typically (Schoof and Hewitt, 2013) parameterised in power law form according to Glen's law (Glen, 1958):

$$\eta = \tfrac{1}{2} B D_2^{1/n-1}. \tag{1.3}$$

Here, B is a coefficient which is often treated as a function of temperature, $D_2 = \sqrt{D_{ij}D_{ij}/2}$ is the second invariant of the strain rate, and n is a constant parameter, typically set to 3 (Schoof and Hewitt, 2013), although the Newtonian limit ($n = 1$) is also sometimes considered for analytical tractability (e.g. Dallaston et al., 2015).

Using this expression for stress, the ice in an ice shelf can be described by the Navier-Stokes equation. However, scale analysis shows that acceleration is negligible and it can be expressed as a Stokes flow only (Schoof and Hewitt, 2013):

$$\frac{\partial \tau_{ij}}{\partial x_j} - \nabla p + \rho \vec{g} = 0, \tag{1.4}$$

where $\vec{g}$ is gravitational acceleration and ρ the density. The ice shelf is assumed to be in hydrostatic balance internally and with the ocean, meaning pressure gradients balance the force of gravity. As such, $s = (1 - \rho_i/\rho_0)h$ and $-b = \rho_i/\rho_0 h$, where s is the altitude of the upper surface, ρ_i is the density of ice, ρ_0 is the density of the ocean (typically treated as a constant reference density under the Boussinesq approximation), h is the ice thickness, and b is the depth of the basal surface. The upper and lower surfaces satisfy, respectively,

$$\frac{\partial s}{\partial t} + u(s)\frac{\partial s}{\partial x} + v(s)\frac{\partial s}{\partial y} = w(s) + a, \tag{1.5a}$$

$$\frac{\partial b}{\partial t} + u(b)\frac{\partial b}{\partial x} + v(b)\frac{\partial b}{\partial y} = w(b) + m, \tag{1.5b}$$

where t is time, a is the rate of accumulation (henceforth assumed to be zero for convenience) on the upper surface of the ice shelf, and m is the melt rate at the base. These equations express that the Lagrangian rate of change of these surfaces is the sum of the vertical ice velocity at the surface and ice gained and lost from accumulation and melting, respectively.

The shallow shelf model, which appears to have first been developed by Morland and Shoemaker (1982), assumes that the ice has a plug flow so that u and v are independent of z. Integrating equation (1.4) vertically and using equation (1.1) to eliminate dependence on w, a 2-D stress tensor can be found with the form (e.g. MacAyeal, 1989, Appendix A)

$$\vec{T} = \begin{bmatrix} 2\eta h \left(2\frac{\partial u}{\partial x} + \frac{\partial v}{\partial y}\right) & \eta h \left(\frac{\partial u}{\partial y} + \frac{\partial v}{\partial x}\right) \\ \eta h \left(\frac{\partial u}{\partial y} + \frac{\partial v}{\partial x}\right) & 2\eta h \left(2\frac{\partial v}{\partial y} + \frac{\partial u}{\partial x}\right) \end{bmatrix}. \tag{1.6}$$

Applying all of these assumptions and splitting the momentum equation into horizontal components, the ice shelf can be described by the system

$$\frac{\partial h}{\partial t} + \frac{\partial}{\partial x}(hu) + \frac{\partial}{\partial x}(hu) = -(\rho_i/\rho_0)m, \tag{1.7a}$$

$$\frac{\partial}{\partial x}\left[2\eta h\left(2\frac{\partial u}{\partial x} + \frac{\partial v}{\partial y}\right)\right] + \frac{\partial}{\partial y}\left[\eta h\left(\frac{\partial u}{\partial y} + \frac{\partial v}{\partial x}\right)\right] - (1-\rho_i/\rho_0)\rho_i g h\frac{\partial h}{\partial x} = 0, \tag{1.7b}$$

$$\frac{\partial}{\partial x}\left[\eta h\left(\frac{\partial u}{\partial y} + \frac{\partial v}{\partial x}\right)\right] + \frac{\partial}{\partial y}\left[2\eta h\left(\frac{\partial u}{\partial x} + 2\frac{\partial v}{\partial y}\right)\right] - (1-\rho_i/\rho_0)\rho_i g h\frac{\partial h}{\partial y} = 0. \tag{1.7c}$$

1.4.2 Plume Model

The plume of melt-water beneath the ice shelf can be described in a similar manner to the shallow-water approximation (e.g. Pedlosky, 1987, Chapter 3). Such models were initially developed for buoyant gas in mine shafts (Ellison and Turner, 1959) and katabatic winds (Manins and Sawford, 1979). Jenkins (1991) extended and applied them to the cavity beneath ice shelves.

The plume adjusts on much shorter timescales than the ice shelf due to faster flow, so it can be modelled as being in steady-state for the instantaneous ice geometry. In three dimensions and using the Boussinesq approximation, ocean flow is described by the equations

$$\nabla \cdot \vec{U} = 0, \tag{1.8a}$$

$$\rho_0 \vec{U} \cdot \nabla \vec{U} = \rho_w \vec{g} - \nabla p + \rho_0 \nabla \cdot \vec{S_{ij}}, \tag{1.8b}$$

$$\nabla \cdot (S\vec{U}) = \nabla \cdot (\kappa \nabla S), \tag{1.8c}$$

$$\nabla \cdot (T\vec{U}) = \nabla \cdot (\kappa \nabla T), \tag{1.8d}$$

representing conservation of mass, momentum, salt, and heat, respectively. The 3-D velocity field is $\vec{U}_3 = (U, V, W)$, p is the pressure, S_{ij} the stress tensor, ρ_w is the density of the water in the plume, S is the salinity, and T is the temperature. It is assumed that turbulent mixing can be described as diffusion, with diffusivity κ. The stress in the interior arises due to eddy viscosity ($\nabla \cdot S_{ij} = \kappa \nabla^2 \vec{U}$, with the eddy viscosity, κ, here assumed to be equal to the eddy diffusivity with both treated as constants). At the boundary between the plume and the ice there is assumed to be a turbulent drag ($S_{ij} \cdot \vec{n} = -C_d|\vec{U}|\vec{U}$, where $\vec{n}$ is the vector normal to the boundary, C_d is the drag coefficient, and $\vec{U} = (U, V)$ is the horizontal velocity components).

Because the plume layer is shallow compared to its length, it is assumed to be approximately in hydrostatic equilibrium, with a vertical momentum balance between pressure gradients and gravitational forces. The plume has a representative thickness D. Below the plume, the ocean is assumed to be motionless, with ambient conditions ρ_a, T_a, and S_a. The Boussinesq approximation is applied, and equation (1.8) is vertically integrated to yield (Holland and Feltham, 2006)

$$\nabla \cdot (D\vec{U}) = e + m, \tag{1.9a}$$

$$\nabla \cdot (D\vec{U}U) = Dg' \left(\frac{\partial b}{\partial x} - \frac{\partial D}{\partial x} \right) + \frac{gD^2}{2\rho_0} \frac{\partial \rho_w}{\partial x} + \nabla \cdot (\kappa D \nabla U) - C_d|\vec{U}|U, \tag{1.9b}$$

$$\nabla \cdot (D\vec{U}V) = Dg' \left(\frac{\partial b}{\partial y} - \frac{\partial D}{\partial y} \right) + \frac{gD^2}{2\rho_0} \frac{\partial \rho_w}{\partial y} + \nabla \cdot (\kappa D \nabla V) - C_d|\vec{U}|V, \tag{1.9c}$$

$$\nabla \cdot (D\vec{U}S) = eS_a + \nabla \cdot (\kappa D \nabla S) + mS_m - \gamma_S(S - S_m), \tag{1.9d}$$

$$\nabla \cdot (D\vec{U}T) = eT_a + \nabla \cdot (\kappa D \nabla T) + mT_m - \gamma_T(T - T_m), \tag{1.9e}$$

where e is rate at which turbulent entrainment transports water from the ambient ocean into the plume, $g' = (\rho_a - \rho_w)/\rho_0$ is the effective gravity due to density differences between the ambient ocean and the plume, $b = -(\rho_i/\rho_0)h$ is the basal draft of the ice shelf, S_i is the salinity of the ice (typically zero), and T_m is the salinity-dependent melting point. S_m is the equilibrium melt salinity at the interface between the ice and the ocean. Transfer coefficients for temperature and salinity from the plume to the boundary layer between the plume and the ice shelf are, respectively, γ_T and γ_S. The model above assumes a well-mixed flow with uniform properties U, V, T, and S within the plume of depth D. However, a similar solution could be obtained even if the plume were not well mixed, with U, V, T, and S treated as depth-averaged values. The equations would differ by the presence of scalar multipliers on various terms, which are shape factors quantifying the plume's departure from uniformity, as in the result of Manins and Sawford (1979).

A linear equation of state of the form

$$\rho_w = \rho_{\mathrm{ref}}[1 + \beta_S(S - S_{\mathrm{ref}}) - \beta_T(T - T_{\mathrm{ref}})] \tag{1.10}$$

is assumed, where β_S is the haline contraction coefficient, β_T is the thermal expansion coefficient, and S_{ref}, T_{ref}, and ρ_{ref} are reference values for salinity, temperature, and density about which the relation has been linearised. Entrainment is a function of plume velocity and the Richardson Number. It can be shown (Magorrian and Wells, 2016, supplementary information) that, when buoyancy is balanced by drag (i.e. when the slope is small), entrainment using common parameterisations (e.g. Kochergin, 1987) approximately reduces to

$$e = E_0|\vec{U}|\sin(\theta) \approx E_0|\vec{U}||\nabla b|, \tag{1.11}$$

where E_0 is usually chacarcterised as a constant and θ is the angle of the basal slope (e.g. Jenkins, 1991; Dallaston et al., 2015). An alternative common parameterisation used in plume models (e.g. Jungclaus and Backhaus, 1994; Holland, Feltham, and Jenkins, 2007; Payne et al., 2007; Sergienko, 2013) is that of Kochergin (1987):

$$e = \frac{c_L^2}{S_m}\sqrt{|\vec{U}|^2 + \frac{g'D}{S_m}}, \tag{1.12}$$

where c_L is constant and S_m is the turbulent Schmidt number. This can be represented as a function of the Richardson number, $Ri = g'D/|\vec{U}|^2$, the ratio of potential to kinetic energy in the stratified flow, with

$$S_m = \frac{Ri}{0.0725(Ri + 0.186 - \sqrt{Ri^2 - 0.316Ri + 0.0346})}. \tag{1.13}$$

Entrainment requires kinetic energy to preform work when lifting denser water into the less dense plume, overcoming the stratification, hence its dependence on Ri. This behaviour is emulated b the slope dependence in equation (1.11).

1.4.3 Coupling and Thermodynamics

The plume and the ice shelf are coupled in two ways: the shape of the ice shelf affects the dynamics of the plume, while the properties of the plume determine the melt rate, which contributes to the evolution of both the plume and the shelf. The melting rate can be determined using thermodynamics and conservation of salt. Although marine ice has been observed to accumulate on the bottom of an ice shelf (Oerter et al., 1992), deposited from frazil ice which has formed in a plume, the emphasis here is on warm ocean conditions, where melting dominates.

The most common approach to finding the melting point of ice is that described by Holland and Jenkins (1999). Their analysis assumes a thin boundary layer at the ice-ocean interface, with different salinity and temperature values than the core of the plume. They use a linear expression for the melting point of ice,

$$T_m = aS_m + b + cp_B, \tag{1.14}$$

where p_B is the pressure at that location, and a, b, and c are empirically determined constants that control the freezing-point depression by salinity, reference melting temperature, and pressure dependent melting temperature, respectively. The latent heat needed to melt the ice must be balanced by the divergence of the heat flux at the interface:

$$Q_P^T - Q_I^T = \frac{\rho_i}{\rho_0} mL, \tag{1.15}$$

where Q_I^T is the heat flux from the boundary to the ice, Q_P^T is the heat flux coming from the plume to the boundary, and L is the latent heat of fusion for ice. Similarly, the salt flux needed to counterbalance the input of fresh melt-water and maintain the equilibrium melt salinity at the ice-ocean boundary must equal the divergence of the salt flux. As salt can not flow into the ice, this condition becomes

$$Q_P^S = \rho_0 m(S_m - S_i), \tag{1.16}$$

where Q_P^S is the flux of salt from the plume to the boundary and S_i is the salinity of the ice. The ice only has a salinity if seawater freezes to the shelf's base. While this can occur, measurements indicate that the salinity is typically very small (Oerter et al., 1992; Eicken et al., 1994) and it is thus usually treated as zero.

The problem now becomes one of estimating heat and salt fluxes. Holland and Jenkins (1999) took these to be driven by diffusion across a molecular sublayer at the ice-ocean interface and thus proposed the relationships

$$T_m = aS_m + b + cp_B, \tag{1.17a}$$

$$\gamma_T c_o(T - T_m) = m(L + c_i[T_m - T_i]), \tag{1.17b}$$

$$\gamma_S(S - S_m) = mS_m, \tag{1.17c}$$

where c_o is the specific heat capacity of sea water, c_i is the specific heat capacity of ice, and T_i the far-field temperature of the ice shelf. This is referred to as the *three-equation formulation*. Note that equation (1.17c) means that the final two terms in equation (1.9d) cancel. Holland and Jenkins (1999) also found that assuming the salinity at the boundary is equal to that in the plume (the *two-equation formulation*) produces acceptable results. Typically, the transfer coefficients are taken to be

$$\gamma_T = \frac{U_*}{2.12\ln\left(\frac{U_* D}{\nu}\right) + 12.5Pr^{2/3} - 9}, \tag{1.18a}$$

$$\gamma_S = \frac{U_*}{2.12\ln\left(\frac{U_* D}{\nu}\right) + 12.5Sc^{2/3} - 9}, \tag{1.18b}$$

a formulation which can be derived from dimensional and self-similarity arguments for shear flow, with coefficients determined from experimental data (Kader and Yaglom, 1972). Here $U_* = \sqrt{C_d}|\vec{U}|$ is the friction velocity, ν is the kinematic viscosity of sea water, Pr is the Prandtl number (ratio of viscosity to thermal diffusivity), and Sc is the Schmidt number (ratio of viscosity to the saline diffusivity). However, on testing various formulations for melting against observations taken at the Ronne Ice Shelf, Jenkins, Nicholls, et al. (2010) found that results obtained using transfer coefficients of the form $\gamma_{\{T,S\}} = \Gamma_{\{T,S\}}U_*$, where $\Gamma_{\{T,S\}}$ were constants tuned to their data, agreed with the data just as well as those obtained using equation (1.18) and recommended using the simpler form. Note that although these equations do not account for buoyancy fluxes which could destabilise or stabilise the boundary layer, Holland and Jenkins (1999) still found them to agree well with more sophisticated models. Recently an alternative representation of melting based on turbulent convection has been derived which does not have any tunable parameters and has been found to agree well with laboratory experiments, although it has not yet been well tested on the scale of ice shelves (McConnochie and Kerr, 2018).

1.5 Statement of Intent

While their overall effect on ice shelf stability is unknown, the origin of most channels on the bottom of ice shelves is thought to be fairly well understood. Longitudinal channels are initiated by spatial variations in basal topography or subglacial discharge, or by shear stress against the side of an ice shelf. These small perturbations then grow due to a feedback effect wherein melt-water is channelised, resulting in locally enhanced melting. However, while this explanation works well for channels running parallel to the ice flow, it remains unclear what processes could initiate the channels observed running transverse to the flow. It has been suggested that seasonal variability in ocean heat could play this role (Bindschadler, Vaughan, et al., 2011). More generally, there is an incomplete understanding of the effects of temporal variability in ice influx and melting on ice shelf structure. The purpose of this research was to examine how variability on seasonal and other timescales modifies the geometry, melt, and dynamics of an ice shelf, and whether this provides a mechanism for transverse channel formation. Variations in subglacial discharge and ice flux across the grounding line were investigated. Both properties have been observed to undergo dramatic seasonal variations for Greenland glaciers (e.g. Sole et al., 2013; Tedstone et al., 2013, and references therein). Variations in ocean heat were not tested as they would have a very similar effect on the ice melt-rate as variations in subglacial discharge.

A 1-D linear perturbation analysis was performed to determine the effect on ice shelf geometry of temporal variations in subglacial discharge and incoming ice flux, as described in Chapter 2. This identified the key physical mechanisms of ice shelf response, and showed that such variation can give rise to small ripples in the ice shelf thickness, but these were one to two orders of magnitude smaller than observations and did not produce overdeepenings (where the ice thins with x and then thickens again). However, varying ice flux forcing did produce some features reminiscent of basal terraces.

Chapter 3 documents the nonlinear simulations which were performed of a 1-D ice shelf subject to seasonal perturbations. It starts by explaining the numerical methods used to perform these calculations, along with the testing and benchmarking performed, before discussing the results. The subglacial discharge-forced simulations had very similar results to the corresponding linearised calculation. However, the ice flux-forced simulations exhibit a feedback effect which causes the ripples to grow into overdeepenings towards the end of the ice shelf. For the cold cavity conditions that were tractable with the present code, typical ripple amplitudes are of order $\sim 1\,\mathrm{m}$ to $\sim 10\,\mathrm{m}$ (for subglacial discharge and ice-flux forcing, respectively). This is considerably smaller than the large overdeepenings observed by Bindschadler, Vaughan, et al. (2011) at Pine Island Glacier.

The development of a new simplified model to capture the transverse component of the plume velocity (vital to the channelisation feedback) and model the Coriolis force in 1-D are detailed in Chapter 4. The derivation of this model is described and its behaviour analysed in simple settings, initially uncoupled from ice shelf evolution. It was found that the model could predict 2-D plume flow that is qualitatively similar to that found with 3-D ocean models. When this model was coupled to an evolving ice geometry it was found that it did not result in channelised plume flow and did not produce overdeepenings.

A new approach for capturing the evolution of internal reflectors/isochrones in a vertically integrated glacier model is documented in Chapter 5. Its use within ice shelf simulations is demonstrated, including prediction of the effect of seasonal variability on internal reflectors. The chapter ends with a discussion of the future potential to use this technique in inverse modelling to calculate current and past ice velocity from radar data.

Finally, the results of all this work are summarised in Chapter 6 and avenues for further research are proposed. Additionally, Appendix A provides an explanation of the design of the software written to perform the nonlinear shelf and plume simulations, so that others may be able to make use of it in future.

2
Linear Perturbations to a 1-D System

Contents

As described in the previous chapter, observations appear to show transverse basal channels under Pine Island Glacier (Bindschadler, Vaughan, et al., 2011). The spacing of these channels is roughly the distance ice would be advected in a year, suggesting they may be formed by some sort of seasonal variability. Potential sources of that variability are the ice flux crossing the grounding line and, due to varying subglacial discharge, the melt rate (e.g. Bartholomew et al., 2010). This mechanism is examined here using a linear analysis of a coupled ice shelf and ocean system.

2.1 Simplified 1-D Shelf Model

For the purposes of this analysis, a greatly simplified model of the shelf and plume was created which could be handled analytically. This involved applying various approximations and assumptions to the ice shelf and plume equations, so as to obtain an analytically tractable model which captures the essential physical processes. The approach detailed below is similar to that of Dallaston et al. (2015). They applied steady-state 2-D perturbations to a 1-D plume/ice shelf solution, in order to investigate the formation of longitudinal channels. Here, time-varying perturbations are applied to a 1-D steady-state in order to study the formation of transverse ripples.

The ice shelf described using a vertically integrated model, while the ocean underneath it is modelled as a vertically-integrated plume over an ambient body of water (see figure 1.1). The systems of equations (1.7) for the ice shelf and (1.9) for the meltwater plume were (unlike in the case of Dallaston et al., 2015) converted to a 1 dimensional form, dropping all terms containing transverse velocities or derivatives in y. The ice was assumed to have a Newtonian rheology (constant viscosity η). Entrainment was parameterised using equation (1.11). Note that this form allows certain terms to cancel which made the system analytically tractable. In order, to make the equations easier to work with the density of the plume was treated as independent of temperature. This is motivated by the fact that, for typical variations in temperature and salinity in a plume, the changes in density due to temperature are an order of magnitude smaller than those due to salinity (Dallaston et al., 2015). The melting temperature was taken to be independent of salinity and pressure. Jenkins (2011) noted that it was a reasonable approximation to set the melt rate as a function of the plume salinity, $T_m(S)$, rather than the salinity of the boundary layer, $T_m(S_b)$. Noting that $T_m(S) - T_m(S_a)$ is much less than the thermal driving $T - T_m(S_a)$, it is clearly also reasonable to set T_m from the ambient salinity value. Thus, this model is similar to previously established ones such as that of Jenkins (2011), albeit without pressure dependence. The ice shelf is taken to be already near the melting point, so that no heat is required to warm it before initiating melt. The heat needed to warm the ice could be accounted for by slightly increasing the latent heat of fusion although, given that the heat capacity is small, this correction is minor. Finally, the simpler approach recommended by Jenkins, Nicholls, et al. (2010) for calculating thermal transfer was used, with $\gamma_T = \Gamma_T^*|\vec{U}|$, where $\Gamma_T^* = \Gamma_T\sqrt{C_d}$ is a dimensionless constant encapsulating the drag coefficient. These simplifications allow the system of equations (1.17) for the thermodynamics at the ice-ocean interface to be reduced to

$$mL = c_o\Gamma_T^*|\vec{U}|(T - T_m). \tag{2.1}$$

Defining $S_\Delta = S_a - S$ and, for convenience, taking the ambient ocean to have uniform salinity, temperature, and density $\rho_a = \rho_0$, the equations for the shelf and the plume are, respectively

$$\frac{\partial h}{\partial t} + \frac{\partial}{\partial x}(hu) = -(\rho_0/\rho_i)m, \tag{2.2a}$$

$$\frac{\partial}{\partial x}\left(4\eta h\frac{\partial u}{\partial x}\right) - \left(1 - \frac{\rho_i}{\rho_0}\right)\rho_i g h\frac{\partial h}{\partial x} = 0, \tag{2.2b}$$

$$\frac{d}{dx}(DU) = e + m, \tag{2.3a}$$

$$\frac{d}{dx}(DU^2) = Dg\beta_S S_\Delta\left(\frac{db}{dx} - \frac{dD}{dx}\right) + \frac{gD^2\beta_S}{2}\frac{dS_\Delta}{dx} + \frac{d}{dx}\left(\kappa D\frac{dU}{dx}\right) - C_dU^2, \tag{2.3b}$$

$$\frac{d}{dx}(DUS) = eS_a + \frac{d}{dx}\left(\kappa D\frac{dS}{dx}\right), \tag{2.3c}$$

$$\frac{d}{dx}(DUT) = eT_a + \frac{d}{dx}\left(\kappa D\frac{dT}{dx}\right) + mT_m - \frac{mL}{c_o}. \tag{2.3d}$$

Note that the melting and salt flux terms were eliminated from equation (2.3c) using equation (1.17c). Grounding line motion was neglected in order to make the equations tractable, although in reality some motion would be expected.

The thickness and velocity of the ice shelf are imposed at the grounding line, $x = 0$, and it is assumed that the ice melts away entirely at some position $x = X$ (to be determined):

$$h(0) = h_g, \quad h(X) = 0, \quad u(0) = u_g. \tag{2.4}$$

An imposed volume flux of subglacial discharge, Q_g, initiates the flow of the plume at the grounding line. Subglacial water is formed from melting of the glacier, so is at the melting temperature of water and has no salinity. The speed of its outflow is prescribed, leading to plume boundary conditions

$$D(0)U(0) = Q_g, \qquad U(0) = U_g, \qquad S(0) = 0, \qquad T(0) = T_m. \tag{2.5}$$

2.1.1 Nondimensionalisation and Simplification

Before further simplifying equations (2.2) and (2.3), they were converted to a dimensionless form. In order to do this, the unitless parameters of Dallaston et al. (2015) were introduced. Note that one parameter used here, γ, varies by a factor of 2 from that used by Dallaston et al. (2015). Equations (2.2) suggest the parameters

$$r \equiv \frac{\rho_0}{\rho_i} \qquad \gamma \equiv \frac{(1-\rho_i/\rho_0)\rho_i g h_0 x_0}{4\eta u_0}, \qquad \lambda \equiv \frac{\rho_0 m_0 x_0}{\rho_i h_0 u_0}, \tag{2.6}$$

to describe the ice shelf. Here, h_0 is the scale of the ice thickness, x_0 is the scale of the horizontal coordinate, u_0 is the scale of the ice velocity, and m_0 is the scale of the melt rate. The parameter r is the density ratio, γ represents the ratio of the hydrostatic pressure gradient to viscous forces in the ice (quantifying the amount of stretching that will occur), while λ represents the ratio of the melt rate to the mass flux of ice through the grounding line.

Rhe temperature was expressed in terms of $T_\Delta \equiv T_a - T$. The plume variables were converted to a dimensionless form (indicated by a prime) according to

$$D = D_0 D', \quad U = U_0 U', \quad S_\Delta = S_{\Delta 0} S'_\Delta, \quad T_\Delta = T_{\Delta 0} T'_\Delta, \quad m = m_0 m',$$

with the scales

$$\begin{aligned} U_0 &= \left(\frac{Q_{g0} g \beta_S S_a}{E_0}\right)^{1/3}, \qquad & m_0 &= \frac{c_o \Gamma_T^* U_0 (T_a - T_m)}{L}, \\ D_0 = E_0 h_0, \qquad S_{\Delta 0} &= \frac{Q_{g0} S_a}{D_0 U_0}, \qquad & T_{\Delta 0} &= \frac{\Gamma_T^* x_0}{D_0}(T_a - T_m). \end{aligned} \tag{2.7}$$

The U_0 scale is set by a balance between buoyancy and momentum loss via entrainment, m_0 comes from the transfer of heat from the ambient ocean to melt the ice, D_0 indicates that plume thickness is set by entrainment, $S_{\Delta 0}$ expresses salinity as that of the ambient ocean diluted by the subglacial discharge, and $T_{\Delta 0}$ is set by the balance between entrained heat and heat used by melting. The characteristic timescale of ice advection is $t_0 = x_0/u_o$. These are the same as the scalings used by Dallaston et al. (2015).

Non-dimensionalizing equations (1.11), (2.1), and (2.3) results in the following six parameters describing the plume:

$$\begin{aligned} \epsilon_m \equiv \frac{m_0 x_0}{D_0 U_0}, \qquad \epsilon_g \equiv \frac{Q_{g0}}{D_0 U_0}, \qquad \nu \equiv \frac{\kappa}{U_0 x_0}, \\ \mu \equiv \frac{C_d x_0}{D_0}, \qquad \delta \equiv \frac{D_0}{h_0} = E_0, \qquad \beta \equiv \frac{c_o(T_a - T_m)}{L}. \end{aligned} \tag{2.8}$$

These represent the ratios of basal melt to entrained flux (ϵ_m), subglacial volume flux to entrained flux (ϵ_g), eddy diffusivity to inertia (ν), deceleration from drag to deceleration from the entrained mass flux (μ), characteristic thickness of the plume to that of the ice shelf (δ, relevant for the buoyancy correction), and the inverse Stefan number which characterises the ratio of sensible to latent heat (β). Typical values for these parameters can be found in table 2.1. These parameters are the same as those adopted by Dallaston et al. (2015).

Using the above parameters, the equations for the ice shelf and plume can be written in a non-dimensional form. For convenience, the primes are dropped from the nondimensional variables and they are given the same symbols as used in equations (2.1)–(2.3). The ice equations become

$$\frac{\partial h}{\partial t} + \frac{\partial}{\partial x}(hu) = -\lambda m, \tag{2.9a}$$

$$\frac{\partial}{\partial x}\left(h\frac{\partial u}{\partial x}\right) - \gamma h \frac{\partial h}{\partial x} = 0. \tag{2.9b}$$

The nondimensional form of the melt rate is

$$m = |U|\left(1 - \frac{\epsilon_m}{\beta} T_\Delta\right) \tag{2.10}$$

Table 2.1: Typical values for the scales and parameters used in the nondimensional form of the couple plume/ice shelf equations. These are the same values as used by Dallaston et al. (2015), with the exception of γ, which is defined differently here so as to be double that in the earlier paper. The value of Γ_T^* was chosen by Dallaston et al. (2015) to give results consistent with the observed melt rate for Petermann Glacier.

Parameter	Description	Typical Value
ρ_0	Reference water density	$1030\,\mathrm{kg\,m^{-3}}$
ρ_i	Ice density	$916\,\mathrm{kg\,m^{-3}}$
g	Acceleration due to gravity	$9.8\,\mathrm{m\,s^{-2}}$
L	Latent heat of fusion	$3.35 \times 10^5\,\mathrm{J\,kg^{-1}}$
c	Specific heat of water	$3.98 \times 10^3\,\mathrm{J\,kg^{-1}\,K^{-1}}$
E_0	Entrainment coefficient	0.036
β_S	Haline contraction coefficient	$7.86 \times 10^{-4}\,\mathrm{psu^{-1}}$
β_T	Thermal contraction coefficient	$3.87 \times 10^{-5}\,\mathrm{K^{-1}}$
C_d	Turbulent drag coefficient	2.5×10^{-3}
Γ_T^*	Thermal transfer coefficient	5.7×10^{-5}
κ	Turbulent diffusivity/viscosity	$10–100\,\mathrm{m^2\,s^{-1}}$
η	Ice viscosity	$2.6 \times 10^{13}\,\mathrm{Pa\,s}$
u_0	Ice velocity scale	$1\,\mathrm{km\,yr^{-1}}$
h_0	Ice thickness scale	$600\,\mathrm{m}$
x_0	Length scale	$11\,\mathrm{km}$
t_0	Time scale	$11\,\mathrm{yr}$
m_0	Melt scale	$18\,\mathrm{m\,yr^{-1}}$
Q_g	Subglacial discharge	$10^{-2}\,\mathrm{m^2\,s^{-1}}$
D_0	Plume thickness scale	$22.6\,\mathrm{m}$
U_0	Plume velocity scale	$0.42\,\mathrm{m\,s^{-1}}$
S_a	Ambient salinity	$34.6\,\mathrm{psu}$
$T_a - T_m$	Ambient temperature	$2^\circ\,\mathrm{C}$
r	density ratio	1.12
γ	dimensionless stretching rate	2
λ	dimensionless melt rate	0.37
ν	dimensionless eddy diffusivity	0.0022–0.022
δ	dimensionless buoyancy correction	0.036
ϵ_g	subglacial flux/entrained flux	1.1×10^{-3}
ϵ_m	subglacial melt/entrained flux	6.9×10^{-4}
μ	dimensionless drag coefficient	1.27
β	inverse Stefan number	0.027

and $b = r^{-1}h$. The plume equations have the dimensionless form

$$\frac{d}{dx}(DU) = |U|\left|\frac{db}{dx}\right| + \epsilon_m m, \tag{2.11a}$$

$$\frac{d}{dx}(DU^2) = DS_\Delta\left(\frac{db}{dx} - \delta\frac{dD}{dx}\right) + \nu\frac{d}{dx}\left(D\frac{dU}{dx}\right) - \mu|U|U + \frac{\delta D^2}{2}\frac{dS_\Delta}{dx}, \tag{2.11b}$$

$$\frac{d}{dx}(DUS_\Delta) = \frac{\epsilon_m}{\epsilon_g}m + \nu\frac{d}{dx}\left(D\frac{dS_\Delta}{dx}\right), \tag{2.11c}$$

$$\frac{d}{dx}(DUT_\Delta) = \beta m + m + \nu\frac{d}{dx}\left(D\frac{dT_\Delta}{dx}\right). \tag{2.11d}$$

Note that the boundary conditions at the grounding line look somewhat different in their dimensionless form than in equation (2.5):

$$DU = \epsilon_g Q_g, \qquad U = U_g, \qquad S_\Delta = \frac{1}{\epsilon_g}, \qquad T_\Delta = \frac{\beta}{\epsilon_m}. \tag{2.12}$$

As in Dallaston et al. (2015), a number of simplifications motivated by the scales in table 2.1 were used to make the plume equations tractable for an analytic solution. It is assumed that the heat entering the plume due to entrainment is much greater than that lost to melting the ice shelf. Then

$$\text{melting rate} \times \text{latent heat} \ll \text{ocean heat} \times \text{entrainment}$$

$$\Rightarrow \frac{\text{melting rate}}{\text{entrainment}} \ll \frac{\text{ocean heat}}{\text{latent heat}}$$

$$\therefore \epsilon_m \ll \beta.$$

Entrainment is assumed to be the dominant source of specific mass flux for the plume, dominating over both melting and subglacial discharge. As such

$$\epsilon_m,\ \epsilon_g \ll 1.$$

Furthermore, it is assumed that

$$\epsilon_m \ll \epsilon_g,$$

meaning subglacial discharge is a significantly larger source of specific mass flux than melting. The scale for the thickness of the plume is much smaller than that for the ice shelf ($\delta \ll 1$) and the plume's thickness is assumed not to change rapidly so that pressure gradients proportional to δ are neglected. Eddy diffusivity is neglected ($\nu \ll 1$) and, finally, the turbulent drag will be treated as negligible ($\mu \ll 1$). Examining the values in table 2.1, it can be seen that all of these assumptions are reasonable, with the exception of those for $\epsilon_m \ll \epsilon_g$ and $\mu \ll 1$. As such, the solutions to the resulting equations will only be quantitatively accurate near the grounding line, since μ and ϵ_m/ϵ_g can be shown to be small over shorter scales (e.g., when $x_0 \sim 1\,\text{km}$, Dallaston et al., 2015). However, as it is the initialisation of channels near the grounding line which is of interest, useful conclusions can still be drawn.

Using these assumptions and defining the buoyancy $B \equiv DS_\Delta$ allows equations (2.10) and (2.11) to be simplified to

$$m = |U|, \tag{2.13}$$

$$\frac{d}{dx}(DU) = |U|\left|\frac{db}{dx}\right|, \tag{2.14a}$$

$$\frac{d}{dx}(DU^2) = B\frac{db}{dx}, \tag{2.14b}$$

$$\frac{d}{dx}(BU) = 0, \tag{2.14c}$$

$$\frac{d}{dx}(DUT_\Delta) = (\beta + 1)m. \tag{2.14d}$$

If U is everywhere non-negative and b is monotonically increasing, then the absolute values are no longer required. Note that temperature has now become uncoupled from this system, meaning equation (2.14d) can henceforth be ignored when calculating the evolution of the plume and ice shelf.

2.1.2 Steady-State Solution

A steady state identical to that of Dallaston et al. (2015) can be found for this simplified plume model. The transformation

$$\frac{d}{dx} = \frac{db}{dx}\frac{d}{dz},$$

was used to convert the plume equations (2.14) to

$$\frac{d}{dz}(DU) = U, \qquad \frac{d}{dz}(DU^2) = B, \qquad \frac{d}{dz}(BU) = 0. \tag{2.15}$$

The latter-most of these can easily be seen to yield

$$B = \frac{Q_g}{U} \tag{2.16}$$

by applying boundary conditions for DU and S_Δ from equation (2.12). Using the substitution $Q = DU$, defining $M \equiv QU$, and integrating the second equation in (2.15) with respect to Q yields the solution

$$U = \frac{Q_g^{1/3}(\epsilon_g^3 U_g^3 Q_g^2 - \epsilon_g^3 Q_g^3 + Q^3)^{1/3}}{Q}, \qquad z - b(0) = \int_{\epsilon_g}^{Q/Q_g} \frac{Q_g^{2/3} q}{\left(\epsilon_g^3 U_g^3/Q_g - \epsilon_g^3 + q^3\right)^{1/3}} dq. \tag{2.17}$$

In the case $\epsilon_g \to 0$ this reduces to

$$D = z - b(0) = \left(h_g - h(x)\right)/r, \qquad U = Q_g^{1/3}, \qquad B = Q_g^{2/3}, \tag{2.18}$$

indicating constant velocity and buoyancy, with a plume thickness that grows linearly as ice shelf thickness is lost. This particular solution will not necessarily satisfy the boundary conditions at the grounding line. However, it can be shown that, for small but nonzero values of ϵ_g, the solution in equation (2.17) converges to equation (2.18) outside of a small boundary layer in which the boundary conditions are satisfied (Dallaston et al., 2015). As such, the limit $\epsilon_g \to 0$ will be taken and the simpler set of equations used, with new boundary conditions

$$D(0) = 0, \qquad U(0) = Q_g^{1/3}, \qquad B(0) = Q_g^{2/3}. \tag{2.19}$$

As Q_g is scaled by Q_{g0}, the value of which can be set arbitrarily, the steady-state value can be set to 1. Using the solution for the plume, the ice shelf has the following steady-state equations:

$$\frac{\partial}{\partial x}(hu) = -\lambda, \qquad \frac{\partial}{\partial x}\left(h\frac{\partial u}{\partial x}\right) - \gamma h \frac{\partial h}{\partial x} = 0. \tag{2.20}$$

Choosing boundary conditions $h_g = u_g = 1$ for the inflowing ice and $h \to 0$ as ice melts away for $x \to X$ for the end of the ice shelf, these equations can be integrated to show

$$X = \frac{1}{\lambda}, \qquad u = \sqrt{1 + \frac{\gamma}{2}X - \frac{\gamma}{2}X(1 - x/X)^2}, \qquad h = \sqrt{\frac{(1 - x/X)^2}{1 + \frac{\gamma}{2}X - \frac{\gamma}{2}X(1 - x/X)^2}}. \tag{2.21}$$

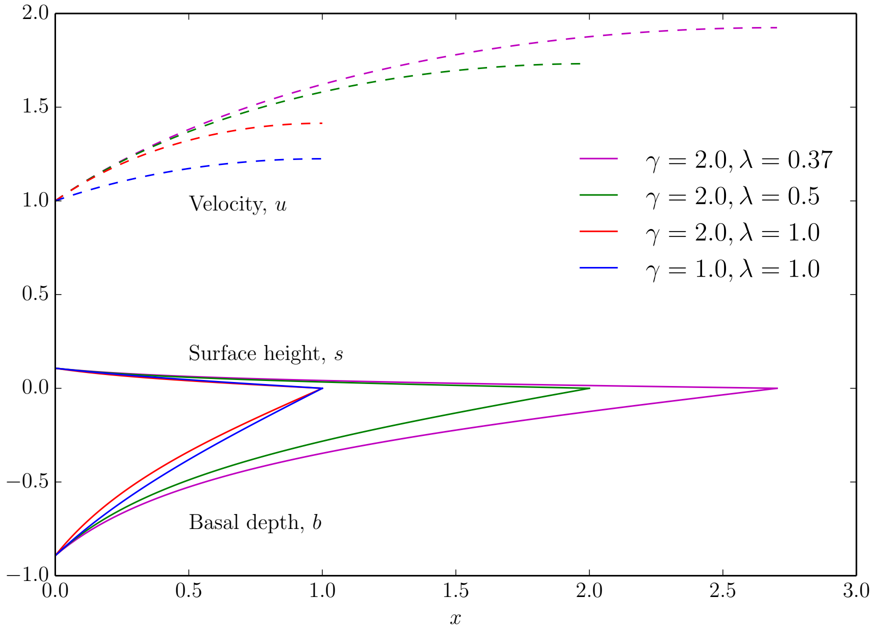

Figure 2.1: The steady state velocity (dashed lines) and thickness (solid lines) profiles for an ice shelf, as derived in equation (2.21). Different colours represent different combinations of stretching (γ) and melting (λ) parameters, with the results for the combination of parameters used in subsequent sections plotted in mauve. For all curves, $r = 1.12$.

This is the same steady state as found by Dallaston et al. (2015), except the different definition of γ results in it being multiplied by a fraction of 1/2. A plot of the velocity and thickness profile can be found in figure 2.1. Increasing λ (i.e. increasing the melt rate) causes the shelf to melt away more quickly, thus decreasing its length and leading to a steeper slope. Increasing γ (i.e. raising the stretching rate) causes the slope of the ice to become more nonlinear; it thins more rapidly near the grounding line and less rapidly near the end of the shelf. Increasing the stretching also means that gravity-driven stretching is more effective at accelerating the ice and leads to ice flow higher velocities.

2.2 Linearisation

In order to investigate how the ice shelf responds to seasonal variations in boundary conditions, a linear perturbation analysis was performed. The method is somewhat similar to that of Dallaston et al. (2015), but with an important distinction. While

Dallaston et al. perturbed a one dimensional background state in the transverse direction, here time-varying perturbations were applied to the steady background state. This was done by prescribing that one or more of the boundary conditions (here denoted schematically as C) representing, e.g., subglacial discharge or incoming ice flux, varies according to

$$C_g = 1 + \Re\left(\tilde{C}_g e^{i\omega t}\right) \tag{2.22}$$

where 1 is the steady-state boundary value, ω is the angular frequency of the perturbations, and $\tilde{C}_g$ is the complex perturbation amplitude. Approximate linearised solutions were sought to equations (2.9) and (2.14) corresponding to temporal oscillations about a steady state with the form:

$$\begin{aligned}[h, u, D, U, B] = {} & [\bar{h}(x), \bar{u}(x), \bar{D}(x), \bar{U}(x), \bar{B}(x)] \\ & + \Re\left([\tilde{h}(x), \tilde{u}(x), \tilde{D}(x), \tilde{U}(x), \tilde{B}(x)]e^{i\omega t}\right),\end{aligned} \tag{2.23}$$

where terms with a bar are the steady state solution in equations (2.18) and (2.21), while terms with a tilde represent the variations in x of the time-dependent component of the solution. Substituting into equations (2.9) and (2.14) and keeping only terms of first order in the perturbed variables, the linearized equations were found to be

$$(\tilde{h}\bar{u} + \bar{h}\tilde{u})' + i\omega\tilde{h} = -\lambda\tilde{U}, \tag{2.24a}$$

$$(\tilde{h}\bar{u}' + \bar{h}\tilde{u}')' - \gamma(\bar{h}\tilde{h})' = 0, \tag{2.24b}$$

$$\bar{D}\tilde{U}' + \tilde{D}'\bar{U} = -\frac{\bar{U}}{r}\frac{\partial\tilde{h}}{\partial x}, \tag{2.24c}$$

$$\bar{D}\bar{U}\tilde{U}' + 2\bar{U}\tilde{U}\bar{D}' = -\frac{\tilde{B}}{r}\frac{\partial\bar{h}}{\partial x}, \tag{2.24d}$$

$$\bar{B}\tilde{U}' + \tilde{B}'\bar{U} = 0. \tag{2.24e}$$

Note that these results make use of the relationship $b = -h/r$ and the fact that $\bar{U}^2 = \bar{B}$ and $\bar{U}' = \bar{B}' = 0$ in the background state. When deriving equation (2.24d), two terms containing the gradient in $\tilde{h}$ cancel. Physically, this occurs because any increase in the buoyancy force that results from a steeper slope is exactly compensated by additional entrainment of (denser) ambient water into the plume as a result of the increased slope. This cancellation would not necessarily happen if a different parameterisation of entrainment were used.

The position of the end of the ice shelf varies according to

$$X = \bar{X} + \Re\left(\tilde{X}e^{i\omega t}\right), \tag{2.25}$$

where $\bar{h}(\bar{X}) = 0$ in the background state. Performing a Taylor expansion of $h(X)$ about $\bar{X}$ and using $h(X) = 0$, it can be shown that

$$\tilde{X} \approx -\frac{\tilde{h}(\bar{X})}{\bar{h}'(\bar{X})}. \tag{2.26}$$

There is a degeneracy in equation (2.24b) at the right boundary due to $\bar{h} \to 0$ at $x = \bar{X}$. This means that it is not necessary to specify a boundary condition here; it is only necessary to ensure that the solution remains bounded and satisfies equation (2.24b) at $x = \bar{X}$. Using the relationship $2\bar{u}' = \gamma\bar{h}$ and $\bar{h}(\bar{X}) = \bar{u}'(\bar{X}) = 0$, this can be shown to be equivalent to requiring

$$\tilde{u}'(\bar{X}) = \tfrac{1}{2}\gamma\tilde{h}(\bar{X}). \tag{2.27}$$

Note that $\tilde{D}$ is only present in equation (2.24c), meaning that it is uncoupled from the rest of the system. As such, $\tilde{D}$ is not solved for directly, but can be diagnosed from other variables.

2.3 Response to Varying Subglacial Discharge

This linear system can be used as a simple model with which to understand the response of the ice shelf and plume to perturbations in the boundary conditions. Variations in subglacial discharge affect both the velocity and buoyancy boundary conditions of the plume. Recalling the results for U and B in equation (2.19) and applying the binomial approximation, the linearised boundary conditions for $\tilde{U}$ and $\tilde{B}$ were determined in the form of equation (2.22), with all other perturbations assumed to be zero at the grounding line:

$$\tilde{U}(0) = \tfrac{1}{3}\tilde{Q}_g, \quad \tilde{B}(0) = \tfrac{2}{3}\tilde{Q}_g, \quad \tilde{D}(0) = 0, \quad \tilde{h}(0) = 0, \quad \tilde{u}(0) = 0. \tag{2.28}$$

The first two conditions represent the time-varying changes to plume velocity and buoyancy caused by perturbations to subglacial discharge. The remaining conditions indicate that there are no changes to the ice flux or plume thickness at the boundary. Equation (2.24) makes up a linear system with amplitude controlled by the initiating flux $\tilde{Q}_g$ through the boundary conditions in equation (2.28). This system was expressed as matrix operating on a vector $[\tilde{h}(x_0), \ldots, \tilde{h}(x_N), \tilde{u}(x_0), \ldots, \tilde{u}(x_N), \tilde{U}(x_0), \ldots, \tilde{U}(x_N), \tilde{B}(x_0), \ldots, \tilde{B}(x_N)]$, where x_j is the jth grid point at which the system is being solved. Chebyshev differentiation matrices were used to represent the derivative operator when constructing the matrix representing equation (2.24) (see § 3.1.1 for more details on this Chebyshev pseudospectral approach). This required the grid to be made up of $N+1$ Chebyshev collocation points spaced according to $x_j = \cos(j\pi/N)$, meaning they were clustered near the boundaries. This has the pleasing side effect of placing high resolution near the grounding line, where it is often most needed. The spatial structure of perturbations was found by solving with $\tilde{Q}_g = 1$. Note that the amplitudes of perturbations for other values of $\tilde{Q}_g$ can be determined by a linear rescaling.

The solution consists of complex numbers, with the physical state of the system at a given time being represented by the real component (figure 2.2). As such, both the magnitude (figure 2.3) and phase (figure 2.4) are of interest. The perturbation magnitudes show oscillatory variations in $\tilde{h}$ and a small drift in $\tilde{u}$. Any increase (decrease) in the ice thickness caused by the perturbations would increase (decrease) the ice stretching rate according to equation (2.9b). This would give rise to a positive (negative) velocity perturbation, explaining the drift in $\tilde{u}$. In the phase plots it can be seen that the phase of $\tilde{h}$ oscillates around $\pi/2$, while that of $\tilde{u}$ asymptotically approaches this value. The varying subglacial discharge Q_g impacts the thickness via the melt rate. Perturbations to the ice thickness accumulate whenever the perturbation to the melt rate is less than zero, meaning that the peak in $\tilde{h}$ occurs a quarter cycle after the minima in $\tilde{Q}_g$. As it is changes to the ice thickness which cause changes in ice velocity, the perturbations to the speed of the ice are also out of phase with the varying subglacial discharge. Because of the parameterisation

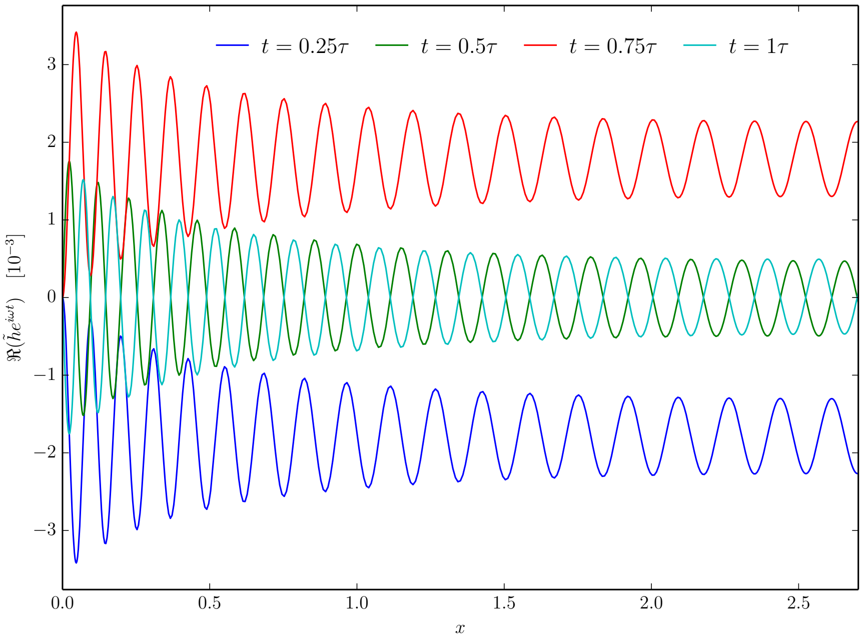

Figure 2.2: The real component of the perturbation to the ice thickness caused by variations in subglacial discharge, $\tilde{h}e^{i\omega t}$, at various times during the oscillatory period $\tau = 2\pi/\omega$. Two effects can be observed here: the development of ripples which propagate along the ice shelf, and overall oscillations in ice shelf thickness. Results in this and all subsequent figures were computed with $\tilde{Q}_g = 1$.

chosen for the entrainment, there is no feedback on $\tilde{U}$ or $\tilde{B}$ and they remain at the boundary values set at the grounding line, meaning that they are exactly in phase with variations in subglacial discharge (see bottom row of figure 2.4).

These changes combine to produce temporal oscillations in ice shelf thickness. Examining the real component of $\tilde{h}e^{i\omega t}$ at various times during the seasonal cycle (see figure 2.2) reveals two different responses to the seasonal forcing. One is the formation of ripples in the ice shelf thickness, which propagate towards the calving front over time (observed via inspection of animations of $h(x,t) - \bar{h}(x)$, not illustrated here). The other is a global oscillation in the thickness of the ice shelf over the course of a year as illustrated by shifts in the mean value of $\tilde{h}$ at given times. Note that negative thickness perturbations here do not imply refreezing, but instead correspond to modulation of melting about the background steady state. The switch of $\tilde{h}$ from positive to negative is a result of individual ice parcels melting more slowly as they are advected by the perturbed ice shelf than they melted in

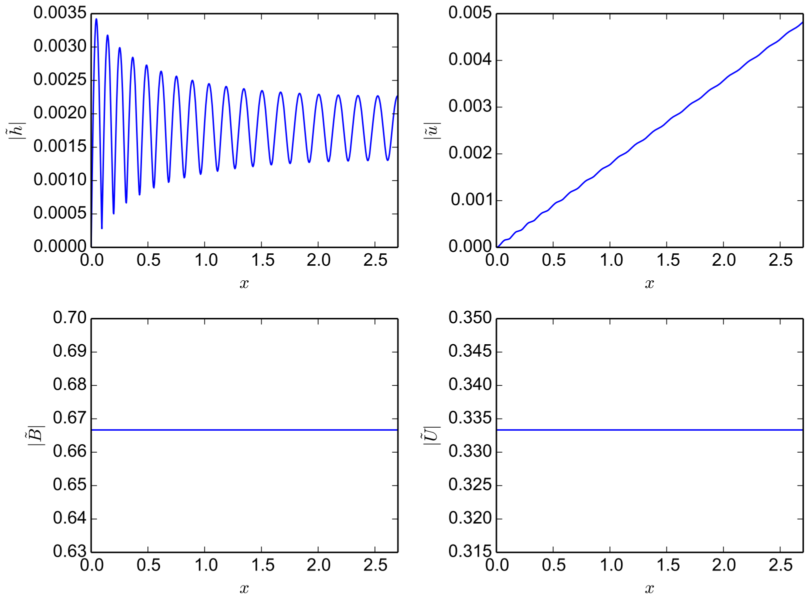

Figure 2.3: The magnitudes of the linear perturbations to the ice shelf caused by variations in subglacial discharge. Oscillatory behaviour is clear in $|\tilde{h}|$ and its effects can be seen in the small ripples in $|\tilde{u}|$. Note, however, that the perturbations to the plume, $|\tilde{U}|$ and $|\tilde{B}|$, do not change from the boundary values across the entire domain.

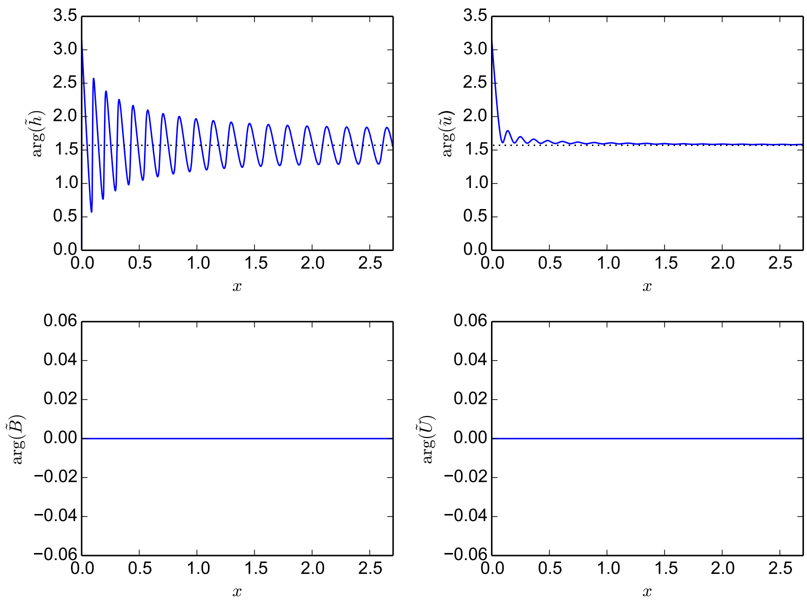

Figure 2.4: The phases of the linear perturbations to the ice shelf caused by variations in subglacial discharge. Variations can be seen in the phases of the ice shelf variables, $\tilde{h}$ and $\tilde{u}$. The phase of $\tilde{h}$ oscillates about $\pi/2$ (black dotted line), while the phase of $\tilde{u}$ asymptotically approaches $\pi/2$. However, the phases of the plume variables, $\tilde{B}$ and $\tilde{U}$, remain constant at zero.

the base state. This can be confirmed by computing the Lagrangian derivative D_t of the total thickness $h = \bar{h} + \tilde{h}e^{i\omega t}$, following the mean flow. The result,

$$D_t(h) = \partial_t(\tilde{h}e^{i\omega t}) + \bar{u}\partial_x(\bar{h} + \tilde{h}e^{i\omega t}) = i\omega\tilde{h}e^{i\omega t} + \bar{u}(\bar{h} + \tilde{h}'e^{i\omega t})$$

can be confirmed to be greater than 0 at all times, indicating that no refreezing occurs.

The basic structure of the ripples at first looks similar to the channels observed by Bindschadler, Vaughan, et al. (2011). However, upon converting the amplitude of these ripples to physical units for $\tilde{Q}_g = 1$ (indicating 100% variations in discharge), it becomes clear they are only of order 1 m in size, two orders of magnitude smaller than the observed channels. Thus, this mechanism would be insufficient to explain the observations of Bindschadler, Vaughan, et al. (2011). At most it might produce initial structures from which a feedback mechanism could lead to growth into full-sized channels. Nonlinear effects offer a potential source of feedback and this possibility is explored in Chapters 3 and 4. It is also important to note that the previously considered channelisation feedback (by which the plume preferentially flows along perturbations, causing them to deepen; see § 1.3) was inherently 2-D and thus could not be captured by this 1-D model. In this respect, the analysis presented here is different from the 2-D one performed by Dallaston et al. (2015), in which this feedback caused significant channel growth. The results nevertheless provide insight into the response of an ice shelf to varying subglacial discharge and the controlling physical mechanism is examined below.

2.3.1 Analysis of Physical Mechanism

In order to better understand the ice thickness oscillations seen in the previous section, the magnitudes of individual components of the system in equation (2.24) were plotted (see figure 2.5). The first plot (ice mass conservation) is the most important part of this figure; it demonstrates that the $i\omega\tilde{h}$, $\bar{u}\tilde{h}'$, and $-\lambda\tilde{U}$ terms in the continuity equation for ice are much larger than any of the remaining terms (which represent stretching processes). Using the expression for the Lagrangian

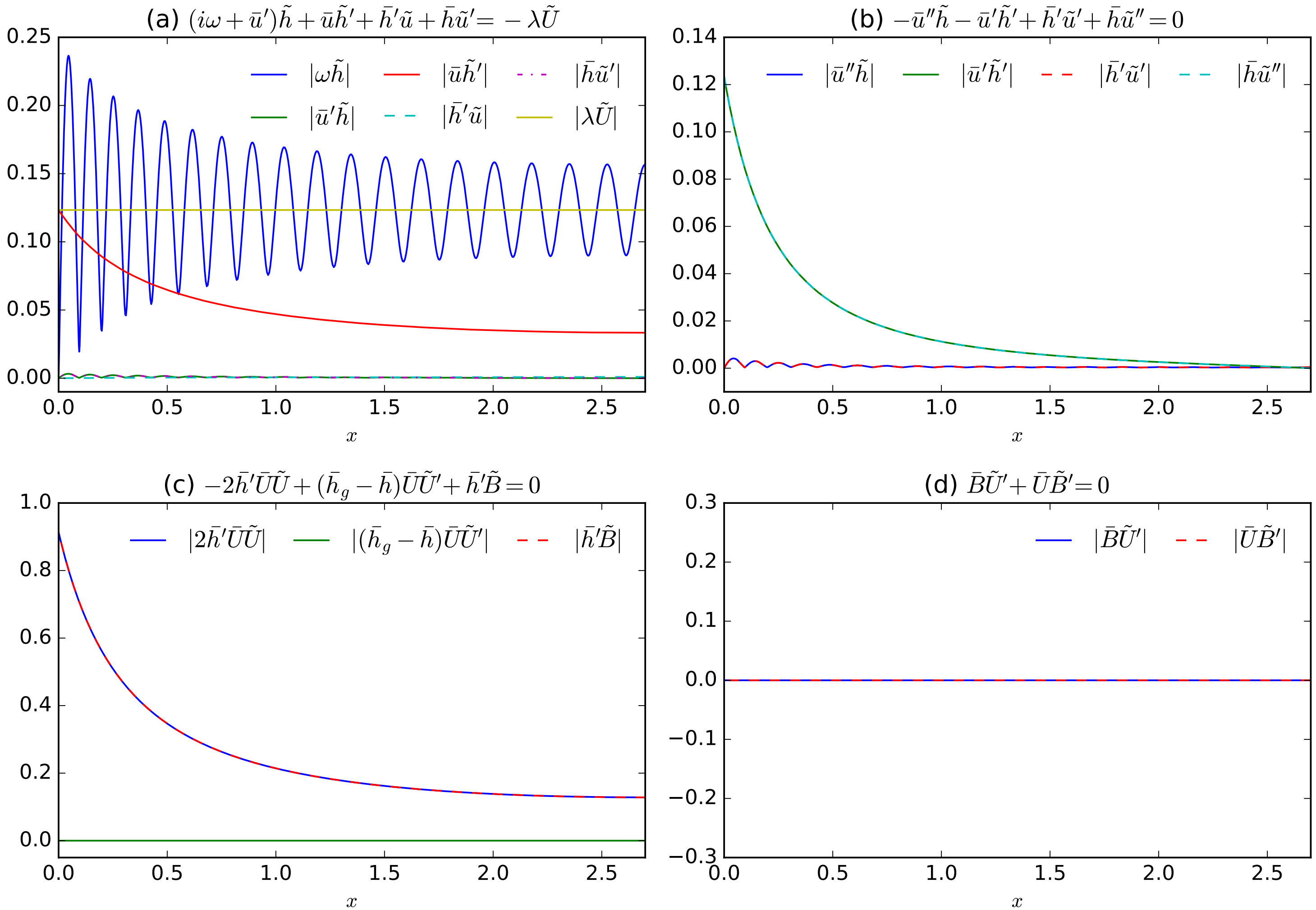

Figure 2.5: The magnitudes of individual components of the linearized equations. Each subplot represents a different equation: (a) ice mass conservation, (b) conservation of ice momentum, (c) conservation of plume momentum, (d) conservation of salt. Components are indicated in the legend of each plot.

derivative $D(\tilde{h}e^{i\omega t})/Dt$ following the background flow derived earlier, it can be seen that the leading order balance in the conservation of ice mass in equation (2.24a) is

$$\frac{D}{Dt}\tilde{h}e^{i\omega t} \approx -\lambda \tilde{U} e^{i\omega t}. \tag{2.29}$$

This indicates that the rate of change of thickness perturbations, following the background flow, is set by melting.

This result has important implications and allows for an understanding of the behaviour of the ice shelf as a whole. At any given time, all ice across the shelf will be experiencing the same rate of change in perturbed thickness due to melting, because the plume velocity $\tilde{U}$ and hence the melt rate are both uniform across the shelf. The global oscillations in the ice shelf thickness are the logical consequence of this spatially uniform melting pattern that oscillates in time. To see why the ripples form, consider the time $t_g(x)$ when the parcel of ice located at x at time t originally crossed the grounding line. The boundary condition sets $\tilde{h} = 0$ for the ice parcel at time t_g. Integrating equation (2.29) reveals that the thickness of this ice parcel at a later time t is then

$$\tilde{h} \approx \frac{i\lambda\tilde{U}}{\omega}\left(1 - e^{i\omega(t_g - t)}\right). \tag{2.30}$$

Clearly, the perturbation to the ice shelf thickness oscillates with the time elapsed since crossing the grounding line, $t - t_g$. Given that $\bar{u}$ is monotonic increasing with x and $\tilde{u}$ is small, t_g is monotonic decreasing with x at a given time. As such, the perturbed ice thickness also oscillates with x, but the non-uniformity of $\bar{u}$ means that the ripples are not a perfect sinusoid. Putting this in physical terms, ice which crosses the grounding line when the discharge (and hence melting) is high will experience more accumulated melting by the time it reaches the end of the ice shelf than would ice which crosses the grounding line when the discharge is low. This effect causes these two parcels of ice to have different thicknesses.

By tracking the position of individual peaks and troughs of the ripples over time, the phase speed of the ripples can be determined. The speed of a given peak/trough was found to be in near perfect agreement with the local velocity $\bar{u}$

of the ice. This indicates that the ripples are being advected with the background ice flow and are not moving relative to it, consistent with the mechanism for their formation described above.

Figure 2.5b (ice momentum) shows that $\bar{u}'\tilde{h}' = \bar{h}\tilde{u}''$. By substituting $\bar{h} = 2\bar{u}'/\gamma$, simplifying, and then integrating in x, it can be seen that the relation $\gamma\tilde{h} = 2\tilde{u}'$ holds for the perturbations. This indicates that, as in the steady state, perturbations to stretching ($\tilde{u}'$) are driven by changing hydrostatic pressure ($\gamma\tilde{h}$). Figure 2.5c (the plume momentum balance) reveals $-2\bar{h}'\bar{U}\tilde{U} + \bar{h}'\tilde{B} = 0$ exactly, meaning that changing momentum fluxes within the plume are driven by changes to the buoyancy flux from varying subglacial discharge. The balance in figure 2.5c (the plume salt budget) is trivially satisfied as both $\tilde{U}$ and $\tilde{B}$ are constant. This is true for $\tilde{U}$ because the chosen entrainment parameterisation causes an exact balance between any increase in buoyancy forces with an increase in entrainment. Hence the increase in buoyancy force is expended accelerating the entrained fluid to the existing plume velocity. Similarly, any change to the salinity of the plume due to entrainment is offset by the increased thickness of the plume, causing $\tilde{B}$ to also be constant. This reflects that the ambient fluid has no buoyancy and thus can't change the buoyancy of the plume.

2.3.2 Sensitivity to Varying Parameters

By varying the driving frequency, ω, a dispersion relationship was obtained for ω and the wavelength of the ripples. Initial attempts to determine a wavelength using a Fourier transform proved troublesome because the spectrum lacked a clean peak. The most effective way to estimate a representative wavelength ultimately proved to be measuring the distance between the first peak and trough in $\Re(\tilde{h})$. The spatially averaged value of $\bar{u}$, $\langle\bar{u}\rangle$, was also found over this range. These results are plotted in figure 2.6, revealing the relationship

$$\omega \approx k\langle\bar{u}\rangle, \tag{2.31}$$

where k is the diagnosed wave-number. This is what would be expected given that the wave-like thickness perturbations are transported via advection of the ice.

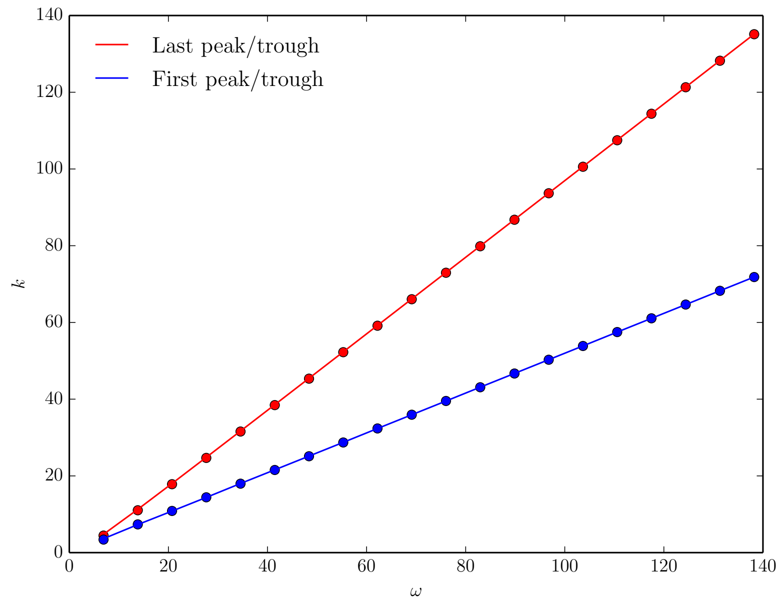

Figure 2.6: A plot comparing the wave-number of the first (blue) and last (red) ripple in the ice shelf with the driving frequency of variations in subglacial discharge (circles). Also plotted is the relationship $k = \omega/\langle\bar{u}\rangle$ (blue/red lines for first/last ripples respectively).

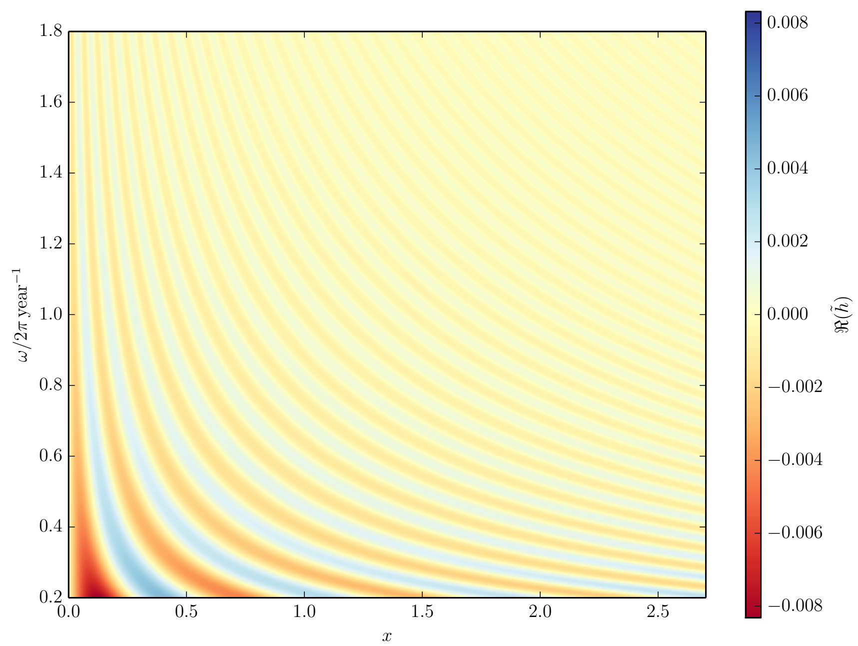

Figure 2.7: A contour plot of the real component of $\tilde{h}$ along the ice shelf at $t = 0$, for different driving frequencies, ω, of the perturbations to the subglacial discharge.

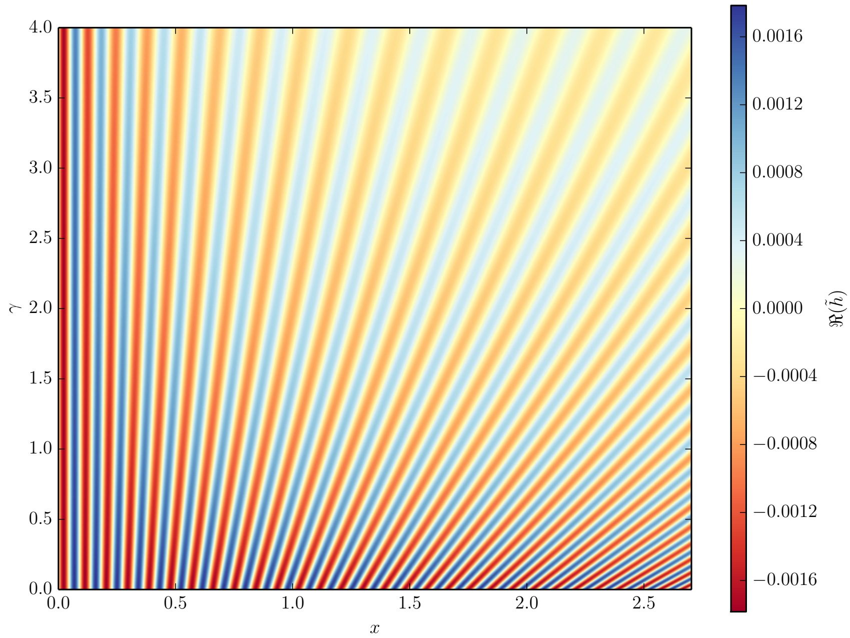

Figure 2.8: A contour plot of the real component of $\tilde{h}$ along an ice shelf forced by variations in subglacial discharge, for a range of values of the parameter γ, which quantifies stretching of the ice.

Note that the aforementioned technique revealed identical results when applied to the last peak and trough on the ice shelf, where the ice velocity $\langle \bar{u} \rangle$ is larger (also plotted in figure 2.6). The response of ripple amplitude to the frequency of variations in subglacial discharge was also examined. Smaller values of the frequency ω result in ripples with larger amplitudes, as there is more time for excess melting to accumulate over each period (see figure 2.7), as predicted by equation (2.30).

Stretching of the ripples would occur due to divergence in the velocity. When the driving force for viscous stretching, γ, is increased, it leads to a more significant decrease in the amplitude and wave-number of ripples towards the end of the shelf (as illustrated in figure 2.8). This is due to changes in the background flow $\bar{u}$; as can be seen in figure 2.1, larger values of γ cause greater change in $\bar{u}$ along the length of the ice shelf, which in turn leads to greater stretching of the ripples and thus reduced amplitude. The opposite is observed when γ is decreased, and when $\gamma = 0$ the amplitude and wave-number of the ripples stays constant across the entire shelf, because no stretching occurs and there is no divergence of the velocity.

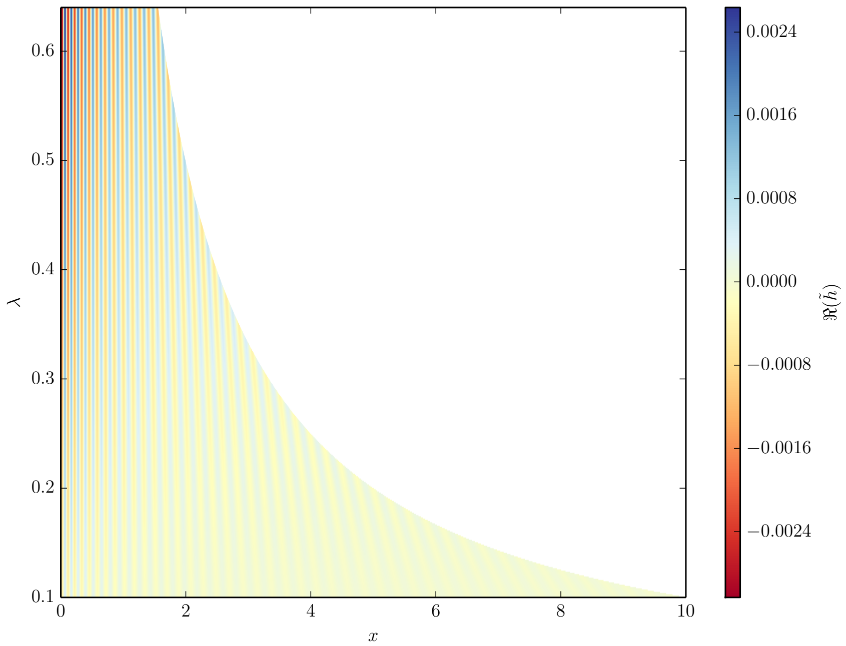

Figure 2.9: A contour plot of the real component of $\tilde{h}$ along an ice shelf forced by variations in subglacial discharge, for different values of the parameter λ, which quantifies melting. Note that the length of the ice shelf is inversely proportional to λ, as seen in equation (2.21). The large white gap in the graph arises due to the shelf being shorter for larger values of λ.

Changing the dimensionless melt rate, λ, changes the length of the ice shelf (see figure 2.9). The shelf shortens as λ increases, as was already known from equation (2.21) of the steady state solution. It was found that there was somewhat more stretching in the low-melt cases, as there was more shelf on which stretching could occur. Stronger melting increased the amplitude of the ripples, as the oscillations in flow due to varying subglacial discharge result in greater variability of total melt.

By evaluating equation (2.30) at $t_g - t = -\pi/2\omega$ and recalling that $\tilde{U}(x) = \tilde{U}(0)$, it was found that

$$\tilde{h}_{\max} \approx \frac{\lambda \tilde{U}}{\omega}(i-1). \tag{2.32}$$

This yields a slight overestimate of $\tilde{h}$ when the default value of $\gamma = 2$ is used (see figure 2.10a) due to the presence of viscous stretching in the full solution, which is neglected in the approximation in equation (2.29). Stretching reduces the amplitude of the ripples compared to the amplitude due to the combination of advection

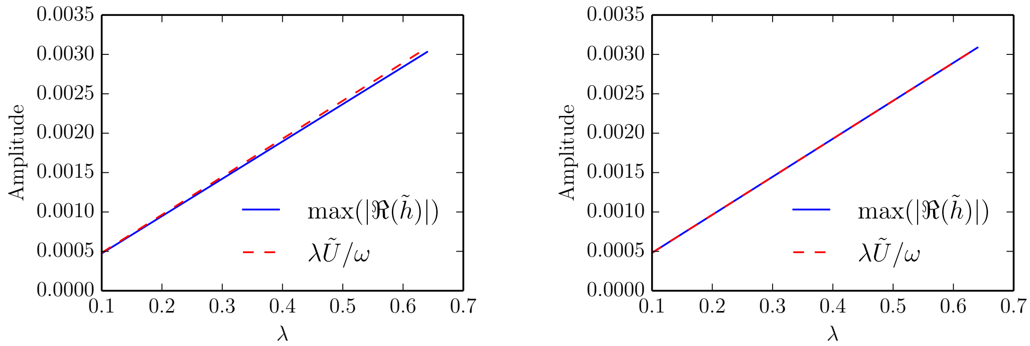

(a) $\gamma = 2$ **(b)** $\gamma = 0$

Figure 2.10: The relationship between the maximum absolute value of the real ice thickness perturbation, $|\Re(\tilde{h})|$ versus scaled melt rate, λ (blue solid line). Also plotted is the relationship expected from equation (2.32) (red dashed line). In the case $\gamma = 0$, these agree perfectly, meaning only the latter is actually visible.

and melt alone. If $\gamma = 0$, no stretching occurs and examining equation (2.24a) reveals that equation (2.29) becomes exact. In this case, the numerical results match equation (2.32) exactly (figure 2.10b).

2.4 Response to Varying Ice Flux

The flux of ice crossing the grounding line might also vary over time, on seasonal or other timescales. This could be caused by processes such as basal slippage causing the ice to flow faster. Periodic forms of such variability can be expressed in the boundary conditions

$$\tilde{U}(0) = 0, \quad \tilde{B}(0) = 0, \quad \tilde{D}(0) = 0, \quad \tilde{h}(0) = 0, \quad \tilde{u}(0) = \tilde{u}_g, \tag{2.33}$$

so that the ice inflow velocity varies sinusoidally with all other variables fixed. As mentioned earlier, the inflowing ice thickness is taken to be fixed and motion of the grounding line is neglected.

The boundary conditions in equation (2.33) were applied to the linear system in equation (2.24), which was solved with the parameter values in table 2.1. The real components of the resulting thickness values at various times over the seasonal cycle can be seen in figure 2.11. The phase and magnitude of the complex solution for each variable can be found in figures 2.12 and 2.13, respectively. Changes

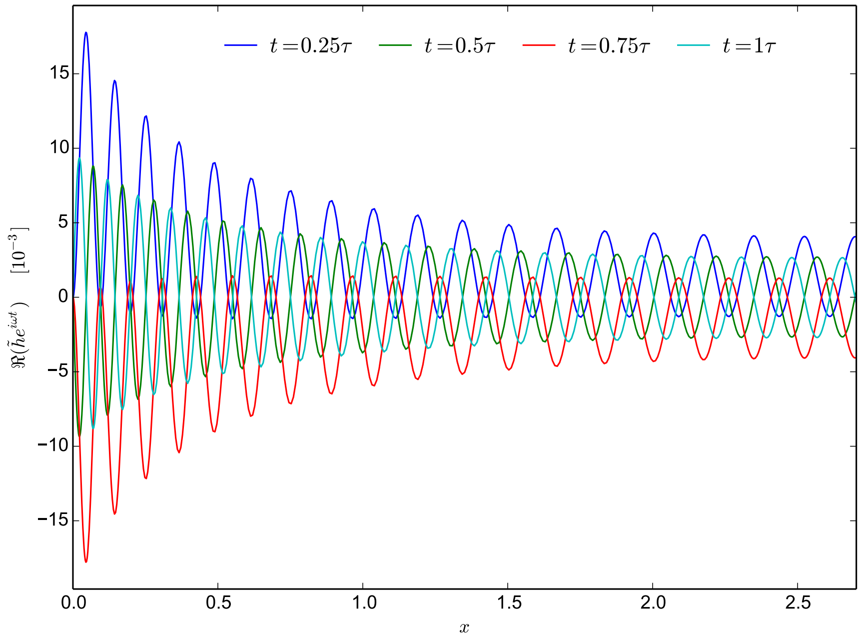

Figure 2.11: The real component of the perturbation to the ice thickness, $\tilde{h}e^{i\omega t}$, in response to variations in ice flux across the grounding line at various times during the oscillatory period $\tau = 2\pi/\omega$. Two effects can be observed here: the development of ripples which propagate along the ice shelf and overall oscillations in ice shelf thickness.

to the ice thickness are an order of magnitude larger than those seen resulting from variations in subglacial discharge with forcing of comparable dimensionless magnitude at the grounding line.

The phase of $\tilde{h}$ rises from zero to π, before cycling to $-\pi$ and more rapidly rising to 0, at which point the cycle repeats. If regions where the phase $\arg(\tilde{h}) < 0$ in the upper left plot of figure 2.13 were ignored then there would be a spatial average value of $\langle \arg(\tilde{h}) \rangle = \pi/2$, a quarter cycle offset from the forcing. However, in a minority of locations $\arg(\tilde{h}) < 0$, so its average value would actually be somewhat less than $\pi/2$, but greater than 0. This suggests accumulation of excess thinning during certain parts of the forcing period, similar to that seen for changes to subglacial discharge.

In this case, changes to the ice velocity are overwhelmingly driven by forcing at the boundary, meaning that the perturbations resulting from changing ice thickness are negligible. Thus, $\tilde{u}$ stays largely in phase with the forcing. However, it does drift somewhat and this is thought to result from the slight speedup of the ice due to changes in stretching driven by thickness perturbations. As noted

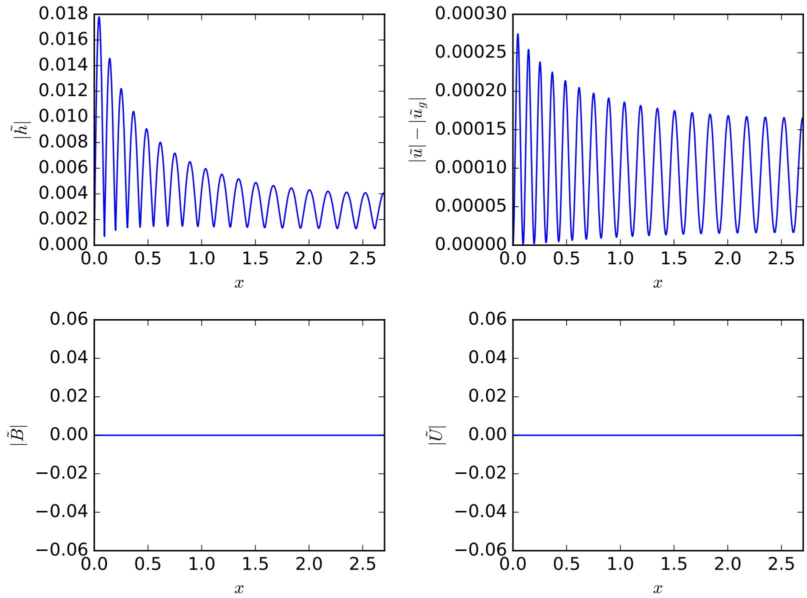

Figure 2.12: The magnitudes of the linear perturbations to the ice shelf when forced with varying ice flux across the grounding line. Oscillatory behaviour is clear in $|\tilde{h}|$ and its effects can be seen in the small ripples in $|\tilde{u}|$ relative to the velocity perturbation at the grounding line, $|\tilde{u}_g|$. Note, however, that $|\tilde{U}|$ and $|\tilde{B}|$ are unaffected.

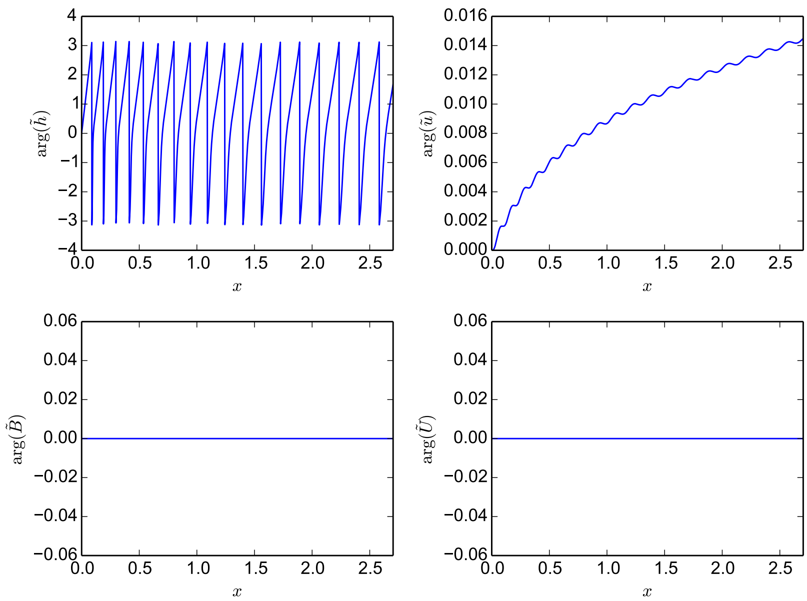

Figure 2.13: The phases of the linear perturbations to the ice shelf when forced with varying ice flux across the grounding line. Variations can be seen in the phase of $\tilde{h}$, whereby it increases to just above π (equivalent to just above $-\pi$) before returning to 0 and repeating the process. Changes to the phase of of $\tilde{u}$ are small but indicate a slight drift, while those of the plume variables, $\tilde{B}$ and $\tilde{U}$, remain constant at zero.

above, thickness perturbations are approximately a quarter cycle out of phase with the velocity forcing. The small changes they make to velocity accumulate along the length of the shelf and slightly increase the phase of $\tilde{u}$. Once again, the compensation between varying slope accelerating the plume and entrainment decelerating it means that the plume variables, U and B, do not change from the boundary values which, in this case, are 0.

As with the case of varying subglacial discharge, examining the real component of $\tilde{h}e^{i\omega t}$ at different times during the seasonal cycle (figure 2.11) reveals two modes of behaviour: ripples inscribed in the ice and global oscillations of the ice thickness. As noted above, the ripples are an order of magnitude larger than those caused by subglacial discharge. An additional difference is in the form of the global oscillations. Whereas those driven by subglacial discharge were of the same magnitude across the entire domain of the ice, here the magnitude decays with x at a similar rate to the magnitude of the ripples. It was again confirmed that, in the regions where the ice appears to be thickening, no refreezing is required; a reduction in the rate of melting is sufficient to explain the behaviour.

While these ripples are considerably larger than those caused by variations in subglacial discharge (on the order of 10 m in physical units for 50% ice flux variations), they remain an order of magnitude smaller than the channels observed underneath Pine Island Glacier. Thus, this mechanism is also insufficient to explain the observations of Bindschadler, Vaughan, et al. (2011).

2.4.1 Analysis of Physical Mechanisms

Repeating the analysis of § 2.3.1, the magnitude of each term of each of the linearised shelf equations was plotted in figure 2.14. The most interesting of these is figure 2.14a, representing ice continuity. This shows that the dominant terms are $i\omega h$, $\bar{u}\tilde{h}'$, and $\tilde{u}\bar{h}'$ (note that there is no perturbation to the melt rate in this case), giving the approximate relation

$$\frac{D}{Dt}\tilde{h}e^{i\omega t} \approx -\tilde{u}e^{i\omega t}\frac{d\bar{h}}{dx}, \tag{2.34}$$

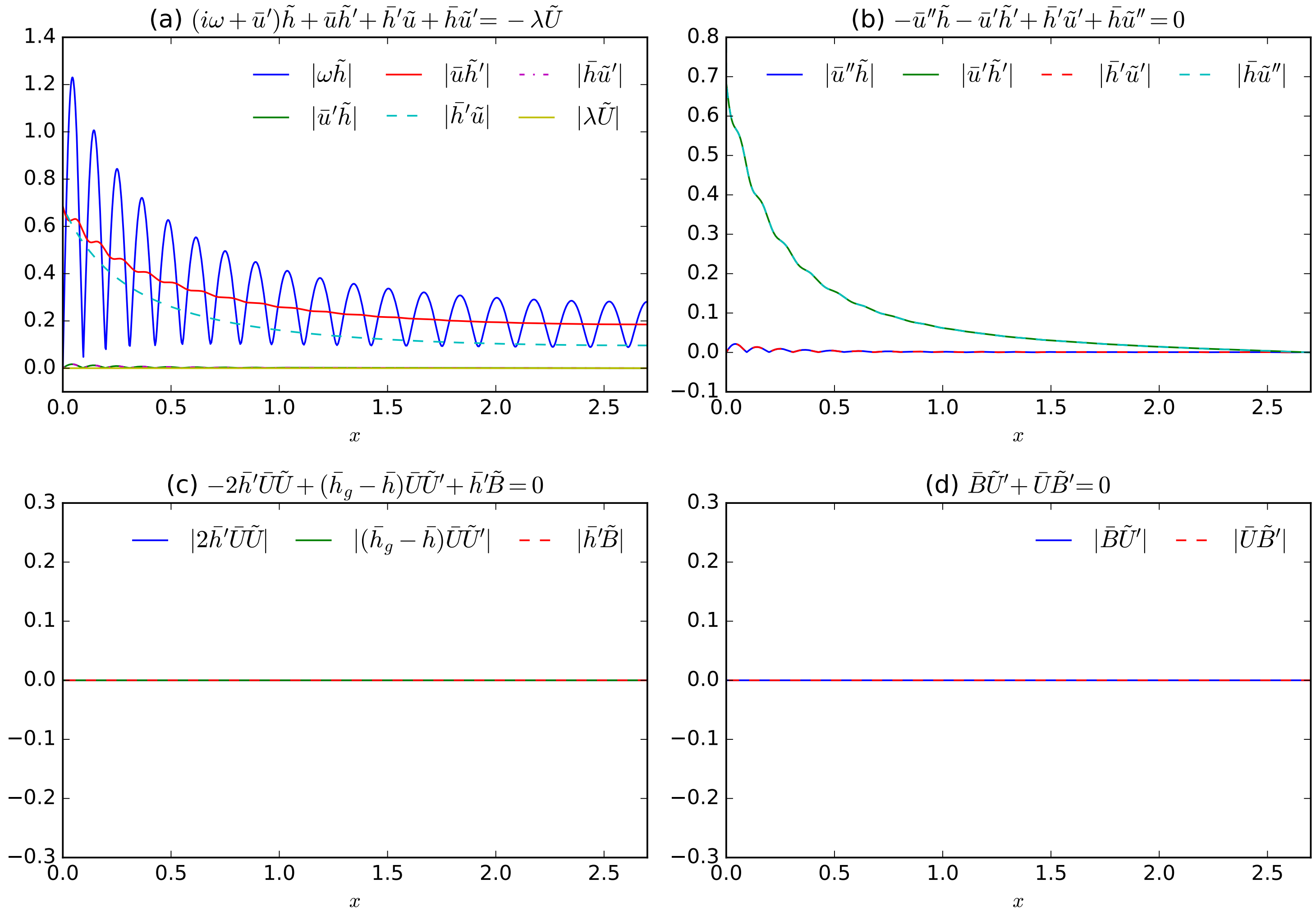

Figure 2.14: The magnitudes of individual components of the linearised equations. Each subplot represents a different equation: (a) ice mass conservation, (b) conservation of ice momentum, (c) conservation of plume momentum, (d) conservation of salt. Components are indicated in the legend of each plot.

where $D/Dt = \partial/\partial t + \bar{u}\partial/\partial x$ is a Lagrangian derivative following the mean flow (see § 2.3). Here it is worth noting that linearisation prevents the advection of thickness perturbations from being affected by perturbations to the velocity. When working on the assumption that $\tilde{u}$ is small (as it was for variations in subglacial discharge) this is a reasonable approximation. However, in this case it is changes to the ice velocity which provide the forcing and $\tilde{u} \approx \tilde{u}_g$ is not small. The linear analysis is only able to capture how velocity perturbations alter advection of the mean state, and not how they advect the thickness perturbations.

Rearranging equation (2.9a) for steady state, recalling that $\bar{U} = 1$, and making use of the previously mentioned relationship $\gamma\bar{h} = 2\bar{u}'$, it can be shown that

$$\bar{h}' = -\frac{2\lambda + \gamma\bar{h}^2}{2\bar{u}}. \tag{2.35}$$

Substituting into equation (2.34) then yields

$$\frac{D}{Dt}\tilde{h}e^{i\omega t} \approx \frac{\tilde{u}}{\bar{u}}\left(\lambda + \frac{1}{2}\gamma\bar{h}^2\right)e^{i\omega t}. \tag{2.36}$$

This indicates that changes to the ice thickness as it is advected down-shelf are caused by the ice being exposed to melting (λ term) and stretching (γ term) for shorter or longer periods when the ice is moving faster or slower.

Unlike in the case of subglacial discharge, the inclusion of the $\bar{h}$ and $\bar{u}$ terms in the right hand side of the equation means that the rate of change of $\tilde{h}$ is not constant across the domain for $\gamma = 0$. That makes it more difficult to analyse the results. However, some insight can be gained by looking at the special case of no stretching with $\gamma = 0$, implying $\bar{u} = 1$ and $\tilde{u} = \tilde{u}_g$ for all x. Taking the ice parcel located at x to have crossed the grounding line at time $t_g(x)$ and integrating equation (2.36) then yields

$$\tilde{h} = -\frac{i\tilde{u}\lambda}{\omega}\left(1 - e^{i\omega(t_g - t)}\right). \tag{2.37}$$

Thus the perturbation to ice shelf thickness oscillates with t_g. Since $\bar{u} = 1$, $t_g = t - x$, it follows that $\tilde{h}$ oscillates in x. Physically, this means that a parcel of ice which crosses the grounding line when the ice is moving slowly will take longer to reach a given location than an ice parcel which crosses the grounding line when the ice is moving quickly. This means there will be more time for melt to accumulate on the slow-moving ice, resulting in this ice parcel being thinner than the fast-moving one.

While such a tidy solution can not be found for $\gamma \neq 0$, examining the form of the equation allows further insight. It is known that $\bar{u}$ increases monotonically with x, while $\bar{h}$ decreases monotonically. Thus, the magnitude of the right hand side of equation (2.36) declines with x. This explains why the size of the global oscillations decreases along the length of the ice shelf. However, near the grounding line, $\bar{u} \approx \bar{h} \approx 1$. The presence of the $\gamma\bar{h}^2/2$ term on the right hand side of the equation thus increases the magnitude considerably compared to the case without stretching. Physically, this means that ice near the grounding line undergoes a high level of thinning due to stretching. Ice parcels are highly sensitive to the amount of time spent in that region due to perturbations to ice velocity. Thus, varying ice flux inscribes a ripple much larger than those resulting from changes to subglacial discharge. This ripple is then advected downstream and stretched so that it has a larger wavelength and lower magnitude.

The dominant balances seen in figure 2.14b for the ice momentum budget are the same as those for subglacial discharge in figure 2.5b. This means that $\gamma\tilde{h} = 2\tilde{u}'$, as was the case in steady state, and that perturbations to stretching ($\tilde{u}'$) are again driven by perturbations to hydrostatic pressure ($\gamma\tilde{h}$). As the forcing did not alter the values of $\tilde{U}$ or $\tilde{B}$, all terms in figures 2.14c and d are zero and the plume equations are trivially satisfied.

2.4.2 Sensitivity to Varying Parameters

Varying the frequency, ω, revealed a dispersion relationship identical to that found for subglacial discharge in equation (2.31). This corresponds to wave advection by the background velocity, $\langle\bar{u}\rangle$, averaged over a ripple. As before, smaller values of ω result in larger perturbations, as there is more time for excess exposure to melting and stretching to accumulate (see figure 2.15).

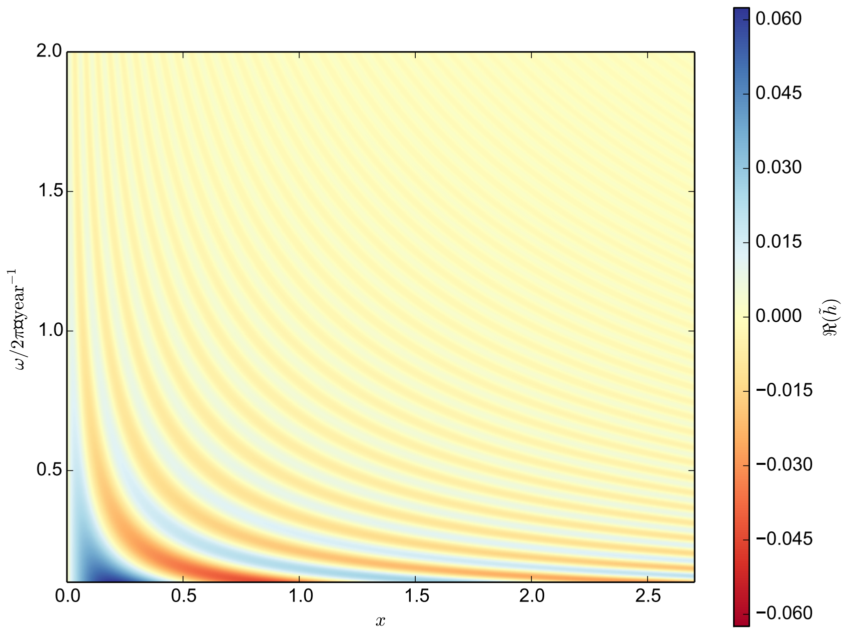

Figure 2.15: A contour plot of the real component of $\tilde{h}$ along the ice shelf at $t = 0$, for different driving frequencies ω of the perturbations to the ice flux across the grounding line.

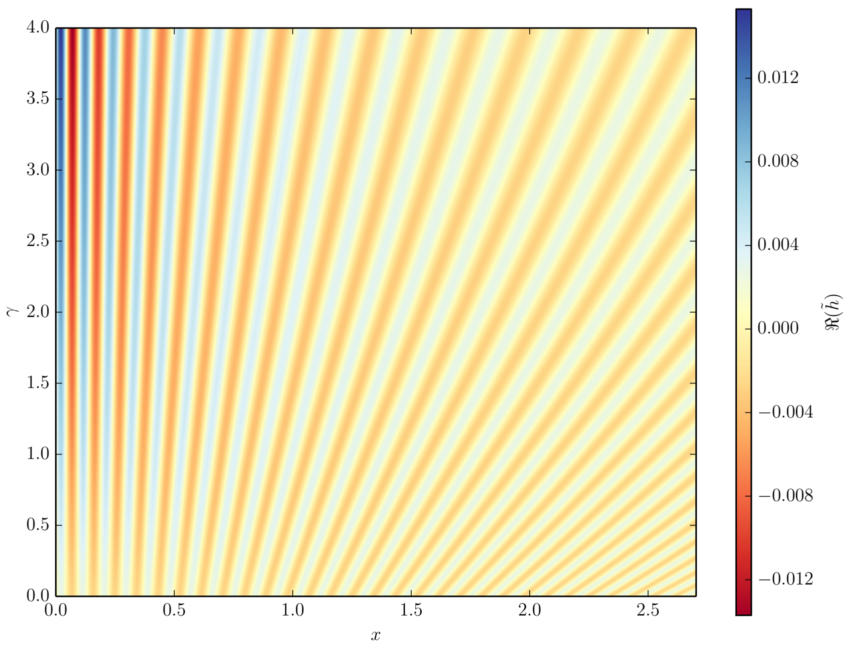

Figure 2.16: A contour plot of the real component of $\tilde{h}$ along an ice shelf driven by variations in the ice flux across the grounding line, for a range of values of the parameter γ, which quantifies stretching of the ice.

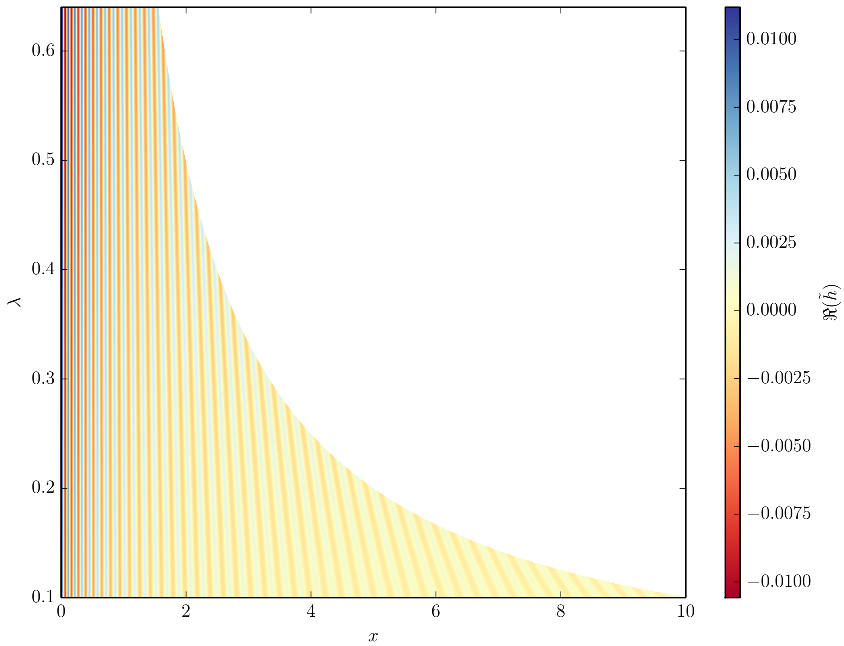

Figure 2.17: A contour plot of the real component of $\tilde{h}$ along the ice shelf forced by variations in the ice flux across the grounding line, for different values of the parameter λ, which quantifies melting. Note that the length of the ice shelf is inversely proportional to λ, as seen in equation (2.21). The large wight gap in the graph arises due to the shelf being shorter for larger values of λ.

Once again, increasing the driving force for stretching (quantified in γ) leads to a greater reduction in amplitude and wavenumber of ripples along the length of the ice shelf relative to their values near the grounding line, as can be seen in figure 2.16. The reduction in amplitude with x is also evident in figures 2.15 and 2.17. Decreasing stretching has the opposite effect and when $\gamma = 0$ the amplitude and wavelength of the ripples stays constant across the entire shelf. However, the results differ from those for variations in subglacial discharge in that stronger stretching results in larger amplitude ripples near the grounding line, as expected from equation (2.36). The amplitude of the ripples near the calving front appears to be relatively insensitive to the value of γ; although large γ results in larger ripples near the grounding line, it also stretches them more, counteracting this effect.

The results of varying the dimensionless melt rate λ (figure 2.17) are broadly similar to those in the case of subglacial discharge variations. Smaller λ results in a longer ice shelf and thus allows more stretching to occur downstream. Stronger melting tends to increase the amplitude of the ripples while weaker melting decreases them. This is expected from equation (2.36). Unlike for increased stretching, here the increased amplitude can be seen across the entire ice shelf.

2.4.3 Fourier Analysis

The solution derived above can be calculated for any value of ω. Because it is the solution to a linear equation, it is possible to construct solutions for any forcing which can be expressed as a linear combination of sinusoids of different frequencies, from a linear combination of the solutions at each frequency. If an arbitrary forcing $f(t)$ is applied to the ice shelf, a Fourier transform (see § 3.1.1 for more information) can be used to decompose it into its component frequencies. The shelf can then be solved at each frequency and these results added together, weighted by the corresponding Fourier coefficient, to find the response of the shelf to $f(t)$.

In reality, the variations in ice flux across the grounding line would not necessarily be expected to be sinusoidal. A somewhat more plausible form would be that of a square wave. This would represent the ice moving slowly for part of the year and then suddenly speeding up. This might be caused by increased flow of water underneath the grounded ice in summer, leading to reorganisation of the subglacial drainage system and modified basal drag (as discussed by Schoof and Hewitt, 2013). The discontinuity of a square wave tends to cause a ringing phenomenon when it is represented by a finite number of Fourier terms, so to avoid this the transition from one state to another will be smoothed slightly. This is achieved using a "smoothstep function" (Ebert et al., 2003):

$$f(t) = \begin{cases} 0.5 & t \leq 0.15\tau \\ 0.5 + 6\theta_1^5 - 15\theta_1^4 + 10\theta_1^3 & 0.15\tau < t < 0.35\tau \\ 1.5 & 0.35\tau \leq t \geq 0.65\tau \\ 1.5 - 6\theta_2^5 + 15\theta_2^4 - 10\theta_2^3 & 0.65\tau < t < 0.85\tau \\ 0.5 & 0.85\tau \leq t, \end{cases} \tag{2.38}$$

where τ is used to indicate the period of the forcing, $\theta_1 = 5(t/\tau - 0.15)$, and $\theta_2 = 5(t/\tau - 0.65)$. The form of the smoothed square wave can be seen in figure 2.18. Its values were found at 32 equispaced locations and this data used to compute

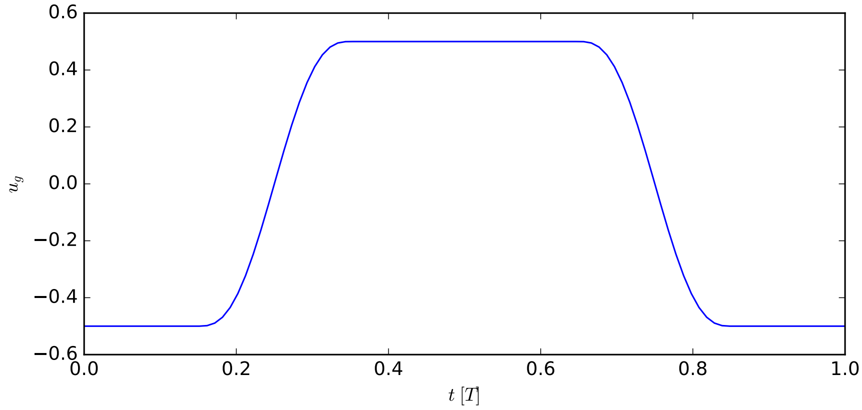

Figure 2.18: The smoothed square wave forcing applied to the ice flux across the grounding line.

a real Fourier transform. More samples resulted in Fourier modes of very high driving frequency and the solution to the linear system could not be resolved in these cases without an impractically high number of grid points.

Using the algorithm described above, the changes to ice thickness resulting from the smoothed-square-wave perturbations to the ice flux were calculated and can be found in the upper panel of figure 2.19. In many ways this result is similar to that for sinusoidal forcing, in that there are both ripples inscribed in the ice shelf base (the magnitude of which declines due to stretching) and global oscillations to the ice thickness. However, the ripples now take the form of triangle waves (with slightly rounded corners) and are of larger amplitude. The triangle form is the result of integrating the smoothed square wave of the forcing. The increased magnitude is the result of the forcing now placing the state of the system at a greater average distance from the background state than would sinusoidal forcing.

Looking at the sum of the background state and the thickness perturbations (figure 2.19, lower panel), the shelf exhibits a step-like structure whereby there are rapid changes of thickness separated by regions of more slowly-changing basal draft. Although on a much larger horizontal scale, this pattern of thickness variability is reminiscent of the basal terraces observed by Dutrieux, Stewart, et al. (2014). Though of similar vertical scale, the observed terraces occur on length-scales of order 200 m, as compared to the wavelength of ~ 3 km (near the grounding line)

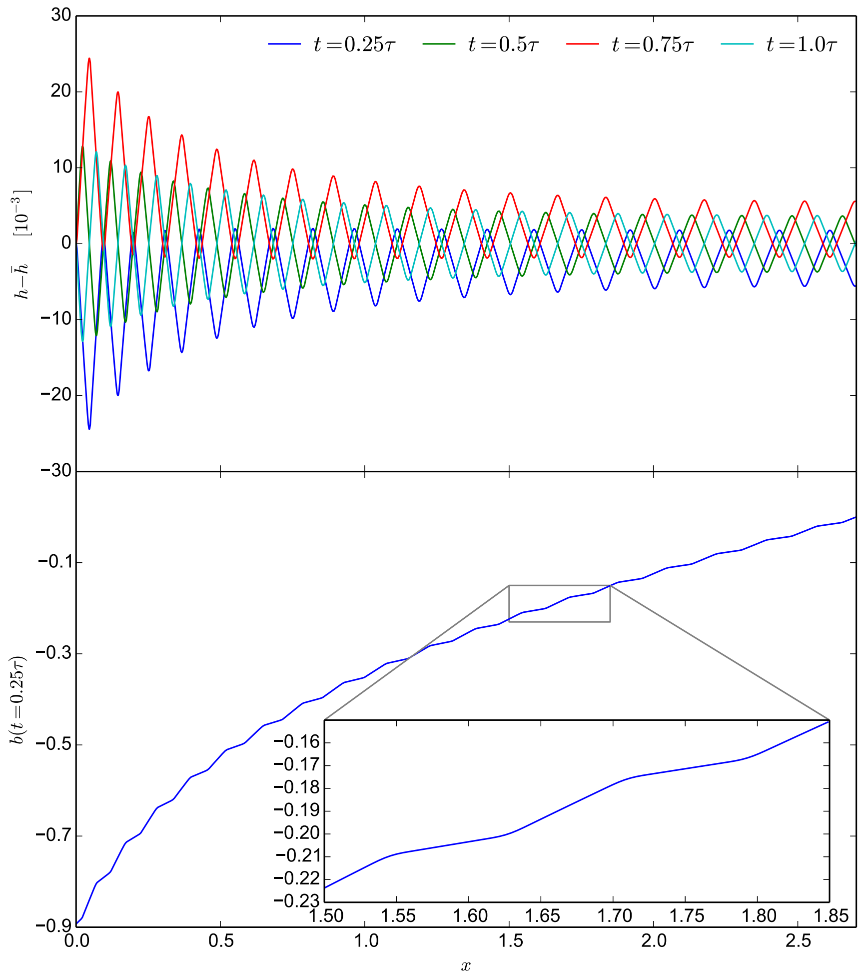

Figure 2.19: Upper panel: the perturbation to the thickness of the ice shelf at various times over the period (τ) of the square-wave forcing of ice flux across the grounding line. Lower panel: the total basal depth of the forced ice shelf at time $t = 0.25\tau$. An inset gives a zoomed-in view of the ripples.

for the present calculation. This suggests that perhaps terraces could be formed as the result of much higher frequency forcing. One potential source would be the changes to ice speed on the spring-neap tidal cycle observed on some Antarctic ice shelves (e.g. Rosier et al., 2017), although this forcing took the form of a sinusoid rather than a square wave. Figure 2.15 indicates that a higher frequency would produce steps of much smaller vertical size, meaning that some sort of feedback mechanism would also be required for them to grow to match observations.

2.5 Conclusions on Linear Results

The linear analysis described in this chapter showed that temporal oscillations in glacier and plume boundary conditions can result in ripples being melted into the base of an ice shelf. Oscillations in subglacial discharge result in global oscillations to the glacier thickness and the melting ripples onto the base of the ice which are then advected by the background ice flow. This was due to ice entering the domain when the discharge (and hence melt rate) would experience less cumulative melting than adjacent ice which entered the domain when discharge was high. However, these ripples are extremely small: even oscillations with a magnitude 100% of the background subglacial discharge rate produce ripples of only $\sim 1\,\mathrm{m}$ in size. The amplitude of the ripples grew in proportion to the melt rate. A higher stretching rate did not change the amplitude of ripples near the grounding line, but led to smaller amplitudes downstream. The local wave-number of a ripple was found to be proportional to the forcing frequency divided by the spatially-averaged background ice velocity in that location (corresponding to a dispersion relation for advective propagation). Ripple amplitude was inversely proportional to the forcing frequency, as longer-period forcing provided more time for excess melt to accumulate and thicken the ice.

Oscillations in the ice flux also produced ripples, along with global oscillations that were comparatively smaller than for varying subglacial discharge. Fast moving ice has less time to accumulate thinning than slow-moving ice, resulting in the former being thicker than the latter. When the ice flux underwent oscillations of 50% of the mean value the magnitude of these ripple perturbations was $\sim 10\,\mathrm{m}$, an order of magnitude larger than the subglacial discharge result. Higher melt rates once again led to greater ripple amplitudes for forcing by varying ice flux, although the effect was less pronounced than for the case with varying subglacial discharge. Increasing the stretching rate led to larger ripples near the grounding line and had little affect on the amplitude near the calving front. As was the case with subglacial discharge forcing, the ripple amplitude varied inversely with forcing frequency and the wave-number was related to the frequency by the background velocity averaged over the ripple.

Both mechanisms considered here were insufficient to produce channels of the type and depth observed by Bindschadler, Vaughan, et al. (2011). The ripples altered the slope of the ice shelf but were not able to produce overdeepenings. However, they may provide an initial perturbation to the ice thickness which could be grown into a channel by nonlinear effects; this possibility is investigated in the following chapter. Even if there is no nonlinear feedback in ice melt and flow, the ripples produced by the linear model would change the flexural stress within the ice shelf, potentially promoting the formation of crevasses (Vaughan et al., 2012). The ripples do bear some resemblance to the basal terraces observed by (Dutrieux, Stewart, et al., 2014), particularly when the ripples are produced by square-wave forcing of the ice flux. While the vertical scale of the ripples agrees well with observations, the horizontal scale is an order of magnitude too large, however, when considering an annual frequency of forcing. This leads to significatly smaller slopes separating the terraces, as discussed in more detail in § 3.6. While higher frequency forcing (e.g., due to the spring-neap tidal cycle, as described by Rosier et al., 2017) would address the issue of the horizontal scale, it would also result in a smaller vertical scale. Whilst the response to temporally varying forcing is capable of generating terraces, an additional feedback mechanism would be required if this process is to explain the observed quantitative properties of basal terraces on Pine Island Glacier.

The above model neglected the Coriolis force, meaning it only applies to relatively narrow ice shelves in which the plume is unable to rotate significantly (such as those confined to narrow fjords, e.g. Petermann Glacier). It used a relatively simple parameterisation of ice melt, although the approximation is reasonable (Jenkins, 2011). A bigger issue is the lack of pressure-dependence in the melt rate. This was necessary for the equations to be analytically tractable, but misses the tendency for the highest melt rates to be near the grounding line. Two of the simplifying assumptions made for the plume model in § 2.1.1 (negligible drag and freshwater flux due to subglacial discharge being much larger than that due to melting) only apply on short length-scales near the grounding line. These assumptions are not required in Chapter 3, allowing their importance to be evaluated. Finally, a linear model such as this one only works well for small perturbations. Some of the perturbations applied were large and thus neglecting nonlinear effects could have been inappropriate.

3

Response of an Ice Shelf to Nonlinear Forcing

Contents

The work in the previous chapter captured some of the basic mechanisms of ice shelf response to seasonal forcing, but found that this response was very small. However, it is possible that the missing nonlinear effects could cause an instability which would make perturbations to the ice shelf thickness grow. Furthermore, the need to find an analytic solution for the shelf and plume constrained the parameterisations which could be used. To overcome these limitations, this chapter considers a set of fully nonlinear numerical simulations for the ice/plume geometry used in Chapter 2 and illustrated in figure 1.1, subject to temporally varying forcing at the grounding line.

3.1 Algorithms and Numerical Method

For the nonlinear model, equations (1.7) and (1.9) were nondimensionalised in a manner more conducive for use with multiple choices of parameterisations than that used in Chapter 2 and scales were chosen which better reflect the ice shelf of Pine Island Glacier. The meanings and values of parameters can be found in table 3.1. After rescaling, the dimensionless ice shelf equations now become

$$h_t + \nabla \cdot (h\vec{u}) = -\lambda m, \tag{3.1a}$$

$$[2\eta h\,(2u_x + v_y)]_x + [\eta h\,(u_y + v_x)]_y - \chi\left(h^2\right)_x = 0, \tag{3.1b}$$

$$[\eta h\,(u_y + v_x)]_x + [2\eta h\,(u_x + 2v_y)]_y - \chi\left(h^2\right)_y = 0. \tag{3.1c}$$

In these equations h is the ice thickness (scaled by reference thickness h_0), $\vec{u} = (u, v)$ is the velocity at which the ice flows (scaled by reference u_0), m is the rate at which the ice shelf is melting (rescaled by reference m_0, defined below), and η is the rescaled ice viscosity. The dimensionless parameters

$$\lambda \equiv \frac{\rho_0 m_0 x_0}{\rho_i h_0 u_0}, \quad \chi \equiv \frac{\rho_i g h_0 x_0}{2\eta_0 u_0}\left(1 - \frac{\rho_i}{\rho_0}\right) \tag{3.2}$$

represent the ratio of melt versus influx of ice and the stretching rate (ratio of gravitational stresses that drive stretching versus viscous stresses resisting), respectively. In Chapter 2 the stretching rate was represented by γ, which had half the value of χ. The ice density is ρ_i, while the reference density for ocean water is ρ_0. Otherwise, the subscript nought indicates a typical scale for a variable.

The timescale for ice flow is given by $t_0 = x_0/u_0$. Gravitational acceleration is g. If viscosity is modelled as being Newtonian, then the dimensionless η is set to 1. Alternatively, Glen's Law can be nondimensionalised to take the form

$$\eta = \frac{1}{2}\xi D_2^{1/n-1}, \tag{3.3}$$

where $D_2 = \sqrt{D_{i,j}D_{i,j}/2}$ is the second invariant of the strain rate and the dimensionless coefficient

$$\xi \equiv \frac{B}{\eta_0}\left(\frac{u_0}{x_0}\right)^{1/n-1}. \tag{3.4}$$

Typically, $n = 3$ (Schoof and Hewitt, 2013) and this value will be used throughout this chapter.

The plume equations are scaled according to

$$\begin{aligned} U_0^2 &= \frac{h_0 g \Delta\rho}{\rho_0}, \quad e_0 = m_0 = \gamma_{T0} = \gamma_{S0} = \frac{D_0 U_0}{x_0}, \\ \Delta T_0 &= \frac{\Gamma_T^* x_0}{D_0}(T_a - T_m), \quad \Delta S_0 = \frac{c_0 \rho_0 \Delta T_0 (S_a - S_m)}{\rho_i L}. \end{aligned} \tag{3.5}$$

As before, the subscript nought indicates the typical scale for a variable. The exception to this is ρ_0, which is a representative value for the water density. Because the density difference is used in the plume equation and this difference is quite small, it was found useful to adopt a different scale, $\Delta\rho$, to use when nondimensionalising $\rho_a - \rho$, ρ_x, and ρ_y. Similarly, temperature and salinity were scaled according to typical differences rather than by their absolute values. An arbitrary point could be set to zero for these two variables and it proved convenient to choose the ambient values as the zero-point. The basal depth, b, is scaled by h_0. Note that the scale m_0 does not correspond to typical physical values of melting but is chosen because it is convenient to have it equal to those of the other variables; as a result, $m \ll 1$.

Table 3.1: Typical scales and values for ice shelf and plume properties, along with the values of non-dimensional parameters which result. "Repr. val." stands for "representative value". [J11] refers to Jenkins (2011), [B11] to Bindschadler, Vaughan, et al. (2011), [D15] to Dallaston et al. (2015), [J91] to Jenkins (1991), [J96] to Jacobs, Hellmer, et al. (1996), [K87] to Kochergin (1987), and [S13] to Sergienko (2013). Scales in the third column are chosen to be comparable to the conditions of the PIG ice shelf and come from the indicated source. Where a scaling is unconstrained it was chosen to provide convenient parameter values (e.g. x_0 fixed by χ). Due to an error, ζ_2 is a factor of r too large.

	Description	Value	Source
ρ_0	Reference water density	$1030\,\mathrm{kg\,m^{-3}}$	Common
ρ_i	Ice density	$916\,\mathrm{kg\,m^{-3}}$	Common
g	Acceleration due to gravity	$9.8\,\mathrm{m\,s^{-2}}$	Common
L	Latent heat of fusion	$3.35\times10^{5}\,\mathrm{J\,kg^{-1}}$	Common
c	Specific heat of water	$3.98\times10^{3}\,\mathrm{J\,kg^{-1}\,K^{-1}}$	Common
E_0	Entrainment coefficient (J91)	0.036	[J11]
c_L	Entrainment coefficient (K87)	0.1059	§ 3.3.2
β_S	Haline contraction coefficient	$7.86\times10^{-4}\,\mathrm{psu^{-1}}$	[J11]
β_T	Thermal contraction coefficient	$3.87\times10^{-5}\,\mathrm{K^{-1}}$	[J11]
C_d	Turbulent drag coefficient	2.5×10^{-3}	[J11]
Γ_T^*	Thermal transfer coefficient	5.7×10^{-5}	[D15]
κ	Turbulent diffusivity/viscosity	$10\text{–}100\,\mathrm{m^2\,s^{-1}}$	Repr. val.
η_0	Ice viscosity	$2.6\times10^{13}\,\mathrm{Pa\,s}$	Repr. val.
B	Glen's Law coefficient	$1.6\times10^{8}\,\mathrm{Pa\,s^{1/3}}$	[S13]
S_g	Subglacial discharge salinity	$0\,\mathrm{psu}$	Repr. val.
S_a	Ambient salinity	$34.6\,\mathrm{psu}$	[J96]
$T_a - T_m$	Thermal Forcing	$2^\circ\,\mathrm{C}$	[J96]
u_0	Ice velocity scale	$2.5\,\mathrm{km\,yr^{-1}}$	[B11]
h_0	Ice thickness scale	$1200\,\mathrm{m}$	[B11]
x_0	Length scale	$13.8\,\mathrm{km}$	(3.2)
t_0	Time scale	$5.5\,\mathrm{yr}$	(3.5)
m_0	Melt scale	$1.94\times10^{4}\,\mathrm{m\,yr^{-1}}$	(3.5)
X	Dimensionless domain length	6	[B11]
Q_g	Subglacial discharge	$8.5\times10^{-3}\,\mathrm{m^2\,s^{-1}}$	Repr. val.
D_0	Plume thickness scale	$43.2\,\mathrm{m}$	(3.5)
U_0	Plume velocity scale	$0.196\,\mathrm{m\,s^{-1}}$	(3.5)
ΔT_0	Temperature scale	$0.0364\,\mathrm{K}$	(3.5)
ΔS_0	Salinity scale	$0.0170\,\mathrm{psu}$	(3.5)
$\Delta\rho$	Density variation scale	$3.38\times10^{-3}\ \mathrm{kg\,m^{-3}}$	(3.7)
χ	Dimensionless stretching rate	4	(3.2)
ξ	Dimensionless Glen's coefficient	1.919	(3.4)
λ	Dimensionless melt rate	100	(3.2)
r	Density ratio	1.12	(3.7)
ν	Dimensionless eddy diffusivity	3.69×10^{-2}	(3.7)
μ	Dimensionless drag coefficient	0.799	(3.7)
δ	Buoyancy correction	0.036	(3.7)
K	Dimensionless K87 coefficient	3.58	(3.10)
ζ_1	Dimensionless transfer coefficient	0.0182	(3.12)
ζ_2	Dimensionless melt coefficient	4.86×10^{-4}	(3.12)

This yields the dimensionless system

$$\nabla \cdot \left(D\vec{U}\right) = e + m, \tag{3.6a}$$

$$\nabla \cdot \left(D\vec{U}U\right) = D(\rho_a - \rho)\left(b_x - \delta D_x\right) + \frac{\delta D^2}{2}\rho_x + \nu\nabla \cdot (D\nabla U) - \mu|\vec{U}|U, \tag{3.6b}$$

$$\nabla \cdot \left(D\vec{U}V\right) = D(\rho_a - \rho)\left(b_y - \delta D_y\right) + \frac{\delta D^2}{2}\rho_y + \nu\nabla \cdot (D\nabla V) - \mu|\vec{U}|V, \tag{3.6c}$$

$$\nabla \cdot \left(D\vec{U}S\right) = eS_a + \nu\nabla \cdot (D\nabla S) + mS_m - \gamma_S(S - S_m), \tag{3.6d}$$

$$\nabla \cdot \left(D\vec{U}T\right) = eT_a + \nu\nabla \cdot (D\nabla T) + mT_m - \gamma_T(T - T_m). \tag{3.6e}$$

Unlike in Chapter 2, these equations were constructed without making any assumptions about the form of m, e, or ρ. For this reason different, more generic, scales are adopted for these values. The velocity scale depends on the density scale, rather than on buoyancy input from subglacial discharge. Instead of scaling the salinity in terms of buoyancy input, its scale is based the level of melt-water input, which is the dominant source of salinity forcing across most of the domain.

The dimensionless parameters

$$\delta \equiv \frac{D_0}{h_0}, \quad r = \frac{\rho_0}{\rho_i}, \quad \nu \equiv \frac{\kappa}{x_0 U_0}, \quad \mu \equiv \frac{C_d x_0}{D_0} \tag{3.7}$$

represent the dimensionless buoyancy correction, density ratio, turbulent eddy diffusivity, and turbulent drag coefficient, respectively. The latter two depend on the dimensional eddy diffusivity κ, which is assumed to be equal to the eddy viscosity (as done by, e.g.: Sergienko, 2013; Dallaston et al., 2015), and the unscaled turbulent drag coefficient C_d.

The simple entrainment parameterisation of Jenkins (1991) in equation (1.11) can be nondimensionalised to have the form

$$e = \frac{E_0}{\delta}|\nabla b||\vec{U}|, \tag{3.8}$$

suggesting it is convenient to take $\delta = E_0$ (or equivalently, $D_0 = E_0 h$) as in Chapter 2. The more complex parameterisation of Kochergin (1987) in equation (1.12) nondimensionalises to

$$e = \frac{K}{S_m}\sqrt{|\vec{U}|^2 + \frac{\delta(\rho_a - \rho)D}{S_m}}, \tag{3.9}$$

with the dimensionless coefficient

$$K = \frac{c_L^2 x_0}{D_0}. \tag{3.10}$$

The turbulent Schmidt number, S_m, depends on the Richardson number as described in equation (1.13). With these scales, the Richardson number is given by $Ri = \delta(\rho_a - \rho)D/|\vec{U}|^2$. The melt rate parameterisation in equation (2.1), taken from Dallaston et al. (2015), has the dimensionless form

$$m = \zeta_1 \zeta_2 |\vec{U}|(T - T_m), \tag{3.11}$$

where

$$\zeta_1 = \frac{\Gamma_T^* x_0}{D_0}, \quad \zeta_2 = \frac{c\Delta T_0}{L}. \tag{3.12}$$

Due to the low efficiency of thermal transfer to the ice shelf, compared to the high rate of entrainment, $\zeta_1 \ll 1$. The large latent heat of ice results in $\zeta_2 \ll 1$, as well. Together, these results mean $m \ll e \sim 1$, so that the mass gain by meltwater input is much smaller than by entrainment. It can be seen that the thermal transfer coefficient nondimensionalises to give

$$\gamma_T = \zeta_1 |\vec{U}|. \tag{3.13}$$

A numerical scheme was developed to solve equations (3.1) and (3.6), which are coupled together by the melt rate and the slope of the ice shelf base. In order to make the problem computationally simpler and to maximise the potential for code reuse, it was decided to separate it into the two components: shelf and plume. For an initial ice shelf thickness profile, the state of the plume is solved for. This provides the melt rate, which is then used to integrate the state of the ice shelf forward one time step. This process is repeated each time step. Details of the numerical methods used to integrate the ice shelf and solve for the plume state are provided below.

3.1.1 Spatial Discretisation

The shelf/plume simulation requires computing various derivatives, for which a pseudospectral method is used. An introduction to this technique is provided below; for a more thorough explanation, see Trefethen (2000). Spectral methods provide a fast and accurate way to numerically differentiate discrete data. While more computationally expensive than finite difference methods for the same number of grid points, spectral methods give exponential convergence and thus often require significantly fewer grid points to achieve the same level of accuracy. Numerical accuracy is of particular importance here, as the purpose of running simulations is to test the stability of an ice-shelf to potentially small perturbations. Spectral methdos are often used for problems with periodic boundary conditions, where a Fourier series, $f(\theta) = \sum_k a_k e^{ik\theta}$, can be used to interpolate between grid points. If the grid points are evenly spaced then the coefficients a_k can easily be calculated with a discrete Fourier transform. Typically this would be done using the highly efficient fast Fourier transform (FFT) algorithm (Cooley and Tukey, 1965), which requires $O(N \log N)$ operations for N grid-points. The derivative is then $f'(\theta) = \sum_k ika_k e^{ik\theta}$ and an inverse FFT can be used to convert the new coefficients ika_k to the values of f' at each grid point.

However, the boundary conditions for equations (3.1) and (3.6) are not periodic. Instead, say there is an interpolant $F(x)$ for data mapped onto $-1 \leq x \leq 1$ using a linear coordinate rescaling. To apply a spectral method, it is necessary to map the interpolant to a function $f(\theta)$, $0 \leq \theta < 2\pi$, where $x = \cos\theta$. Regardless of the boundary conditions on F, f will be periodic and even in θ and can thus be differentiated as before. The results can then be mapped back onto the grid points in the x-domain. By choosing x grid points to be *Chebyshev collocation points*, defined below, the corresponding grid points in θ will be equally spaced and an FFT can be used to find the Fourier coefficients. This is known as the *Chebyshev pseudospectral method* (Trefethen, 2000). If $N + 1$ Chebyshev collocation points are needed, their positions are given by

$$x_j = \cos(j\pi/N), \quad j = 0, \ldots, N. \tag{3.14}$$

This approach provides uneven spacing of points in x, with a clustering of resolution near the domain boundaries, and hence is also well suited to capture rapid variation near the grounding line.

Following Trefethen (2000), the practical algorithm used to differentiate discrete data $v_j = v(x_j)$, for $0 \leq j \leq N$, corresponding to values at Chebyshev collocation nodes $x_0 = 1, \ldots, x_N = -1$, is as follows:

1. Take a type-I discrete cosine transform of the data, to determine the Fourier coefficients
$$\hat{v}_j = \frac{\pi}{N}\left[v_0 + v_N \cos(\pi j) + 2\sum_{k=1}^{N-1} v_k \cos\left(\frac{\pi j k}{N-1}\right)\right].$$
2. Let $\hat{w}_j = -j\hat{v}_j$ for $1 \leq j \leq N-1$ and $\hat{w}_N = 0$.
3. Take a type-I discrete sine transform of $\hat{w}_j$ from $j = 1$ to $j = N-1$, yielding
$$w_j = \frac{1}{\pi}\sum_{k=1}^{N-1} \hat{w}_k \sin\left(\frac{\pi k j}{N}\right).$$
4. Compute
$$v'_j = \begin{cases} \frac{1}{2\pi}\left[\frac{N^2}{2}\hat{v}_N + \sum_{k=1}^{N-1} k^2 \hat{v}_k\right], & j = 0 \\ \frac{-w_j}{\sqrt{1-x_j^2}}, & 1 \leq j \leq N-1 \\ \frac{1}{2\pi}\left[\frac{(-1)^{N+1}N^2}{2}\hat{v}_N + \sum_{k=1}^{N-1} (-1)^{k+1} k^2 \hat{v}_k\right], & j = N \end{cases}$$

Discrete sine and cosine transforms are variations of the discrete Fourier transform which take advantage of data being real and either even or odd. The FFTW3 package (Frigo and Johnson, 2005) was used to compute these. A more rigorous and detailed explanation of the above methods for periodic and non-periodic functions is provided by Trefethen (2000) in chapters 3 and 8, respectively.

If a domain other than $-1 \leq x \leq 1$ is desired then the Collocation points can be scaled and offset as necessary, giving a coordinate system x_j^*. The above differentiation algorithm is applied unchanged, except that the result is scaled by twice the inverse of the domain-width.

While the above method was used for the nonlinear simulations, it is also possible to construct a matrix which, when applied to a vector $\boldsymbol{v} = [v_0, v_1, \ldots, v_N]^T$ (using the same definition of v_j as above) performs the pseudospectral differentiation. Such a matrix can be thought of as generalising a finite difference matrix to the case where the order of the finite difference is the same as the number of data points. The $N \times N$ differentiation matrix Δ has the form (Trefethen, 2000, chapter 6)

$$\Delta_{00} = \frac{2N^2+1}{6}, \quad \Delta_{NN} = -\frac{2N^2+1}{6} \tag{3.15}$$

$$\Delta_{jj} = \frac{x_j}{2(1-x_j^2)}, \quad j = 1, \ldots, N-1 \tag{3.16}$$

$$\Delta_{ij} = \frac{c_i(-1)^{i+j}}{c_j(x_i - x_j)}, \quad 1 \neq j,\ i,j = 0, \ldots, N, \tag{3.17}$$

where

$$c_i = \begin{cases} 2 & i = 0, N \\ 1 & \text{otherwise} \end{cases}.$$

Matrices of this form were used to solve the linear equations in Chapter 2. However, the FFT approach is preferred for the nonlinear problem as it is more computationally efficient, requiring only $O(N \log N)$ operations to calculate a derivative compared to $O(N^2)$ with the matrix method.

3.1.2 Implicit Integration of the Ice Shelf

Simulating the evolution the ice shelf mass balance using equation (3.1a) requires a time-stepping scheme. In order to allow numerical stability with large time steps, a semi-implicit method is used. This works by defining the residual operator

$$\boldsymbol{f}(h_n) = \frac{h_n - h_{n-1}}{\Delta t} + \frac{\partial}{\partial x}(h_n u_n(h_n)) + \lambda m_{n-1} \tag{3.18}$$

where the subscript n indicates the value at the time step being solved for, while subscript $n-1$ indicates the value at the previous time step. This is a semi-implicit scheme (rather than fully implicit) because melt rate m_{n-1} is used from the previous time step, rather using m_n from the current time step. In this equation, h_n and u_n

represent vectors of thickness and velocity values at each grid point at time step n, while h_{n-1} is a vector of thickness values at the previous time step and $\partial/\partial x$ is evaluated using the Chebyshev differentiation procedure described in § 3.1.1. This is a nonlinear system and can be solved using Newton's method, where the root is determined iteratively by solving the linear equation

$$\boldsymbol{J}\delta\boldsymbol{s}_n^k = -\boldsymbol{f}(\boldsymbol{s}_n^k). \tag{3.19}$$

Here, $\boldsymbol{s}_n = h_n$ is the current value of the ice thickness, $\boldsymbol{J}$ is the Jacobian of f, and the new iterate $\boldsymbol{s}_n^{k+1} = \boldsymbol{s}_n^k + \delta\boldsymbol{s}_n^k$.

In order to avoid having to evaluate the Jacobian of this system, a Jacobian-free Newton-Krylov method (Knoll and Keyes, 2004) is used. This solves the linear equation (3.19) iteratively via a Krylov method which only requires the product of the Jacobian with the iterate, and not the actual Jacobian itself. This product is approximated as a finite difference:

$$\boldsymbol{J}\boldsymbol{v} \approx \frac{\boldsymbol{f}(\boldsymbol{s}+\epsilon\boldsymbol{v}) - \boldsymbol{f}(\boldsymbol{s})}{\epsilon}. \tag{3.20}$$

The NITSOL implementation (Pernice and Walker, 1998) of a Newton-Krylov solver was chosen, as it is very flexible and written in Fortran, which was the language other portions of the code were to be implemented with.

The spectral discretisation used here corresponds to dense matrices, making equation (3.19) very poorly conditioned. As a result, the Krylov solvers in NITSOL were unable to converge on a solution without a preconditioner. Even with relatively-sparse matrices, preconditioners are often needed for iterative methods (e.g. Pernice and Walker, 1998; Knoll and Keyes, 2004). A right preconditioner, $\boldsymbol{P}^{-1}$, is chosen so that the modified problem $(\boldsymbol{J}\boldsymbol{P}^{-1})\boldsymbol{q} = -\boldsymbol{f}(\boldsymbol{s})$ is well-conditioned and can be solved for $\boldsymbol{q}$. It is then easy to find $\boldsymbol{s}$ using $\boldsymbol{P}\delta\boldsymbol{s} = \boldsymbol{q} \Rightarrow \delta\boldsymbol{s} = \boldsymbol{P}^{-1}\boldsymbol{q}$. A good preconditioner will have $\boldsymbol{P}^{-1} \approx \boldsymbol{J}^{-1}$, so that $\boldsymbol{J}\boldsymbol{P}^{-1} \approx \boldsymbol{I}$ to a decent approximation. A tradeoff must be made between a preconditioner which is a sufficiently good approximation of $\boldsymbol{J}^{-1}$ to be useful and one which is not too expensive or unstable to apply (e.g. $P^{-1} = J^{-1}$ would be a perfect preconditioner but constructing it is of equal difficulty to solving the original, unpreconditioned problem).

The Jacobian of equation (3.18) can be expressed as

$$\boldsymbol{J} = \frac{1}{\Delta t} + \mathcal{D}_x u, \tag{3.21}$$

where we define $\mathcal{D}_x A \equiv \partial A/\partial x + A\Delta_x$, and Δ_x is the differential operator in the x-direction. Although Δ_x will be a dense matrix when using a spectral method, it can be approximated as a sparse finite difference operator, as proposed by Orszag (1980). In this case Δ_x, and thus also $\mathcal{D}_x$, are tridiagonal matrices. This means that the finite difference form of the Jacobian can be "inverted" simply by solving the tridiagonal system, which can be done efficiently using a routine in LAPACK (Anderson et al., 1999). This proved effective at preconditioning the Krylov solver in NITSOL, whilst maintaining the accuracy of the underlying pseudospectral method.

The $u_n(h_n)$ term in equation (3.18) can itself be found by solving a nonlinear system, this time with the form

$$\boldsymbol{f}(u_n) = \frac{\partial}{\partial x}\left(4\eta_n h_n \frac{\partial u_n}{\partial x}\right) - \chi\frac{\partial h_n^2}{\partial x}. \tag{3.22}$$

This has a Jacobian

$$\boldsymbol{J} = \mathcal{D}_x(4\eta h)\Delta_x. \tag{3.23}$$

Every time a new residual is calculated using equation (3.18), equation (3.22) is solved iteratively using NITSOL.

It is also possible to construct a nonlinear system which takes both h_n and u_n as arguments and solve for both simultaneously. While this avoids the need to repeatedly solve for u_n, it proved to be much less stable and tended to require smaller time-steps in order to prevent failure. As such, the approach outlined above proved to be computationally cheaper overall.

Of the three linear solvers provided with NITSOL, only GMRES proved reliable, with the BiCGSTAB and TFQMR solvers typically failing. Consult Pernice and Walker (1998) for more details on these routines. It was also found that the "backtracking" globalisation used in NITSOL, which is meant to prevent the solution from starting to diverge, had a tendency to make the solver get trapped in local minima for this problem. As such, it was turned off and this was found to greatly improve the robustness of the nonlinear solver.

3.1.3 Solving for the Quasistatic Plume

For a one-dimensional domain, equations (3.6) become second order ODEs. If boundary conditions are applied only at the grounding line then this means that they can be solved using initial value problem methods such as Runge-Kutta integration. However, the diffusive terms in equations (3.6b)–(3.6e) require two boundary conditions each for velocity, salinity, and temperature. The logical choice would use Dirichlet conditions at the grounding line and outflow conditions (setting the first derivative to zero) at the calving front. This turns equation (3.6) into a boundary value problem and makes it more difficult to solve.

One strategy for solving boundary value problems such as this is the shooting method (see, e.g., Press et al., 2007). With this technique, unknown boundary values are guessed at the grounding line to create an initial value problem. This initial value problem is then integrated and the difference between the values at the calving front and the required boundary conditions there is noted. A nonlinear solver is then used to change the guesses at the grounding line in order to get the correct boundary conditions at the calving front. However, the diffusion term in these equations leads to solutions involving exponential growth. If the guesses of grounding line conditions are not sufficiently good then these exponentials can lead to overflow and the failure of the solver. It was found that this made the shooting method unsuitable in practice.

A relaxation method was also tried, wherein a time-dependent version of the plume model was evolved forward in time (using an explicit method) until it reached steady state. However, the weakness of the diffusion coefficient and nearly hyperbolic character of the time-dependent plume model means that significant waves often arise, and considerable time is needed to reach a steady state.

Finally, an approach called the quasilinearisation method (Mandelzweig and Tabakin, 2001), or QLM, was tried. This is a technique, based on Newton's method, for solving boundary value problems. Though Mandelzweig and Tabakin (2001) present the technique for single-variable problems, it is trivial to generalise it to the multivariate case. Consider the differential equation

$$L^{(n)}\boldsymbol{s}(x) = \boldsymbol{f}[\boldsymbol{s}(x), \boldsymbol{s}^{(1)}(x), \ldots, \boldsymbol{s}^{(n-1)}(x), x], \qquad \boldsymbol{s} \in \mathbb{R}^m, \tag{3.24}$$

being solved on the domain $[0, b]$. Here, $L^{(n)}$ is an n^{th} order linear differential operator, $\boldsymbol{f}$ is a nonlinear function, and $\boldsymbol{s}^{(i)}$ is the i^{th} derivative of $\boldsymbol{s}$. Boundary conditions are specified by

$$\begin{aligned} g_k[\boldsymbol{s}(0), \boldsymbol{s}^{(1)}(0), \ldots, \boldsymbol{s}^{(n-1)}(0)] = 0, &\qquad k = 1, \ldots, l; \\ g_k[\boldsymbol{s}(b), \boldsymbol{s}^{(1)}(b), \ldots, \boldsymbol{s}^{(n-1)}(b)] = 0, &\qquad k = l+1, \ldots, mn; \end{aligned} \tag{3.25}$$

where $g_1, g_2, \ldots, g_{mn}$ are (potentially) nonlinear functions. This can be solved iteratively for the $r+1$ iterate $\boldsymbol{s}_{r+1}$ using the equation

$$\begin{aligned} L^{(n)}\boldsymbol{s}_{r+1}(x) = \boldsymbol{f}[&\boldsymbol{s}_r(x), \boldsymbol{s}_r^{(1)}(x), \ldots, \boldsymbol{s}_r^{n-1}(x), x] + \\ &\sum_{i=0}^{n-1} \boldsymbol{f}_{\boldsymbol{s}^{(i)}}[\boldsymbol{s}_r(x), \boldsymbol{s}_r^{(1)}(x), \ldots, \boldsymbol{s}_r^{n-1}(x), x]\left[\boldsymbol{s}_{r+1}^{(i)}(x) - \boldsymbol{s}_r^{(i)}(x)\right], \end{aligned} \tag{3.26}$$

with boundary conditions for each iteration set by

$$\begin{aligned} \sum_{i=0}^{n-1} g_{k,\boldsymbol{s}^{(s)}}[\boldsymbol{s}_r(0), \boldsymbol{s}_r^{(1)}(0), \ldots, \boldsymbol{s}_r^{n-1}(0), x] \cdot [\boldsymbol{s}_{r+1}^{(i)}(0) - \boldsymbol{s}_r^{(i)}(0)] = 0, &\qquad k = 1, \ldots, l; \\ \sum_{i=0}^{n-1} g_{k,\boldsymbol{s}^{(i)}}[\boldsymbol{s}_r(b), \boldsymbol{s}_r^{(1)}(b), \ldots, \boldsymbol{s}_r^{n-1}(b), x] \cdot [\boldsymbol{s}_{r+1}^{(i)}(b) - \boldsymbol{s}_r^{(i)}(b)] = 0, &\quad k = l+1, \ldots, mn. \end{aligned} \tag{3.27}$$

In these equations, $\boldsymbol{f}_{\boldsymbol{s}^{(i)}} = \partial\boldsymbol{f}/\partial\boldsymbol{s}^{(i)}$ (i.e. the Jacobian of $\boldsymbol{f}$) and $g_{k,\boldsymbol{s}^{(i)}} = \partial g_k/\partial\boldsymbol{s}^{(i)}$. Note that, for linear boundary conditions, equation (3.27) reduces to the boundary conditions being constant across iterations. This technique can be proven to give quadratic convergence to the solution given certain easily-satisfied assumptions (see Mandelzweig and Tabakin, 2001, for details). Furthermore, convergence is often monotonic.

To apply this method to the plume model, new variables $U' = U_x$, $V' = V_x$, $S' = S_x$, and $T' = T_x$ were introduced, where a subscript x denotes a derivative. Equation (3.6a) was rewritten so that the left-hand-side is just D_x, while equations (3.6b)–(3.6e) were rewritten such that the left hand sides are U'_x, V'_x, etc. This allowed a linear operator to be constructed with the form

$$L[D, U, U', S, S', T, T']^T = \left[\frac{dD}{dx}, \frac{dU}{dx} - U', \frac{dU'}{dx}, \frac{dS}{dx} - S', \frac{dS'}{dx}, \frac{dT}{dx} - T', \frac{dT'}{dx}\right]^T. \tag{3.28}$$

The nonlinear operator is zero for U, S, and T and elsewhere consists of the right-hand-side of the rearranged version of equation (3.6).

In order to find successive iterates, a linear equation must be solved, consisting of the linear operator and the Jacobian $\boldsymbol{f}_{\boldsymbol{s}^{(i)}} = \partial \boldsymbol{f}/\partial \boldsymbol{s}^{(i)}$. It is neither feasible nor efficient to explicitly evaluate the Jacobian, especially if the solver is to be agnostic to parameterisation choices. The iterative GMRES solver implemented in NITSOL (very slightly modified to accept an initial guess of the solution) was used because it can work knowing only the product of the Jacobian and the current iterate. Initially these products were calculated using the finite-difference approximation to the Jacobian in equation (3.20). While this was sufficiently accurate to run many simple simulations, it proved unreliable when the plume undergoes a sudden change or when nonlinear parameterisations are used. To address this, automatic differentiation (Neidinger, 2010) was applied instead and this proved far more robust. This calculated the product of the Jacobian with a vector (i.e., the directional derivative) via operator overloading. See Appendix A for further details of the implementation. All results displayed in this chapter were obtained using automatic differentiation.

The GMRES algorithm required preconditioning to work properly, as was the case with the ice shelf solver. The preconditioner was chosen to be $\boldsymbol{P}^{-1} = L^{-1}$, equivalent to finding the inverse of equation (3.28), which involves integration of the derivatives. Spectral integration was performed by reversing the steps for spectral differentiation described on page 84. A similarly modified version of the NITSOL implementation of the biconjugate gradient stabilised method (BiCGSTAB) was also found to work when solving the preconditioned linear system, but it proved less robust.

When solving the linear equation at each iteration, the initial guess was the previous iterate. The GMRES solver was expected to reduce the error in the linear system by a factor ϵ compared to the initial guess. It was found that gradually decreasing the magnitude of ϵ over each nonlinear iteration, the final answer could be determined with a residual norm smaller than $7N \times 10^{-9}$, where N is the number of grid points used and 7 indicates the number of plume variables being solved for. The QLM proved to be highly efficient, typically converging within a few iterations of equations (3.26) and (3.27), although up to a few hundred iterations would often be needed by the GMRES solver to perform the necessary intermediate linear solves.

3.1.4 Testing and Benchmarking

3.1.4.1 Ice Shelf

After programming the nonlinear solver using the algorithms described in the previous section, various tests were run to ensure that it would give the correct results. First, the ice shelf component was tested with a prescribed melt rate matching that of the analytic steady state solution in § 2.1. It was confirmed that when the ice shelf was initialised to the matching steady state it remained there. Initialising the ice shelf to a wedge-shape, it was found to evolve to the correct steady state.

As a test of the time-stepping for transient evolution, the 1-D shelf equations were analysed for the special case where there is no stretching ($\chi = 0$) and the melt rate m is constant in t and x. The velocity of the ice at the grounding line (and thus across the entire shelf, since there is no stretching) was prescribed to be $u(t) = \bar{u} + \tilde{u}_0 \sin(\omega t)$. With these assumptions, equation (3.1a) becomes

$$\frac{\partial h}{\partial t} - u(t)\frac{\partial h}{\partial x} = -\lambda m, \tag{3.29}$$

which can be solved using the method of characteristics. In this method, a Lagrangian coordinate s is introduced such that the thickness of a parcel of ice following the trajectory $x(s)$, $t(s)$ evolves according to $h(s)$. It can then be shown that

$$\frac{dx}{ds} = u(t), \quad \frac{dt}{ds} = 1, \quad \frac{dh}{ds} = -\lambda m.$$

With the initial conditions $x = \sigma$, $t = 0$, and $h = h_0(\sigma)$ these equations can be integrated to yield the transient solution

$$h = h_0(\sigma) - \lambda m t, \tag{3.30}$$

where σ can be computed from x and t according to $\sigma = x - \bar{u}t + \tilde{u}/\omega\,[\cos(\omega t) - 1]$. This solution applies to ice starting in the domain, but a different form is needed for ice parcels crossing the grounding line at time $t = t_g > 0$. Then $\sigma < 0$ and the initial conditions are set to $x = 0$ and $h = 1$. In this case the method of characteristics provides the implicit solution

$$h - \frac{\lambda m \tilde{u}_0}{\omega \bar{u}} \cos\left[\omega t + \frac{\omega}{\lambda m}(h-1)\right] = 1 - \frac{\lambda m}{\bar{u}}\left[x + \frac{\tilde{u}_0}{\omega}\cos(\omega t)\right]. \tag{3.31}$$

This algebraic equation can easily be solved numerically for h using a bisection-secant method, such as that of Brent (1973, Chapter 4). Possible solutions can be bracketed using the physical insight that $h \in [0, 1]$.

These solutions provide a way to test accuracy of the ice shelf solver in time and space. However, the fact the melt rate is constant means that the semi-implicit approach to time-discretisation is not fully tested. Using the same technique, a solution can be found for melt rate $m = m_t t$, where m_t is a constant rate of change in the melt. For $\sigma > 0$ (calculated as before) the transient solution applies:

$$h = h_0(\sigma) - \frac{\lambda m_t}{2} t^2. \tag{3.32}$$

Elsewhere, the solution is again given implicitly:

$$h - 1 + \lambda m_t (t_g + s/2)s = 0 \tag{3.33}$$

where the time since the ice parcel crossed the grounding line and the time at which it crossed the grounding line are given by

$$s = \frac{x}{\bar{u}} + \frac{\tilde{u}_0}{\omega \bar{u}}\left(\cos(\omega t) - \cos(\omega t_g)\right), \quad t_g = \sqrt{\frac{2(h-1)}{\lambda m_t} + t^2},$$

respectively. Bracketing this solution is slightly more difficult than in the constant-melt case, as if the value of h is too small it will result in an imaginary value of t_g.

As such, the lower bound was set to the value of $h = 1 - \lambda m_t t^2/2$, which corresponds to $t_g = 0$ at the time being solved for, plus some small value ϵ to ensure that floating point error does not become an issue. The upper bound remains set to 1.

A series of simulations were run under these conditions using different time steps. Parameter values $\bar{u} = 1$, $\tilde{u}_0 = 0.5$, $\lambda = 100$, $m_t = 2 \times 10^{-4}$, and $\omega = 34.56$ were chosen, corresponding to the scale choices described in the next section. A domain of $x \in [0, 6]$ was used, with a wedge-shaped initial ice profile $h_0(x) = 1 - 0.1x$. All simulations used 300 grid-points.

Figure 3.1 shows the results of two simulations at time $t = 5$, with time-steps fixed at 10^{-2} and 10^{-4}, compared to the analytical solution given in equations (3.32) and (3.33). Both simulations give reasonably good agreement with the large-scale features of the solution, although there is more significant error at the transition to the transient solution. The numerical solutions tend to smooth out those sorts of discontinuities, although reducing the time-step helps with this considerably. The main issue, however, is how the numerical solution handles the ripples which form due to the seasonal forcing of shelf velocity. These are very small in magnitude, meaning that very high levels of accuracy are demanded to resolve them. Even the simulation with the smaller time-step shows signs of diffusion, causing the ripples to loose amplitude as they move across the domain.

This can be seen more clearly in figure 3.2, which is produced at $t = 10$ when the transient feature has been advected out of the domain. All results in this plot are differences between the time-dependent solution h with $\tilde{u}_0 = 0.5$ and the steady-state result $\bar{h}$ of equation (3.33) for $\tilde{u}_0 = 0$, which corresponds to the unforced background state. In order to make the plot easier to read, the domain only goes to $x = 1.5$. As can be seen, the amplitude of the ripples decays, indicating the presence of some numerical diffusion. Smaller time-steps result in less of this diffusion. The root-mean-square and the maximum error at times $t = 5$ and $t = 10$ were found for a range of time-steps (figure 3.3). The error declines fairly slowly with the time-step. Given that high accuracy is needed for these simulations, in

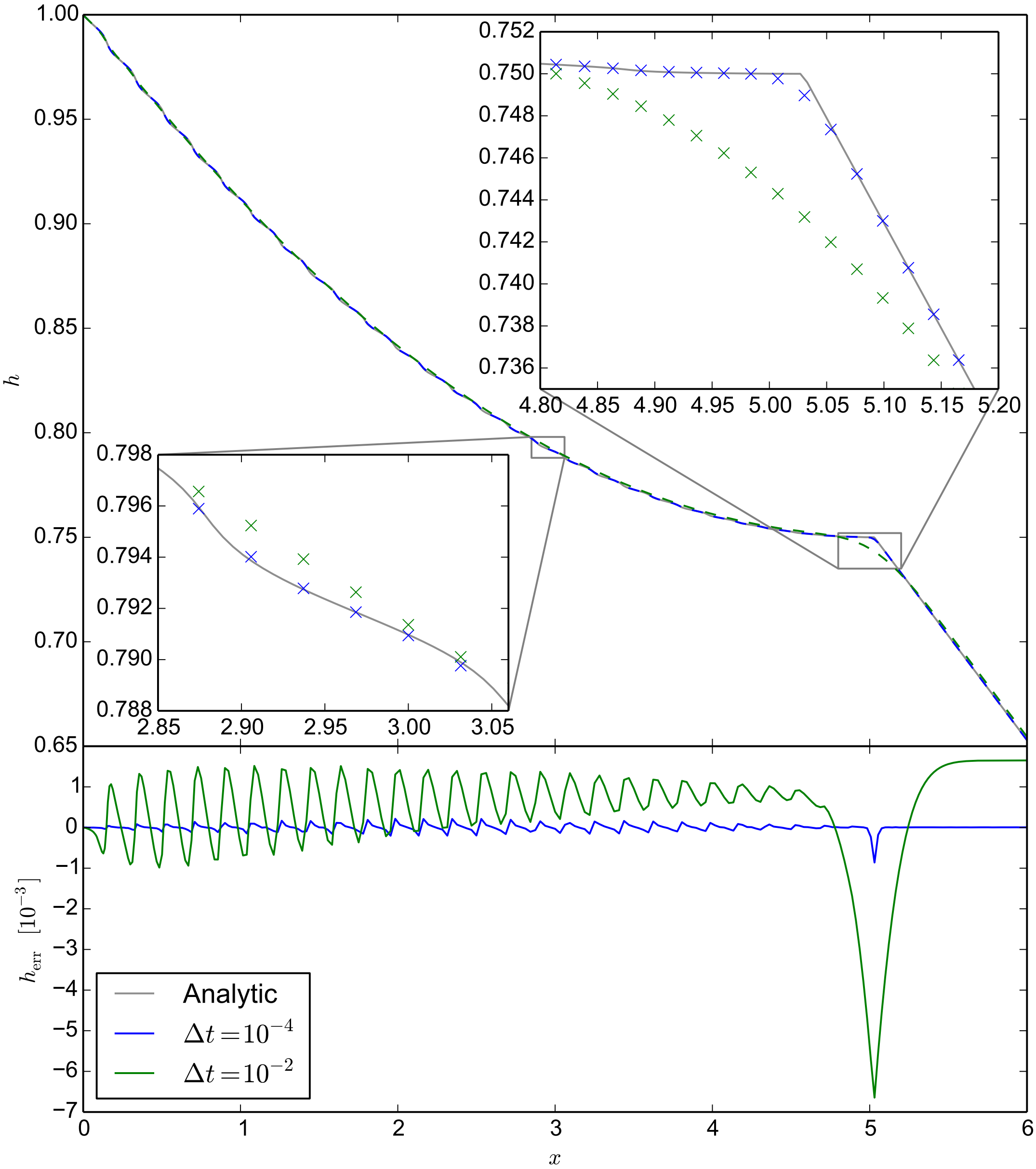

Figure 3.1: Comparison of the analytic solution given in equations (3.32) and (3.33) with numerical solutions at $t = 5$, using 300 grid-points. These are plotted alongside each other in the top panel, while the bottom panel displays the differences between the numerical and analytical solutions. Insets offer a zoomed-in view of the error, with values at individual grid-points indicated by an $\times$. Parameter values $\bar{u} = 1$, $\tilde{u}_0 = 0.5$, $\lambda = 100$, $m_t = 2 \times 10^{-4}$, and $\omega = 34.56$ were chosen, corresponding to the scale choices described in the next section.

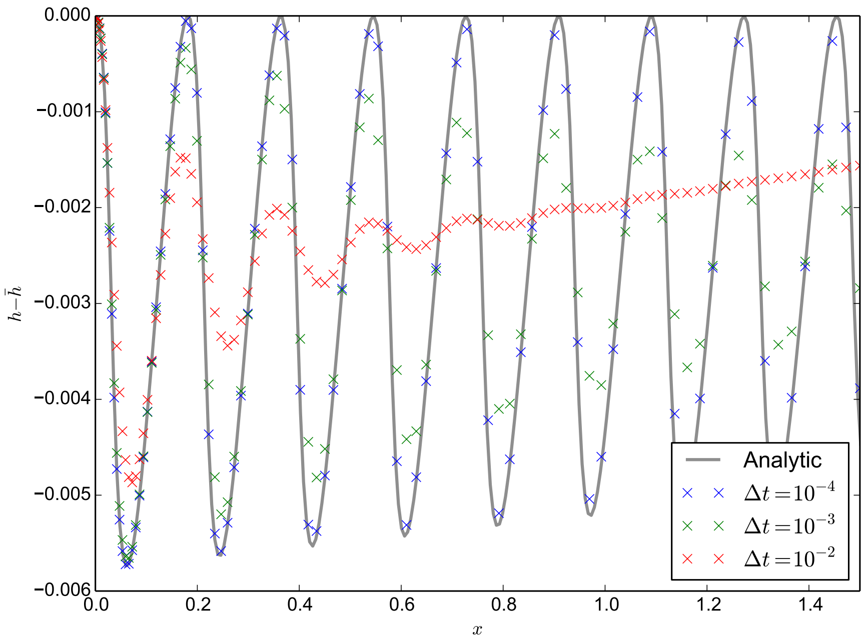

Figure 3.2: Comparison of the analytic solution given in equation (3.33) with numerical solutions at $t = 10$, using 300 grid-points. In all cases, the plot shows the difference between the solution h and the unforced background state $\bar{h}$ corresponding to the solution to equation (3.33) for $\tilde{u}_0 = 0$. Only the first quarter of the domain is displayed, to make the plot easier to read; decay continues to contribute downstream. Parameter values $\bar{u} = 1$, $\tilde{u}_0 = 0.5$, $\lambda = 100$, $m_t = 2 \times 10^{-4}$, and $\omega = 34.56$ were chosen, corresponding to the scale choices described in the next section.

any future developments of this algorithm it may be useful to update the time-integration to a second-order or third-order method, allowing larger time-steps to be used. The memory requirements of this would be fairly modest, as only the ice thickness would need to be saved between time-steps.

Similarly, the error was found to fall with an increasing number of Chebyshev nodes used in the calculation. However, after a certain point, the error stagnated and adding more nodes did not cause further improvement. The point at which this stagnation occurs seems to depend on the time-step, with smaller time-steps permitting higher numbers of nodes before stagnation. Similarly, the beginnings of stagnation with any further reductions in the time step can be seen in figure 3.3. This is consistent with the total error being the sum of error arising due to temporal discretisation and spatial discretisation. Increased resolution was found to be a more computationally expensive means to improve accuracy than reducing the time-step.

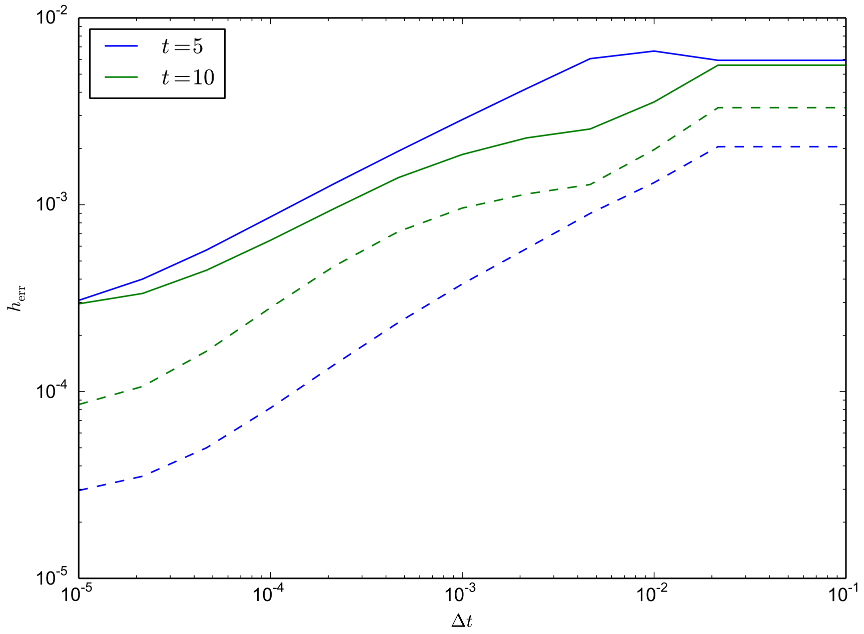

Figure 3.3: The root-mean-square (dashed) and the maximum (solid) error of simulations at times $t = 5$ and $t = 10$ for different time-steps, using 300 grid-points. Parameter values $\bar{u} = 1$, $\tilde{u}_0 = 0.5$, $\lambda = 100$, $m_t = 2 \times 10^{-4}$, and $\omega = 34.56$ were chosen, corresponding to the scale choices described in the next section.

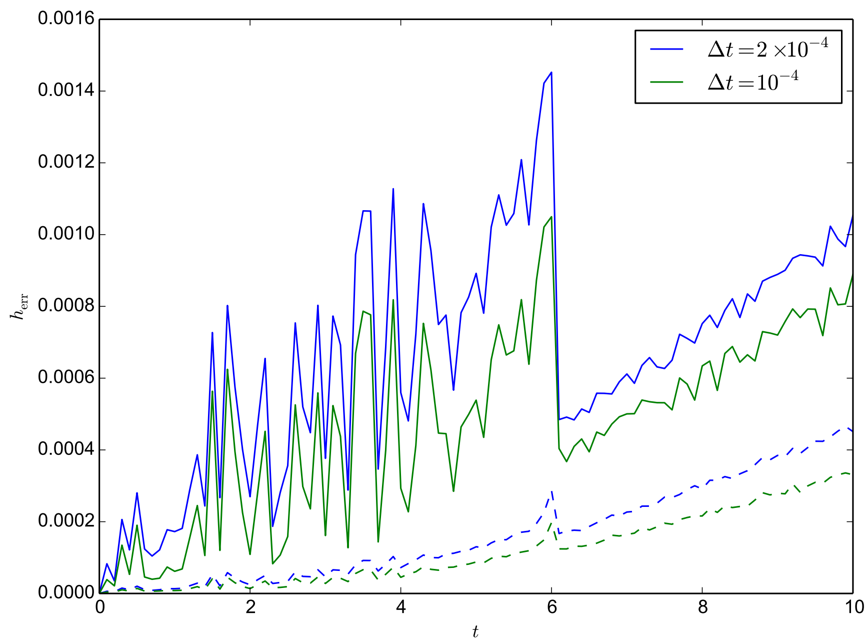

Figure 3.4: The root-mean-square (dashed) and the maximum (solid) error over the course of two simulations with different time-steps, both using 300 grid-points. Parameter values $\bar{u} = 1$, $\tilde{u}_0 = 0.5$, $\lambda = 100$, $m_t = 2 \times 10^{-4}$, and $\omega = 34.56$ were chosen, corresponding to the scale choices described in the next section.

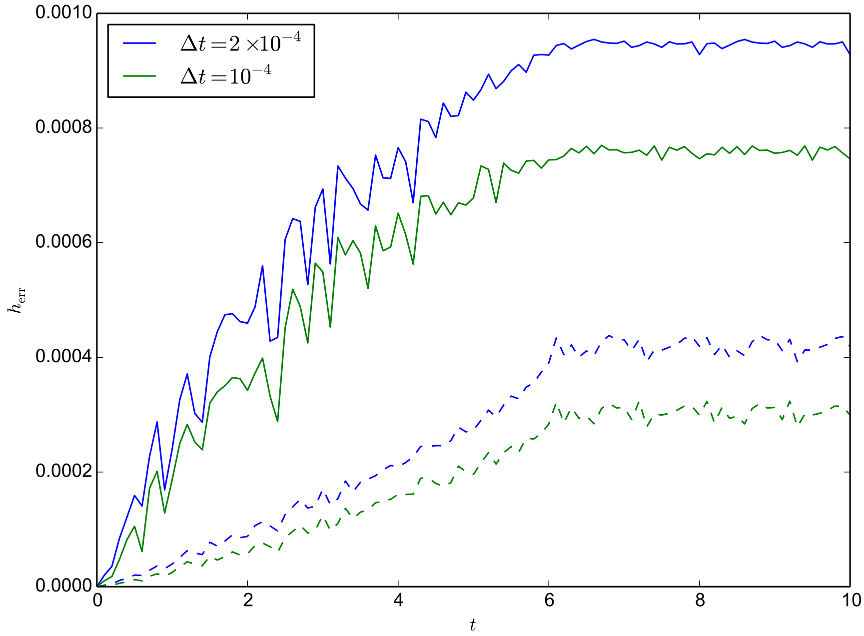

Figure 3.5: The root-mean-square (dashed) and the maximum (solid) error over the course of two simulations with different time-steps, both using 300 grid-points. In this case a constant melt rate was applied, with error found relative to the solution in equations (3.30) and (3.31). Parameter values $\bar{u} = 1$, $\tilde{u}_0 = 0.5$, $\lambda = 100$, $m = 10^{-3}$, and $\omega = 34.56$ were chosen, corresponding to the scale choices described in the next section.

Plotting the root-mean-square and maximum error over the course of a simulation shows that both grow approximately linearly (figure 3.4), although the latter is very noisy. Presumably this noise is due to aliasing of small-scale features of the oscillations onto a discrete grid. The rate of growth increases with the size of the time-step. There is a spike in error which occurs as the kink at the transient feature reaches the end of the domain around $t = 6$. The reason for the continued error growth after the transient has been advected away is the growth in melt rate. This means that ripples will tend to be larger and thus display larger absolute error. Running a simulation with a constant melt rate of $m = 10^{-3}$ and comparing to the solution in equations (3.30) and (3.31) indicates that the error becomes roughly constant after the transient feature leaves the domain (figure 3.5).

Experiments with this benchmarking problem showed that using 320 grid-points with a time step of 10^{-5} resulted in absolute error no larger than 10^{-4}. Error in the amplitude of the ripples at the end of the domain was no more than $\sim 10\%$, which was felt to be acceptable when running simulations.

3.1.4.2 Plume

Testing the plume solver was more difficult, as the structure of the solver required a non-zero diffusivity, while the analytic solution in equation (2.19) assumed $\nu = 0$. To avoid this problem, the equation of state was altered for the benchmark test so that it would always return the same density profile, regardless of plume salinity or temperature. The density was chosen so that the plume would have the same velocity as in the analytic solution. Now uncoupled from the continuity and momentum equations (3.6a) and (3.6b), the salinity and temperature equations (3.6d) and (3.6e) could be analytically solved individually. A plume was initialised by giving this analytic solution a sinusoidal perturbation of amplitude 0.1 and a wavelength twice the size of the domain. Starting from this initial guess and a prescribed wedge-shaped ice thickness, the solver was able to converge to the expected result.

The coupled behaviour of the ice shelf/ocean received less rigorous testing as there are no analytical benchmark solutions available for the full nonlinear problem. The two components were initialised much as they were in the plume test (except that the plume density was now made dependent on salinity) and then allowed to evolve together. As the resulting steady-state was not known, it was simply ensured that numerical convergence was achieved as the number of Chebyshev nodes increased and the time step reduced, and that the results looked plausible.

3.2 Simulations

A large suite of simulations was run to examine the effects of seasonal variability on ice shelf structure. In order to facilitate comparisons to the linear analysis described in Chapter 2, some of these used the same parameterisation choices, while others examined the effect of using different parameterisations of ice viscosity and plume entrainment. A few simulations were run without basal drag, although most included it. A complete list of these simulations, giving identifiers and information on their characteristics, can be found in table 3.2. Ice viscosity was treated as either

Table 3.2: A list of the simulations performed. The first column indicates the identifier for that particular simulation. In the next column the "driver" which undergoes sinusoidal seasonal variation is specified. The choices are between no seasonal variation ("Steady"), varying subglacial discharge ("Discharge"), or varying the speed of ice across the grounding line ("Ice flux"). The third column indicates the viscosity law used for the ice. This could be either a uniform viscosity ("Newtonian") or the power law rheology described by Glen's Law in equation (3.3) (Glen, 1958). The entrainment parameterisation is specified in the fourth column and could be that of either Jenkins (1991)—"J91", given in equation (3.8)—or that of (Kochergin, 1987)—"K87", given in equation (3.9). The final column indicates any other noteworthy characteristics of the simulations, such as the plume's turbulent drag parameter being set to zero or the driver forcing being applied as a square wave rather than the usual sinusoid.

Name	Driver	η	e	Notes
`ssNeJeDa`	Steady	Newtonian	J91	
`ssNeJeDand`	Steady	Newtonian	J91	No drag
`ssNeKoDa`	Steady	Newtonian	K87	
`ssGLJeDa`	Steady	Glen's Law	J91	
`ssNeJeDad0`	Steady	Newtonian	J91	$\delta = 0$
`ssNeJeDandd0`	Steady	Newtonian	J91	No drag, $\delta = 0$
`ssNeKoDad0`	Steady	Newtonian	K87	$\delta = 0$
`ssGLJeDad0`	Steady	Glen's Law	J91	$\delta = 0$
`diNeJeDa`	Discharge	Newtonian	J91	
`diNeJeDand`	Discharge	Newtonian	J91	No drag
`diNeKoDa`	Discharge	Newtonian	K87	
`diGLJeDa`	Discharge	Glen's Law	J91	
`ifNeJeDa`	Ice flux	Newtonian	J91	$\delta = 0$
`ifNeJeDadn0`	Ice flux	Newtonian	J91	$\delta \neq 0$
`ifNeJeDand`	Ice flux	Newtonian	J91	No drag
`ifNeJeDacm`	Ice flux	Newtonian	J91	Constant melt, $\delta = 0$
`ifNeKoDa`	Ice flux	Newtonian	K87	$\delta = 0$
`ifGLJeDa`	Ice flux	Glen's Law	J91	$\delta = 0$
`ifNeJeDasw`	Ice flux	Newtonian	J91 x	Square wave forcing, $\delta = 0$

Newtonian or following Glen's Law, as specified in equation (3.3). Entrainment was parameterised using either equation (3.8) (Jenkins, 1991) or equation (3.9) (Kochergin, 1987), while melting was parameterised according to equation (3.11). The three-equation formulation given in equation (1.17) was not used, as other sensitivity tests were considered more interesting. Simulations were run with 320 grid points and a time step of 10^{-5}. Unless otherwise noted, all simulations used the parameter values listed in table 3.1.

Initially a set of simulations were run to steady state (§ 3.3). These results were then used to initialise a series of simulations undergoing seasonal forcing (§ 3.4–3.5).

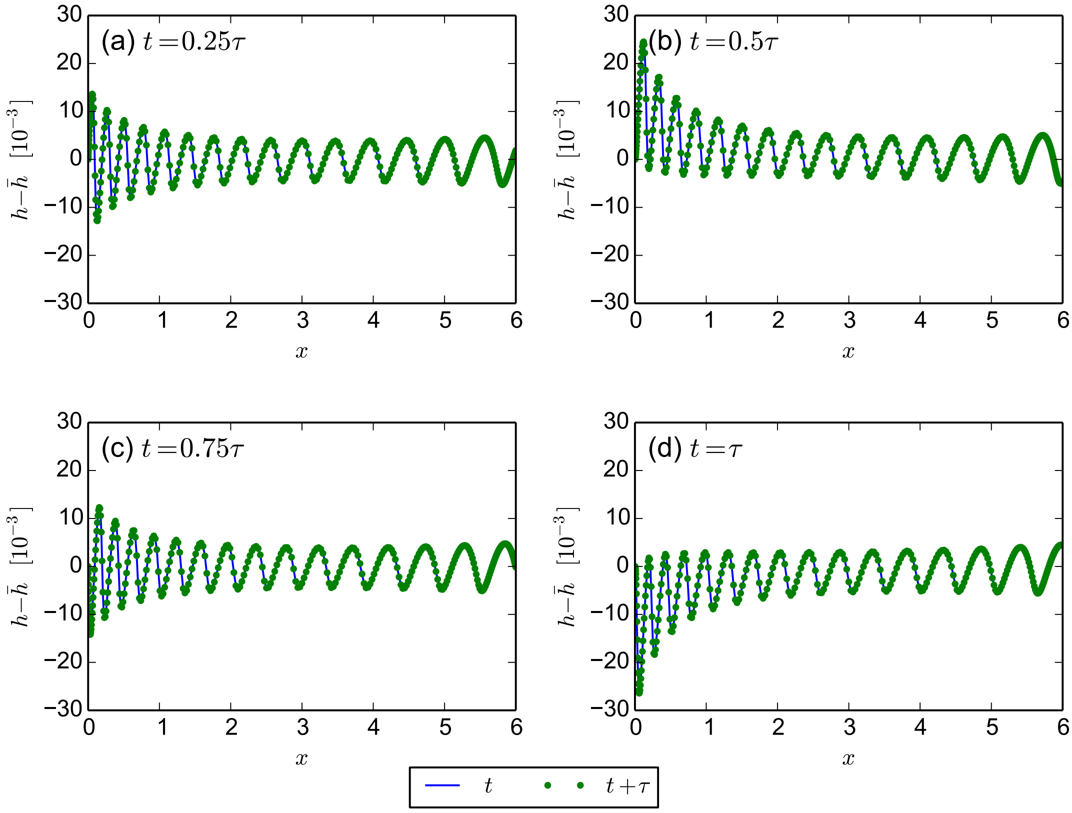

Figure 3.6: A comparison of thickness perturbations $h - \bar{h}$ (where $\bar{h}$ is the thickness in steady state) at various times in successive oscillatory cycles of simulation `ifNeJeDa` after it was run to $t = 10$. As can be seen, they are identical within numerical accuracy.

The simulations were run from $t = 0$ to $t = 10$ to allow initial transients to be advected out of the domain. At this point the shelf was in a statistically-steady state, with each cycle identical to the last (within numerical error), as illustrated in figure 3.6. The simulations were then run for one additional oscillatory period with more frequent output, for use in producing plots and animations.

3.3 Evolution to Steady State

It is useful to know the steady state of the ice shelf for a given choice of parameters and boundary conditions, so that there is a mean state against which to compare seasonal variations. Running a simulation to steady state also acts as a further test of the nonlinear solver, using the new set of scalings and parameter values.

At the grounding line, inflow boundary conditions were set to

$$h = 1, \quad u = 1, \quad D = \epsilon, \quad U = Q_g/\epsilon, \quad S = 0, \quad T = 0, \quad \text{at } x = 0. \tag{3.34}$$

The mass flux, DU, of the plume at the grounding is equivalent to the subglacial discharge Q_g. The plume thickness is set to some small value, ϵ, to avoid a singularity and the velocity is then chosen to be consistent with the subglacial discharge. The exact value of ϵ is arbitrary, so long as the plume remains supercritical; after a narrow boundary layer the plume will take on the same thickness and velocity regardless of the choice of ϵ (c.f. Dallaston et al., 2015). Typically, a value of $\epsilon = 3 \times 10^{-4}$ was used.

The aforementioned boundary layer which emerges in the plume near the grounding line proved difficult for the QLM to handle and would often result in the simulation failing. While larger diffusivities tended to improve numerical stability, $\nu = 3.69 \times 10^{-2}$ is the largest plausible value and it proved insufficient. In order to address this issue, an initial value problem (IVP) was constructed from the plume equations with diffusion set to zero and values at the grounding line set to those in equation (3.34). This was then integrated a small distance ($\Delta x = 0.05$) past the grounding line, using the current basal draft of the ice, until largely outside of the boundary layer. The resulting values for the plume variables were provided to the plume solver as boundary conditions. The integration was performed using the highest-order Runge-Kutta algorithm (Prince and Dormand, 1981) in the `rksuite_90` package (Brankin and Gladwell, 1994).

The vertically integrated normal stress of the ice is set equal to the vertically integrated hydrostatic pressure of the ocean at the end of the ice shelf. In dimensionless units, this corresponds to

$$4\eta h u_x = \chi h^2 \quad \text{at } x = X. \tag{3.35}$$

Note that for this 1-D shelf model without buttressing stresses, the condition in equation (3.35) in fact holds across the entire length of the shelf. This indicates that the end of the domain does not necessarily correspond to the calving front; it may equally be treated as just the end of the region of the ice shelf which is

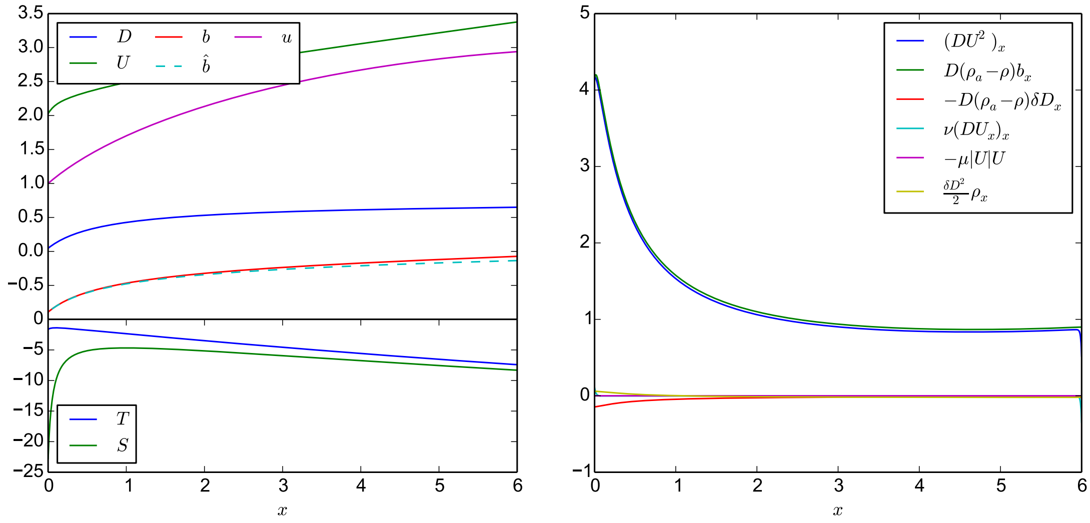

(a) **(b)**

Figure 3.7: (a) The steady state plume thickness D, plume velocity U, basal ice draft b, and ice velocity u resulting from simulation `ssNeJeDand`. Also plotted is the analytic basal draft of the ice shelf ($\hat{b}$) expected for this level of subglacial discharge using equation (2.21), which sets $\delta = \mu = \nu = 0$ and neglects meltwater release into the plume. The lower pane displays plume temperature T and salinity S. (b) The components of the momentum equation for the plume in steady state. The dominant balance is between buoyancy and inertia.

of interest. In the plume, the gradient of velocity, salinity and temperature are all taken to be zero at the outflow boundary:

$$U_x = 0, \quad T_x = 0, \quad S_x = 0, \quad \text{at } x = X. \tag{3.36}$$

Simulation `ssNeJeDand` was run with $\mu = 0$ (no turbulent drag on the plume), as was the case in the linear analysis. The ice was initialised with the profile given by equation (2.21). The resulting steady state basal draft and plume properties can be found in figure 3.7a with a diagnosis of key terms in the plume momentum balance in figure 3.7. In equation (2.18), the plume velocity was constant across the domain. This was the result of a balance between inertia and buoyancy, $(DU^2)_x \sim D(\rho_a - \rho)b_x$, a balance which also holds in this simulation to a good approximation (figure 3.7b). However, the uniformity also required the assumption that melting contributed much less mass to the plume than did entrainment and could therefore be ignored. Although the volume of meltwater is small, in this simulation it proved to be a

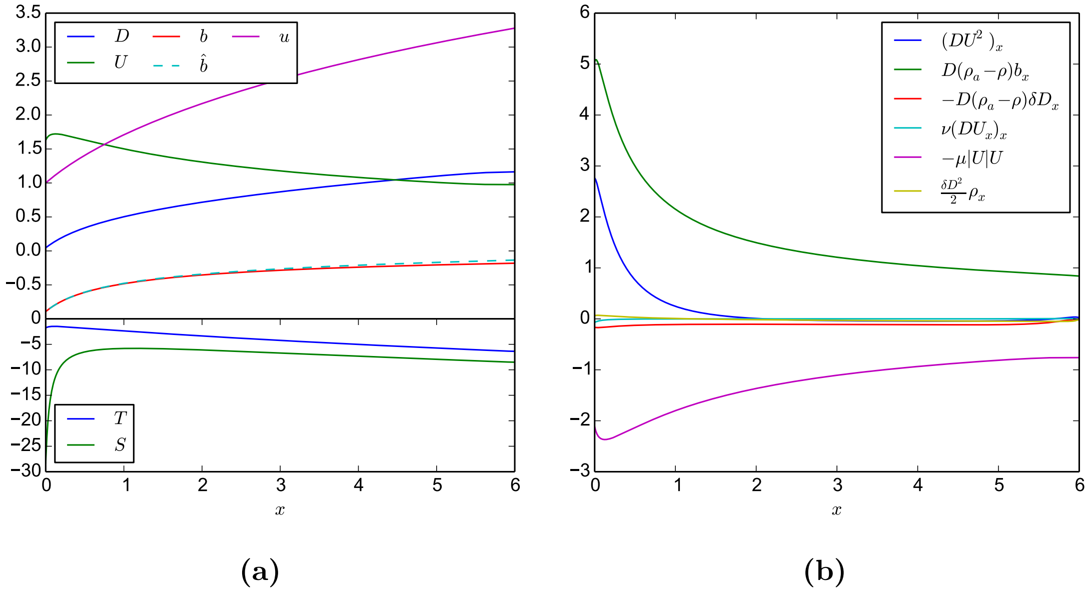

Figure 3.8: (a) The steady state plume thickness D, plume velocity U, basal ice draft b, and ice velocity u resulting from simulation `ssNeJeDa`. Also plotted is the basal draft of the ice shelf expected for this level of subglacial discharge using the analytic solution of equation (2.21) which sets $\delta = \mu = \nu = 0$ and neglects meltwater release into the plume. The simulation `ssNeJea` included turbulent ice-ocean drag on the plume. The lower pane displays plume temperature T and salinity S. (b) The components of the momentum equation for the plume in steady state. Downstream, the dominant balance is between buoyancy and drag, while closer to the grounding line inertia is also significant.

significant source of buoyancy (as seen by the gradual downstream decline in salinity in figure 3.7), causing the plume to accelerate throughout the domain (see $u(x)$ in figure 3.7a) and leading to greater levels of melting. As such, the ice shelf is slightly thinner towards the calving front than predicted by equation (2.21).

Simulation `ssNeJeDa` (including basal drag in the plume, with $\mu = 0.799$) was initialised with the output from simulation `ssNeJeDand`. The resulting basal draft and plume properties are shown in figure 3.8a. In this case, the buoyant force on the plume is balanced by drag across most of the domain, $D(\rho_a - \rho)b_x \sim \mu|\vec{U}|U$, although inertia also plays a role in the balance closer to the grounding line (figure 3.8b). This results in a slower-moving plume, with less transfer of heat to the base of the ice shelf (as characterised by the velocity-dependent heat transfer parameterisation) and hence less melting. As such, the ice shelf is slightly thicker in this simulation with ice-ocean drag compared to that without drag and to the prediction of equation (2.21),

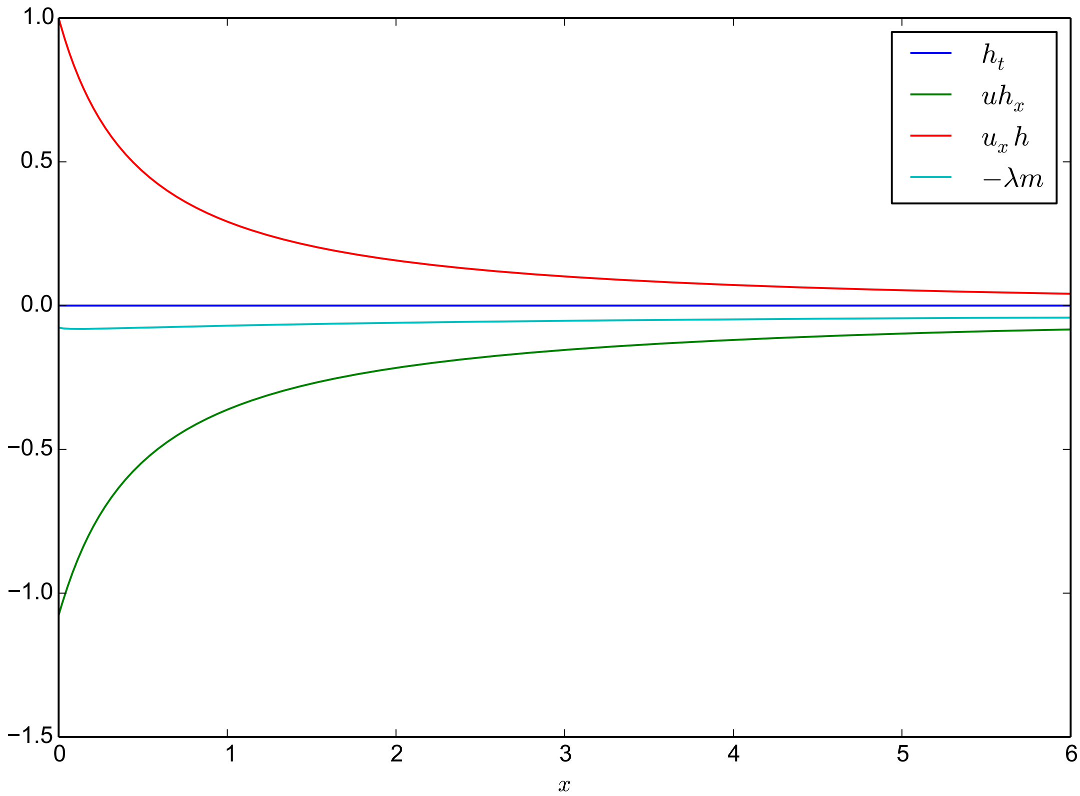

Figure 3.9: The components of the ice shelf continuity equation in steady state for simulation `ssNeJeDa`. Stretching ($u_x h$) is the dominant source of thinning near the grounding line, while stretching and melting (λm) are of comparable magnitude towards the calving front. As this is steady state, the Eulerian derivative $h_t = 0$ and the Lagrangian rate of change is purely advective (uh_x).

as seen by comparing red and dashed cyan lines in figure 3.8a. Counter-intuitively, the reduced melt rate in figure 3.8 compared to figure 3.7means that less heat is transferred from the plume to the ice and thus leads to a slightly higher plume temperature. As drag slows the plume it leads to convergence in the velocity field and, due to the plume being incompressible, causes the plume to grow thicker with drag relative to the $\mu = 0$ simulation, as can be seen by comparing figures 3.7 and 3.8. As can be seen in figure 3.9, thinning of the ice-shelf is dominated by stretching near the grounding line, where the majority of thinning occurs. Only towards the calving front (end of the domain), where the thinning rate is much lower, do melting and stretching approach comparable magnitudes.

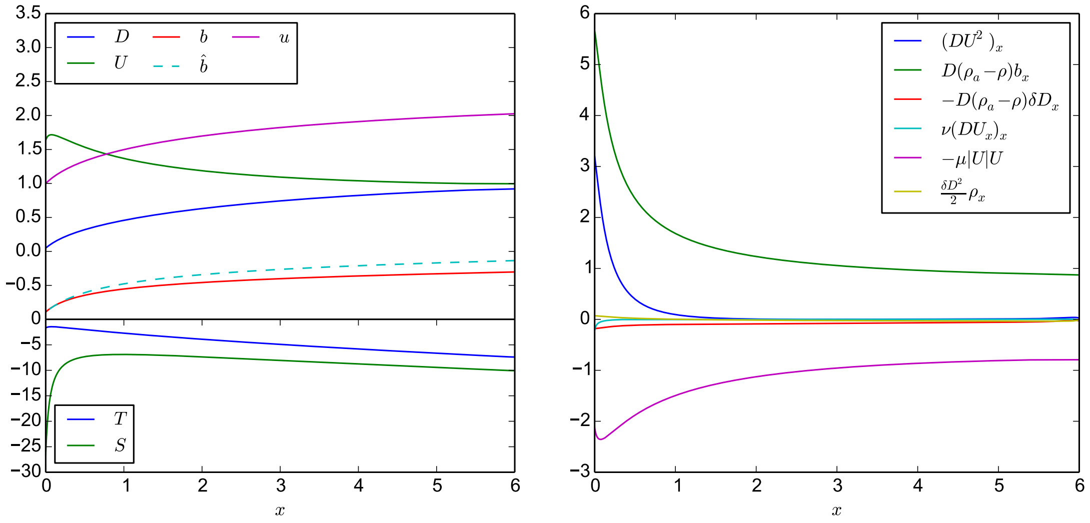

(a) **(b)**

Figure 3.10: (a) The steady state plume thickness D, plume velocity U, basal ice draft b, and ice velocity u resulting from simulation `ssGLJeDa` featuring Glen's Law rheology. Also plotted is the basal draft of the ice shelf expected for this level of subglacial discharge using the analytic solution of equation (2.21) which sets $\delta = \mu = \nu = 0$ and neglects meltwater release into the plume. The lower pane displays plume temperature T and salinity S. (b) The components of the momentum equation for the plume in steady state. Downstream, the dominant balance is between buoyancy and drag, while closer to the grounding line inertia is also significant.

3.3.1 Glen's Law Ice Rheology

Simulations were also run with the more realistic ice rheology of Glen's Law to test the importance of the choice of ice rheology. While Newtonian viscosity results in the ice stretching at the same rate everywhere, Glen's Law means that ice undergoing greater strain will be able to stretch more easily. The steady state of simulation `ssGLJeDa` using Glen's Law can be found in figure 3.10 and should be compared to the run with Newtonian rheology in figure 3.8. The simulation with Glen's Law shows significantly thicker ice towards the calving front than seen in the previous simulations and predicted in the analytic solution. Even with a Newtonian rheology, the velocity gradient towards the calving front is lower than the gradient close to the grounding line (figure 3.11). Glen's Law causes a feedback, resulting ice having a higher viscosity downstream, and further reducing stretching (i.e., an even smaller velocity gradient is present, as can be seen in figure 3.11).

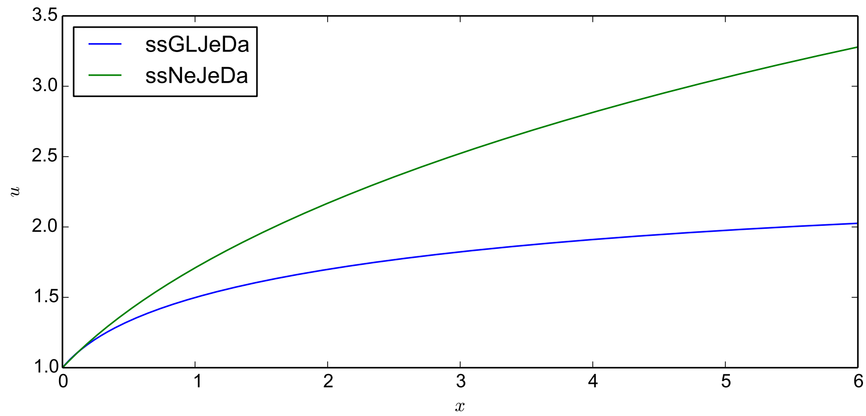

Figure 3.11: A comparison of steady state ice flow velocity in a simulation using Glen's Law (`ssGLJeDa`) and one with a Newtonian rheology (`ssNeJeDa`).

This produces thicker and slower flowing ice than in simulation `ssNeJeDa`. As no parameterisations have been changed in the plume dynamics, the force balance of the plume (figure 3.10b) is fairly similar to simulation `ssNeJeDa`.

3.3.2 Alternative Entrainment Parameterisation

To test the sensitivity to the entrainment parameterisation, simulation `ssJeKoDa` was run with entrainment parameterised using equation (3.9) (Kochergin, 1987) rather than equation (3.8) (Jenkins, 1991). The entrainment coefficient c_L was selected to minimise the difference in the domain-averaged melt rate found when the plume was solved using the parameterisation in equation (3.8) compared to when using that in equation (3.10). Solutions were found for a fixed ice profile described by equation (2.21) with $\gamma = 2$ and $X = 10$. The minimisation was performed using the `lmdif1` routine in MINPACK (Moré et al., 1984). It was found that the result of this routine depended on the initial guess of c_L, so it was run iteratively using the previous output as a new input until convergence was achieved. This gave a result of $c_L = 0.1059$, which is approximately four times greater than those used in previous work by Payne et al. (2007) and Holland, Feltham, and Jenkins (2007). However, Payne et al. (2007) gives no justification for their choice of value. Holland, Feltham, and Jenkins (2007) chose the parameter value by tuning it to match observations of marine ice deposition. Given the rather

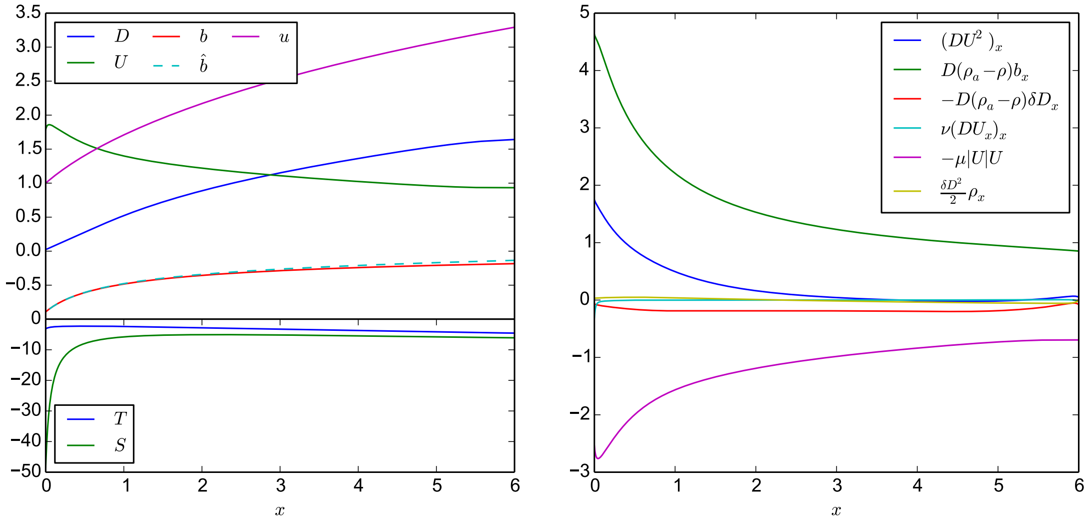

(a) **(b)**

Figure 3.12: (a) The steady state plume thickness D, plume velocity U, basal ice draft b, and ice velocity u resulting from simulation `ssNeKoDa`. Also plotted is the basal draft of the ice shelf expected for this level of subglacial discharge using the analytic solution of equation (2.21) which sets $\delta = \mu = \nu = 0$ and neglects meltwater release into the plume. The lower pane displays plume temperature T and salinity S. (b) The components of the momentum equation for the plume in steady state. Downstream, the dominant balance is between buoyancy and drag, while closer to the grounding line inertia is also significant.

arbitrary nature by which the value of c_L has been chosen in the past, the larger value used here is considered to be justifiable. Note that, in a sensitivity analysis, Holland, Feltham, and Jenkins (2007) showed that the melt rate stagnated for $c_L \gtrsim 0.04$. This is consistent with the experience when calculating c_L here, where it was found that the differences in the melt rate were only weakly sensitive to the exact value. The Kochergin (1987) parameterisation tended to produce higher melt rates near the grounding line and lower ones towards the calving front when compared to the Jenkins (1991) parameterisation.

The steady-state results of this simulation are shown in figure 3.12. The ice is somewhat thicker than in the analytic solution and similar in thickness to the ice in simulation `ssNeJeDa` (see figure 3.8). This is to be expected, as the parameter c_L was tuned to minimise differences in melt rate. There is slightly more entrainment in simulation `ssNeKoDa` than `ssNeJeDa`. The greater entrainment (as seen by increased plume thickness) leads to a slightly higher temperature and salinity, as seen in the lower panel of figure 3.12a. The thicker plume also means that the buoyancy force component arising from changing plume thickness is more noticeable than in previous simulations (see red line in figure 3.12b).

3.3.3 Simulations Without Hydrostatic Pressure Gradient

In § 3.5, when examining the effect of seasonally varying the ice flux crossing the grounding line, it was necessary to run a number of simulations with $\delta = 0$. In effect, this is setting hydrostatic pressure gradients to zero and turning off gravity waves in the plume, as is commonly done in 1-D plume models under ice shelves (e.g. Jenkins, 1991; Payne et al., 2007; Magorrian and Wells, 2016). Doing so required steady-state results for this parameter choice with which to initialise simulations and compare perturbed results. As such, a second version of each of the above simulations was run with $\delta = 0$, the results of which are plotted in figure 3.13. These simulations have the same name as their $\delta \neq 0$ counterparts, but with the suffix `d0`. The steady state ice thickness is little changed compared to the simulations where $\delta \neq 0$, but the plume flows slightly faster and (except in `ifNeKoDa`) is slightly thinner towards the calving front.

3.3.4 Hydraulic Shocks

This section documents a particular case where the transient development from a specific initial condition resulted in the development of a shock-like feature and subsequent failure of the numerical solver. When simulation `ssNeJeDa` (with $\mu = 0.799$) was initialised with a wedge-shaped ice shelf of the form $h(x, t = 0) = 1 - 0.1rx$, the simulation was unable to reach a steady state. New ice which entered the domain took on a profile near to the grounding line similar to what would be expected at steady state, with a significant slope. Meanwhile, old ice from the initial condition was transformed by a combination of advection, stretching, and melting. Together, these processes flattened the profile of the old ice so that it had a very small, nearly uniform slope. Over time, an overdeepening developed at the transition between these two regions, where the basal slope of the ice was slightly

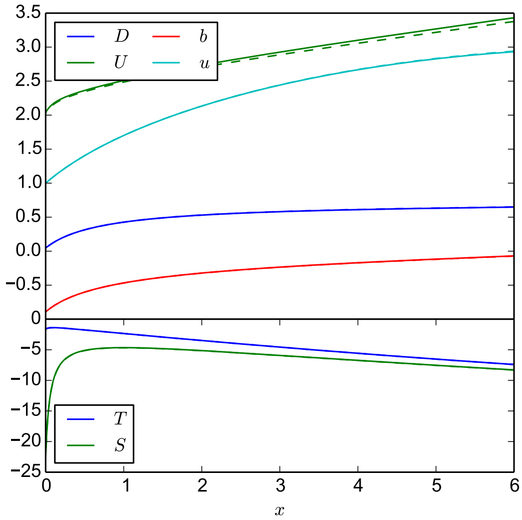

(a) `ssNeJeDandd0`

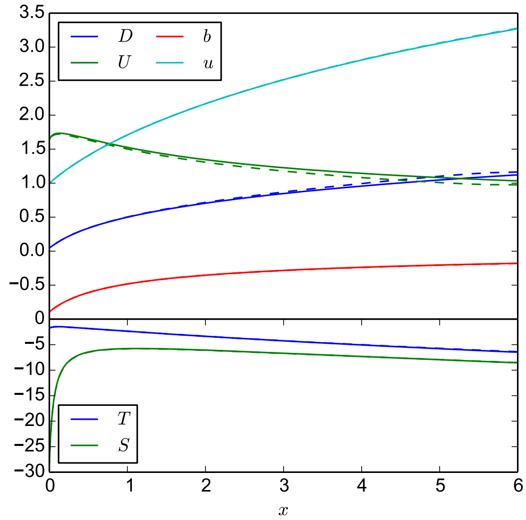

(b) `ssNeJeDad0`

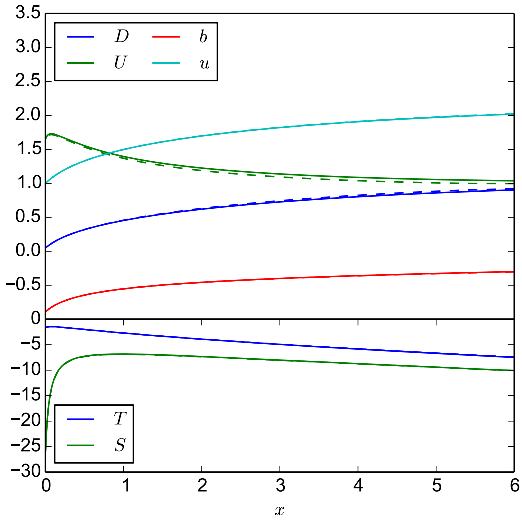

(c) `ssGLJeDad0`

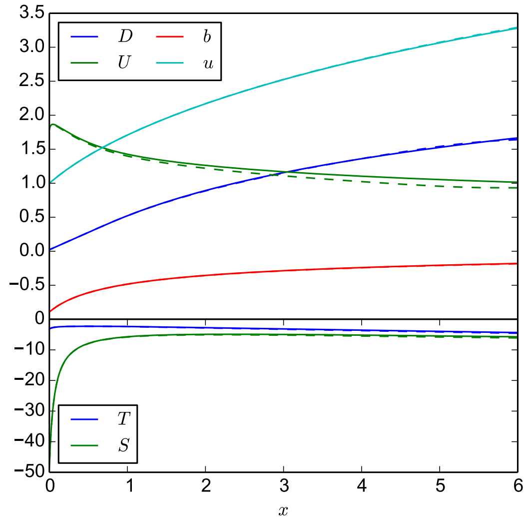

(d) `ssNeKoDad0`

Figure 3.13: Steady state results from simulations where $\delta = 0$ (solid lines), along side the corresponding ones with $\delta \neq 0$ (dashed lines).

negative. At the location where these regions of the shelves met, the plume formed a shock, experiencing a rapid decrease in velocity and increase in thickness, as seen near $x = 1$ in figure 3.14a. Eddy viscosity and gradients in hydrostatic pressure smear out this feature, giving a continuous transition rather than a discontinuous shock of the type that would be present in an inviscid adiabatic plume. Upstream of the shock, buoyant forces are balanced by a combination of inertia and drag, whereas buoyancy is balanced only by drag downstream of the shock (figure 3.14b).

Support for this feature being a genuine hydraulic shock is given by examining the Froude number, $\mathrm{Fr} = |U|/\sqrt{\delta D(\rho_a - \rho)}$, the ratio between the plume speed and the propagation speed of gravity waves. The Froude number is plotted in figure 3.14c, which shows that at the grounding line $\mathrm{Fr} > 1$, indicating that the plume is supercritical. However, within the region of the shock, the Froude number falls below 1 and stays there across the rest of the domain, meaning that the plume is now subcritical. The shock forms at the transition between the super- and subcritical regimes, similar to those in adiabatic gases (e.g. James and Keith, 2006, chapter 4). Over time, this shock tends to steepen and approach a discontinuous state. Discontinuities lead to ringing and error in spectral differentiation, causing slow convergence in the plume solver.

Nonetheless, the simulation was able to progress until the negative-slope feature neared the end of the domain. At this point the shock appeared to grow in an unstable fashion (see figure 3.15) and the GMRES component of the plume solver began to stagnate. Increasing the diffusivity (ν) did not solve this problem. It may be that an alternative implementation of the GMRES algorithm, which has been modified to be resistant to stagnation (e.g., de Sturler, 1999), would perform better. Alternatively, there may be a physical instability at play which is causing the model to break down when features of negative ice shelf slope interact with the outflow boundary.

As the shock formed at a location where the slope of the ice shelf approached zero, it seems possible that such a feature could arise at the apex of any transverse channels, or precursors thereof, inscribed on the underside of the ice shelf. While it was not possible to investigate in more detail here, due to failure of the plume solver, it may be interesting for future work to consider what effect this shock could have on melt-patterns and further evolution of ice topography. It is worth noting that, in simulations run with $\beta_T = 0$ (i.e., with the plume density insensitive to temperature), while a shock was produced there was no negative slope. This is unexpected, given that $\beta_T \Delta T \ll \beta_S \Delta S$ and thermal buoyancy contributions were weak, suggesting the system may be close to some critical threshold. If any small

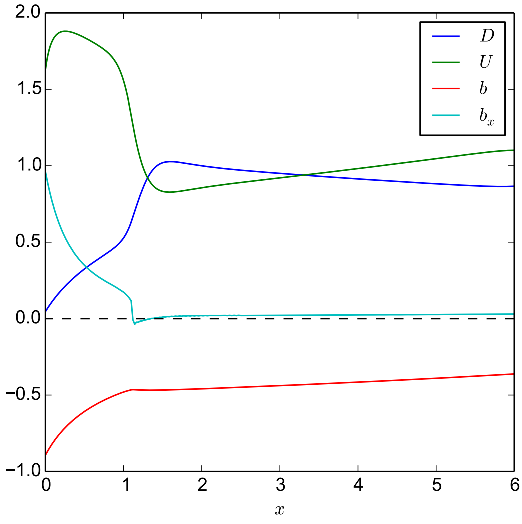

(a)

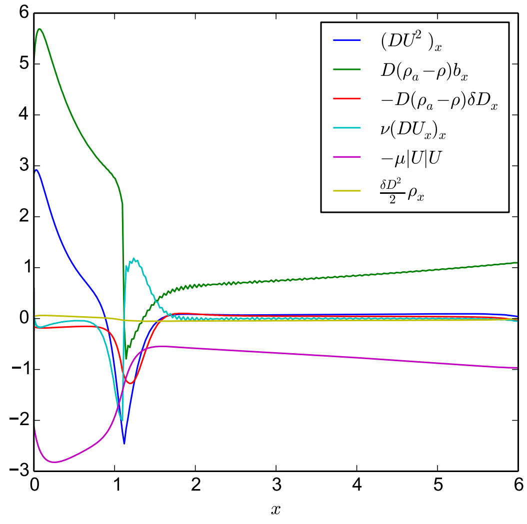

(b)

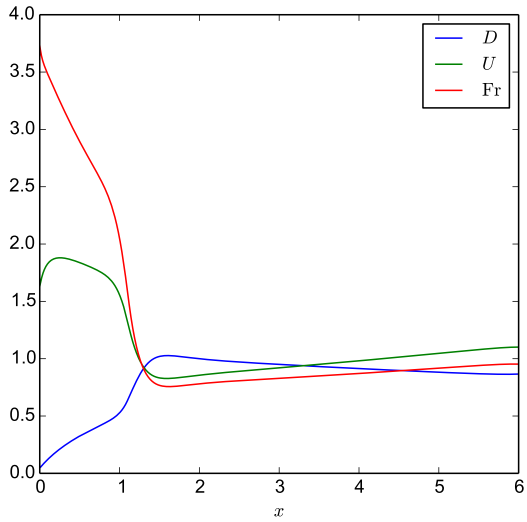

(c)

Figure 3.14: The diffusively smeared shock which forms in a plume with $\nu = 0.799$ at time $t = 0.8$ for a simulation like `ssNeJeDa` but initialised with $h(x, t = 0) = 1 - 0.1rx$. (a) The plume thickness D, plume velocity U, basal ice draft b, and ice velocity u. The lower pane displays plume temperature T and salinity S. (b) The components of the momentum equation for the plume. Upstream of the shock at $x = 1$ there is a balance of buoyancy, inertia, and drag, while downstream only buoyancy and drag play a role. The eddy diffusion, $\nu(DU_x)_x$, and hydrostatic pressure gradient, $-\delta D(\rho_a - \rho)D_x$, become significant near the shock and likely lead to the continuous transition. Sharp gradients in buoyancy and diffusion terms resulted in some ringing when spectral differentiation was applied. Internally, the plume solver stored each variable's gradient separately from its value and required that they agree with each other for convergence to be achieved. Although the plume solver did converge, only the values (not the derivatives) were saved as output and differentiating them exhibited some ringing. (c) The Froude number (Fr) of the plume, alongside the thickness and velocity. The Froude number is less than 1, indicating a subcritical plume, downstream of the shock.

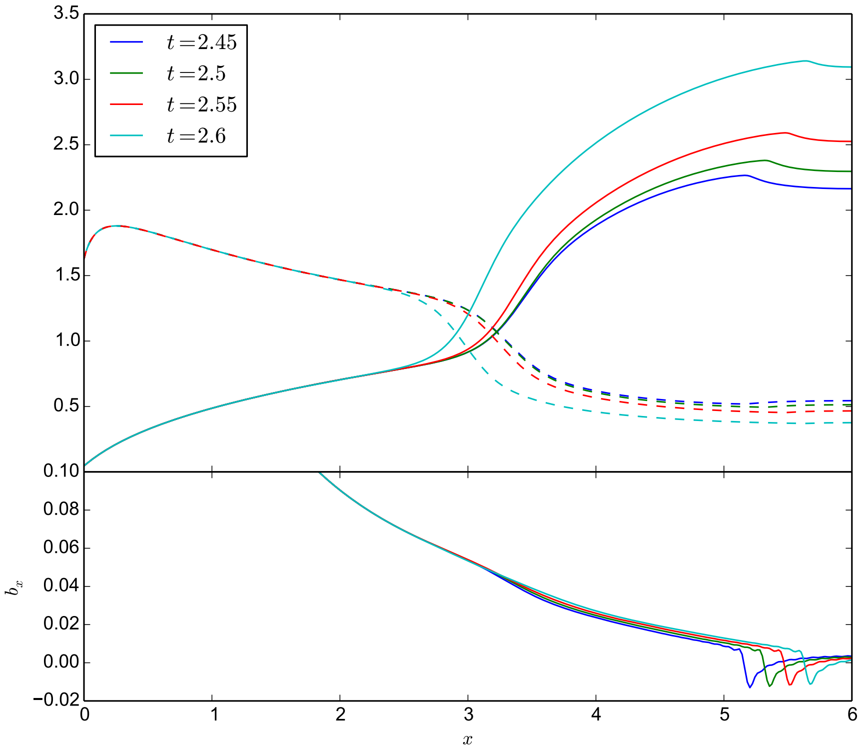

Figure 3.15: Upper: The thickness (solid lines) and velocity (dashed lines) of a plume at successive output times in a simulation, exhibiting larger and larger shock-type features as an overdeepening in the ice shelf approaches the outflow boundary. Lower: the basal slope of the ice shelf, showing an overdeepening (aligned with the dip in plume thickness in the upper panel) approaching the outflow boundary. Note that the sharp change in the shelf gradient results in some ringing when spectral differentiation is applied.

change could shift the system from one side to the other then the result may be very sensitive to parameterisation choices of entrainment and melting. Furthermore, these results indicate that evolution to steady state may be sensitive to initial conditions; some choices of initial conditions will result in dramatically different transient behaviour. While it has not be possible to conclusively test this, it is assumed that once the initial ice profile has advected past the calving front the ice shelf would start evolving towards the usual steady state.

3.4 Seasonal Subglacial Discharge Forcing

A further two simulations were run with periodic variations in subglacial discharge to compare with the results of the linear analysis in § 2.3: one with turbulent

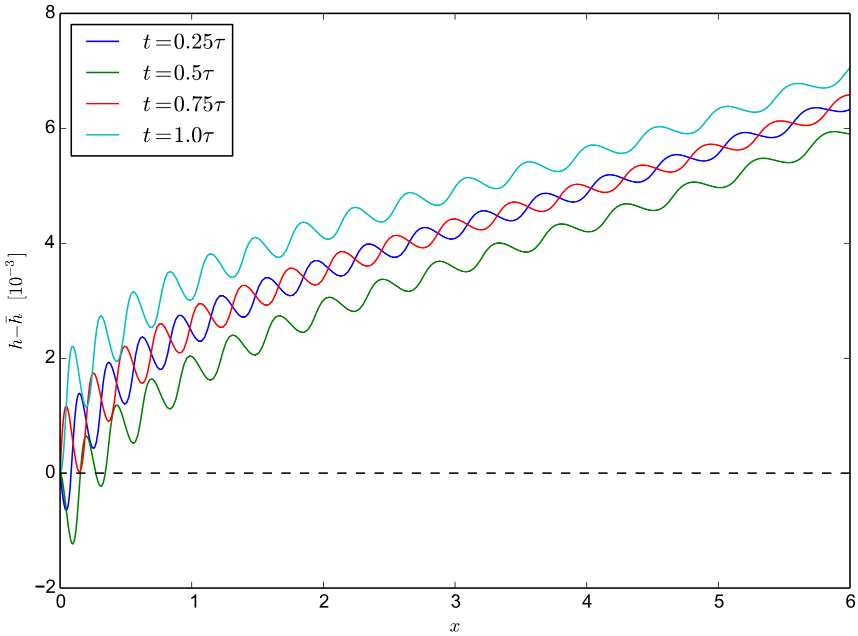

Figure 3.16: The difference between the ice thickness (h) at different points in the oscillatory cycle for simulation `diNeJeDand` with no ice-ocean drag, compared to the thickness in steady state ($\bar{h}$) simulation `ssNeJeDand`. The results are from after the ice shelf has reached a statistically-steady state. In the legend of this plot, τ refers to the oscillatory period.

drag on the plume and the other with the drag coefficient set to zero. In both cases, subglacial discharged oscillated according to

$$Q_g = Q_{g0}\left[1 + A\sin(\omega t)\right], \tag{3.37}$$

where Q_{g0} is the value used in the steady state simulations (table 3.1), $A = 0.9$ is the amplitude of the forcing, and ω is the angular frequency of oscillations, set corresponding to a period of $\tau = 1\,\text{yr}$. The choice of $A = 0.9$ was to see the response to large amplitude forcing, but sensitivity is tested later. This forcing was applied by changing the boundary value of the plume velocity. It was decided to avoid reducing the discharge to zero as this resulted in problems for the plume solver if the plume had $\text{Fr} < 1$ at the grounding line.

Animations showed variations in ice thickness which were periodic in time. Plots of perturbations to ice thickness relative to steady state at different points in the cycle were produced for the simulation without ice-ocean drag (figure 3.16) and the

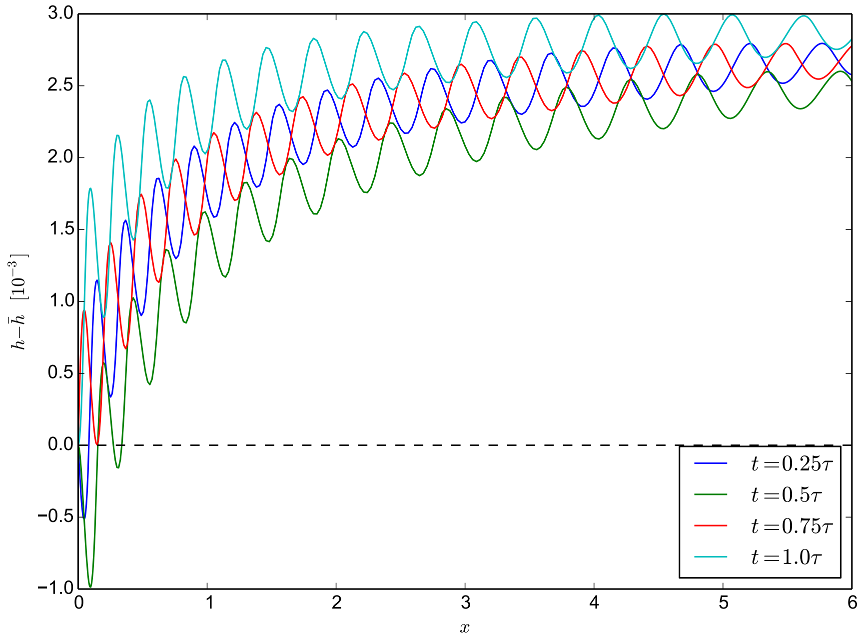

Figure 3.17: The difference between the ice thickness (h) at different points in the oscillatory cycle for simulation `diNeJeDa` with ice-ocean drag, compared to the thickness in steady state ($\bar{h}$) simulation `ssNeJeDa`. The results are from after the ice shelf has reached a statistically-steady state. In the legend of this plot, τ refers to the oscillatory period.

one with drag (figure 3.17). As was found in the linear analysis, in both simulations seasonal variations in subglacial discharge caused two responses: global oscillations of the shelf thickness across the entire domain, along with ripples inscribed in the ice which are advected towards the calving front. Once again, the amplitude of these variations is of order 10^{-3} compared to the inflowing ice thickness and decreases to 10^{-4} towards the calving front. The ripples are approximately 20% larger in the simulation without drag than the one with, due to greater plume velocity (and thus larger melt rate) for a given inflow of subglacial discharge.

The perturbations to the terms in the ice mass balance equation (3.1a) relative to steady state were plotted in figure 3.18 for simulation `diNeJeDa`. Looking at the largest terms, it is clear the leading-order balance

$$\left(\frac{\partial}{\partial t} + \bar{u}\frac{\partial}{\partial x}\right)\tilde{h} = \frac{D\tilde{h}}{Dt} \approx -\lambda\tilde{m} \tag{3.38}$$

holds. In this equation, variables with a bar are the steady state values, while those with a tilde are the difference between the perturbed value and the steady

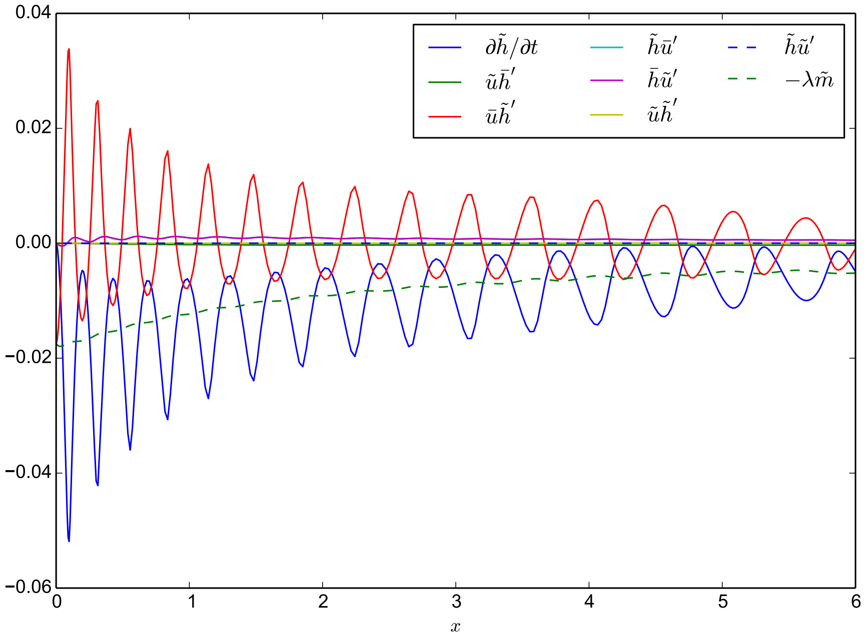

Figure 3.18: The magnitudes of perturbations to the terms in equation (3.1a) at time $t = 0.25\tau$ into a season cycle of simulation `diNeJeDa`, where here τ represents the period of the forcing. The forcing takes the form of variations in subglacial discharge. In the legend, a bar over a variables indicates it is the value at steady state (from simulation `ssNeJeDa`), while a tilde indicates it is the difference between the variable at this time and the steady state value.

state value. This relationship is the same as that found for in the linear analysis in equation (2.29), and shows that changes to the ice thickness are caused by changes to the melt rate accumulated following a Lagrangian parcel of ice.

There are differences between the results in this section and those of the linear analysis. Both the ripples and the global oscillations are non-symmetric, with a bias towards the ice becoming thicker downstream on the shelf. This is due to the response of the plume velocity to varying subglacial discharge, because the melt rate is proportional to the plume velocity. In the case without drag, a scale analysis of equation (3.6b) reveals

$$U \sim \left(\frac{g\beta_S S_a}{E_0} Q_g \right)^{1/3}, \tag{3.39}$$

from the balance between inertial and buoyancy terms, similar to the scaling found by Jenkins (2011) for a planar ice slope. The nonlinear relationship between U and Q_g means that periods of low discharge decrease the plume velocity more than periods of high discharge increase it. Since melt is proportional to plume velocity, the result is that varying discharge reduces the melt rate on average, leading to a thicker shelf. In the case with drag, there is an additional mechanism: in absolute terms, drag reduces the plume velocity more when U_g is larger than when it is small. In the linear analysis of § 2.3, the cube-root of equation (3.39) was linearised using the binomial approximation and it was assumed $\mu = 0$, so the asymmetry could not occur.

Despite the large oscillations in the melt rate resulting from equation (3.39), the ripples in simulations `diNeJeDand` and `DiNeJeDa` are small. Examining the corresponding steady state ice mass balance in figure 3.9, it is apparent that near the grounding line, for an ice shelf of this geometry, stretching is a much more significant source of thinning than is melt. As this is the region in which the ripples are inscribed into the shelf (after which they are passively advected and stretched), even large changes in the melt rate will result in only small changes to ice shelf thickness. Although figure 3.9 was for the unforced shelf, the perturbations to the shelf in simulations `diNeJeDand` and `diNeJeDa` were small and relative magnitudes of melting and stretching are similar.

In these simulations, the structure of the ice shelf was perturbed by altering the melt rate by a factor of ~ 2.5 (relative to its lowest value) via variations in plume flow. Although there may be some small quantitative differences, seasonal variations in the temperature forcing (T_a) of the system would likely have a similar magnitude effect on the melt rate. It can thus be concluded that temperature variations would produce similar ripples to the ones displayed here.

3.4.1 Glen's Law Ice Rheology

Simulation `diGLJeDa` was run to determine whether a different rheology would alter the behaviour of the ripples in the ice. The results of this simulation at different points in the seasonal cycle are shown in figure 3.19. There are no qualitative differences between these results and those of simulation `diNeJeDa`: ripples and global oscillations are both present, perturbations are of a similar magnitude, and the same bias towards thickening persists. The bias towards thickening is

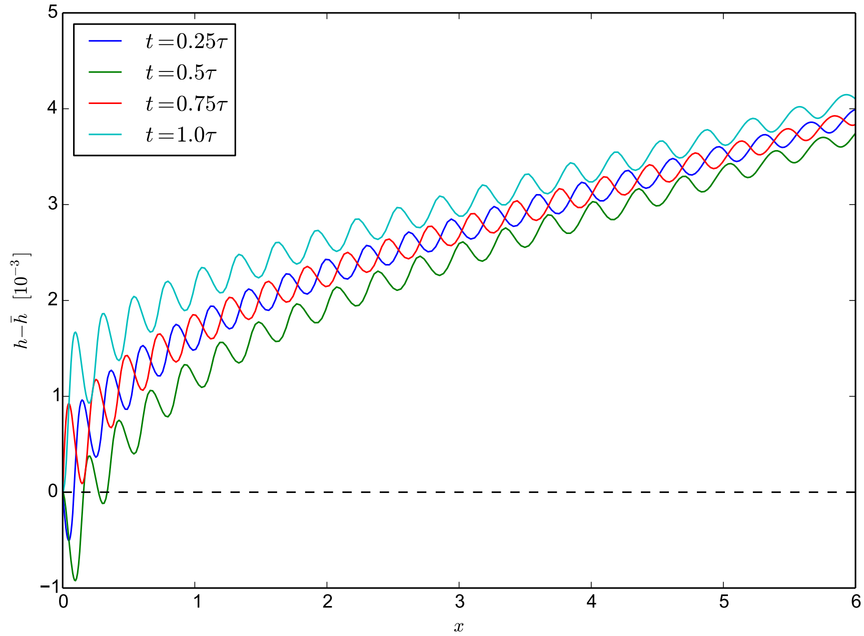

Figure 3.19: The difference between the ice thickness (h) at different points in the oscillatory cycle for simulation `diGLJeDa` with Glen's Law rheology and ice-ocean drag, compared to the thickness in steady state ($\bar{h}$) simulation `ssGLJeDa`. The results are from after the ice shelf has reached a statistically-steady state. In the legend of this plot, τ refers to the oscillatory period.

stronger in this case, however. This is thought to be due to the ice moving more slowly (see figure 3.11) and thus having more time for the perturbation to build up before reaching the calving front. The ripples have a shorter wavelength than in simulations using Newtonian rheology, as they are advected a shorter distance while forming and undergo less stretching.

3.4.2 Alternative Entrainment Parameterisation

Finally, simulation `diNeKoDa` was run using the entrainment parameterisation of Kochergin (1987). This was to determine whether the above results were dependent on the proportionality of the Jenkins (1991) parameterisation to the ice shelf slope, which tends to inhibit ripples feeding back into faster plume flow. However, the results in figure 3.20 show that the shape and size of the ripples remains largely unchanged, with a small reduction in the ice thickness at the end of the shelf.

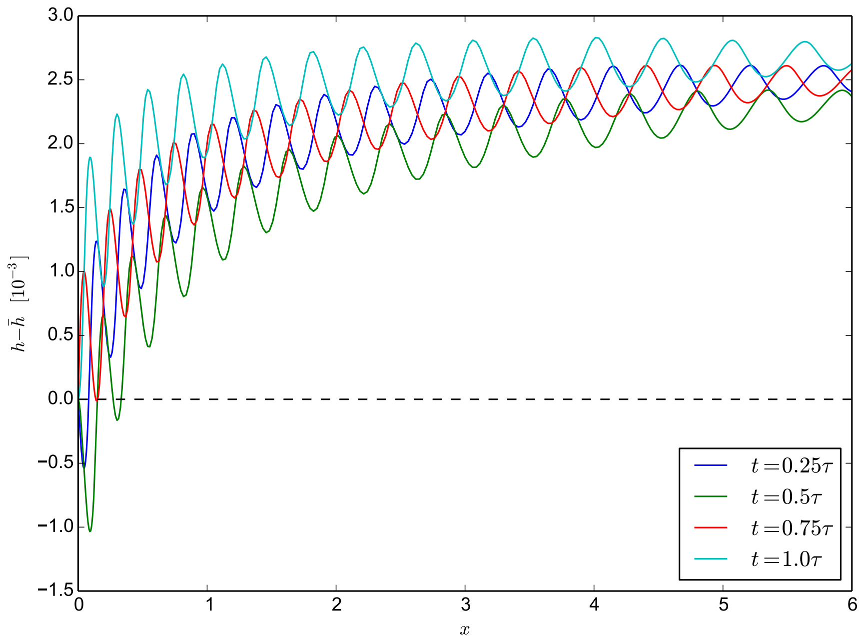

Figure 3.20: The difference between the ice thickness (h) at different points in the oscillatory cycle for simulation `diNeKoDa` with the Kochergin (1987) entrainment parameterisation and ice-ocean drag compared to the thickness in steady state ($\bar{h}$) simulation `ssNeKoDa`. The results are from after the ice shelf has reached a statistically-steady state. In the legend of this plot, τ refers to the oscillatory period.

3.4.3 Sensitivity to Forcing Frequency and Amplitude

Simulation `diNeJeDa` was rerun a number of times with different amplitude and frequency for the subglacial discharge forcing. It was not physically meaningful to significantly increase the amplitude of the discharge forcing, so instead four simulations were run with smaller values. The amplitude of the ice shelf ripples (either the first or the last) was found to scale slightly super-linearly with the magnitude of the forcing (see figure 3.21). This is due to the nonlinear relationship between plume velocity and subglacial discharge which means that the amplitude of plume velocity (and hence melt) variations grows superlinearly with the amplitude of subglacial discharge variations. This can be seen by taking the difference between the plume velocity calculated from equation (3.39) for $Q_g = Q_{g0} + A$ and the velocity for $Q_{g0} - A$.

Testing for different values of ω was slightly complicated by the requirement to compare the results at the same point in the cycle for each. The simulations

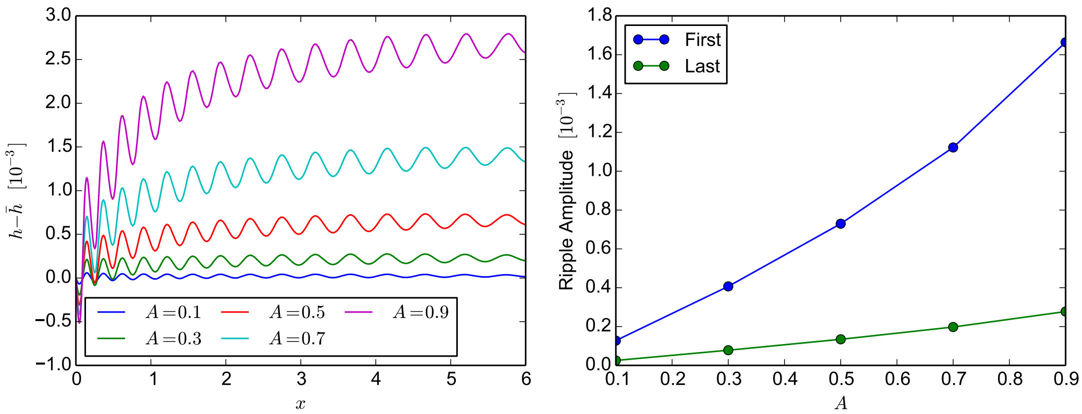

Figure 3.21: Response of ice shelf thickness perturbations to the amplitude of subglacial discharge forcing A. Results are from a quarter of the way through a seasonal cycle, after the ice shelf has reached quasi-steady state. Other than forcing amplitude, all simulation parameters are the same as in `diNeJeDa`. Left: Ice thickness perturbations for each simulation. Right: Amplitude of the first and last ripples on the ice shelf as a function of the forcing amplitude.

were all run to $t = 10$ as before and then, if necessary, continued running until the current cycle was completed. Each simulation was then run for an additional cycle (the exact length of which varied inversely with ω), with the state of the ice shelf and plume saved at intervals of 0.01τ. The results, plotted in figure 3.22, showed that the amplitude of the ripples increases with the inverse of the forcing frequency, as was expected from equation (2.37). However, the relationship between amplitude and ω^{-1} is slightly nonlinear, the reason for which is not clear. In the case of the last ripple it may just be an issue of choosing where to measure the amplitude from, as the ripple peaks and troughs are located at different positions along the shelf as the frequency changes. The wave-number of the ripples is linearly related to the forcing frequency, similar to the $\omega = \langle u \rangle k$ scaling found in § 2.3.2. However, extrapolating backwards to $\omega = 0$ gave $k = -3.65$ for the first ripple and $k = 1.07$ for the last, rather than $k = 0$ as would be expected. In neither case can this be explained by the error of the fit ($\sigma = 0.09$ and $\sigma = 0.10$, respectively). This likely indicates nonlinear behaviour at very low frequencies.

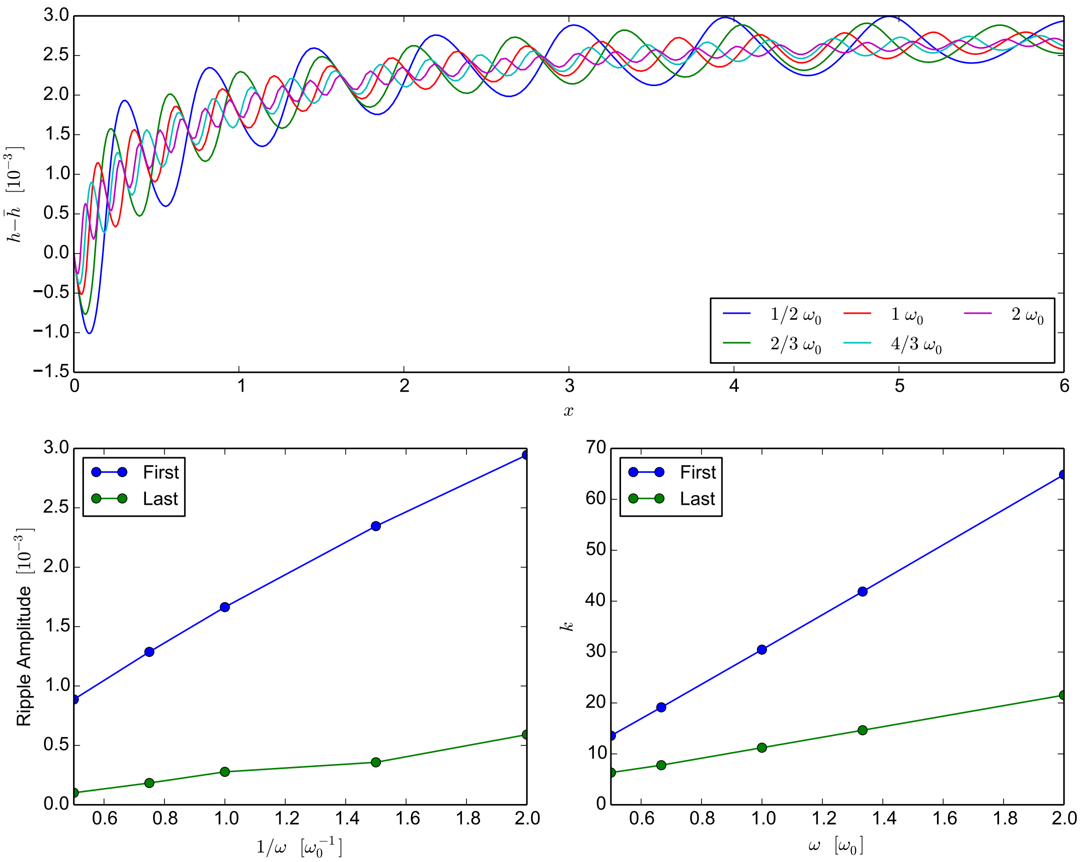

Figure 3.22: Response of ice shelf thickness perturbations to the frequency of subglacial discharge forcing, ω. Results are from a quarter of the way through an oscillatory period, after the ice shelf has reached a statistically-steady state. Other than forcing frequency, all simulation parameters are the same as in `diNeJeDa`. Upper: Ice thickness perturbations for each simulation. Lower left: Amplitude of the first and last ripples on the ice shelf as a function of the inverse forcing frequency. Lower right: Wave number k of the first and last ripple on the ice shelf as a function of the forcing frequency.

3.5 Seasonal Ice Flux Forcing

A number of simulations with varying ice flux were also run for comparison with the results in § 2.4. This was achieved by setting the boundary condition for the ice velocity at the grounding line to

$$u_g = u_{g0}\left[1 + A\sin(\omega t)\right], \quad \text{at } x = 0, \tag{3.40}$$

where u_{g0} is the value used in the steady state simulations (see table 3.1), $A = 0.5$ is the amplitude of the oscillations, and ω is the angular frequency of oscillations, set corresponding to a period $\tau = 1\,\text{yr}$. Such variability could arise in nature

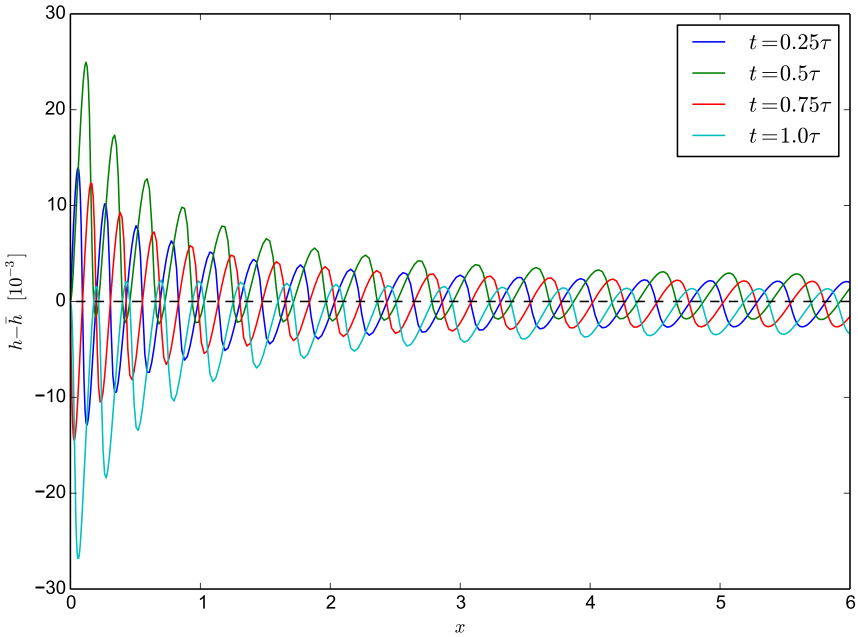

Figure 3.23: The difference between the ice thickness (h) at different points in the oscillatory cycle for simulation `ifNeJeDand` with seasonally varying ice flux and without ice-ocean drag, compared to the thickness in steady state ($\bar{h}$) simulation `ssNeJeDand`. The results are from after the ice shelf has reached a statistically-steady state. In the legend of this plot, τ refers to the oscillatory period.

due to seasonal melting events lubricating the glacier bed and allowing it to slip. The ice thickness was kept constant at the grounding line, as there is no intuitive reason to expect it to undergo periodic oscillations. The grounding line position was assumed to be fixed. This was purely a matter of convenience to simplify the calculation and in reality there likely would be some movement. Future work could incorporate grounding line motion by coupling together grounded and floating ice sheet models, as described by Schoof (2007).

The results for simulation `ifNeJeDand` (without ice-ocean drag) are shown in figures 3.23, which displays the difference between the perturbed ice thickness during seasonal forcing and steady state thickness (from simulation `ssNeJeDand`) at different times in the seasonal cycle. It shows a great deal of similarity with the linear results in figure 2.11. As before, there are ripples inscribed in the ice which are advected and stretched, as well as global oscillations in the thickness. Unlike the simulations in § 3.4, the nonlinearity is insufficient to break the symmetry of

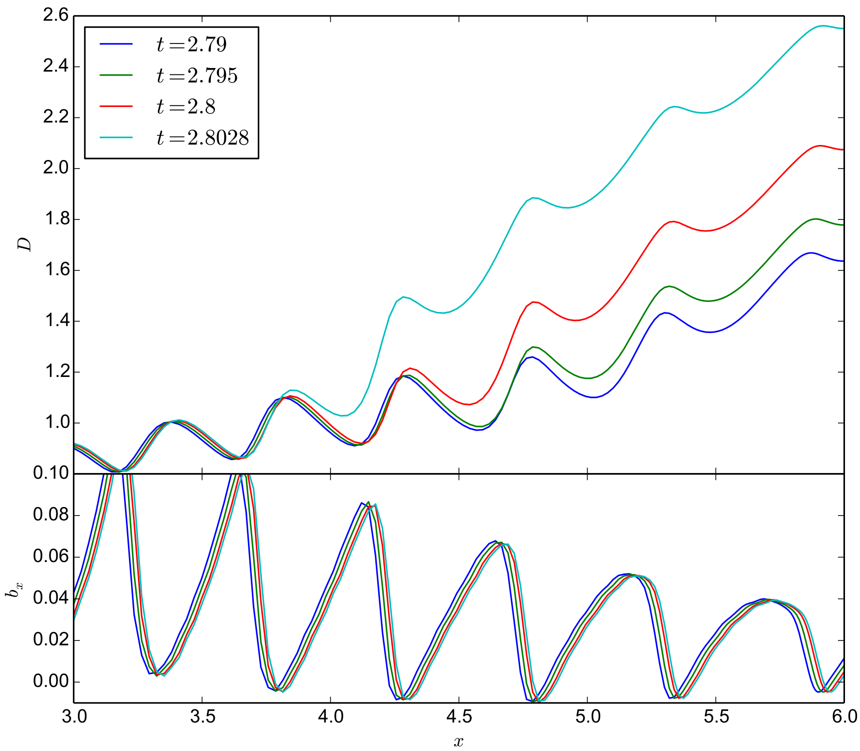

Figure 3.24: Illustration of plume thickness D and ice shelf basal slope b_x when an instability occurred as $b_x \to 0$ near the outflow boundary in the simulation `ifNeJeDadn0`, for $\delta \neq 0$. This resulted in the plume thickness (D) growing over time until the solver failed at $t = 2.8028$.

the forcing and cause the ice to preferentially thin or thicken.

Attempting to run this simulation with basal drag included (`ifNeJeDadn0`) produced small regions with negative basal shelf slope. When the first of these features approached the outflow boundary, the plume responded by undergoing shock-like behaviour, with increasing thickness and decreasing velocity. This feature grew over time (see figure 3.24) until the plume solver failed due to stagnation in the GMRES routine. There appears to be a physical instability of some sort which arises when the basal slope approaches zero at the outflow boundary. Whether this would actually cause the model to break down if integration were able to continue is unclear; it may be that this is simply an issue of insufficiently robust numerics. Alternatively, there may be a feedback at play between the negative basal slope and the outflow boundary conditions for the plume.

It was found that setting $\delta = 0$ (i.e., removing feedback due to pressure gradients

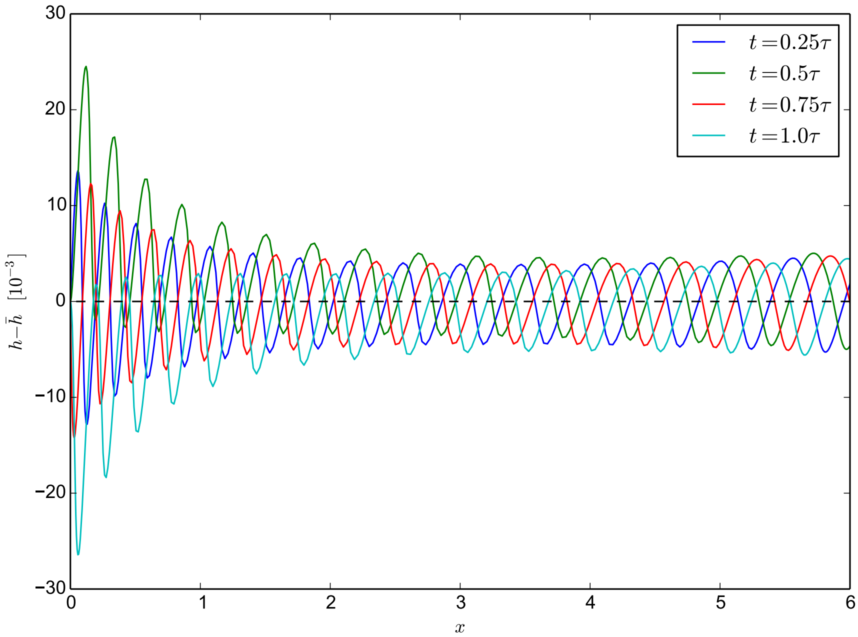

Figure 3.25: The difference between the ice thickness (h) at different points in the oscillatory cycle for simulation `ifNeJeDa`, with varying ice flux and including ice-ocean drag, compared to the thickness in steady state ($\bar{h}$) simulation `ssNeJeDad0`. The results are from after the ice shelf has reached a statistically-steady state. In the legend of this plot, τ refers to the oscillatory period.

within the plume and turning off any gravity waves) allowed the simulation to run successfully. As similar errors occurred for all of the ice flux-forced simulations except `ifNeJeDand`, all were run with $\delta = 0$. As discussed in § 3.3.3, this approximation is commonly used in plume models and leads to only small changes to the background steady state, but the potential for time-dependent effects has not been fully assessed. The runs with $\delta = 0$ were initiated with the steady state results produced for $\delta = 0$ described in § 3.3.3. A simulation was also run with no drag and $\delta = 0$, but the results were virtually indistinguishable from those of `ifNeJeDand` even when plotted on the same axes, suggesting the impact of setting $\delta = 0$ may be modest.

Simulation `ifNeJeDa` (figure 3.25) produced broadly similar results to those of simulation `ifNeJeDand` (figure 3.23). The most noticeable difference is that the downstream ripples are larger in figure 3.25. The perturbations also appear to be growing slightly as they approach the calving front. This is due to a correlation in the perturbation to the melt rate and to the ice thickness in this region, illustrated in

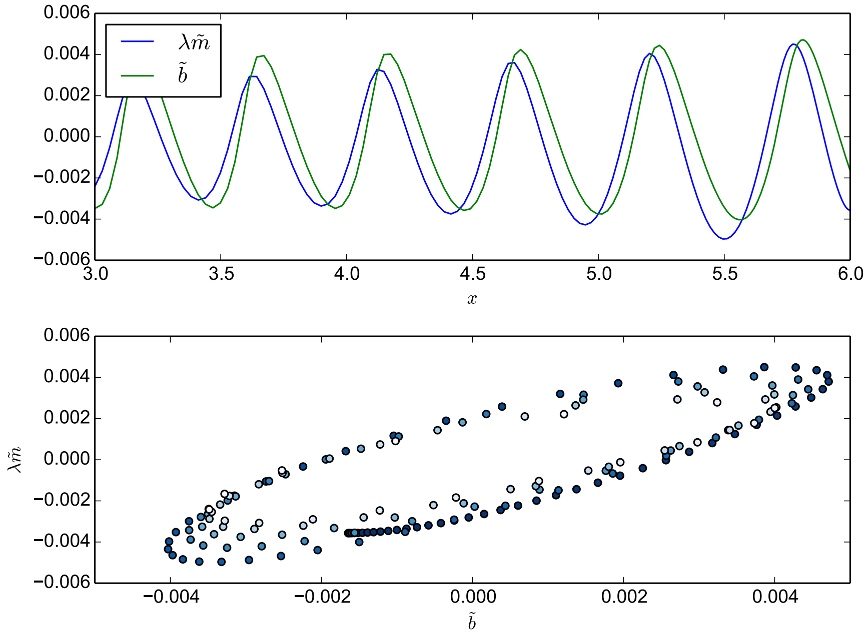

Figure 3.26: Upper: perturbations to melt rate ($\lambda\tilde{m}$) and basal depth ($\tilde{b}$) of the ice shelf in simulation `ifNeJeDa` in the latter half of the domain, a quarter of the way through a seasonal cycle after the ice shelf has reached a statistically-steady state. Lower: these two quantities plotting against each other, showing a clear correlation, with a small phase-lag (leading to the elliptical clustering). The colour of a point indicates its location on the shelf, with white corresponding to $x = 3$ and navy to $x = 6$.

figure 3.26. This can be intuitively understood as being due to the plume accelerating and flowing faster where the ice slope increases, driving greater melting. Conversely, where the plume decelerates melting is reduced and the ice becomes thicker. The greatest acceleration (deceleration) occurs where the slope is greatest (smallest/most negative) rather than at the apex (keel) of ripples. This means there is a slight lag between the thickness perturbation and the melt-feedback, which results in ripples migrating slightly upstream relative to the Lagrangian trajectory of an ice parcel.

As figure 3.27 shows, the melt-feedback allows ripples to grow large enough to produce a series overdeepenings in the ice shelf near the calving front. However, comparing to the ice thickness perturbations at the time of the last output before simulation `ifNeJeDadn0` failed ($t = 2.8$, just before the last of the transient features were advected out of the shelf, allowing the ice to approach a statistically-steady state) indicates that ripple growth downstream may not occur for $\delta \neq 0$, as can

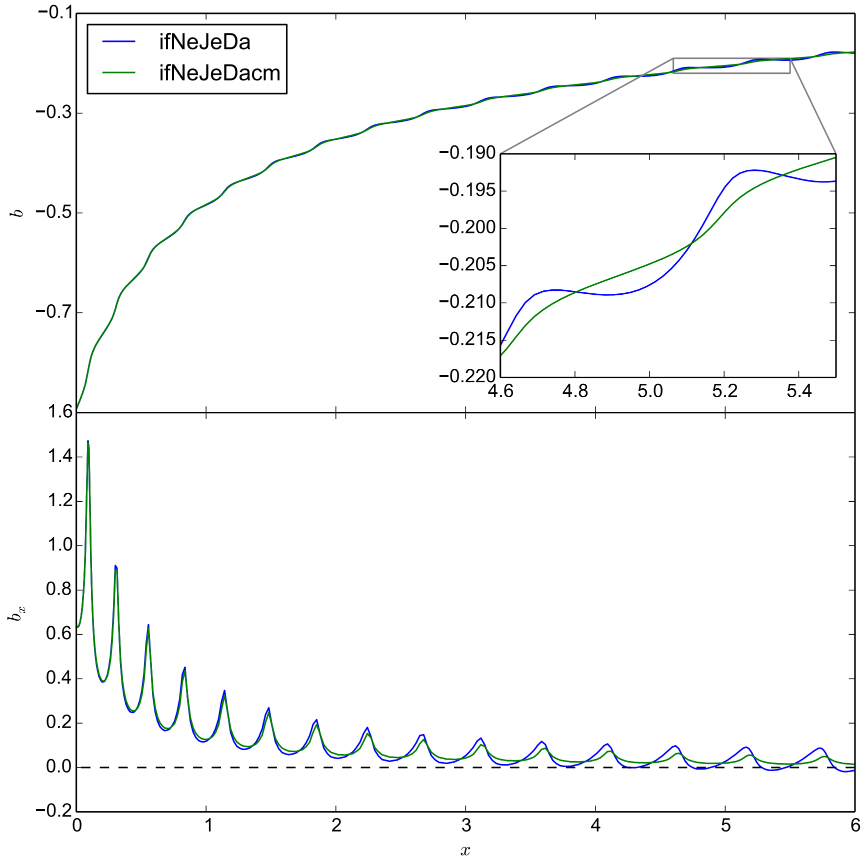

Figure 3.27: Upper: comparison of the basal depth of the ice shelf in simulations `ifNeJeDa` and `ifNeJeDacm`, at $t = 0.25\tau$ after the shelf has reached a statistically-steady state (where τ is the period of the seasonal forcing). In the former the plume is coupled to the ice shelf, allowing melt-driven feedback to occur, while in the latter the melt-rate is taken to be constant in time. The inset axes illustrate that a slight overdeepening develops near the calving front only in the former simulation. Lower: The corresponding basal slope of the ice shelf in simulations `ifNeJeDa` and `ifNeJeDacm` at $t = 0.25\tau$. In the latter simulation the slope is positive definite throughout the domain.

be seen in figure 3.28. This suggests that there is the potential that hydrostatic pressure gradients may disrupt the melt-feedback mechanism, although it is unclear exactly how. Unfortunately, the instability of the numerical solver prevents the impact of non-zero δ on ripples from being conclusively resolved here.

The importance of melt-feedback to the formation of these overdeepenings was tested by running simulation `ifNeJeDa` again with melting fixed at the steady state value of `ssNeJeDad0`. This was referred to as simulation `ifNeJeDacm`. It was found that without the melt feedback no overdeepenings could form (see

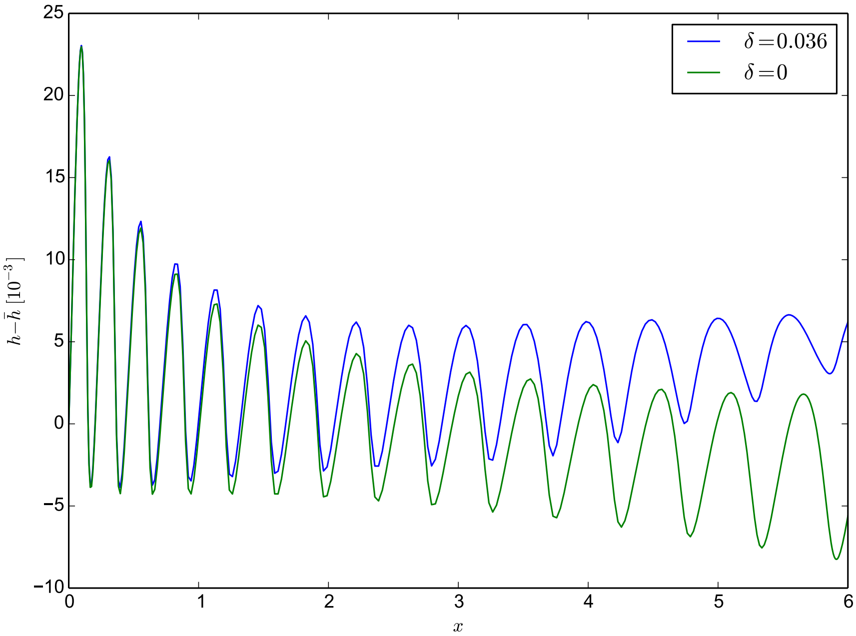

Figure 3.28: Comparison of perturbed ice thickness at $t = 2.8$ for simulations `ifNeJeDadn0` and `ifNeJeDa`, in which $\delta = 0.036$ and $\delta = 0$, respectively. The growth of ripples towards the end of the ice shelf which is seen in the latter (with $\delta = 0$) is not present in the former (with $\delta \neq 0$ and gradients of hydrostatic pressure included in the model).

figure 3.27). Thus, the ice flux mechanism is only sufficient to initiate the formation of varying slope in the present configuration, but melt-driven feedback is needed for development of overdeepenings.

The magnitudes of the perturbations to the terms in equation (3.1a) are plotted in figure 3.29 for simulation `ifNeJeDa`. The dominant balance is revealed to be

$$\left(\frac{\partial}{\partial t} + (\bar{u} + \tilde{u})\frac{\partial}{\partial x}\right)\tilde{h} = \frac{D\tilde{h}}{Dt} \approx -\tilde{u}\frac{\partial \bar{h}}{\partial x}, \tag{3.41}$$

which is the same as the result in equation (2.34) except that the nonlinear perturbation term $\tilde{u}\partial\tilde{h}/\partial x$ is now included in the Lagrangian derivative, characterising advection of thickness perturbations by the ice velocity perturbations. The fact that this term is significant indicates that the linear analysis of § 2.4 does not directly apply to the present nonlinear regime. The forcing term on the right-hand-side of the equation is significant near the grounding line, but decays downstream, indicating that ripples are generated near the grounding line and then undergo nearly-passive

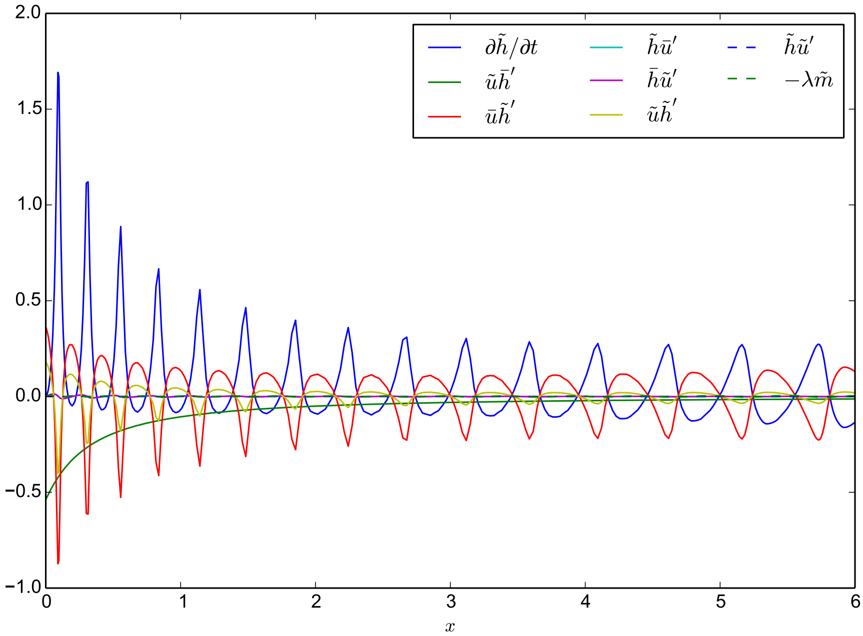

Figure 3.29: The magnitudes of perturbations to the terms in equation (3.1a) at time $t = 0.25\tau$ into a seasonal cycle of simulation `ifNeJeDa` after it has reached a statistically-steady state. Here τ represents the period of the forcing with varying ice flux across the grounding line. In the legend, a bar over a variable indicates it is the value at steady state, while a tilde indicates it is the difference between the variable at this time and the steady state value.

advection. Rearranging equations (3.1a) and (3.1b) for 1-D steady state shows

$$\frac{\partial \bar{h}}{\partial x} = -\frac{\lambda \bar{m} + \frac{\chi}{4\eta}\bar{h}^2}{\bar{u}},$$

which can be substituted into equation (3.41) to give

$$\frac{D\tilde{h}}{Dt} \approx \frac{\tilde{u}}{\bar{u}}\left(\lambda \bar{m} + \frac{\chi}{4\eta}\bar{h}^2\right). \tag{3.42}$$

This expresses the same physics as equation (2.36) did for the linear case: changes to the ice thickness are the result of increased or decreased time the ice spends exposed to thinning (due to melting and stretching) when the ice is moving slower ($\tilde{u} < 0$) or faster ($\tilde{u} > 0$), respectively.

The ripples are larger than predicted in the linear analysis (compare figures 2.11 and 3.25). This is due to the different parameter values chosen for the nonlinear simulation, representing a thicker ice shelf which undergoes greater stretching. Thus the thinning rate will be greater and changes to the time exposed to thinning will have a greater effect on ice thickness. As noted above, there is also a feedback between ice thickness perturbations and the melt rate which causes the ripples to begin growing towards the end of the ice shelf.

3.5.1 Asymmetry in Perturbations

Careful examination of figure 3.23 and 3.25 reveals slight asymmetries in the perturbations to the ice thickness ($h - \bar{h}$), most noticeably near the grounding line. First, it can be seen that the ripples have a larger amplitude when the ice is thinner ($t = \tau$) compared to when it is thicker ($t = 0.5\tau$). Additionally, the distance from the location of a trough to the next peak is larger than that from a peak to the next trough. Alternatively, this may be thought of as perturbations to the ice slope being more (less) extreme when the slope perturbation is positive (negative).

To try to understand these effects, a special case was considered where there is no stretching ($\chi = 0$) and the melt rate is constant in t and x. As changes to melting and stretching were seen to be insignificant in figure 3.29 (i.e. $-\lambda\tilde{m}$ and $h\tilde{u}'$ were small), it was thought that these assumptions would not alter the main mechanism. The velocity of the ice at the grounding line (and thus across the entire shelf, since there is no stretching) is $\bar{u} + \tilde{u}_0 \sin(\omega t)$. Under these conditions, after an initial transient state has been advected out of the domain, the ice shelf has the implicit solution given in equation (3.31). This equation was solved numerically using the same parameter choices as in the nonlinear simulation and a nondimensional melt rate of $m = 10^{-3}$. A steady-state was calculated by setting $\tilde{u}_0 = 0$. Without any stretching, the ripples stay at the same amplitude and wavelength across the entire length of the shelf, which makes plots of the whole domain difficult to read. As such, only the solution for $x \leq 1$ was plotted and can be found in figure 3.30. Note that, in the absence of stretching, the magnitude of the ripples is similar to those when forced by variations in subglacial discharge, as expected from equation (3.42).

It can be seen that there is no asymmetry present in the magnitude of the ripples. However, the different steepness of upward downward sloping perturbations remains. The reason for this is the nonlinear advection term in equation (3.41),

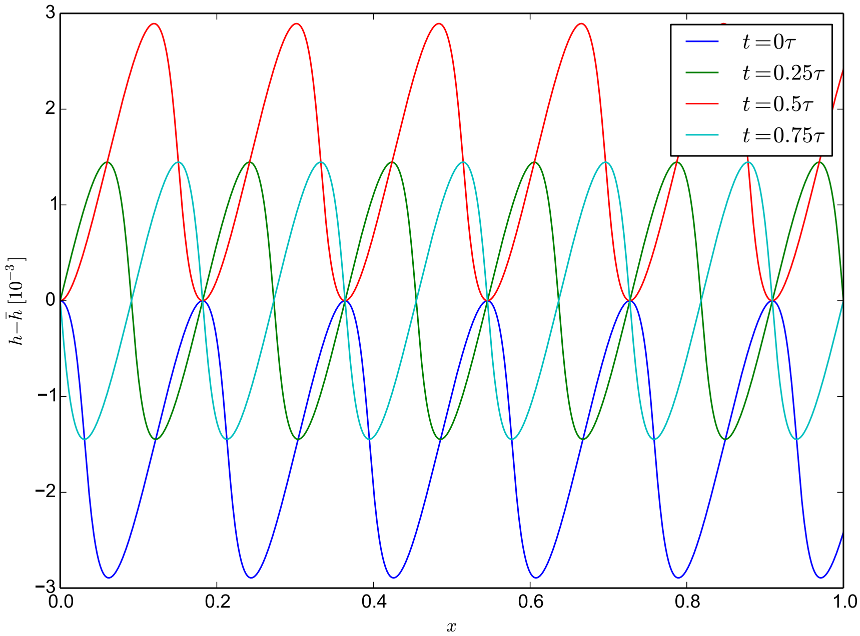

Figure 3.30: Numerical solution to the analytical equation (3.31), which gives an implicit form for h when there is no ice stretching ($\chi = 0$) and a constant melt rate. Here, $\omega = 2\pi/(1\,\mathrm{yr})$, $\bar{u} = 1$, $\tilde{u}_0 = 0.5$, $\lambda = 100$, and $m = 10^{-3}$. Perturbations are shown relative to the steady state, which was calculated using $\tilde{u}_0 = 0$.

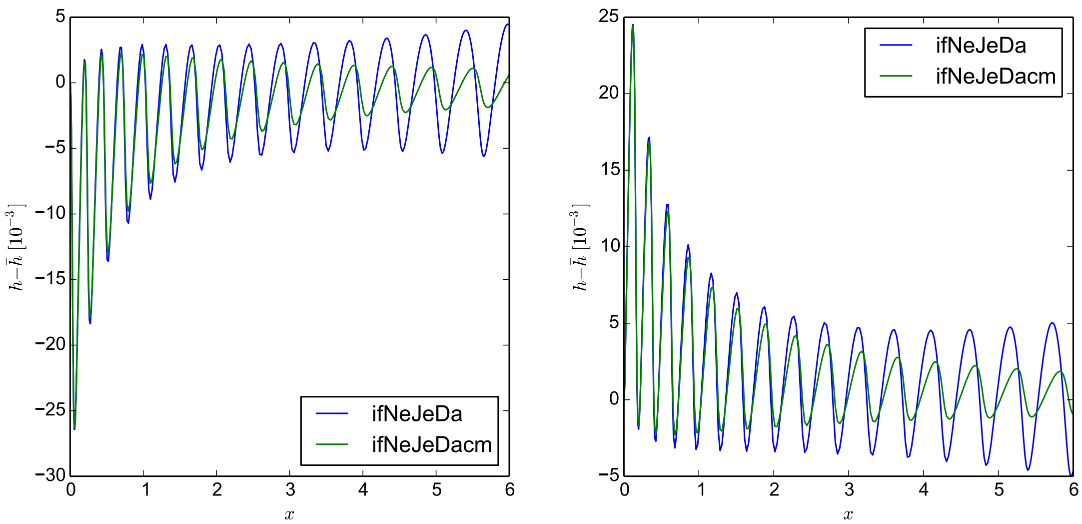

Figure 3.31: Comparison of thickness perturbations in simulations `ifNeJeDa` and `ifNeJeDacm` at the start (left) and half-way through (right) a seasonal cycle, after having reached a statistically-steady state.

which means that the perturbations move at different speeds along the ice shelf depending on the phase of the forcing. When the speed at the grounding line is higher than average (and the ice is thickening there), ice moves further per unit time and more enters the shelf. This increases the amount of ice exposed to this forcing. When the ice is moving more slowly (and the ice is thinning at the grounding line), it moves a smaller distance and less ice enters the shelf. Thus, the thinning affects smaller lengths of ice than thickening.

The only remaining potential causes of the asymmetric ripple magnitude are perturbations to melting and stretching. To test the former, the results of simulation `ifNeJeDacm` (figure 3.31) were examined. It was found to produce perturbations which are qualitatively similar to those in figure 3.23 and also featured an asymmetry in ripple magnitude. Hence, the asymmetry in ripple heights can be produced without variations in melt rate. Placing the perturbations on the same axis (figure 3.31), it could aslo be seen that the ripples generated by time-independent melt have less extreme peaks and troughs, indicating feedback from spatial variation in the melt rate. It also appears that the ripples in the two simulations become slightly out of phase towards the end of the shelf. This is due to the melt feedback and lag illustrated in figure 3.26.

Since the asymmetry can be generated without variations in melt rate, potential mechanisms by which stretching stretching can generate the asymmetry are examined. When constructing equation (3.42) the perturbed stretching terms $\tilde{h}\bar{u}'$, $\bar{h}\tilde{u}'$ and $\tilde{h}\tilde{u}'$ were neglected as insignificant. Using the 1-D form of equation (3.1b) and the boundary condition for u in equation (3.35), it can be shown that

$$\frac{\partial u}{\partial x} = \frac{\chi}{4\eta} h \tag{3.43}$$

throughout the length of the shelf, which applies equally to the steady state and perturbed values of u and h. Substituting equation (3.43), $h = \bar{h} + \tilde{h}$, and $u = \bar{u} + \tilde{u}$ into equation (3.1a), then eliminating $\partial\bar{h}/\partial x$ using the steady state form of equation (3.1a) a more exact form of equation (3.42) can be derived:

$$\frac{D\tilde{h}}{Dt} \approx \frac{\tilde{u}}{\bar{u}} \left(\lambda \bar{m} + \frac{\chi}{4\eta} \bar{h}^2 \right) - \frac{\chi \bar{h}}{2\eta} \tilde{h} - \frac{\chi}{4\eta} \tilde{h}^2. \tag{3.44}$$

Note that the approximately-equals sign persists as this still neglects the effect of changes to the melt rate. The penultimate term provides a damping on the growth of the perturbations. However, the final term, $-\chi\tilde{h}^2/4$, is negative regardless of the sign of $\tilde{h}$. It represents a nonlinear rectification to changes in the stretching rate due to the fact that increasing the ice thickness will increase stretching more than decreasing ice thickness reduces it. This rectification biases the ice shelf towards thinning, reducing the peaks in $\tilde{h}$ and increasing the troughs. While small in magnitude, it would appear that this is the source of asymmetry in the magnitude of the ripples.

3.5.2 Glen's Law Ice Rheology

While using Glen's Law in place of Newtonian viscosity had no major impact when forcing with varying subglacial discharge, stretching plays an important role in creating the perturbations for the simulations forced by changing ice flux. As these perturbations tend to be larger, they will also have a more significant impact on the force balance in the ice. Furthermore, the asymmetric ripples which arise due to nonlinearity in stretching may be altered by a change in rheology. For all of these reasons, it was decided to run a simulation using Glen's Law viscosity.

Before presenting the results of this simulation, it is useful to investigate the ice shelf equations analytically. Equation (3.1b) can be integrated once again and simplified for Glen's Law in 1-D (using $\eta = \xi|du/dx|^{-2/3}/2$ when index $n = 3$ and the boundary condition in equation 3.35), giving the result

$$\frac{\partial u}{\partial x} = \left(\frac{\chi}{2\xi}h\right)^3. \tag{3.45}$$

Decomposing u and h into background and perturbed portions and applying the binomial approximation, it can also be seen that

$$\frac{\partial \tilde{u}}{\partial x} \approx \frac{3\chi^3\bar{h}^2}{8\xi^3}\tilde{h}, \tag{3.46}$$

for $\tilde{h} \ll \bar{h}$. Substituting this result into equation (3.1a) and eliminating $\partial\bar{h}/\partial x$ using the steady state version of equation (3.1a), the Lagrangian derivative of the

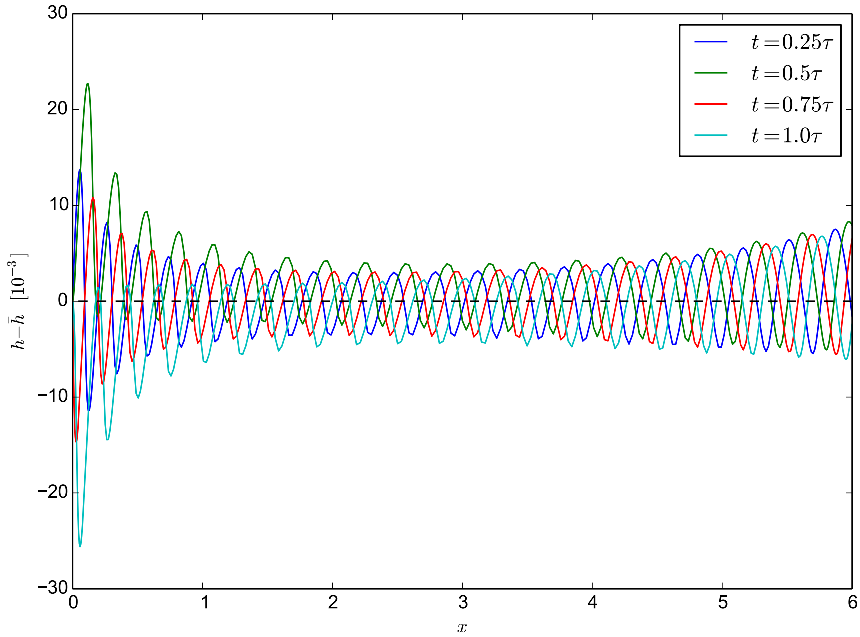

Figure 3.32: The difference between the ice thickness (h) at different points in the oscillatory cycle for simulation `ifNeGLDa`, with Glen's Law rheology and ice-ocean drag, compared to the thickness in steady state ($\bar{h}$) simulation `ssNeGLDad0`. The results are from after the ice shelf has reached a statistically-steady state. In the legend of this plot, τ refers to the oscillatory period.

thickness perturbation was found to be

$$\frac{D\tilde{h}}{Dt} \approx \frac{\tilde{u}}{\bar{u}} \left(\lambda \bar{m} + \frac{\chi^3}{8\xi^3} \bar{h}^4 \right) - \frac{\chi^3 \bar{h}^3}{2\xi^3} \tilde{h} - \frac{3\chi^3 \bar{h}^2}{8\xi^3} \tilde{h}^2, \tag{3.47}$$

for $\tilde{h} \ll \bar{h}$ and $\tilde{m} \approx 0$, analagous to the result in equation (3.44) for the Newtonian case. As before, the first term on the right hand side of this equation represents changes to the amount of time the ice spends exposed to thinning (which is caused by melting and stretching, represented by the first and second term in parentheses, respectively). The second term on the right hand side is the damping of the ripples caused by stretching, with damping rate $\chi^3 \bar{h}^3 / 2\xi^3$, while the third indicates the nonlinear rectification of the damping. This rectification means damping gives more significant thickness changes when $\tilde{h} > 0$ than when $\tilde{h} < 0$.

Simulation `ifGLJeDa` was run using Glen's Law, with results shown in figure 3.32. The most noticeable difference from previous simulations is more significant growth of the ripples towards the calving front. This is likely due to the damping term in equation (3.47) being smaller than that in the Newtonian case, in this region:

$$\frac{\chi^3\bar{h}^3}{2\xi} < \frac{\chi\bar{h}}{2\eta},$$

hence ripples are damped less by stretching with Glen's Law. This results in more net growth of the ripples after accounting for the melt feedback. Near the grounding line, the change in rheology had little effect on the outcome of the simulation. The ripples are slightly smaller in amplitude than before, but otherwise unchanged. The smaller ripple amplitude is due to the ice stretching less when subject to Glen's law than with Newtonian viscosity, as can be seen in figure 3.11. This can also be demonstrated comparing the stretch-driven thinning term in equations (3.44) and (3.47), with

$$\frac{\chi^3\bar{h}^4}{8\xi^3} < \frac{\chi\bar{h}^2}{4\eta}$$

everywhere except very near the grounding line.

Careful examination of the ripples near the grounding line in figure 3.32 shows the asymmetry is slightly more extreme than previously seen in simulations `ifNeJedand` and `ifNeJeda` (figures 3.23 and 3.25, respectively). The final term in equation (3.47) is larger than that in equation (3.44), indicating that the nonlinearity of the damping is greater than before. This is due to the cubic expression for stretching in equation (3.45), which means that stretching increases more with thickening than it reduces with thinning. Another result of this nonlinearity is that, overall, there will tend to be an increase in the rate of ice-stretching. This means ice will tend to flow slightly faster on average than in the steady-state simulation, resulting in less time spent exposed to thinning and thus causing a bias towards the ice being thicker towards the calving front.

3.5.3 Alternative Entrainment Parameterisation

Though it was seen in § 3.4.2 that results were insensitive to the choice of entrainment paramerisation for varying subglacial discharge, for completeness simulation `ifNeKoDa` was run with varying ice flux and the plume using the entrainment parameterisation of Kochergin (1987). Using the present non-dimensionalisation,

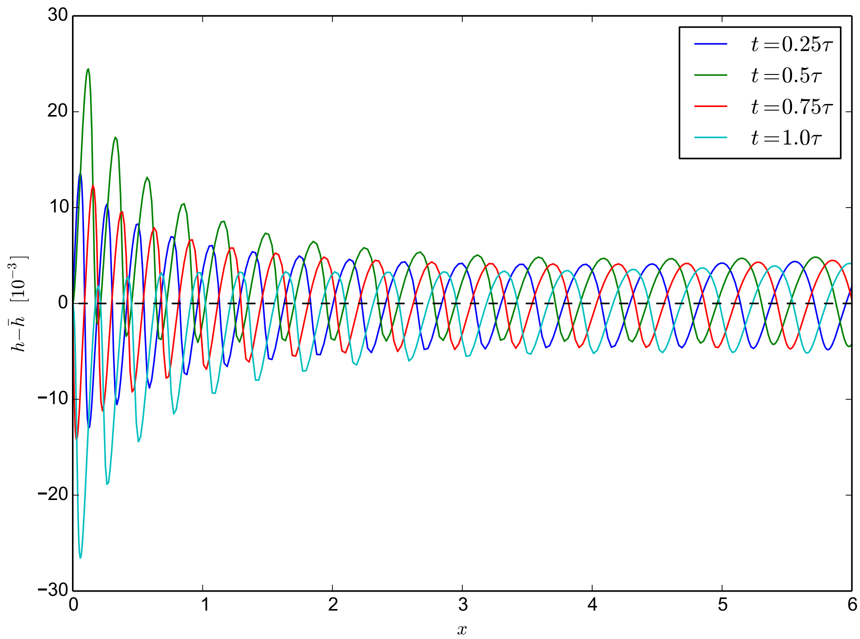

Figure 3.33: The difference between the ice thickness (h) at different points in the oscillatory cycle for simulation `ifNeKoDa` with varying ice flux and the plume entrainment parameterisation of Kochergin (1987) compared to the thickness in steady state ($\bar{h}$) simulation `ssNeKoDad0`. The results are from after the ice shelf has reached a statistically-steady state. In the legend of this plot, τ refers to the oscillatory period.

this parameterisation depends on the parameter δ and, for $\delta = 0$, it is undefined. However, the Kochergin (1987) approach is a parameterisation of entrainment due to stratified shear instability characterised by a Froude number, rather than the physical effects of gravity wave propagation. Here we suppress gravity waves by setting $\delta = 0$ in all parts of the code except for within the entrainment parameterisation where $\delta = 0.036$ as before to retain its influence on shear instability. Once again, there were minimal changes to the shape and magnitude of the ripples compared to the simulations using the parameterisation of Jenkins (1991) (see figure 3.33, as compared to figure 3.25).

3.5.4 Square Wave Forcing

To understand the fully nonlinear version of the results of § 2.4.3, simulation `ifNeJeDasw` was run where the sine term in equation (3.40) was replaced with a square wave. No Fourier transform of the forcing was performed here, so

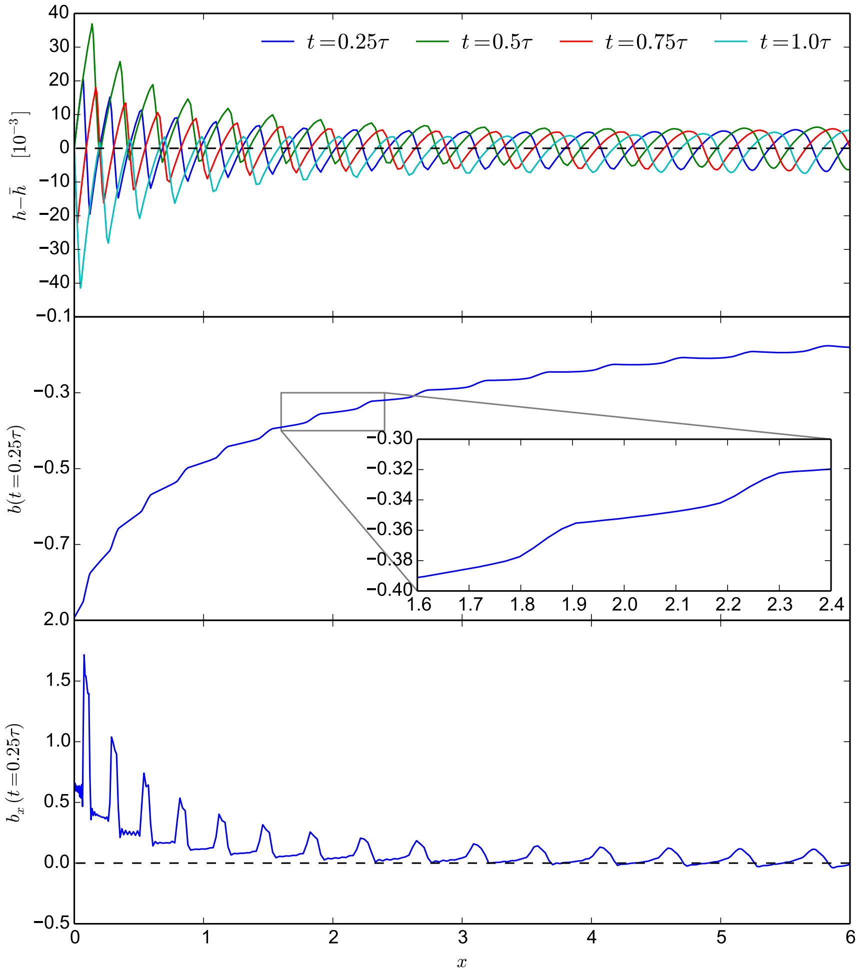

Figure 3.34: Upper: the difference between the ice thickness (h) at different points in the oscillatory cycle for simulation `ifNeJeDasw`, with ice flux varying according to a square-wave, compared to the thickness in steady state ($\bar{h}$) simulation `ssNeJeDad0`. The results are from after the ice shelf has reached a statistically-steady state. In the legend of this plot, τ refers to the oscillatory period. Middle: the total basal depth of the forced ice shelf at time $t = 0.25\tau$ into a seasonal cycle. An inset gives a zoomed-in view of the ripples. Lower: The basal slope of the ice shelf at time $t = 0.25\tau$. The sudden changes in slope near the grounding line cause some ringing when spectral differentiation is applied. Despite that, the numerical shelf and plume solver did fully converge.

smoothing was no longer needed to avoid ringing. For reasons of simplicity it was thus decided to leave out smoothing and use an ordinary square wave and equation (3.40) was replaced with

$$u_g(t) = \begin{cases} 1.5u_{g0}, & t \leq 0.5\tau \\ 0.5u_{g0}, & t > 0.5\tau \end{cases}. \tag{3.48}$$

The results of this simulation can be found in figure 3.34. The results are broadly comparable the linear case. The asymmetric perturbations to ice shelf slope noted in § 3.5.1 makes the plateaus slightly shallower than in figure 2.19 and closer to the observations of basal terraces by Dutrieux, Stewart, et al. (2014). Nonlinear effects smooth out some of the sharpness of the peaks as ice propagates downstream (compared to sharper peaks in figure 2.19), slightly reducing the differences between square wave and sinusoidal forcing towards the calving front. Nonetheless, terrace-like features persist.

As seen in the linear analysis, the size of the ripples produced by square wave forcing is larger than those produced by sinusoidal forcing. As before, this is because square-wave forcing results, on average, in the inflow velocity being perturbed further from the steady state value. The asymmetry in ripple thickness in figure 3.34 is more pronounced than was seen in figure 3.25. This is due to the larger ripple amplitude; the asymmetry in stretching becomes more pronounced the larger the perturbation from steady state thickness.

3.5.5 Sensitivity to Forcing Frequency and Amplitude

Simulation `ifNeJeDa` was rerun a number of times with different amplitude A and frequency ω for the ice flux forcing. The amplitude of the ice shelf ripples (either the first or the last) was found to scale linearly with the magnitude of the forcing (see figure 3.35). Performing a linear regression and extrapolating backwards to $A = 0$ gave amplitudes of 0.051 and 0.23 for the first and last ripples, respectively. Both of these are considered to be consistent with amplitudes of 0 within the error of the fit (which had standard deviation $\sigma = 0.037$ and $\sigma = 0.099$, respectively), supporting a scaling $h - \bar{h} \propto A$.

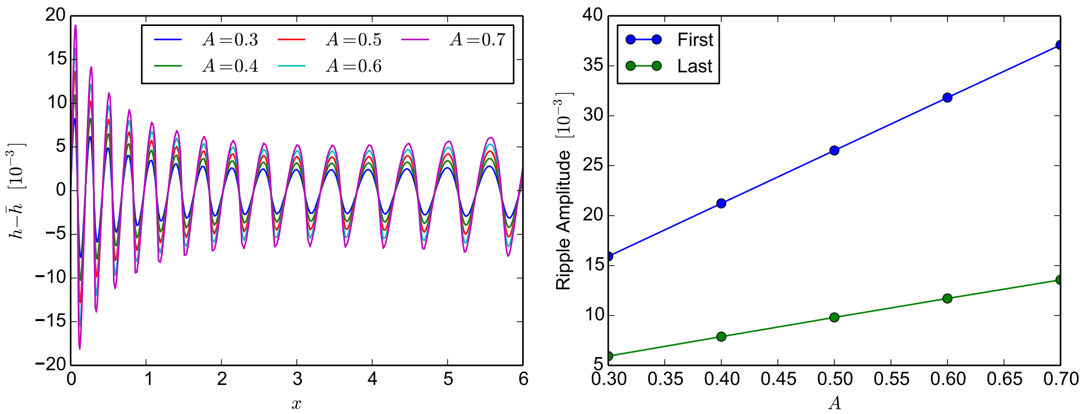

Figure 3.35: Response of ice shelf thickness perturbations to the amplitude of ice flux forcing A. Results are from a quarter of the way through a seasonal cycle, after the ice shelf has reached a statistically-steady state. Other than forcing amplitude, all simulation parameters are the same as in `ifNeJeDa`. Left: Ice thickness perturbations for each simulations. Right: Amplitude of the first and last ripples on the ice shelf as a function of the forcing amplitude.

The forcing frequency was also varied, in the same manner as in § 3.4.3, with the results plotted in figure 3.36. As in § 3.4.3, the amplitude of the ripples varies inversely with the inverse of the forcing frequency, as was expected from equation (2.37). However, the relationship between amplitude and ω^{-1} is slightly sublinear, the reason for which is not clear. The wave-number of the ripples is linearly related to the forcing frequency but, once again, extrapolating backwards to $\omega = 0$ gave nonzero values for k (-3.46 for the first ripple and 0.51 for the last). As before, error in the fit ($\sigma = 0.10$ and $\sigma = 0.038$, respectively) is inadequate to explain this and it is likely due to nonlinear behaviour at very low frequencies, leading to the relationship $k \propto (\omega - \omega_0)$ for moderate frequencies, with ω_0 controlled by the low-frequency limit.

3.6 Conclusions and Discussion of Geophysical Implications

The nonlinear simulations in this chapter produced results which were broadly in agreement with the linear analysis of Chapter 2. Oscillations in the subglacial discharge of 90% the mean value (ranging from $8.5 \times 10^{-4}\,\mathrm{m^2\,s^{-1}}$ to $1.6 \times 10^{-2}\,\mathrm{m^2\,s^{-1}}$,

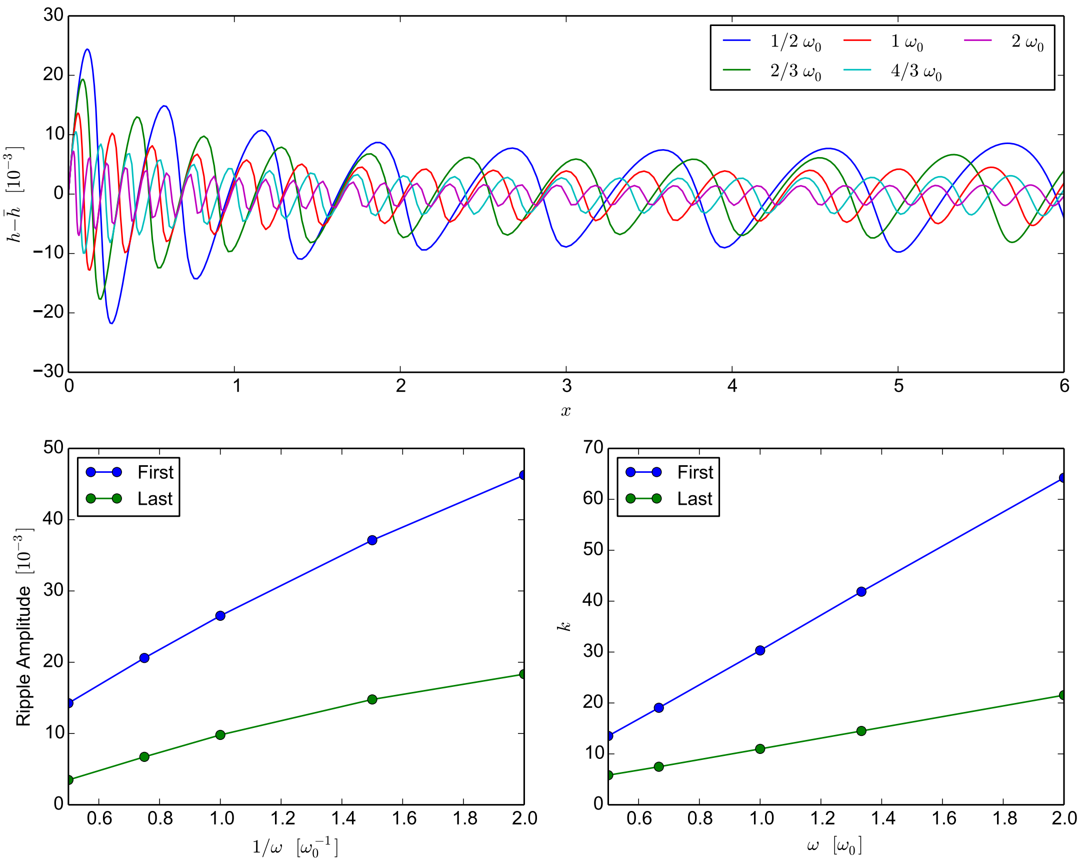

Figure 3.36: Response of ice shelf thickness perturbations to the frequency of ice flux forcing, ω. Results are from a quarter of the way through an oscillatory period, after the ice shelf has reached a statistically-steady state. Other than forcing frequency, all simulation parameters are the same as in `ifNeJeDa`. Upper: Ice thickness perturbations for each simulation. Lower left: Amplitude of the first and last ripples on the ice shelf as a function of the inverse forcing frequency. Lower right: Wave number k of the first and last ripple on the ice shelf as a function of the forcing frequency.

in physical units) produced ripples in the base of the ice shelf of amplitude $h - \bar{h} \sim 1\,\mathrm{m}$. This forcing also caused global oscillations in the ice shelf thickness. Unlike in the linear case, however, the ice shelf displayed a noticeable bias towards thickening, due to the sublinear relationship between upstream plume velocity (and hence melt rate) and subglacial discharge. Seasonal oscillations in the ice flux crossing the grounding line of 50% the mean value (with the ice velocity varying between $1.25\,\mathrm{km\,yr^{-1}}$ and $3.75\,\mathrm{km\,yr^{-1}}$, in physical units) resulted in the formation of ripples of amplitude $h - \bar{h} \sim 10\,\mathrm{m}$. Towards the end of the ice shelf, a feedback occurred whereby increased melting within these ripples caused them to grow into overdeepenings of depth $\sim 3\,\mathrm{m}$, which did not happen in the linear analysis. However, this feedback may be an artefact of setting hydrostatic pressure gradients to zero ($\delta = 0$) in those simulations.

The configuration of the simulations in this chapter was motivated by Pine Island Ice Shelf. However, in error, a non-standard value of the thermal transfer coefficient, Γ_T^*, from Dallaston et al. (2015) was used. This resulted in melt rates of $\sim 10\,\mathrm{m\,yr^{-1}}$, while actual values have been measured to be of order $100\,\mathrm{m\,yr^{-1}}$ near the grounding line (Dutrieux, Vaughan, et al., 2013). As such, the simulations in this chapter are effectively of a cold-cavity ice shelf with the geometry of PIIS.

The deviations in configuration between the simulations and the actual PIIS conditions makes it difficult to evaluate the geophysical implications of the results of this chapter. Had an appropriate melt rate been used then ripples generated by both subglacial discharge and ice flux variations would likely have been larger. Given that the ripples formed by varying subglacial discharge are two orders of magnitude smaller than the transverse channels observed under PIIS (Bindschadler, Vaughan, et al., 2011), it seems implausible that this mechanism could explain channel formation, even if the melt rate were to increase by an order of magnitude. The ice-flux forcing produced ripples able to grow into overdeepenings and that were only one order of magnitude smaller than the observed channels, however. On a long enough ice shelf they might be able to grow to the size of the observed channels on PIIS (although the observations placed these channels close to the grounding line). It may also be possible that a higher melt rate would allow them to form transverse channels; a higher background melt rate $\lambda\bar{m}$ would increase the growth rate of thickness perturbation according to equation (3.44) and increased melt perturbations $\lambda\tilde{m}$ would lead to stronger melt feedback. Sergienko (2013) found channel formation to be more significant in higher melt regimes and calculations by Bindschadler, Vaughan, et al. (2011) indicated that most thinning in the section of PIIS where transverse channels were observed was driven by melting rather than stretching. However, attempts to run simulations with higher melt rates were found to produce very strong gradients in plume thickness (when $\delta = 0$) which caused the solver to fail. Even the small ripples which were produced in these simulations would tend to alter the flexural stress, as described by Vaughan et al. (2012) for full-sized channels. This may lead the ice to more readily crack, reducing buttressing and thus increasing the rate of ice loss.

The ice flux forcing does, however, produce features which appear qualitatively similar to the basal terraces observed under PIG ice shelf by Dutrieux, Stewart, et al. (2014), especially when the ice is forced by a square wave (§ 3.5.4). The vertical separation between successive terraces is of order $\sim$ 10 m, comparable to the observations of Dutrieux, Stewart, et al. (2014) under the PIG ice shelf. However, the simulated terraces are a few kilometres in length, at order of magnitude larger than observations. This means that the slopes separating the terraces in figure 3.34 ($\sim 1°$) are much more gradual than those under Pine Island ($\sim 30°$). A higher frequency forcing, such as that provided by the spring-neap tidal cycle (Rosier et al., 2017), would generate ripples of the correct wavelength to agree with observations. If the melt rate were similar to that observed for PIIS then the terraces would likely be of the correct vertical scale as well. Note that a very large number of grid points would be needed to resolve features of that horizontal size, making such a simulation challenging.

Interactions between the ice shelf, plume, and seasonal variability could also have consequences for ocean circulation. Temporal variations in subglacial discharge result in lower melt rates and plume outflow from under the ice shelf than would be expected were the subglacial discharge at a constant, average value. This is due to the plume dynamics and is not related to coupling with the ice shelf. While ice flux variations can give rise to local deviations in the melt rate, the ice thickness perturbations don't display a noticeable thickening or thinning bias, indicating the average melt rate is not significantly altered. However, the changes to the ice shelf geometry affect the plume dynamics. This means that, on average, the volume flux of the plume increases by about $0.2m^2\,\mathrm{s}^{-1}$ (about 2%), as illustrated by figure 3.37, which would slightly strengthen the overturning cell underneath the ice shelf.

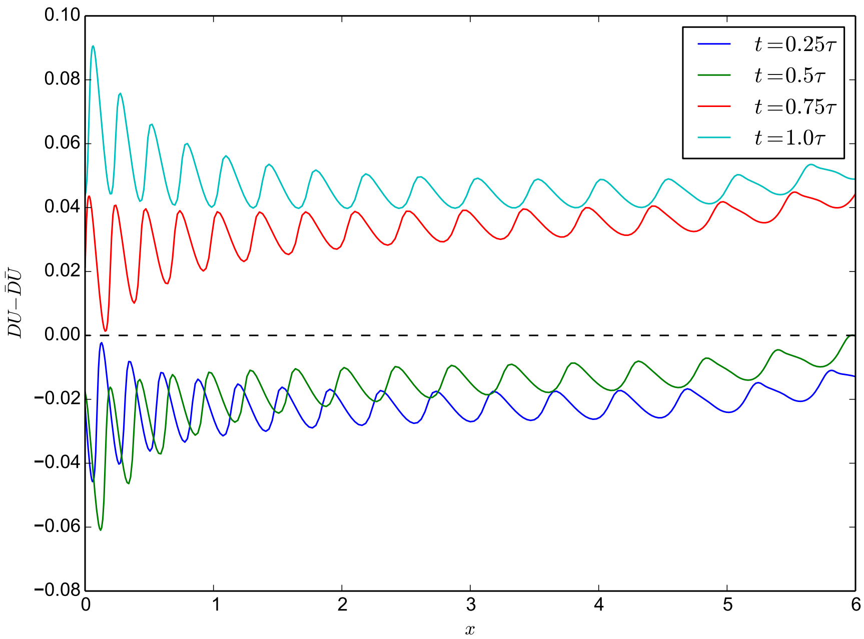

Figure 3.37: Perturbations to the volume flux (DU) relative to that in steady state ($\bar{D}\bar{U}$) at different points in the seasonal cycle of simulation `ifNeJeDa` with varying ice flux, after it has reached a statistically-steady state. The steady state values are taken from simulation `ssNeJedadn0`.

The simulations in this section made numerous simplifying assumptions. Some of these, such as the use of Newtonian ice rheology and a simple entrainment parameterisation, were tested and found not to alter the results. The assumption of 1-D flow would be appropriate for ice shelves which have weak variation in the y-direction, e.g. due to being very large or experiencing only limited drag from the side-walls. The melting temperature of ice and the ambient ocean properties were assumed to be uniform, whereas around Antarctica the ocean tends to be warmer at depth and the melting point also lower at depth. This would tend to concentrate melting near the grounding line of the ice, giving rise to a different steady-state thickness profile. In these simulations, melting was weak compared to stretching near the grounding line, but this balance might be altered with a more accurate treatment of varying ocean properties or with different thermal forcing that allows stronger melt. If so, it is possible that the melt-feedback seen in figure 3.27 could be initiated closer to the grounding line. Conversely, if ocean stratification and the depth dependence of freezing temperatures were accounted for then melting would tend to be lower towards the calving front, weakening the melt-feedback there.

The analysis has treated variation in subglacial discharge and ice flux independently. However, increases in subglacial discharge would be expected to correlate with increased ice flux and velocity (Bartholomew et al., 2010). Whereas higher ice flux gives rise to thicker ice, increased subglacial discharge would tend to thin the ice. Thus, these processes would counteract each other and the subglacial discharge variations would slightly reduce the magnitude of the ripples formed by the ice flux variations. In a regime where ice thinning is dominated by melting rather than stretching, then the countervailing forcing from subglacial discharge would likely be more severe and may strongly reduce the magnitude of the ripples that form.

4
Transverse Plume Velocity and the Coriolis Force

Contents

The 1-D plume model used in Chapters 2 and 3 neglected the Coriolis force. While this is a reasonable approximation for narrow ice shelves, past modelling has shown that the Coriolis force steers plume flow within subglacial cavities of wide ice shelves (Payne et al., 2007; Sergienko, 2013; Jordan et al., 2018, e.g.). The results of Chapter 3 did not exhibit ripples in ice shelves of the size seen by Bindschadler, Vaughan, et al. (2011), but the plume channelisation feedback may allow the small existing perturbations to grow to the size of those ripples. However, the 1-D plume model used was unable to capture this effect. To do so requires modelling the transverse plume velocity. Although 2-D plume models have been developed and applied before (e.g. Payne et al., 2007; Gladish et al., 2012; Sergienko, 2013), they are

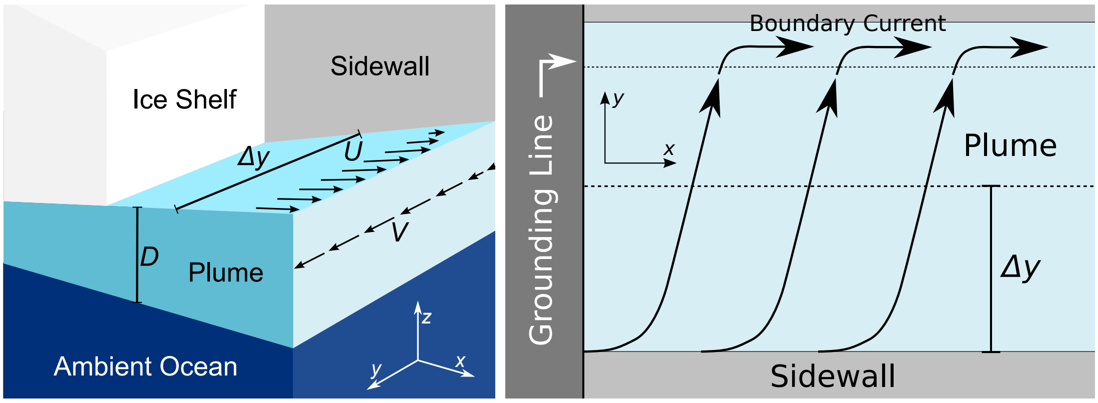

Figure 4.1: Left: A cartoon diagram of the horizontal integration performed on the plume equations. Arrows are shown for each component of the horizontal velocity, illustrating the assumptions (described in § 4.2) that the velocity is uniform over most of the width of the plume, except in a boundary layer near the side-wall. The model will be applied in the Southern hemisphere, but the illustration has been reflected in y for reasons of visual clarity. Right: A planar view of the horizontal integration, with velocity streamlines indicating the assumed flow profile of the plume. At the opposite sidewall, outside of the region Δy which is horizontally-integrated, the plume would turn and form a boundary current.

computationally expensive. Here a different approach is taken, with a “horizontally integrated” 1-D model, containing information on the transverse flow, developed instead. While Jenkins (2016) developed a 1-D Ekman layer model which included rotation, unlike the model described below it did not include advection or inertia. In addition to its computational simplicity, the horizontally-integrated model developed here provides a conceptual tool which can be useful in understanding of the results of observations and more complex simulations.

To develop such a horizontally-integrated model, the averaging approach that has proved useful for developing plume models (Ellison and Turner, 1959; Manins and Sawford, 1979) is adapted. In this model, illustrated in figure 4.1, the plume variables are averaged over both the thickness of the plume and also some lateral width Δy across the shelf. At the lower limit of this domain in y is a sidewall of the subglacial cavity, through which there can be no plume flow. The location of the upper limit is a parameter which can be adjusted, but it is assumed to be an open boundary through which transverse outflow is allowed. In order for transverse flow to begin there must be something to break the horizontal symmetry in the plume equations. This naturally arises due to the Coriolis force. Simulations (e.g. Millgate et al., 2013; Jordan et al., 2018) indicate that, in a rotational plume such as this, there would be a narrow longitudinal boundary current on the opposite side of the cavity. The presence of such a boundary current is assumed here, rather than being explicitly modelled; this current would act to drain the transverse flux of water out from under the ice shelf.

4.1 Modifications to the Plume Equations

To derive the horizontally integrated equations, one begins with the 2-D depth-integrated plume model in equation (3.6). However, the momentum balance is modified to capture the Coriolis force using the f-plane approximation with Coriolis parameter $f = 2\Omega \sin(\phi)$ (where Ω is the Earth's rotational frequency and ϕ is the latitude). In dimensionless form this becomes

$$\nabla \cdot \left(D\vec{U}U\right) = D(\rho_a - \rho)\left(b_x - \delta D_x\right) + \nu\nabla \cdot (D\nabla U) - \mu|\vec{U}|U + \frac{\delta D^2}{2}\rho_x + \Phi DV, \tag{4.1a}$$

$$\nabla \cdot \left(D\vec{U}V\right) = D(\rho_a - \rho)\left(b_y - \delta D_y\right) + \nu\nabla \cdot (D\nabla V) - \mu|\vec{U}|V + \frac{\delta D^2}{2}\rho_y - \Phi DU. \tag{4.1b}$$

Here, $\Phi \equiv f x_0/U_0$ is a dimensionless parameter, corresponding to the inverse Rossby number, and all other symbols were defined in Chapters 1 and 3. Using the scales described in the previous chapter, a typical value of Φ for an Antarctic ice shelf is -9.94, indicating largely geostrophic flow. Coriolis forces do not play a significant role in the ice shelf, where the Ekman number is large.

The plume variables are assumed to be separable in x and y, with the forms

$$D(x, y) = \hat{D}(x) f_D(y), \quad U(x, y) = \hat{U}(x) f_U(y), \quad \dots \tag{4.2}$$

and similar for V, T, and S. As in Chapter 3, the temperature and salinity are offset such that the temperature and salinity difference are zero for ambient conditions, although the results presented hold regardless of the offset. A width-averaging operator, represented by an over-bar, is defined according to

$$\overline{G} = \frac{1}{\Delta y}\int_{y_1}^{y_2} G(y) dy, \tag{4.3}$$

where G is an arbitrary y-dependent variable and $\Delta y = y_2 - y_1$. The shape functions $f(y)$ are defined such that

$$\overline{f_D} = 1, \quad \overline{f_U} = 1, \quad \ldots$$

There is no general way to relate $\widehat{|\vec{U}|}(x)$ to $\hat{U}(x)$ and $\hat{V}(x)$, so instead it is treated as an independent variable with its own shape function:

$$|\vec{U}(x,y)| = \widehat{|\vec{U}|}(x) f_{|\vec{U}|}(y). \tag{4.4}$$

However, $\widehat{|\vec{U}|} = \sqrt{\hat{U}^2 + \hat{V}^2}$ is exactly true if $f_U(y) = f_V(y)$ or approximately true if $U \gg V$ or $V \gg U$.

The relationships in equations (4.2) and (4.4) were substituted into the plume equations (3.6) and (4.1). For simplicity, the ambient conditions were assumed to be uniform and lateral variations in ice shelf thickness were neglected so that b was a function of x and t only. Integrating the resulting equations from y_1 to y_2, then dividing by Δy, gives the results below (hats have been dropped from the x-dependent variables for convenience going forward, with any y-dependence explicitly specified).

$$\alpha_{DU} \frac{d}{dx}(DU) + \left. \frac{f_D f_V}{\Delta y} \right|_{y_1}^{y_2} DV = \overline{e} + \overline{m}, \tag{4.5a}$$

$$\begin{aligned} \alpha_{DU^2} \frac{d}{dx}\left(DU^2\right) + \left. \frac{f_D f_U f_V}{\Delta y} \right|_{y_1}^{y_2} DUV = {} & D\rho_a \frac{d}{dx}\left(b - \delta\alpha_{D^2} D\right) \\ & - D\left(\overline{\rho}\frac{db}{dx} - \delta\alpha_{D^2}\tilde{\rho}\frac{dD}{dx}\right) \\ & + \nu\alpha_{DU}\frac{d}{dx}\left(D\frac{dU}{dx}\right) + \nu \left. \frac{DU}{\Delta y} f_D f_U' \right|_{y_1}^{y_2} \\ & - \mu\alpha_{|\vec{U}|U}|\vec{U}|U + \frac{\delta\alpha_{D^2}D^2}{2}\frac{d\tilde{\rho}}{dx} + \Phi\alpha_{DV}DV, \end{aligned} \tag{4.5b}$$

$$\begin{aligned} \alpha_{DUV}\frac{d}{dx}(DUV) + \left. \frac{f_D f_V^2}{\Delta y} \right|_{y_1}^{y_2} DV^2 = {} & \nu\alpha_{DV}\frac{d}{dx}\left(D\frac{dV}{dx}\right) + \nu \left. \frac{DV}{\Delta y} f_D f_V' \right|_{y_1}^{y_2} \\ & - \mu\alpha_{|\vec{U}|V}|\vec{U}|V - \left. \frac{\delta D^2}{2\Delta y} f_D^2 [\rho_a - \rho(x,y)] \right|_{y_1}^{y_2} \\ & - \Phi\alpha_{DU}DU, \end{aligned} \tag{4.5c}$$

$$\alpha_{DUS}\frac{d}{dx}(DUS) + \left.\frac{f_D f_S f_V}{\Delta y}\right|_{y_1}^{y_2} DSV = \overline{e}S_a + \nu\alpha_{DS}\frac{d}{dx}\left(D\frac{dS}{dx}\right) + \nu\left.\frac{DS}{\Delta y}f_D f_S'\right|_{y_1}^{y_2} + \overline{m}S_m - \overline{\gamma_S(S-S_m)}, \tag{4.5d}$$

$$\alpha_{DUT}\frac{d}{dx}(DUT) + \left.\frac{f_D f_T f_V}{\Delta y}\right|_{y_1}^{y_2} DTV = \overline{e}T_a + \nu\alpha_{DT}\frac{d}{dx}\left(D\frac{dT}{dx}\right) + \nu\left.\frac{DT}{\Delta y}f_D f_T'\right|_{y_1}^{y_2} + \overline{m}T_m - \overline{\gamma_T(T-T_m)}, \tag{4.5e}$$

with the constants involving α defined below. Capturing transverse diffusion requires knowledge of $f_U' = df_U/dy$, $f_V' = df_V/dy$, etc. This derivation assumes the linear equation of state given in equation (1.10), for which

$$\overline{\rho} = \rho_{\text{ref}}[1 + \beta_S(\alpha_{DS}S - S_{\text{ref}}) - \beta_T(\alpha_{DT}T - T_{\text{ref}})], \tag{4.6}$$

and

$$\tilde{\rho} = \rho_{\text{ref}}[1 + \beta_S(\tilde{\alpha}_{DS}S - S_{\text{ref}}) - \beta_T(\tilde{\alpha}_{DT}T - T_{\text{ref}})]. \tag{4.7}$$

When using the Jenkins (1991) entrainment parameterisation, $\overline{e}$ takes the same form as equation (1.11). The one-equation melt formulation of equation (2.1) becomes

$$\overline{m} = \zeta_1\zeta_2|\vec{U}|(\alpha_{|\vec{U}|T}T - T_m), \tag{4.8}$$

when horizontally integrated. The ice is assumed to be impermeable to salt, meaning $\overline{\gamma_S(S-S_m)} = \overline{m}S_m = 0$. After horizontal integration, the thermal transfer term becomes

$$\overline{\gamma_T(T-T_m)} = \zeta_1|\vec{U}|(\alpha_{|\vec{U}|T}T - T_m). \tag{4.9}$$

These parameterisations are used throughout this chapter. The α coefficients in these equations contain information on the transverse shape of the plume variables and are defined as

$$\begin{aligned}
&\alpha_{DU} = \overline{f_D f_U}, && \alpha_{DU^2} = \overline{f_D f_U^2}, && \alpha_{D^2} = \overline{f_D^2},\\
&\alpha_{DV} = \overline{f_D f_V}, && \alpha_{DUV} = \overline{f_D f_U f_V}, && \alpha_{|\vec{U}|V} = \overline{f_{|\vec{U}|} f_V},\\
&\alpha_{|\vec{U}|U} = \overline{f_{|\vec{U}|} f_U}, && \alpha_{DUS} = \overline{f_D f_U f_S}, && \alpha_{DUT} = \overline{f_D f_U f_T},\\
&\alpha_{|\vec{U}|T} = \overline{f_{|\vec{U}|} f_T}, && \alpha_{DS} = \overline{f_D f_S}, && \alpha_{DT} = \overline{f_D f_T},\\
&\tilde{\alpha}_{DS} = \frac{\overline{f_D^2 f_S}}{\alpha_{D^2}}, && \tilde{\alpha}_{DT} = \frac{\overline{f_D^2 f_T}}{\alpha_{D^2}}.
\end{aligned} \tag{4.10}$$

The second term on the left hand side of equations (4.5a)–(4.5e) represents transport via lateral inflow and outflow from the region of integration. The terms on the right hand side containing y-gradients represent the depth-integrated viscous shear at the lateral boundaries and the diffusive flux of scalar quantities in and out of the integration region. To determine these values and those in equation (4.10) requires further assumptions about the transverse profile of the plume (in the same way that interfacial fluxes are parameterised when deriving a plume model by depth integration).

4.2 Solving for a Steady, Uniform Plume

Some basic insight into the behaviour of this model can be gained by making various simplifying assumptions. First, diffusion is neglected ($\nu \approx 0$) so that this becomes an initial value problem which can easily be integrated numerically from the grounding line. The lower limit of the horizontal integration, y_1, was taken to correspond to a side-wall of the subglacial cavity, meaning there is no inflow here. All plume variables were assumed to be approximately uniform across the integration width, including at the lateral boundary $y = y_2$. For V and U there would be a narrow boundary layer near the sidewall where there is a transition from zero-velocity to the width-averaged velocity, as illustrated in figure 4.1. This boundary layer is assumed to be sufficiently narrow not to contribute significantly to integrals when taking average values or computing the α terms.

With these assumptions, all α values are approximately equal to 1, $f_D(y_1) \approx f_S(y_1) \approx f_T(y_1) \approx 1$, $f_U(y_1) \approx f_V(y_1) \approx 0$, $f_D(y_2) \approx f_U(y_2) \approx f_V(y_2) \approx f_S(y_2) \approx f_T(y_2) \approx 1$, and $f'_U(y_2) \approx f'_V(y_2) \approx f'_S(y_2) \approx f'_T(y_2) \approx 0$. These assumptions are sufficient to close the model. Under these conditions, the term involving δ in equation (4.5c) goes to zero because $f_D^2(y_2) \approx f_D^2(y_1)$. The same scales and parameter values were used as in Chapter 3. Initial conditions at the grounding line ($x = 0$) were set to $D = \epsilon$, $U = Q_g/\epsilon$, $V = 0$, $S = S_m$, and $T = T_m$ (where ϵ is some small value and $Q_g = 10^{-3}$ is the subglacial discharge), corresponding to imposing fresh subglacial discharge at the melting temperature, with negligible

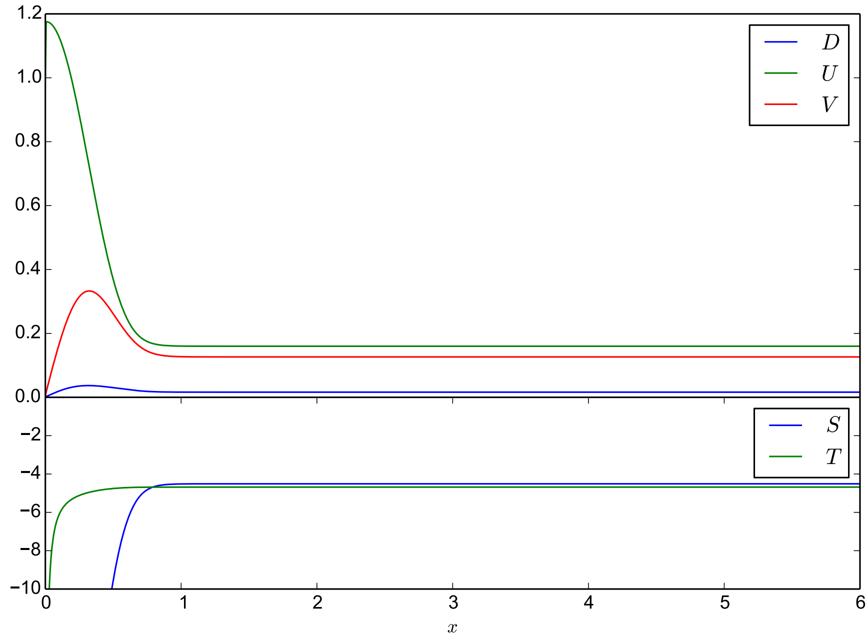

Figure 4.2: Results of solving the initial value problem provided by the dimensionless horizontally integrated plume equations without diffusion. The ice shelf has a constant basal slope $b_x = 0.2$ and the plume variables are taken to be approximately uniform across the width of integration, except for a narrow boundary layer where $V \to 0$ and $U \to 0$ at the sidewall.

lateral momentum. For initial illustration, the ice shelf was set to have a constant basal slope of $b_x = 0.2$ (a moderate slope in between those typical near the grounding line and those near the calving front) and the plume width was set to $\Delta y = 0.05$ (a narrow plume, 690 m wide). Using the `lsoda` Adams method initial value problem solver in SciPy (Jones et al., 2001), the system of equations was integrated to give the results in figure 4.2.

There are clearly two distinct regimes to this solution. Near the grounding line, a transient regime is characterised by initial growth of plume thickness and transverse velocity V. Longitudinal velocity U, however, declines as the Coriolis force rotates the plume flow into a cross-slope direction. Eventually the high value of V causes both volume and transverse momentum to be drained away via the outflow, until a new balance is obtained. At this point, the plume transitions to an asymptotic state where the variables no longer change downstream. Examining the relative magnitude of different terms in equation (4.5) shows that, in this regime, forcing terms (entrainment, melting, buoyancy, Coriolis force, and drag) are balanced by lateral drainage of the plume at y_2. This can be expressed as

$$f_D(y_2)f_V(y_2)DV = E_0|\vec{U}||b_x|\Delta y + \left[\zeta_1\zeta_2|\vec{U}|(\alpha_{|\vec{U}|T}T - T_m)\Delta y\right] \tag{4.11a}$$

$$f_D(y_2)f_U(y_2)f_V(y_2)DUV = (D[\rho_a - \overline{\rho}]b_x + \Phi\alpha_{DV}DV - \mu\alpha_{|\vec{U}|U}|\vec{U}|U)\Delta y \tag{4.11b}$$

$$f_D(y_2)f_V(y_2)^2DV^2 = (-\Phi\alpha_{DU}DU - \mu\alpha_{|\vec{U}|V}|\vec{U}|V)\Delta y \tag{4.11c}$$

$$f_D(y_2)f_S(y_2)f_V(y_2)DSV = (E_0|\vec{U}||b_x|S_a + \zeta_1\zeta_2|\vec{U}|[\alpha_{|\vec{U}|T}T - T_m]S_m)\Delta y \tag{4.11d}$$

$$f_D(y_2)f_T(y_2)f_V(y_2)DTV = (E_0|\vec{U}||b_x|T_a - \zeta_1|\vec{U}|[1 - \zeta_2T_m][\alpha_{|\vec{U}|T}T - T_m])\Delta y. \tag{4.11e}$$

Terms indicating the shape function value at the upper boundary, such as $f_D(y_2)$, are retained for generality. The melt term in square brackets in the continuity equation (4.11a) is much smaller than the others and can, in certain situations, be ignored. This convention was not used for square brackets in any of the other equations.

Dividing equations (4.11d) and (4.11e) by equation (4.11a), the asymptotic temperature and salinity can be solved for exactly:

$$T = \frac{-A \pm \sqrt{A^2 + 4\zeta_1\zeta_2\alpha_{|\vec{U}|T}f_T(y_2)(E_0|b_x|T_a + \zeta_1T_m - \zeta_1\zeta_2T_m^2)}}{2\zeta_1\zeta_2\alpha_{|\vec{U}|T}f_T(y_2)}, \tag{4.12}$$

$$S = \frac{E_0|b_x|S_a + \zeta_1\zeta_2(\alpha_{|\vec{U}|T}T - T_m)S_m}{f_S(y_2)(E_0|b_x| + \zeta_1\zeta_2[\alpha_{|\vec{U}|T}T - T_m])}, \tag{4.13}$$

where $A = E_0|b_x|f_T(y_2) - \zeta_1\zeta_2T_m[f_T(y_2) + \alpha_{|\vec{U}|T}] + \alpha_{|\vec{U}|T}\zeta_1$. Assuming $\overline{e} \gg \overline{m}$ in equation (4.11a), then D can be eliminated from equation (4.11c) to express the transverse velocity in terms of the longitudinal velocity according to

$$V = \sqrt{\frac{-E_0\Phi U\Delta y|b_x|\alpha_{DU}}{f_D(y_2)f_V(y_2)[E_0f_V(y_2)|b_x| + \mu\alpha_{|\vec{U}|V}]}}. \tag{4.14}$$

This result is only valid in the Southern hemisphere, where $\Phi < 0$. In the Northern hemisphere the entire model is invalid and would need to be reformulated around the opposite sidewall.

Meanwhile, using equations (4.11a) and (4.12)–(4.14) to eliminate DV, T, and S, the longitudinal velocity can be expressed as the cubic equation

$$\begin{aligned}0 = f_D(y_2)^2 f_V(y_2)^2 \left(f_U(y_2) + \frac{\mu\alpha_{|\vec{U}|U}}{E_0|b_x|}\right)^2 U^3 \\ - 2f_D(y_2)f_V(y_2)\left(f_U(y_2) + \frac{\mu\alpha_{|\vec{U}|U}}{E_0|b_x|}\right)\Phi\Delta y\alpha_{DV}U^2 + \Phi^2\Delta y^2\alpha_{DV}^2 U \\ + \frac{(\rho_a - \overline{\rho})^2|b_x|\Delta y f_D(y_2)f_V(y_2)[E_0 f_V(y_2)|b_x| + \mu\alpha_{|\vec{U}|V}]}{E_0\Phi\alpha_{DU}}. \end{aligned} \tag{4.15}$$

The plume thickness can not be obtained in general terms without knowing something about the transverse structure of the velocity components so that $|\vec{U}|$ can be calculated. If that value is known then

$$D = \frac{E_0|\vec{U}||b_x|\Delta y}{f_D(y_2)f_V(y_2)V}, \tag{4.16}$$

where V is determined via equation (4.14). When making the assumption that $f_U(y) = f_V(y)$, as done to calculate the results in figure 4.2, $|\vec{U}| = \sqrt{U^2+V^2}$ and equation (4.16) becomes

$$D = E_0|b_x|\Delta y\sqrt{1 - \frac{E_0 b_x + \mu}{E_0\Phi\Delta y|b_x|}U}.$$

These expressions allow the asymptotic state of the plume to be easily calculated for a wide range of parameter values. The results of doing so can be seen in figures 4.3 and 4.4, where those parameters not being varied have the same values as used to produce figure 4.2. Asymptotic salinity and temperature only depend on the shelf slope, so are only plotted for that parameter (figure 4.3). Also plotted are the asymptotic results obtained by numerically integrating the full plume equation, which agree well with the analytic predictions. These could not be found for strongly negative values of the Coriolis parameter or larger values of Δy. In these cases the plume would transition from super- to sub-critical flow and develop a shock, causing the integration to fail. Including diffusion in the equations would alleviate this problem by smoothing out the shock. The initial conditions of the plume at the grounding line do not alter the asymptotic state, only affecting the

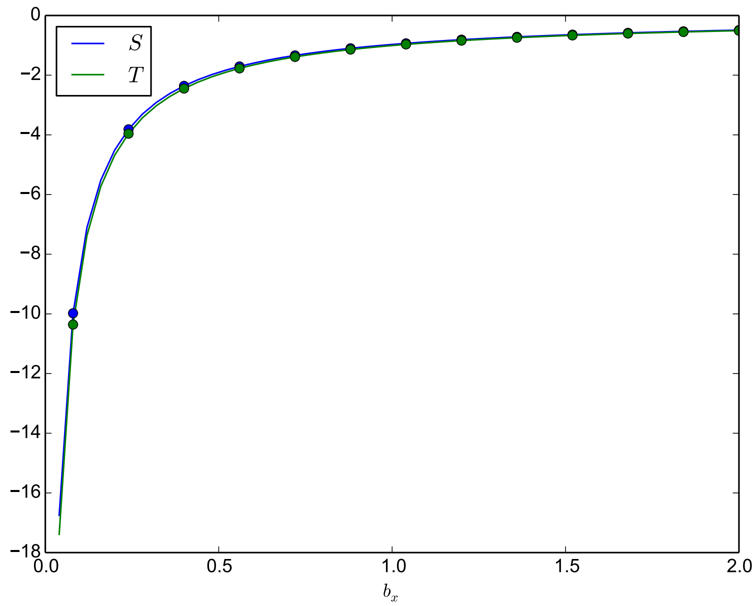

Figure 4.3: Predicted (lines) and numerically-determined (circles) asymptotic values of salinty S and temperature T for the horizontally-integrated plume equations with different shelf slopes b_x. Both variables are offset such that their ambient values are 0.

initial transient region. This can be seen from equations (4.12)–(4.16), which have no dependence on initial conditions.

Salinity and temperature both increase with the shelf slope (figure 4.3), as this leads to greater entrainment and thus brings them closer to the ambient values. The increased entrainment also causes the plume thickness to grow with shelf slope (figure 4.4a, blue line). Thicker plumes are less affected by drag forces, allowing the transverse velocity to increase with slope as well (figure 4.4a, red line). Initially, increased buoyancy forces causes the longitudinal velocity to grow with the slope, but eventually interactions with drag and the Coriolis force cause it to gradually slow (figure 4.4a, green line). Increasing the magnitude of the Coriolis parameter (i.e., increasing $|\Phi|$) tends to reduce the magnitude of the longitudinal velocity and the plume thickness (figure 4.4b). The transverse velocity, on the other hand, increases with $|\Phi|$ as the plume is more strongly rotated. This strengthens the outflow, explaining the decreases in D and U due to enhanced export of plume mass and momentum. Increases to the drag impede the flow and results in a

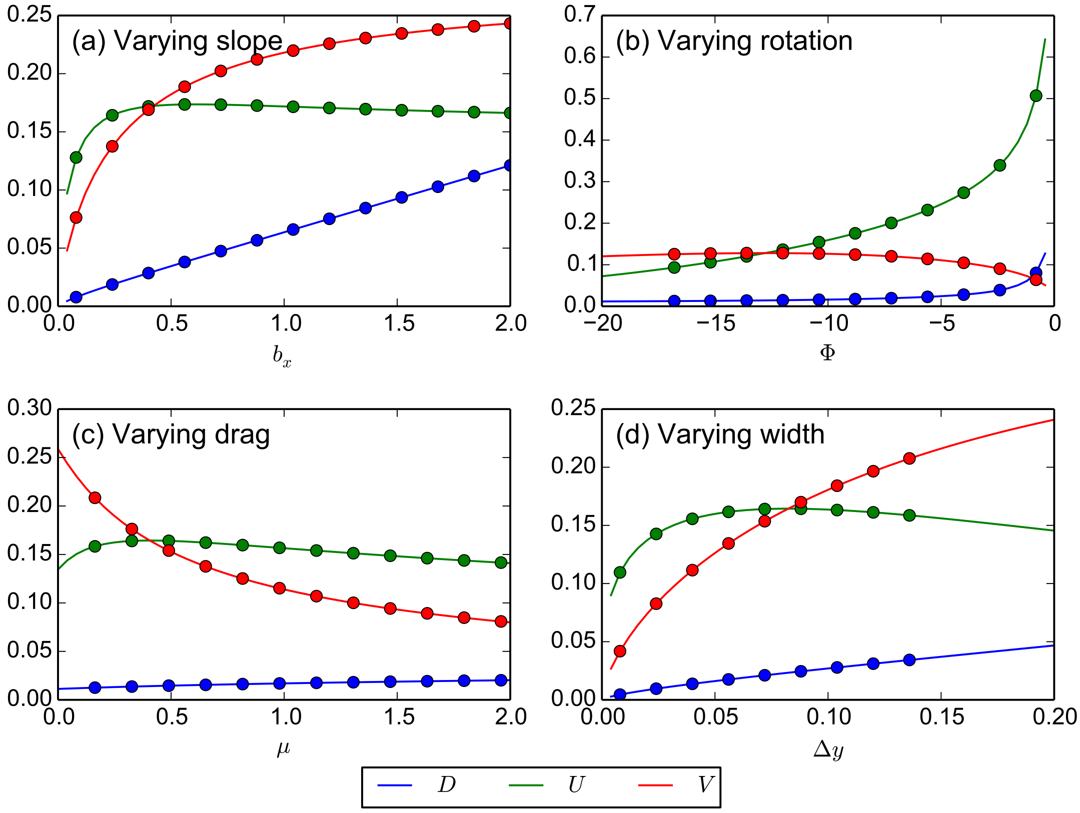

Figure 4.4: Predicted (lines) and numerically-determined (circles) asymptotic values for the horizontally-integrated plume equations with different parameter choices. Parameters not being varied are fixed to the values used to produce figure 4.2. Note that $\Phi < 0$ in panel (b).

smaller transverse velocity, thus compressing the plume and increasing its thickness. Initially drag causes the longitudinal velocity to grow as it disrupts the rotation of the plume into the transverse direction. Even when U begins to decline, the longitudinal velocity does so more gradually than the transverse velocity (which is monotonic decreasing with μ). The changes to the variable values with Δy reflect the plume's transverse structure, which is discussed in § 4.3.

The results of equations (4.12)–(4.16) were calculated assuming a constant basal slope of the ice shelf. However, it was found that the values of plume variables calculated by numerical integration using an ice shelf with a gradually varying slope can be approximated well using the local slope value in the analytic equations. This can be seen in figure 4.5, where the slope is set according to the analytic ice shelf thickness of equation (2.21) for $X = 7$. There is good agreement between

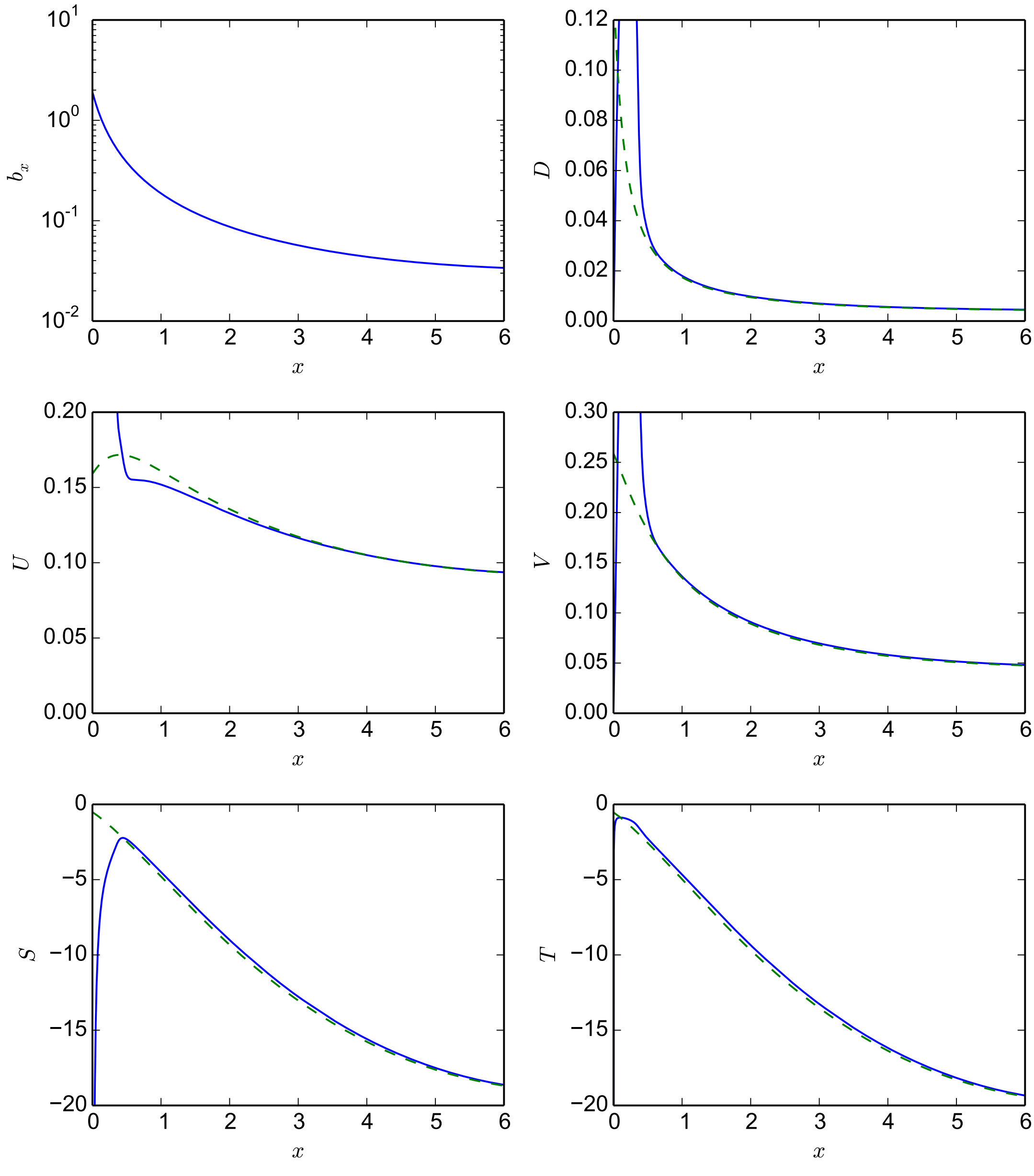

Figure 4.5: Comparison of numerically determined (blue solid lines) and analytically predicted (green dashed lines) values for horizontally-integrated plume variables when the ice shelf slope varies along its length according to the analytic solution in equation (2.21), calculated with $X = 7$. The upper-left plot indicates the prescribed slope of the ice shelf at each location. All other parameters were the same as those used to calculate the results in figure 4.2. Plot ranges are chosen to display the asymptotic portion of the plume and therefore cut off portions of the numerical solution in the transient region.

the numerical results and the analytic predictions after the plume approaches its asymptotic state at around $x \sim 0.5$, which is commensurate with the scale for transient adjustment in figure 4.2.

4.3 Asymptotic Transverse Structure

Although the previous section assumed the plume variables were approximately uniform in the transverse direction, the results in figure 4.4 ultimately prove inconsistent with this assumption. Panel (d) of figure 4.4 shows that the thickness and both components of the velocity of the plume vary as the integration width is increased. This indicates a nonuniform transverse structure to the plume, because width-averaged variables vary with y. The width-averaged thickness, D, appears to grow linearly with Δy, while the relationships for longitudinal and transverse velocity are less clear. A resolution to this issue is explored in the following two subsections, where an IVP is derived which can be solved for f_D, f_U, and f_V. However, as an intermediate step it is first useful to analyse the limits for the $f_D \approx f_U \approx f_V \approx 1$ case to build insight.

4.3.1 Limit Analysis

If there is a power-law relationship between the variables and Δy, then the slope of a log-log plot can be used to determine the exponent (figure 4.6a). The derivative $d\log(D)/d\log(\Delta y)$ was evaluated using the Chebyshev pseudo-spectral method (see § 3.1.1), along with similar derivatives for U and V, showing two limiting cases for the transverse plume structure (figure 4.6b). Salinity and temperature do not depend on Δy and thus were not analysed. For $\Delta y \lesssim 10^{-3}$,

$$D \propto \Delta y^{2/3}, \quad U \propto \Delta y^{1/3}, \quad V \propto \Delta y^{2/3},$$

while for $\Delta y \gtrsim 1$,

$$D \propto \Delta y, \quad U \propto \Delta y^{-1}, \quad V \propto \Delta y^{0}.$$

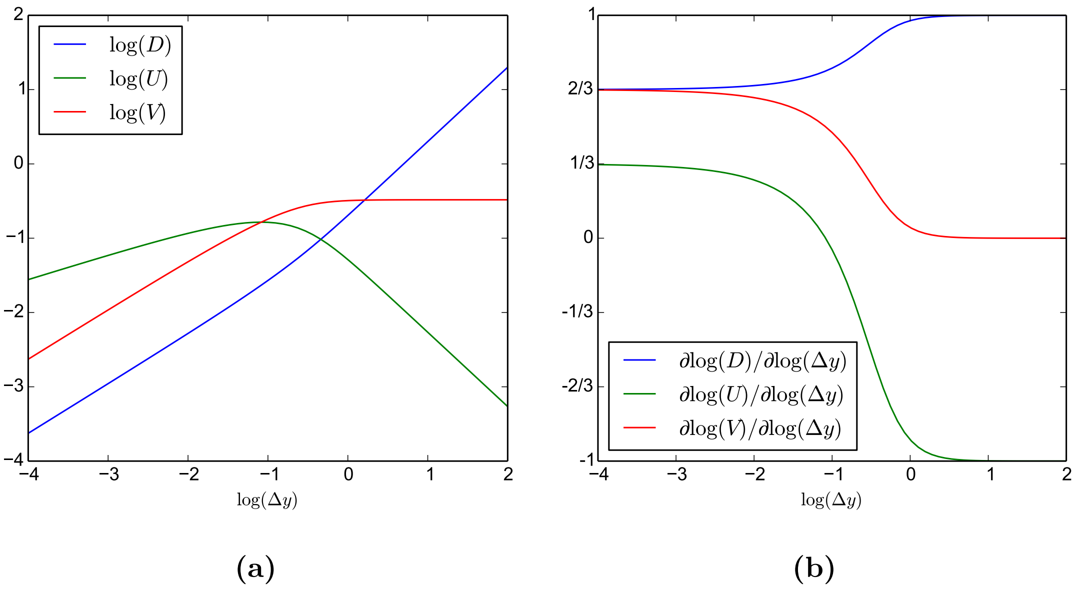

Figure 4.6: (a) Log-log plot of how asymptotic values for plume variables depend on the width over which they are horizontally integrated. (b) The derivative of the logarithm of plume variables with-respect-to to the logarithm of Δy. This reveals the power laws which these variables obey at different limits for Δy.

The lower limit corresponds to a plume width of 13.8 m when the longitudinal length-scale is $x_0 = 13.8\,\text{km}$. At this scale it is questionable if the plume model or the balances in equation (4.11) would continue to hold. Thus, it is considered unlikely that this limit corresponds to physical boundary-layer behaviour.

The upper limit remains of interest, however. At this point it is useful to adopt slightly altered notation with which to express the transverse shape of the plume in an un-normalised fashioned. Define $F_D(x, y) = D(x, \Delta y) f_D(y, \Delta y)$, where $D(x, \Delta y)$ is the average thickness over Δy and $f_D(y, \Delta y)$ has been normalised over the same range. The same procedure can be used for the other plume variables. Using

$$D(x, \Delta y) = \frac{1}{\Delta y} \int_0^{\Delta y} F_D(x, y) dy \quad \Rightarrow \quad \int_0^{\Delta y} F_D(x, y) dy = \Delta y D(x, \Delta y)$$

and differentiating with respect to Δy, it can then be shown that

$$F_D(x, y) = y \left. \frac{\partial D(x, \Delta y)}{\partial \Delta y} \right|_{\Delta y = y} + D(x, \Delta y = y). \tag{4.17}$$

With the power law $D(x, \Delta y) = B_D(x) \Delta y^n$, where $B_D(x) = D(x, \Delta y = 1)$, this gives the result

$$F_D(x, y) = (n + 1) B_D(x) y^n. \tag{4.18}$$

For the upper limit of plume width, this means

$$F_D = 2B_D y, \quad F_V = B_V \tag{4.19}$$

However, there is a singularity for $n = -1$, as was the case for longitudinal velocity. In this case one finds

$$F_U = B_U \delta(y), \tag{4.20}$$

where $\delta(y)$ is the Dirac delta function. Results for F_D, F_U, etc. can be normalised for a given Δy to get the corresponding shape functions f_D, f_U, etc. with which to calculate $|\vec{U}|$ and the α values in equation (4.10). However, the singularity at 0 caused by the Dirac delta means not all of these results converge.

It is worth taking a step back to consider what the result of F_U means physically. In effect, it is saying that all longitudinal flow is confined to a narrow layer next to the side-wall of the cavity, the width of which is much less than 1. This causes the width-averaged value of U to be inversely related to Δy, analogous to the $1/r$ drop-off in electric field strength from a line of charge. However, figure 4.4d clearly shows that the structure of the longitudinal velocity at this scale is not actually a delta function. Rather, F_U is just some function which is approximately zero when $y \gtrsim 1$. It could, for example, be a box function of width less than one. In the electrostatic analogy, this corresponds to a finite but compact charge being approximated as a point source sufficiently far away. However, the exact value of the α coefficients will depend on this structure.

4.3.2 A Transverse Initial Value Problem

While the previous section gives insight into the transverse structure of the plume, it can not be taken to be more than qualitatively accurate. In particular, its results were found by looking at how the plume's average values changed as calculated when assuming it to be uniform. These were inconsistent assumptions. However, the approach of § 4.3.1 indicates it may be useful to consider the transverse structure in more detail. Realising that, in the asymptotic region, gradients in

x are approximately zero while gradients in y are still significant, the 2-D plume equations (3.6) and (4.1) can be simplified to become a system of ODEs in the transverse direction. Once again assuming that diffusion is negligible, the following initial value problem is obtained:

$$\frac{d}{dy}(DV) = e + m \tag{4.21a}$$

$$\frac{d}{dy}(DVU) = D(\rho_a - \rho)b_x - \mu|\vec{U}|U + \Phi DV \tag{4.21b}$$

$$\frac{d}{dy}(DV^2) = -D(\rho_a - \rho)\delta D_y - \mu|\vec{U}|V + \frac{\delta D^2}{2}\rho_y - \Phi DU \tag{4.21c}$$

$$\frac{d}{dy}(DVS) = eS_a + mS_m - \gamma_s(S - S_m) \tag{4.21d}$$

$$\frac{d}{dy}(DVT) = eT_a + mT_m - \gamma_T(T - T_m). \tag{4.21e}$$

Taking $y = 0$ to be the side-wall gives boundary conditions $U(0) = V(0) = 0$, while figure 4.4d suggests $D(0) = 0$. These conditions are singular, however, and therefore can not be used to initiate an IVP solver. Instead, boundary conditions are calculated at some small distance $y = \epsilon$ using the predictions of equations (4.12)–(4.16) with $y_2 = 2\epsilon$. It is assumed that in this narrow region D, U, and V vary linearly in y, while S and T are constant. The average values which the equation calculates will then exist at $y = y_2/2$. In effect, this is a linearisation of the plume equations. These assumptions result in $f_D(y_2) = f_U(y_2) = f_V(y_2) = 2$, $f_T(y_2) = f_S(y_2) = 1$, $\alpha_{DU} = \alpha_{DV} = \alpha_{|\vec{U}|U} = \alpha_{|\vec{U}|V} = 4/3$, and $\alpha_{|\vec{U}|T} = 1$ for use in the analytical predictions equations. For the integration to succeed it was necessary to set $\delta = 0$, as was done in § 3.5 and is common in published work (e.g. Jenkins, 1991, 2011; Dallaston et al., 2015). Strangely, for small but non-zero values ($\delta \sim 10^{-4}$) the system enters a non-physical regime in which longitudinal velocity grows linearly in y and thickness grows quadratically, reaching massive values that exceed the cavity thickness within 30 m of the side-wall.

The results of integrating equation (4.21) in y, using parameter values from table 3.1 and a basal slope of $b_x = 0.2$, are plotted in figure 4.7 over the domain $y \in [0, 2]$. As the analysis in § 4.3.1 predicted, at large scales the plume thickness is

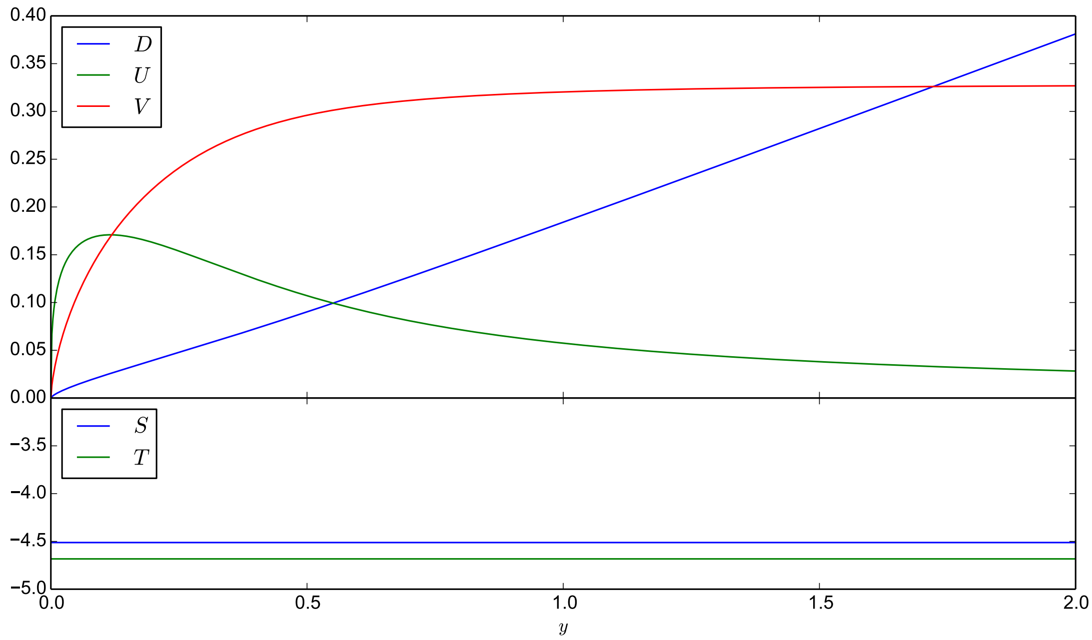

Figure 4.7: The results of solving the initial value problem describing the transverse structure of the plume in the asymptotic regime. The ice shelf is taken to have a constant basal slope $b_x = 0.2$.

approximately linear in y, while the longitudinal velocity decays and the transverse velocity approaches an asymptote. While the preliminary analysis of § 4.3.1 appeared to indicate that $U = 0$ for large values of y, figure 4.7 shows $U > 0$ when accounting for the detailed structure. The salinity and temperature remain uniform. The shape coefficients and values of the shape functions at the boundaries of a plume can thus be calculated for the desired width and parameter choices. While these results are for the asymptotic regime, it seems a reasonable approximation to apply them to the entire length of the plume in the absence of knowledge of transverse structure in the initial transient region.

There remains a question of how to relate the horizontally-averaged velocity norm, $|\vec{U}|$, to the horizontally-integrated values of the two component U and V. As the two components do not have the same transverse shape and are of comparable magnitude, $|\vec{U}| \neq \sqrt{U^2 + V^2}$. In principle a function θ could defined such that

$$|\vec{U}| = \theta(U/V)\sqrt{U^2 + V^2}.$$

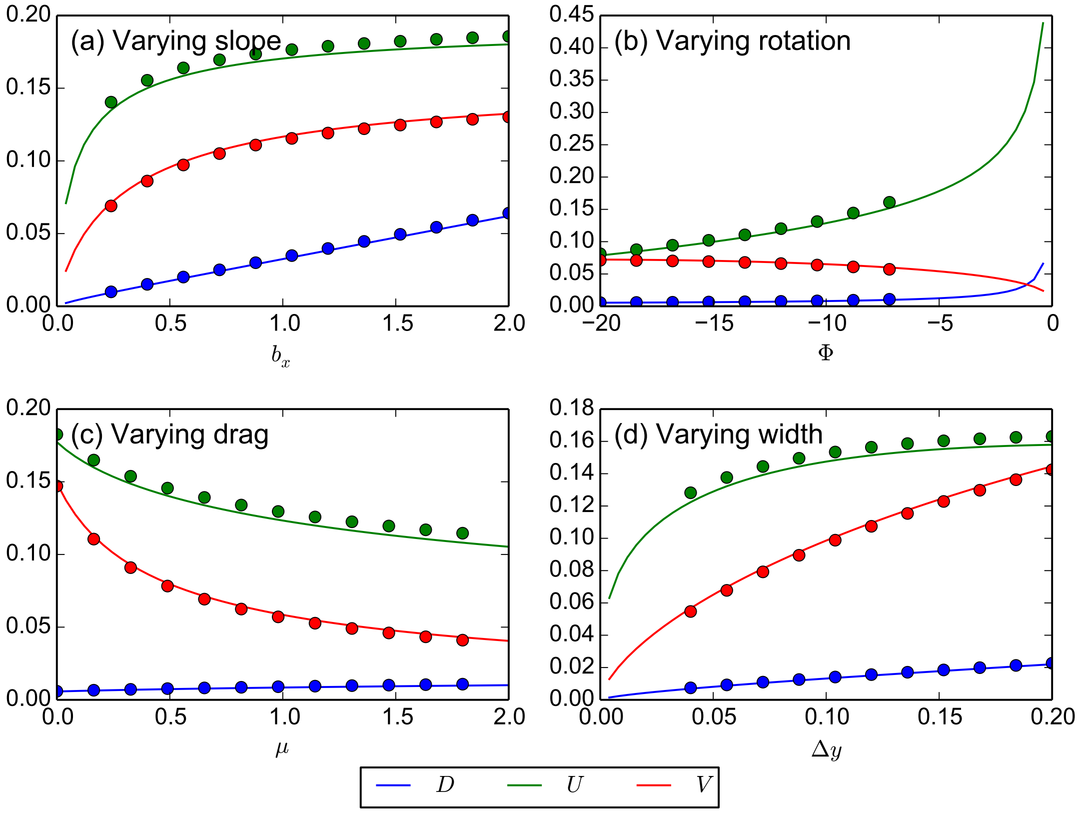

Figure 4.8: Asymptotic values for the horizontally-integrated plume, predicted from equations (4.12)– (4.16) (lines) and numerically determined by integrating equation (4.5) (circles). The plume is not assumed to be uniform here, with shape coefficients determined for each set of parameter values by integrating the IVP in y given in equation (4.21).

This function could be calculated numerically from the results of the transverse integration. However, the value of $|\vec{U}|$ is only used in parameterisations of turbulent processes, which come with uncertainty. Rather than averaging the parameterisation, it is thus not unreasonable to set $\theta(U/V) = 1$. This returns to the usual relationship between these variables. This approach was used in all subsequent calculations.

When plume thickness, salinity, and temperature were taken to be uniform in the transverse direction, the hydrostatic term in equation (4.5c) went to zero. This was a useful simplification when deriving the asymptotic results in § 4.2. However, it is now clear that the thickness is not uniform in y, meaning that hydrostatic gradients will play a role. By integrating the transverse IVP in equation (4.21) for each combination of parameter values and then solving the longitudinal IVP in equation (4.5), figure 4.4 was recreated using the appropriate shape coefficients

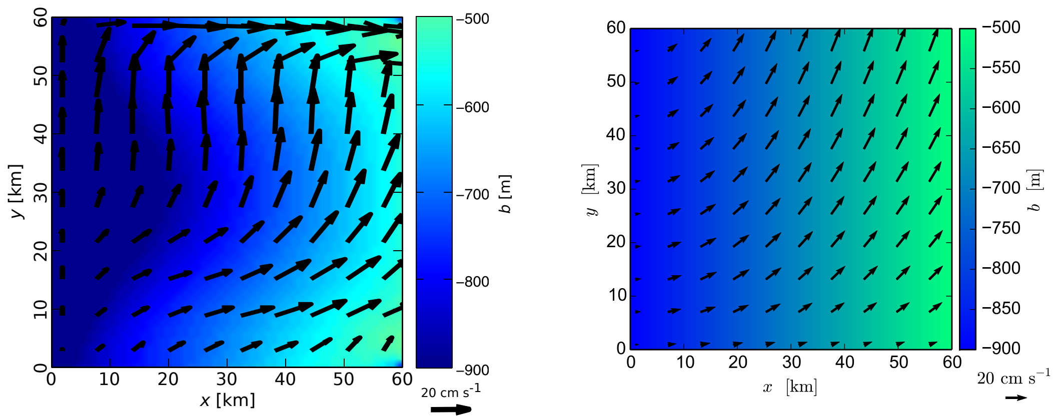

(a) mitGCM **(b)** Horizontally integrated model

Figure 4.9: Comparison of the ice-ocean boundary layer velocities (arrows) of the horizontally integrated model presented in this chapter and those found by Jordan et al. (2018) using mitGCM 3-D ocean simulations. Also plotted is the basal draft of the ice shelf in each case (colours). Note the different scales of the arrows in the two subplots. The horizontally-integrated results assume outflow at the upper y-boundary, unlike the Jordan et al. (2018) model which assumes no-flux conditions. This results in a western boundary current being resolved in the (a), which is assumed but not specifically solved for in the theory in (b).

(see figure 4.8). This revealed good agreement between the asymptotic results and those from integrating the full set of equations, with differences that are slightly larger than in figure 4.4, but still small.

A recent paper (Jordan et al., 2018) calculated ice-ocean boundary layer velocity fields for an idealised ice shelf geometry using the fully 3-D ocean model mitGCM. This particular study is focussed on here as the idealised geometry is useful for comparison with the present theory. Of especial interest is the state of the "warm cavity" simulation in the first year of the simulation. This simulation featured uniform ambient salinity and temperature in the cavity as has been assumed when solving the plume equations in this chapter. Comparing the ice-ocean interface velocity in that simulation (figure 4.9a) to the plume velocity predicted by the horizontally-integrated model (figure 4.9b) allows the theory to be qualitatively validated. In order to make a fair comparison, the horizontally-integrated calculation was done for the same width of domain ($\Delta y = 60\,\mathrm{km}$), Coriolis parameter ($f = 1.37 \times 10^{-4}\,\mathrm{s}^{-1}$), average basal slope ($b_x \approx 83.3\,\mathrm{m\,km}^{-1}$), and thermal transfer coefficient ($\Gamma_T^* = 1.33 \times 10^{-3}$, approximately 20 times greater than the value given in table 3.1) as the mitGCM run. The ambient temperature and salinity values for the "warm cavity" 3-D simulation were comparable to those used for the horizonally-integrated model in this chapter. As the mitGCM simulation did not include subglacial discharge, the plume was given boundary conditions of $D = 4 \times 10^{-7}$ and $U = 2 \times 10^{-3}$ at $x = 0$, the smallest values for which the IVP could be successfully solved. It was not possible for the horizontally integrated model to capture the transverse basal slope of the ice shelf which was present mitGCM simulation, so a planar basal slope was adopted.

Comparing the results in figure 4.9 shows a remarkable degree of similarity, given the simplicity of the horizontally-integrated model and the fact that it took mere seconds to perform that calculation on a desktop computer. Both show relatively low velocity near the lower y-boundary, with a significant longitudinal component. However, away from that boundary the velocity grows and tends to be oriented in the across-shelf direction. Both results show that the magnitude of the velocity will tend to be larger further away from the grounding line and predict similar magnitudes. The most noticeable difference is the strong boundary current at the upper limit of y in the mitGCM case. The assumptions of the horizontally-integrated model do not allow this to be explicitly captured in the present theory, as the upper boundary is taken to permit outflow whereas in the mitGCM run that boundary had a no-flux condition. However, the presence of such a boundary current, outside the region of Δy, is assumed in the horizontally-integrated model. Other differences include the stronger and more transverse flow at the grounding line in mitGCM and larger longitudinal velocity components in the upper half of the plot for the horizontally integrated model. Some of these characteristics may be explained by the slightly different ice shelf shape in mitGCM.

4.4 Relaxing the Seperability Assumptions

The above approach works well when calculating the state of a plume under an ice shelf with a constant basal slope. However, ice shelves typically have a varying slope. The value of many of the shape factors depend on the basal slope (figure 4.10),

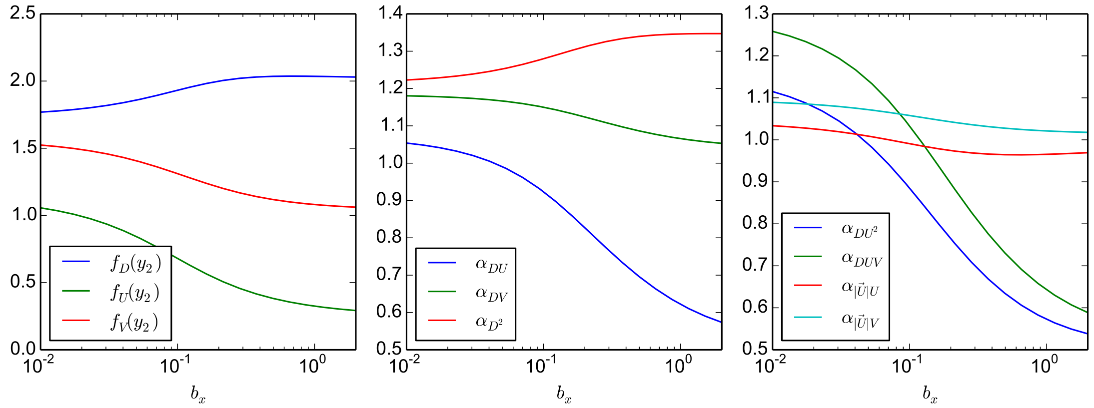

Figure 4.10: Plots indicating how different factors describing the transverse shape of the plume vary with the basal slope b_x of the overlying ice shelf. The values of $f_S(y_2)$ and $f_T(y_2)$ are not plotted as they are unity for all values of b_x. Values of $f_U'(y_2)$, $f_V'(y_2)$, $f_S'(y_2)$, $f_T'(y_2)$ do vary but remain close to zero. Unplotted α coefficients are equal to unity for any basal slope, with the exception of α_{DUS} and α_{DUT} which are both equal to α_{DU}.

which means they would not be constant throughout the plume domain. If the slope varies gradually then the coefficients might be calculated using the local slope values, as done successfully for the analytic predictions of the asymptotic values (figure 4.5). However, this is unlikely to work in cases where the slope changes rapidly and, more fundamentally, the assumption of separability in x and y does not rigorously apply. This problem is ignored for the remaining calculations in this chapter, but it is worth exploring how it might be addressed in future.

Consider if the separation of variables is redefined such that

$$D(x,y) = f_D(x,y)\hat{D}(x), \quad U(x,y) = f_U(x,y)\hat{U}(x), \quad \ldots \tag{4.22}$$

where f_D, f_U, etc. remain normalised over $y \in [y_1, y_2]$ for all x. For the most part, the horizontal integration can proceed as before. However, the diffusive terms can not be integrated quite so easily. Consider, for example viscosity in the x-direction:

$$\begin{aligned}
\int_{y_1}^{y_2} \frac{\partial}{\partial x}\left(D\frac{\partial U}{\partial x}\right) dy &= \frac{d}{dx}\left(\int_{y_1}^{y_2} D\frac{\partial U}{\partial x}\right) \\
&= \frac{d}{dx}\left(\hat{D}(x)\int_{y_1}^{y_2} f_D(x,y)\left[\frac{d\hat{U}(x)}{dx}f_U(x,y) + \hat{U}(x)\frac{df_U(x,y)}{dx}\right]dy\right) \\
&= \frac{d}{dx}\left(\alpha_{DU}\hat{D}\frac{d\hat{U}}{\mathcal{D}_x} + \hat{D}\hat{U}\int_{y_1}^{y_2} f_D\frac{\partial f_U}{\partial x}dy\right).
\end{aligned}$$

The first term in the parentheses on the right hand side of the equation is analogous to the diffusion terms in equation (4.5) and can easily be integrated. However, it is not clear how to calculate the value of the second term. The simplest approach would be to set it to zero, noting that the diffusion term is simply a parameterisation of turbulence in any case and it is therefore acceptable to alter that parameterisation slightly (much as argued for the relationship between $|\vec{U}|$, U, and V). With this approximation, the plume equations take the form

$$\frac{d}{dx}\left(\alpha_{DU}DU\right) + \left.\frac{f_D f_V}{\Delta y}\right|_{y_1}^{y_2} DV = \overline{e} + \overline{m}, \tag{4.23a}$$

$$\begin{aligned}
\frac{d}{dx}\left(\alpha_{DU^2}DU^2\right) + \left.\frac{f_D f_U f_V}{\Delta y}\right|_{y_1}^{y_2} DUV = {}& D(\rho_a - \overline{\rho})\frac{db}{dx} \\
& - \frac{\delta}{2}\frac{d}{dx}\left(\alpha_{D^2}D^2[\rho_a - \tilde{\rho}]\right) \\
& + \nu\frac{d}{dx}\left(\alpha_{DU}D\frac{dU}{dx}\right) + \nu\left.\frac{DU}{\Delta y}f_D f_U'\right|_{y_1}^{y_2} \\
& - \mu\alpha_{|\vec{U}|U}|\vec{U}|U + \Phi\alpha_{DV}DV,
\end{aligned} \tag{4.23b}$$

$$\begin{aligned}
\frac{d}{dx}\left(\alpha_{DUV}DUV\right) + \left.\frac{f_D f_V^2}{\Delta y}\right|_{y_1}^{y_2} DV^2 = {}& -\left.\frac{\delta D^2}{2\Delta y}f_D^2[\rho_a - \rho(x,y)]\right|_{y_1}^{y_2} \\
& + \nu\frac{d}{dx}\left(\alpha_{DV}D\frac{dV}{dx}\right) + \nu\left.\frac{DV}{\Delta y}f_D f_V'\right|_{y_1}^{y_2} \\
& - \mu\alpha_{|\vec{U}|V}|\vec{U}|V - \Phi\alpha_{DU}DU,
\end{aligned} \tag{4.23c}$$

$$\begin{aligned}
\frac{d}{dx}\left(\alpha_{DUS}DUS\right) + \left.\frac{f_D f_S f_V}{\Delta y}\right|_{y_1}^{y_2} DSV = {}& \overline{e}S_a + \nu\frac{d}{dx}\left(\alpha_{DS}D\frac{dS}{dx}\right) \\
& + \nu\left.\frac{DS}{\Delta y}f_D f_S'\right|_{y_1}^{y_2} + \overline{m}S_m - \overline{\gamma_S(S - S_m)},
\end{aligned} \tag{4.23d}$$

$$\begin{aligned}
\frac{d}{dx}\left(\alpha_{DUT}DUT\right) + \left.\frac{f_D f_T f_V}{\Delta y}\right|_{y_1}^{y_2} DTV = {}& \overline{e}T_a + \nu\frac{d}{dx}\left(\alpha_{DT}D\frac{dT}{dx}\right) \\
& + \nu\left.\frac{DT}{\Delta y}f_D f_T'\right|_{y_1}^{y_2} + \overline{m}T_m - \overline{\gamma_T(T - T_m)}.
\end{aligned} \tag{4.23e}$$

The main difference from equation (4.5) is that the α coefficients (defined the same way as before) are now a function of x and as such must remain inside derivatives. The hydrostatic terms in the x-momentum equation have also been rearranged slightly to better facilitate integration.

It should be noted, however, that the shape coefficients in figure 4.10 show only modest variations. Even the largest changes are less than a factor of 3, with b_x varying by two orders of magnitude. Other parameters, such as ν, Γ_T, and E_0 have significantly greater uncertainty. There is also the potential for equivalent scale errors in assuming a "top-hat" vertical profile for the plume variables when deriving the initial vertically-integrated model. Thus, the approach described in this subsection is simply a way to improve the first estimate and should not be taken to denigrate the horizontally-integrated model in equation (4.5).

4.5 Interaction with Seasonal Forcing

The motivation for developing this horizontally-integrated model was to investigate whether transverse flow contributes to the channelisation of the plume in coupled simulations with ice shelves. Fully coupled simulations were run using the numerical methods described in § 3.1. The linear operator for the plume solver, defined in equation (3.28), was modified to contain the Coriolis forcing terms, becoming

$$L[D, U, U', S, S', T, T']^T = \left[\frac{dD}{dx}, \frac{dU}{dx} - U', \frac{dU'}{dx} - \frac{\Phi\alpha_{DV}}{\nu\alpha_{DU}}V, \frac{dV}{dx} - V', \right. \\ \left. \frac{dV'}{dx} + \frac{\Phi\alpha_{DU}}{\nu\alpha_{DV}}U, \frac{dS}{dx} - S', \frac{dS'}{dx}, \frac{dT}{dx} - T', \frac{dT'}{dx}\right]^T. \quad (4.24)$$

Shape coefficients, drainage terms, and the equation for y-momentum were added to the nonlinear operator. It was found that the existing preconditioner was adequate to solve the modified equations. The solver was tested first by running it in the trivial case with $\Phi = 0$ and $V = 0$ throughout the domain, with uniform thickness in y, to ensure that it converged to the same results as the model in § 3.1.4.2. It was then further tested by checking that the values of each variable at the end of the domain agreed with the asymptotic predictions in § 4.2 when $\Phi \neq 0$ and b_x was constant.

Boundary conditions are the same as those used in Chapter 3, with the addition of $V = 0$ at $x = 0$ and $V' = 0$ at $x = X$, where X is the length of the ice shelf. These correspond to no transverse flow at the grounding line and no gradient in V at the outflow boundary. Given that the ice shelf slope is nonuniform, it wasn't clear what

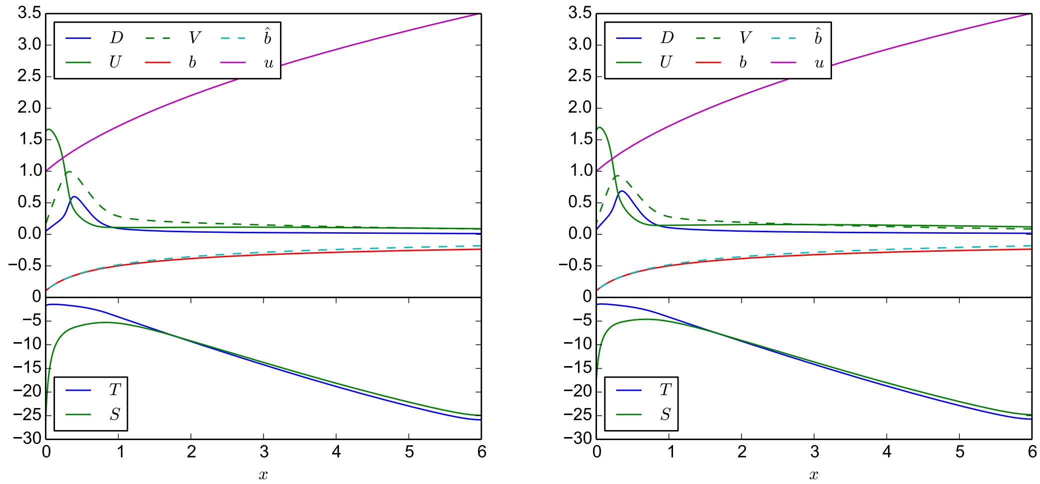

(a) Shape coefficients for $b_x = 0.1$ (b) Shape coefficients for $b_x = 1$

Figure 4.11: Steady state results for coupled simulations of the ice shelf and horizontally-integrated plume. Also plotted is the steady state basal depth for simulation `ssNeJeDa` without the Coriolis force ($\hat{b}$).

choice of shape coefficients should be used, so two sets of simulations were run: one using coefficients calculated for $b_x = 0.1$ (representative of slopes towards the end of the ice shelf) and the other using coefficients calculated with $b_x = 1$ (representative of slopes near the grounding line). Parameter values are the same as those given in table 3.1 and the same set of parameterisations were used as in simulation `ssNeJeDa`.

Simulations were first run to steady state with the coupled plume. A continuation approach was used to obtain a good guess for the initial steady state of the plume, to aid the iterative solver. Prior to the first time step it was necessary to initially solve for the plume without Coriolis forcing, then gradually step the Coriolis parameter up to its appropriate value. During this process, the hydrostatic term in equation (4.5c) was turned off by artificially setting $f_D(y_1) = f_D(y_2)$. The value of $f_D(y_1)$ was then gradually reduced to its appropriate level (~ 0). Once this was done, the ice shelf could be integrated forward in time. While the plume solver sometimes struggled to handle rapid increases in Φ, once the correct value was reached it displayed similar levels of performance as in the irrotational, non-horizontally integrated case. The results of these simulations can be seen in figure 4.11. For both sets of shape coefficients the ice is slightly thicker ($\sim 70\,\mathrm{m}$) than it was in simulation `ssNeJeDa`

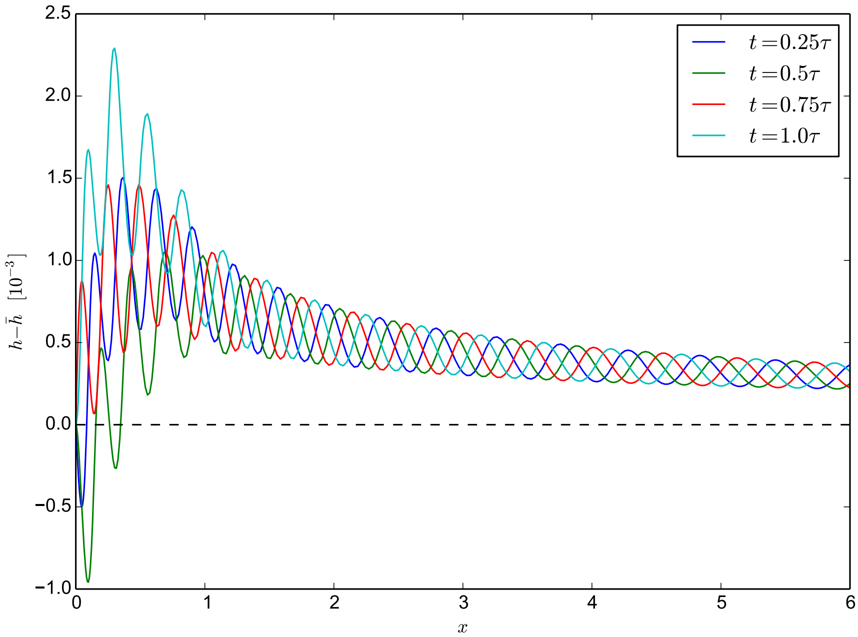

Figure 4.12: The difference between the ice thickness (h) at different points in the oscillatory cycle and the steady state thickness $\bar{h}$ for an ice shelf forced by variations in subglacial discharge. The shelf is coupled to a horizontally-integrated plume using shape factors calculated with $b_x = 0.1$.

without rotation (see § 3.3). This is due to the plume velocity being significantly lower across most of the domain, resulting in smaller melt rates. The two rotational simulations are very similar, but V tends to be slightly larger for the $b_x = 0.1$ coefficients case and D slightly smaller. This suggests that the change in shape coefficients with slope does not have a major impact on the plume behaviour.

Next, a pair of simulations were run with seasonally varying subglacial discharge, similar to `diNeJeDa` in § 3.4. While in Chapter 3 the magnitude of the subglacial discharge variations was 90% of the mean state, it was found that this caused the solver to fail for the rotational plumes. The exact reason for this is unclear, but given that it happens suddenly when the discharge is approaching its minimum value it seems reasonable to assume that it is an issue with the plume becoming subcritical. To avoid this problem, the variations were instead set to 85% of the mean state. The results of these simulations are presented in figures 4.12 and 4.13 for the $b_x = 0.1$ and $b_x = 1.0$ coefficients cases, respectively. The ripples in these results are of similar amplitude to those in simulation `diNeJeDa`, although the ripple

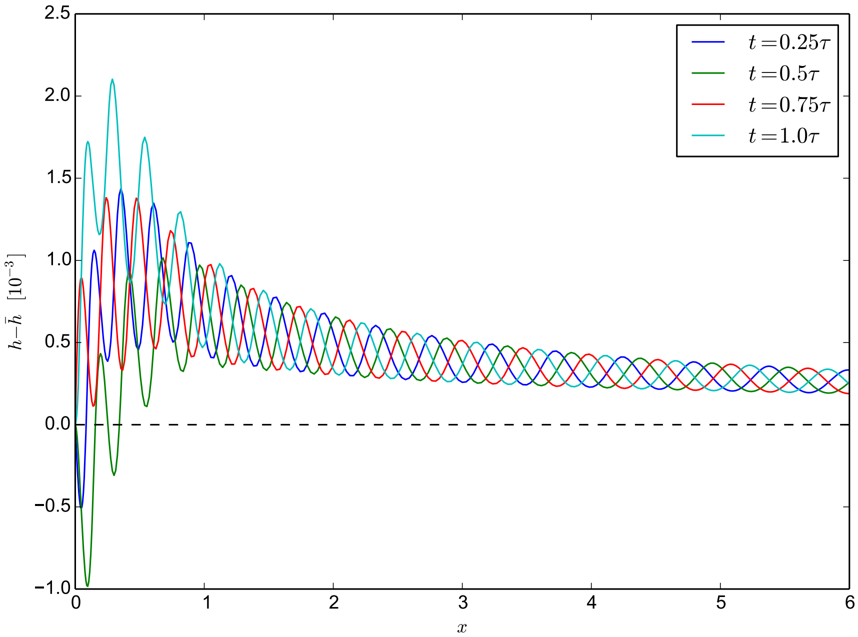

Figure 4.13: The difference between the ice thickness (h) at different points in the oscillatory cycle and the steady state thickness $\bar{h}$ for an ice shelf forced by variations in subglacial discharge. The shelf is coupled to a horizontally-integrated plume using shape factors calculated with $b_x = 1$.

magnitude decays more strongly downstream. This is likely because the ice shelves are thicker in these simulations, resulting in greater stretching. Global oscillations are not present downstream, due to the plume flow being in the asymptotic state in this region and not affected by the subglacial discharge forcing. As a result, melting only varies from the steady state near the grounding line and can not drive global oscillations downstream. This lack of downstream melting perturbation also explains the reduced bias towards thickening in these simulations compared to simulation `diNeJeDa`. There are only minor differences between the two horizontally-integrated simulations, with that using $b_x = 0.1$ coefficients displaying slightly larger ripples and a greater bias towards thickening.

Finally, simulations were run with the ice shelf forced by seasonally varying flux across the grounding line, as in simulation `ifNeJeDa` in § 3.5. However, unlike in the earlier simulation, in the horizontally-integrated case it proved possible to run the simulations with $\delta \neq 0$. The choice was made to use a non-zero value of δ as this is the more physically realistic choice. As in `ifNeJeDa`, ice flux oscillations at the

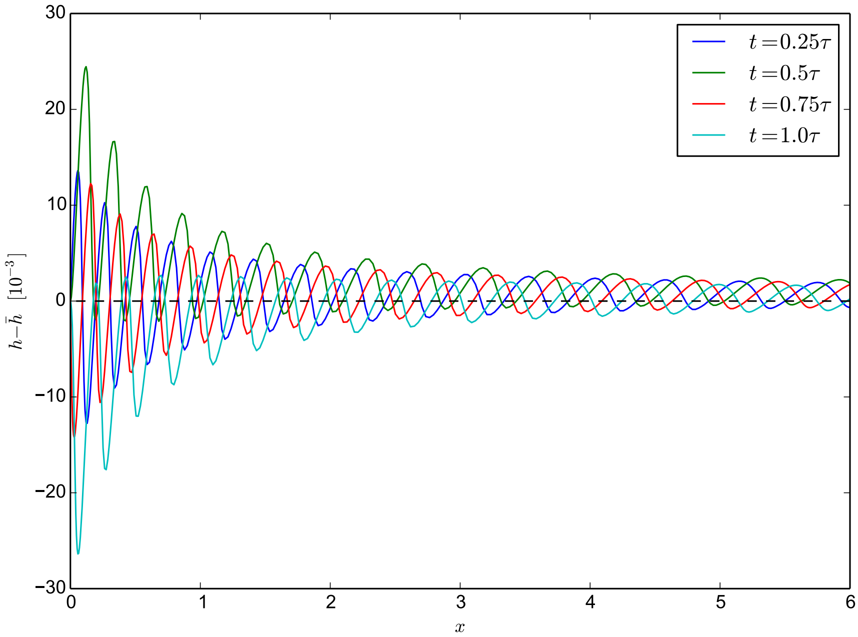

Figure 4.14: The difference between the ice thickness (h) at different points in the oscillatory cycle and the steady state thickness $\bar{h}$ for an ice shelf forced by variations in ice flux across the grounding line. The shelf is coupled to a horizontally-integrated plume using shape factors calculated with $b_x = 0.1$.

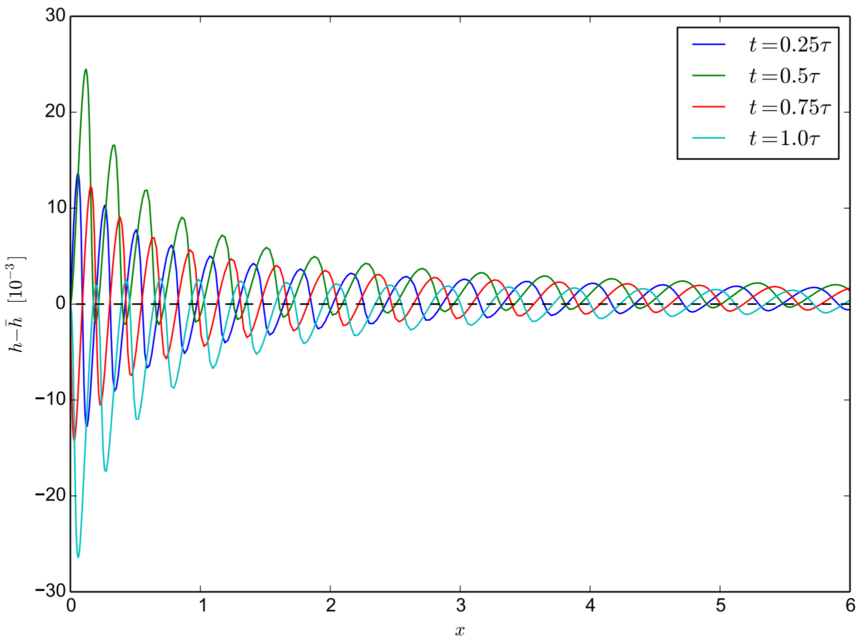

Figure 4.15: The difference between the ice thickness (h) at different points in the oscillatory cycle and the steady state thickness $\bar{h}$ for an ice shelf forced by variations in ice flux across the grounding line. The shelf is coupled to a horizontally-integrated plume using shape factors calculated with $b_x = 1$.

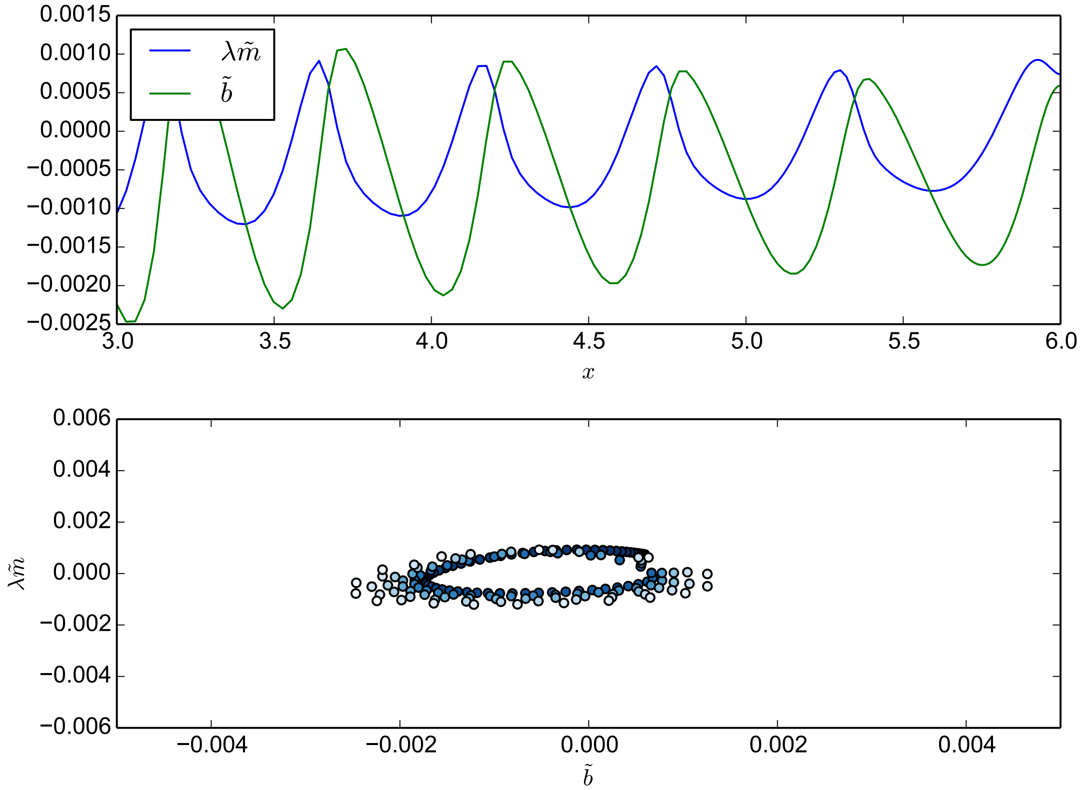

Figure 4.16: Upper: perturbations to the melt rate and basal depth of the ice shelf in the horizontally-integrated simulation with shape factors calculated using $b_x = 0.1$. Data is for the second half of the domain only and is from a quarter of the way through a seasonal cycle after the ice has reached a statistically-steady state. Lower: these two quantities plotted against each other, showing little correlation. The colour of a point indicates its location on the shelf, with white corresponding to $x = 3$ and navy to $x = 6$.

grounding line had a magnitude of 50% of the mean value. The results of a simulation run with coefficients calculated using $b_x = 0.1$ are shown in figure 4.14, while those for a simulation with coefficients calculated using $b_x = 1$ are in figure 4.15.

The results are very similar to those in simulation `ifNeJeDa`, especially near the grounding line where ripples are of similar magnitude. Disagreement between the two simulations with different shape factors is negligible. There is a slight bias towards the ice thickening near the calving front which was not present in the simulation without Coriolis forces. It is hypothesised that this is due to the nonlinear dependence of asymptotic plume velocity on basal slope, which can be seen in figure 4.4a. While the forcing causes the shelf to have regions of both increased and decreased basal slope, the velocity will fall more in the regions of

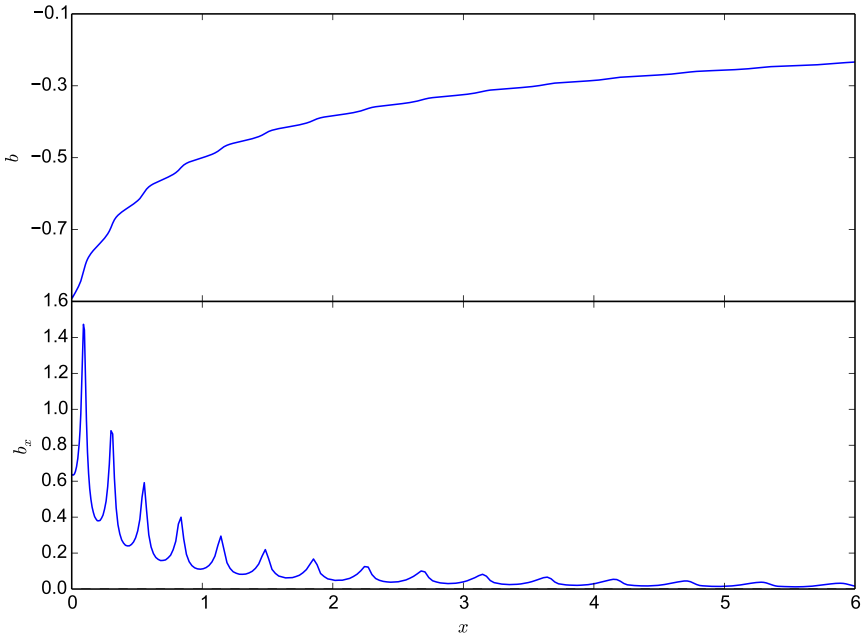

Figure 4.17: Upper: the total basal depth of an ice shelf at time $t = 0.25\tau$ into a seasonal cycle. The shelf has been forced with seasonally varying ice flux and is coupled to a horizontally-integrated plume model, with the plume's shape parameters calculated for a basal slope of $b_x = 1$. Lower: The basal slope of the ice shelf at time $t = 0.25\tau$. It is positive definite throughout the domain, indicating no overdeepenings.

decreased slope than it rises in regions of increased slope. As such, the average plume velocity is reduced, leading to a lower average melt rate. This is similar to the mechanism which caused the bias towards thicker ice in the simulations forced by varying subglacial discharge.

The amplitude of the ripples is slightly smaller towards the calving front in these simulations than those in § 3.5. This is likely due in part to greater stretching, as in the discharge-forced case. However, there is no evidence of the perturbation growth seen in § 3.5. This is due to much less feedback between the plume thickness perturbation and the melt rate (figure 4.16) compared to simulation `ifNeJeDa`. This may be because $\delta \neq 0$ in the horizontally-integrated simulation. The smaller size of the ripples mean they are not large enough to produce overdeepenings, as can be seen by inspecting the basal depth of the ice shelf and its gradient in figure 4.17 (where shape factors were for $b_x = 1$).

It was hypothesised that, by accounting for the transverse velocity component,

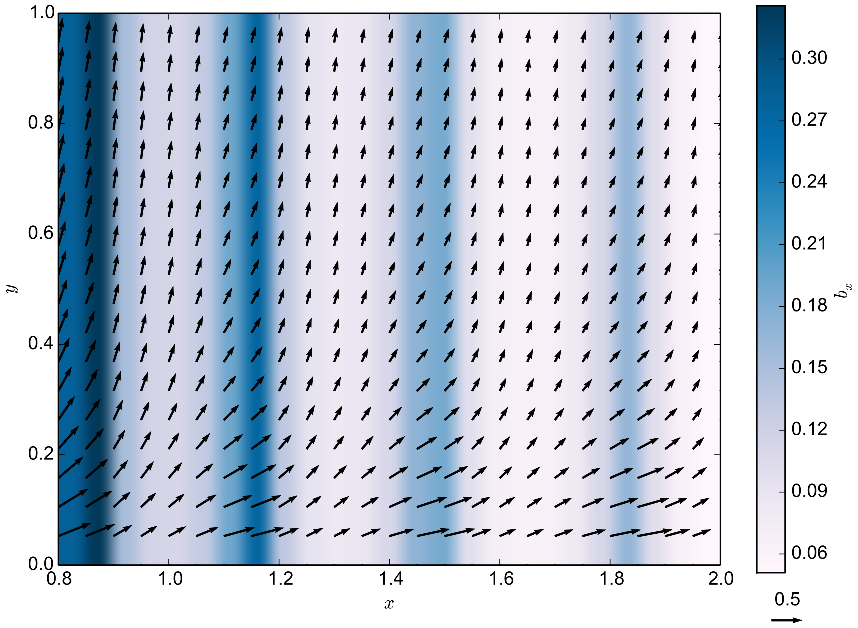

Figure 4.18: The 2-D velocity field (arrows) for the ice flux-forced simulation with shape factors calculated for $b_x = 1$. Also plotted is the local basal slope of the ice shelf (colours). It can be seen that channelised flow did not occur along the regions of increased slope.

the horizontally-integrated model would be able to capture the channelisation of plume flow and thus lead to the development of a basal channel in the coupled ice shelf. However, examining the 2-D vector field shows that this did not in fact happen (see figure 4.18). Indeed, in regions with increased slope the plume flow tends to be more directed in the longitudinal direction than elsewhere. It would thus appear that transverse ripples do not tend to channelise plume flow, which limits their ability to grow. Although the horizontally-integrated model did not lead to the growth of transverse channels as hoped, it remains a potentially useful tool for efficiently investigating plume flow beneath ice shelves.

4.6 Conclusions on Transverse Flow

In this chapter, the derivation of a horizontally-integrated plume model was presented which included the effects of the Coriolis force and lateral export in a simplified 1-D model for evolution of flow along the length of the shelf. This model includes a number of coefficients representing the transverse shape of the plume variables. Some basic insights could be gained when assuming the plume was uniform in the transverse direction. Solving for the plume with these assumptions showed that the plume went through a transient downstream evolution near the grounding line before reaching an asymptotic state. Analytic predictions for the asymptotic values of each plume variable were derived and found to give good agreement with numerical results. In order to more realistically represent the transverse shape coefficients, a transverse initial value problem was formulated to describe the transverse structure of the plume in the asymptotic region. The 2-D velocity field predicted by this model agrees well with the qualitative structure and approximate magnitude of the ice-ocean boundary layer velocity field calculated by Jordan et al. (2018) using a fully 3-D ocean model. In particular, the rotation of the plume flow into the across-shelf direction was well represented in the horizontally-integrated model, as was the largely longitudinal direction of flow near the side-wall of the cavity.

The horizontally-integrated plume model was also coupled to a co-evolving ice shelf in order to run simulations similar to those in Chapter 3 to investigate the impact of seasonally varying forcing on the ice shelf. The ripples in ice thickness produced in simulations with the coupled horizontally-integrated model forced by time-varying subglacial discharge or ice flux were smaller than those seen in the results of Chapter 3. The ripples caused by varying ice flux were not able to grow into overdeepenings in the horizontally-integrated case. The ripples in the ice flux-forced simulations in § 3.5 exhibited growth towards the end of the ice shelf, due to a feedback between thickness perturbation and melt rate. This feedback was not observed when using the horizontally-integrated plume model and the Coriolis force appears to disrupt channelisation of the plume flow along the ripples. This result suggests that seasonal variability may not be a viable mechanism to explain the formation of large transverse basal channels on ice shelves with significant overdeepenings, at least for ice shelves with low melt rates.

The horizontally-integrated model has the potential to be applied far beyond studying channel formation in ice shelves. For example, it offers a computationally cheap way to parameterise ice melt, which may be useful in larger-scale climate models.

The version of the horizontally-integrated model presented here makes use of many of the same simplifications used in Chapter 3. Only a one-equation formulation of ice melt was used and the melting temperature was taken to be independent of pressure (i.e., depth). It would be fairly straightforwards to horizontally-integrate the three equation treatment of melt and incorporate it into the model in future. The thermal transfer coefficient, Γ_T^*, used in this thesis was much smaller than the commonly accepted value and produced unrealistically low melt rates compared to observations under Pine Island Ice Shelf. While higher melt rates present numerical difficulties for the plume solver used here, in future work it may be worth trying alternative approaches to overcome this problem in order to run simulations which can better evaluate the potential for channel formation under PIIS. Another assumption made by the plume model used here is that the ambient layer beneath the plume has large (effectively infinite) depth. Near the grounding line this approximation would not hold well and a two-layer approximation may be needed to characterise the return flow and satisfy conservation of vorticity.

There are numerous other opportunities to further develop the horizontally-integrated plume model. For example, it may be generalised to account for transverse ice-shelf slope, perhaps by coupling it to a similarly horizontally-integrated ice model. It may also be possible to apply the plume model to a cavity with variable width (i.e., nonuniform Δy), allowing its use with less idealised geometries. Another avenue for future development would be to try to explicitly capture boundary currents, such as seen in figure 4.9a, in the model. This could be done by coupling together two horizontally-integrated plume models, with the outflow through the upper y-boundary of one providing inflow through the lower y-boundary of the other. The first of these plumes would have an impermeable lower y-boundary, as described in this chapter, while the second would have an impermeable upper y-boundary along which the boundary current would form.

5

Internal Reflectors and Ice Dynamics

Contents

While using ground penetrating radar to measure glacier thickness, it has been observed that faint internal reflectors also exist within the ice (e.g. Gudmandsen, 1975; Jacobel and Hodge, 1995). An example of such internal reflectors in the Fimbul Ice Shelf can be found in figure 5.1. These are caused by changes in the dielectric constant of ice, which can result from differences in density (Robin et al., 1969; Harrison, 1973), orientation of ice crystals (Harrison, 1973), or the presence of impurities (Harrison, 1973; Hammer, 1980). It is widely thought that such changes in ice properties occur when the ice first accumulated at the surface of the glacier. Therefore, internal reflectors are often interpreted as *isochrones*, or surfaces on which the ice is of the same age (Robin et al., 1969).

These isochrones encode information about the past evolution of the ice sheet (Leysinger Vieli et al., 2007). As such, there has been interest in using them as a

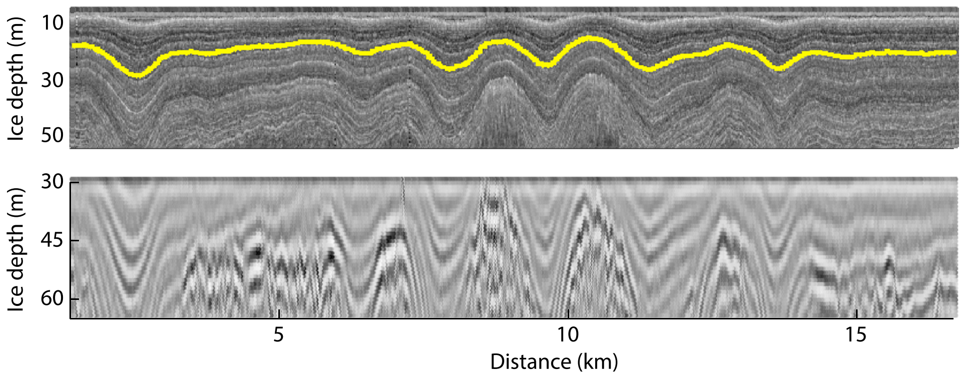

Figure 5.1: Radar transect of the Fimbul Ice Shelf, showing internal reflectors. One particular reflector is marked by the yellow line. The upper panel was produced with high frequency radar, while the lower was produced with low frequency radar. *(Image source: Langley et al., 2014)*

way to measure current and historical ice sheet properties. A variety of types of data can be extracted from englacial layers. For example, Ng and Conway (2004) used englacial layer data to estimate the velocity of Kamb Ice Stream prior to its stagnation $\sim$ 150 years ago and Siegert, Ross, et al. (2013) have discerned isochronal evidence of past slowdown or glacial advance in the Weddell Sea sector of Antarctica. Internal radar reflectors have also been used to estimate basal melt rates over subglacial lakes (Siegert, Hindmarsh, et al., 2004) or due to possible historical grounding line motion (Catania et al., 2006).

In addition to observational papers such as these, more theoretically inclined work exists which tried to mathematically model internal layer evolution. Using a simple model, Vaughan David G. et al. (1999) devised a criterion with which to classify whether ripples in internal layers formed due to changes in accumulation or vertical strain rate. Authors such as Nereson et al. (2000) and Karlsson et al. (2014) have used 2-D ice flow models in x and z to constrain past and present accumulation patterns with internal layer data. Parrenin, Hindmarsh, and Rémy (2006) and Parrenin and Hindmarsh (2007) were able to derive analytic solutions for layer geometry in a grounded ice sheet by making a number of different simplifying assumptions (e.g., steady state, spatially uniform velocity profiles in z). This allowed easy exploration of the dependence of the layer geometry on factors such as accumulation, basal topography, and the velocity shape function. The analyses described above have largely taken the form of comparing observations with simulations run for a few representative accumulation or ice flow configurations. A formal inverse method was developed by Waddington et al. (2007) for a steady-state flowband in an ice sheet, allowing the spatially-varying accumulation rate to be determined. Most modelling of isochrone evolution has featured only one horizontal dimension, although (Hindmarsh et al., 2009) presented a horizontally 2-D numerical model. Almost all internal layer models discretise the vertical coordinate (with the exception of Waddington et al., 2007), whereas most ice sheet models are vertically integrated. The work discussed above, and almost all work to date, has focused on internal layers within grounded ice sheets rather, than ice shelves.

5.1 Modelling Reflectors

Here a model is developed to characterise the evolution of internal layers within a shallow-ice shelf, to give insights into whether such layers provide useful information on ice flow. Consider a scalar field $k(x, y, z, t)$ indicating the age of the ice. As the ice accumulates on much longer time-scales than those of ice shelf flow, the field is treated as an inert Lagrangian tracer:

$$\frac{\partial k}{\partial t} + \vec{u}(x, y, z) \cdot \nabla k = 0. \tag{5.1}$$

To be useful, this must be converted into a form compatible with the vertically integrated equations in § 1.4.1. However, it is the vertical structure which is of interest and this would normally be lost when integrating over depth. To avoid this, we express k as a Taylor series in z with r terms:

$$k = \sum_{n=0}^{r} \kappa_n (s - z)^n,$$

where $s(x, y, t)$ is the surface elevation and $\kappa_n(x, y, t)$ are coefficients to be determined.

This is substituted into equation (5.1) and expanded. Integrating the incompressibility equation and using the result to eliminate $w(z)$ yields

$$\sum_{n=1}^{r} n\kappa_n (s-z)^{n-1}\left(\frac{\partial s}{\partial t}+\vec{u}\cdot\nabla_h s - w(s)\right)+\sum_{n=0}^{r}\left(\frac{\partial \kappa_n}{\partial t}+\vec{u}\cdot\nabla_h\kappa_n\right)(s-z)^n \\ -\int_z^s \nabla_h\cdot\vec{u}dz'\sum_{n=1}^{r} n\kappa_n(s-z)^{n-1}=0,$$

where ∇_h is the horizontal gradient operator. The boundary conditions specify that $\partial s/\partial t+\vec{u}\cdot\nabla_h s-w(s)$ is equal to the rate of accumulation of ice at the surface, which is assumed to be zero. This is a typical assumption for ice shelves, where basal melting is much greater than surface accumulation. If accumulation were not zero then one would retain a weak coupling of κ_n to the higher order coefficient κ_{n+1}, proportional to the surface accumulation. This would tend to cause κ_0 to become slightly positive or negative, depending on the sign of the surface mass balance. Once again, plug flow is assumed, with horizontal components of $\vec{u}$ independent of z, yielding

$$\sum_{n=0}^{r}\left(\frac{\partial \kappa_n}{\partial t}+\vec{u}\cdot\nabla_h\kappa_n - n\kappa_n\nabla_h\cdot\vec{u}\right)(s-z)^n=0.$$

Note that the binomials $(s-z)^n$ are linearly independent for different values of n. Thus

$$\frac{\partial \kappa_n}{\partial t}+\vec{u}\cdot\nabla_h\kappa_n = n\kappa_n\nabla_h\cdot\vec{u}. \tag{5.2}$$

The evolution of an arbitrary number of these coefficients $\kappa_n(x, y, t)$ can be tracked, with the number and values chosen to give a plausible initial configuration.

One concern with this approach is the effect of truncating the Taylor series describing the vertical structure. In effect, this truncation sets the coefficients of the higher modes in the series to zero, which represents a steady state solution to equation (5.2). However, the physical values of these modes would not be zero and would continue to evolve as the ice advects. It must be considered whether they could grow to the point where it is no longer reasonable to neglect them. To evaluate this, consider a perturbation of the form $\epsilon e^{i(ct-k_1x-k_2y)}$ to the $\kappa_n = 0$ steady state (where

ϵ is some small real coefficient, c is a complex wave speed, and k_1 and k_2 are real wave-numbers). Substituting this ansatz into equation (5.2) and simplifying yields

$$c = \begin{pmatrix} k_1 \\ k_2 \end{pmatrix} \cdot \vec{u} - i\left(n\nabla \cdot \vec{u}\right).$$

The solution is stable for $\mathrm{Im}(c) < 0$, meaning

$$\nabla \cdot \vec{u} > 0 \quad \Rightarrow \quad \text{stability}.$$

This condition is always satisfied on ice shelves, so this approach to modelling internal layers can be useful in that setting. However, if it is to be applied to a grounded ice sheet then care must be taken to ensure the divergence condition is met.

5.1.1 Steady State

As a proof of concept, consider a 1-D ice shelf in steady state. Equation (5.2) becomes

$$u\frac{d\kappa_n}{dx} = n\kappa_n\frac{du}{dx},$$

which, if boundary conditions are specified at $x = 0$, has the solution

$$\kappa_n = \kappa_n(0)\left(\frac{u}{u(0)}\right)^n. \tag{5.3}$$

An analytic solution was found using the steady-state ice shelf described in equation (2.21) and boundary values $\kappa_n(0)$ set to the first 10 Taylor coefficients for

$$k(z) = (1.05 - z)^{-1/2} - 1.05^{-1/2}, \tag{5.4}$$

which is chosen for illustrative purposes to give a plausible monotonic increasing age profile. These boundary values will be used for all subsequent calculations in this chapter. The age field, k, was computed from the coefficients and plotted in figure 5.2. It can be seen that the oldest ice at the bottom of the shelf is melted away across the shelf's length. Stretching causes the shelf to thin and deep isochrones to be lifted upwards along shelf by the corresponding strain as the shelf adjusts to a new hydrostatic equilibrium.

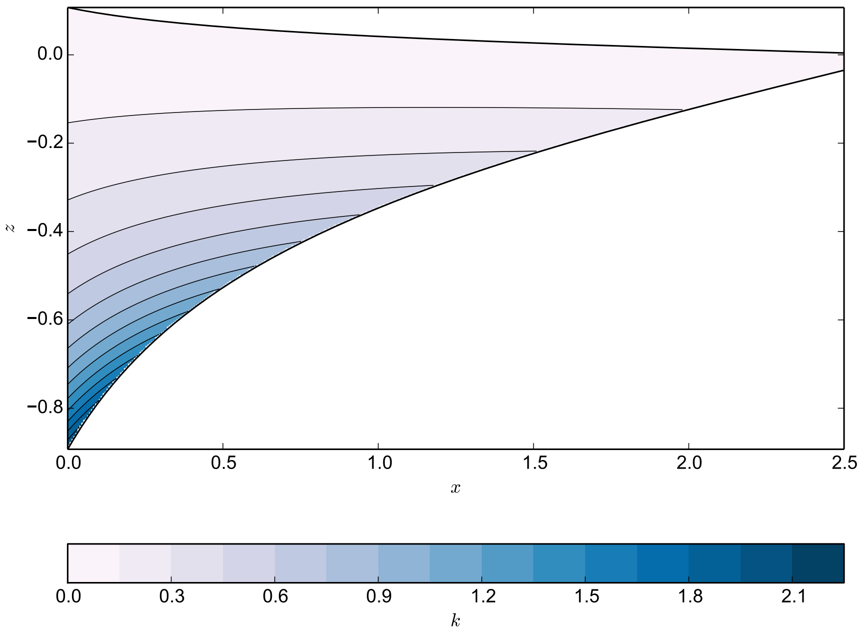

Figure 5.2: The steady state synthetic age, k, of the ice in an ice shelf like that described in equation (2.21). The age is in arbitrary units and the lines between different colours represent isochrones. The age profile at the boundary is given by equation (5.4) with $r = 10$ coefficients used.

5.1.2 Linear Response

A simple way to examine how seasonal variability alters the internal reflectors within the ice shelf is to perform a linear analysis like that done in Chapter 2. If the steady state results are $\bar{\kappa}_n$, we assume the time varying form of κ_n is $\bar{\kappa}_n(x) + \tilde{\kappa}_n(x)e^{i\omega t}$, where ω is the angular frequency of seasonal forcing. Equation (5.2) was then linearised about the steady state to yield

$$i\omega\tilde{\kappa}_n + \tilde{u}\frac{d\bar{\kappa}_n}{dx} + \bar{u}\frac{d\tilde{\kappa}_n}{dx} = n\tilde{\kappa}_n\frac{d\bar{u}}{dx} + n\bar{\kappa}_n\frac{d\tilde{u}}{dx}. \tag{5.5}$$

Using the values for $\tilde{u}$ obtained in § 2.3 and taking $\tilde{\kappa}_n(0) = 0$, this equation was solved numerically to get the linear response of the internal reflectors to seasonal variations in subglacial discharge. A Chebyshev pseudo-spectral method (Trefethen, 2000) was applied to do this using the differentiation matrices in § 3.1.1 to form and solve a linear system for $\tilde{\kappa}_n(x_j)$ at the Chebyshev collocation points. The resulting differences between the steady-state values of k and their perturbed values at $t = 0$ are shown in figure 5.3.

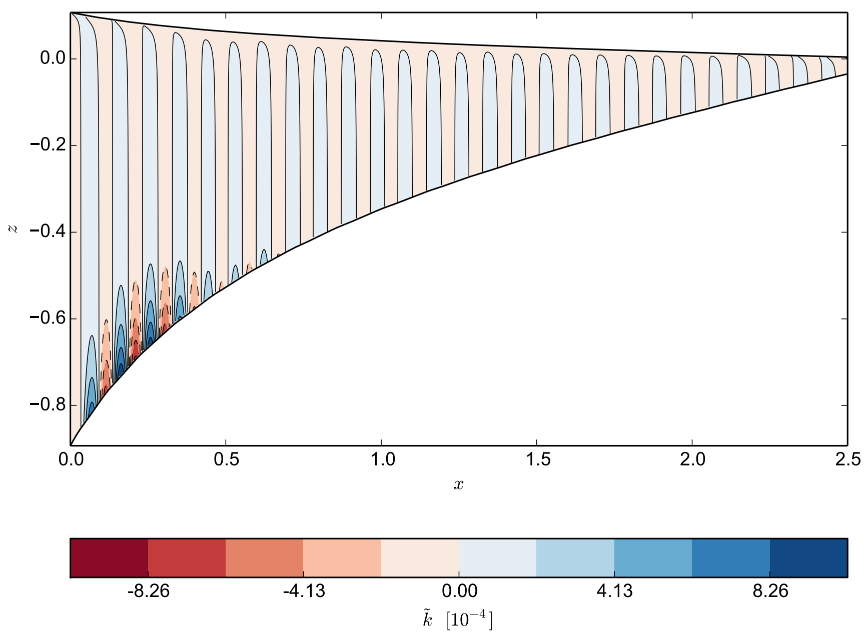

Figure 5.3: Differences ($\tilde{k}$) between the age field of an ice shelf at $t = 0$ when being linearly perturbed by 90% seasonal variation in subglacial discharge, compared to the age field when the shelf is in steady state. The same parameter choices are used in this calculation as in the linear analysis of subglacial discharge forcing found in § 2.3.

The perturbation analysis shows that there would be only very small changes made to the position of the isochrones, with a maximum vertical offset of $\sim 0.2\,\mathrm{m}$ near the base of the ice at the grounding line (less elsewhere) and a horizontal wavelength of $\sim 1.3\,\mathrm{km}$. These would not be noticeable by visual examination and would likely be too small to be detectable by radar. This is unsurprising, as the linear analysis has previously shown that changes to the structure and velocity of the ice shelf would also be too small to notice (§ 2.3). Note, however, that the perturbations to the isochrones are an order of magnitude smaller than those to the ice shelf thickness. This could suggest that the isochrones respond less strongly than the ice shelf as a whole. Equation (5.2) shows that evolution of the age field is controlled by $\nabla_h \cdot \vec{u}$. Subglacial discharge variations thin the ice by melt-induced mass loss and only weakly affect velocity through changes to the ice geometry. Where the isochrones do respond most strongly is near the base of the ice shelf and near the grounding line. This is due to the steady-state isochrones being most tightly spaced at this location and the response to variations in melting being strongest here. For radar to penetrate deep enough to detect internal reflectors at the grounding line would require the use of low frequencies and thus low resolution, making any perturbations difficult to detect.

A similar analysis can be performed using the values of $\tilde{u}$ resulting from seasonal variations in the ice flux crossing the grounding line, as calculated in § 2.4. The differences in the age field (figure 5.4) are much larger in this case and are of the same order of magnitude as the perturbations to the ice thickness. This would offset an isochrone depth by up to up to $\sim 10\,\text{m}$ (with a wavelength of $\sim 1.3\,\text{km}$, as before), which is significant enough to visibly offset the total age field $k = \bar{k} + \tilde{k}$, as can be seen in figure 5.5. These differences may be detectable in radar data. The only ice property by which the age field is effected is the velocity. This is only minimally altered by variations in subglacial discharge, so this had little effect on the age field. However, ice flux forcing takes the form of substantial changes to the ice velocity, resulting in much greater alterations to the age field. Observations of basal ripples would provide insufficient information to distinguish whether they were formed by forcing to the melt rate or to the ice flux. However, the presence or absence of ripples in internal layering data could allow the mechanism to be determined.

5.2 Response in Nonlinear Simulations

Because equation (5.2) is uncoupled from the others describing ice shelf evolution, it can easily be incorporated into the nonlinear solver used to run the simulations in Chapter 3. After the ice shelf has been integrated in each time-step, equation (5.2) can be solved using the updated value of u. As the equation is linear, implicit integration (which enhances numerical stability) is inexpensive and can be performed by solving the linear system

$$\left(1 - \Delta t n \frac{du^{m+1}}{dx} + \Delta t u^{m+1} \frac{d}{dx}\right) \kappa_n^{m+1} = \kappa_n^m, \tag{5.6}$$

where superscripts are indices for the time-step. Arbitrary initial conditions can be specified for κ_n^0 and Dirichlet boundary conditions set the value of κ_n at $x = 0$. The modified version of the NITSOL GMRES routine discussed in § 3.1.3, preconditioned

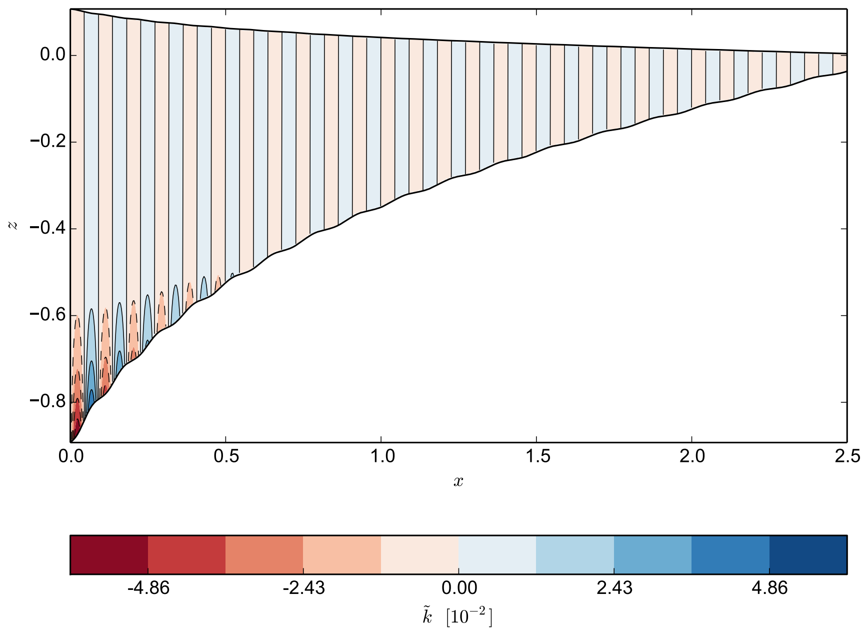

Figure 5.4: Differences ($\tilde{k}$) between the age field of an ice shelf at $t = 0$ when being linearly perturbed by 50% seasonal variation in ice flux across the grounding line, compared to the age field when the shelf is in steady state. The same parameter choices are used in this calculation as in the linear analysis of ice flux forcing found in § 2.4.

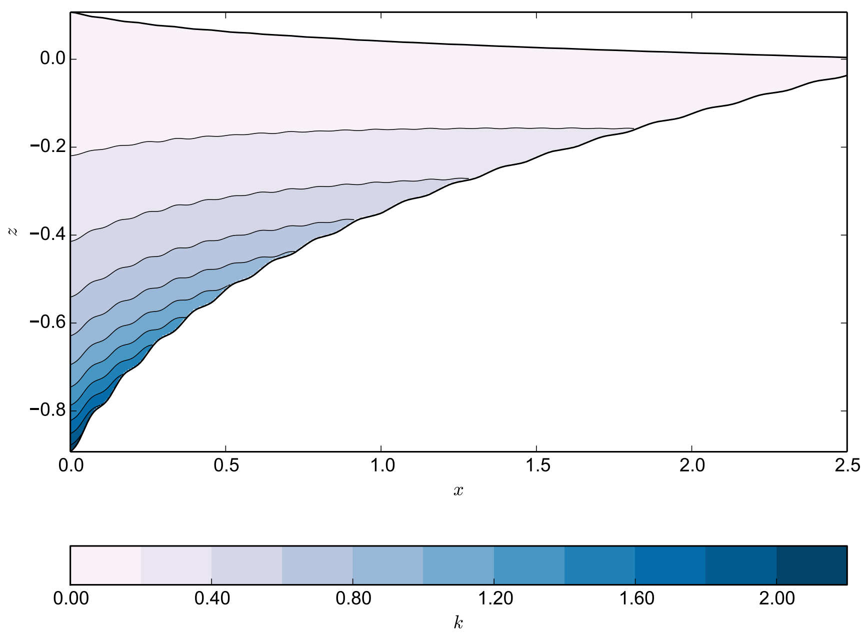

Figure 5.5: The total age field of an ice shelf at $t = 0$ when being linearly perturbed by 50% seasonal variation in ice flux across the grounding line. The same parameter choices are used in this calculation as in the linear analysis of ice flux forcing found in § 2.4.

by solving the tridiagonal matrix representing the finite-difference version of the linear operator in equation (5.6), was used to solve for κ_n^{m+1}. The form of the preconditioner matrix is similar to that in equation (3.21). The solver was tested to ensure the internal layers evolve to the predicted steady state. These simulations did not take significantly longer to run than those without the age field information. However, if run for long periods, noise eventually accumulated in the internal layer data, making it meaningless. The reason for this is unclear and should be investigated in future. In the meantime, useful results can still be obtained before the noise becomes significant.

The steady-state age field is known from equation (5.3), making it unnecessary to re-run a simulation to steady state. Instead, the final output of simulation `ssNeJeDad0` was modified to include the expected layer information. This was then used to initialise a new version of simulation `ifNeJeDa` which computed the effects on the internal reflectors of seasonal forcing of the ice flux crossing the grounding line, with results at time $t = 2.91$ displayed in figure 5.6. It was confirmed that even at this early point in the simulation a statistically steady state had been approximately obtained. The results are similar to those from the linear perturbation analysis in figure 5.5, with ripples in the internal reflectors similar to those in the base of the ice shelf. These are most prominent towards the base of the ice. Near the calving front it can also be seen that an overdeepening has melted through an internal reflector, which remains upstream of the overdeepening.

It was also considered of interest to examine how the age field responds to a sudden change in the grounding line ice flux, as this might produce features which could be seen in radargrams. The modified output of simulation `ifNeJeDa` was used it initialise a new simulation which was identical except that the boundary condition for u at the grounding line was now twice its previous value. The age field at various times during the ice evolution is illustrated in figure 5.7. This shows a sudden discontinuity in the slope of the internal layers (and the base of the shelf) at the ice which was located at the grounding line when the speedup occurred. The discontinuity was the result of faster-flowing ice spending less time exposed to

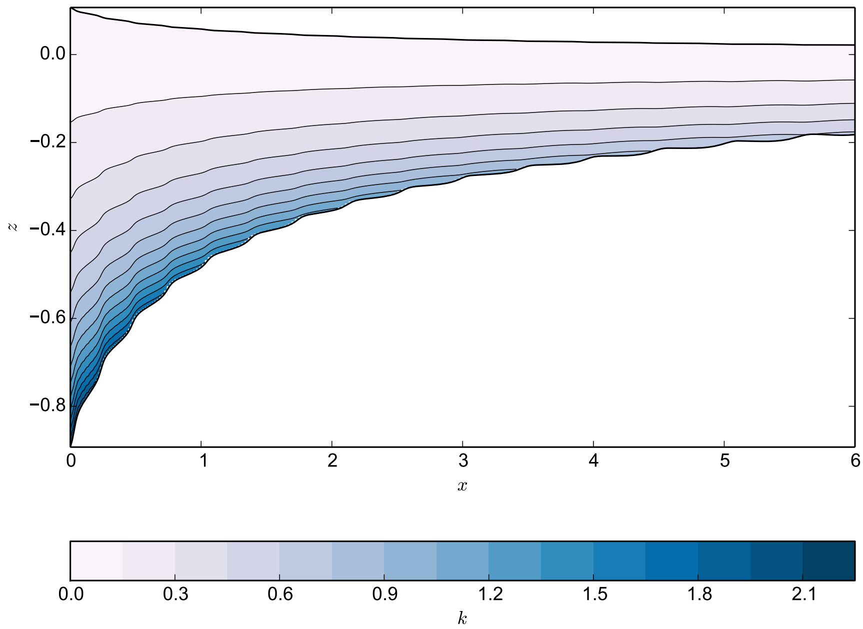

Figure 5.6: The age field (k) of an ice shelf forced by seasonally varying ice flux across the grounding line, shown at the beginning of a seasonal cycle at $t = 2.91$. This was computed by re-running the nonlinear simulation `ifNeJeDa` from Chapter 3 to include the evolution of κ_n for $n = 1, \ldots, 10$.

thinning. The discontinuity was advected along the length of the shelf, eventually leaving the domain and allowing the ice to reach a new steady state. The sharpest discontinuity is near the base of the ice shelf and quickly melts out. This, combined with damping due to stretching of isochrones, weakens the signal downstream.

5.3 Potential Use in Inverse Modelling

As well as providing qualitative insight as discussed above, this formulation may also have use for inverse modelling. A simple way to do this would be to use isochrone information, coupled with the assumption of steady state, to calculate the velocity field of an ice shelf from equation (5.3). By comparing this result to that calculated from ice thickness data using equations (1.7b) and (1.7c), conclusions can be drawn about how close the glacier is to steady state.

Information on even one of the modes of the Taylor expansion would be sufficient to calculate the 1-D steady-state velocity. Consider the $n = 1$ mode. In steady state

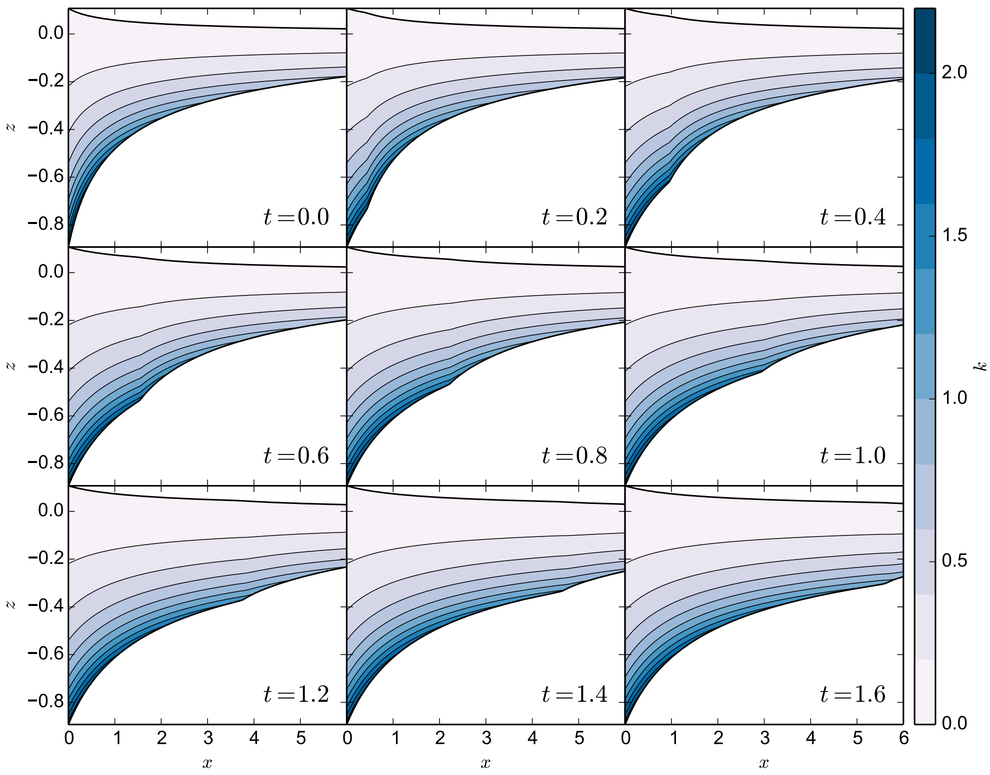

Figure 5.7: The age field (k) at various times during the evolution of an ice shelf experiencing a sudden doubling of the ice flux crossing the grounding line.

this describes deformation due to horizontal stretching and the resulting vertical contraction of a slab of ice. This information, combined with knowledge of ice thickness, is sufficient to allow the mass balance of an ice shelf to be calculated, revealing the melt rate.

While ice velocity can be calculated from equations (1.7b) and (1.7c) using the ice thickness, doing so requires knowledge of boundary conditions, which often must be assumed. However, the only boundary conditions needed to solve equation (5.2) in steady state can be directly measured from the internal layers observed in radar data. Thus, the velocity field can be calculated without assumptions about boundary conditions; indeed, the actual velocity boundary conditions may be determined in this way. Such an approach could yield independent estimates of ice velocity to compare against other methods based on surface feature tracking (e.g. Rignot and Steffen, 2008, and references therein).

Such inverse calculations become much more complex if the assumption of steady state is dropped. However, doing so may allow some information to be gleaned on the history of the ice flow. A simple example of this is that sudden changes in the slope of internal layers, such as seen in figure 5.7, would indicate surges in past ice flow. At present, quantitatively rigorous techniques of this sort have not been developed. The linear response theory in equation (5.5) might provide a useful tool for employing in such inverse calculations. Developing such methods may not be trivial but could provide a wealth of information on ice dynamics, much of which would be of interest to paleo-glaciologists.

5.4 Conclusions on Modelling Internal Reflectors

This chapter develops a method to model the evolution of internal reflectors, represented by a Lagrangian tracer, within a vertically integrated ice shelf model. This could be applied to both linear and nonlinear analysis of ice shelves. It was found that variations in the ice shelf melting rate have only a very weak effect on the structure of internal layers, as the melt does not strongly affect the ice velocity field which drives the evolution of the layers. However, variations in ice flux crossing the grounding line (i.e., ice velocity) drive the formation of ripples within the internal layers similar to those which form on the base of the ice. Examining a combination of internal reflector and ice thickness data may therefore allow ripples formed by varying melting to be distinguished from those formed by varying ice flux. A nonlinear simulation run for ice undergoing a sudden increase in grounding line velocity showed that this would form a discontinuity in the slope of internal reflectors. The presence of such features in observations may provide a record of past changes to ice shelf velocity. In addition to use of this treatment of internal layers in forward modelling, it is hoped that inverse methods may be derived which would allow ice velocity to be calculated from internal layer data. This presents and interesting opportunity for future work.

6

Conclusions on Seasonal Forcing

Contents

6.1 Summary of Results

To date, relatively little has been known about the response of ice shelves to temporal variability in their environment. The previous chapters have presented the first systematic investigation of how oscillations in subglacial discharge and ice flux crossing the grounding line alter ice shelf structure and its coupling to the underlying plume. In particular, they represent an attempt to determine whether such forcing could give rise to the transverse basal channels observed under Pine Island Ice Shelf by Bindschadler, Vaughan, et al. (2011).

The 1-D linear analysis performed in Chapter 2 showed that seasonal variability in both subglacial discharge (of amplitude 100%) and ice flux (of amplitude 50%) could alter the thickness of an ice shelf and provided understanding of the physical mechanisms responsible for such changes. Such forcing caused the formation of ripples in the ice of size $\sim 1\,\mathrm{m}$ and $\sim 10\,\mathrm{m}$, respectively, on a Petermann-like ice shelf 30 km long, 600 m thick at the grounding line, and with melt rates of $18\,\mathrm{m\,yr^{-1}}$. Variations in subglacial discharge caused the melt rate to oscillate across the length of the ice shelf. Ice which entered the domain when the melt was low thus tended to be thicker than that which entered when the melt rate was high, leading to the superposition of ripple-like perturbations on the background ice thickness gradient. The varying melt rate caused global oscillations to the ice thickness on a seasonal basis as well. Varying ice flux also caused ripples to form because high-flux (i.e., fast moving) ice spent less time exposed to thinning by stretching and melting and thus was thicker than low-flux (slow moving) ice. Global thickness oscillations were present in this case too, but were not very large except near the grounding line.

Increasing the melt rate led to larger ripples in both cases, while increasing the rate of stretching led to larger amplitude ripples in the ice flux case but not the subglacial discharge case. The ripple amplitude was inversely proportional to the frequency of the forcing in both cases, as a longer period provided more time for perturbations to accumulate. The wavelength of the ripples was also found to be inversely proportional to the frequency, related by the background ice velocity. In both cases, the ripples were too small to cause channels such as those seen under PIIS and could only change the level of the upwards ice-slope rather than create overdeepenings. However, the ice-flux derived ripples had some resemblance to the basal terraces observed by (Dutrieux, Stewart, et al., 2014), albeit with a much larger wavelength for annual forcing. It may be that shorter period forcing coupled with higher melt rates would be able to explain the formation of basal terraces. This analysis could not rule out the possibility that a nonlinear process which was not captured would cause the ripples to grow into channels.

To address this, a nonlinear solver for the 1-D coupled ice shelf and plume equations was developed and tested, as described in Chapter 3. This was applied to an ice shelf 1200 m thick at the grounding line, with a domain length of 80 km, and a melt rate of $\sim 10\,\mathrm{m\,yr^{-1}}$. This roughly corresponds to an ice shelf with Pine Island-like geometry but a cold cavity. Interestingly, depending on the initial conditions of the ice shelf, evolution to steady state could give rise to a shock-like feature in the plume. Unfortunately, analysis of subsequent development after shock formation was not possible as the shock caused convergence issues in the nonlinear solver. Simulations forced by variations in subglacial discharge behaved in much the same way as predicted by the linear analysis, producing ripples of similar amplitude. The main difference was that there was a bias towards the ice shelf becoming thicker. This was due to nonlinearities in the relationship between subglacial discharge and the resulting plume velocity. This meant reductions to discharge reduced the melt rate more than increases to discharge amplified it.

The ice flux simulations also produced similar amplitude ripples as their linear counterparts. However, a feedback between the thickness perturbation and the melt rate caused the ripples to begin growing into overdeepenings towards the end of the domain. This represents an instability mechanism potentially capable of growing channels, although it may be an artefact of neglecting hydrostatic forces on the plume (which was necessary for numerical convergence). A simplified dynamical relationship was derived to explain the impact of varying ice flux on ice thickness perturbations: equation (3.44) for Newtonian viscosity, or equation (3.47) for Glen's Law rheology. These equations show that varying ice flux changes the time over which a parcel is subjected to background stretching and melting, which drives ripple growth, whilst the impact of perturbations on modifying the stretching drives perturbation decay and nonlinear rectification. Even without the feedback and overdeepening, the ripples remain reminiscent to basal terraces. The above results proved relatively insensitive to choices of ice viscosity and plume entrainment parameterisation. There was a small increase to the ice thickness when using Glen's Law ice rheology due to reductions in stretching.

The 1-D simulations described above were incapable of capturing the inherently 2-D channelisation feedback believed to be responsible for the growth of longitudinal basal channels. For this reason, a "horizontally-integrated" plume model was developed in Chapter 4, which sought to include the Coriolis force and transverse velocity component in a set of 1-D plume equations. By averaging 2-D plume equations across a lateral cross-section, a model was derived for along-slope variations of a meltwater plume including lateral flow driven by Coriolis forces and lateral export into an assumed boundary current. This model was found to depend on assumptions about the transverse shape of the plume variables which control $O(1)$ shape factors, as often occurs in plume models (Manins and Sawford, 1979, e.g.). Initially the transverse shape was assumed to be nearly uniform and turbulent diffusion was set to zero. Integrating the resulting initial value problem revealed the plume to undergo transient evolution in a narrow region near the grounding line, before reaching an asymptotic state with the plume flowing in a predominantly across-shelf direction. Simple analytic solutions were determined for the asymptotic state, which were independent of x for a planar slope. They also gave good agreement when applied to an ice shelf with slowly varying slope.

Such solutions revealed a dependence on the width over which the horizontal integration was performed, suggesting non-uniform variations in the transverse direction. Hence, the model was refined, with the transverse shape determined in the asymptotic regime by solving a new initial value problem in y. These results were used to set shape parameters in the horizontally-integrated equations, yielding surprisingly good agreement with the flow structure when comparing with the results of a fully 3-D ocean model, given the simplicity of the theory. Running a coupled simulation with a co-evolving ice shelf and horizontally-integrated plume showed a similar response to seasonal forcing as seen in Chapter 3. However, no overdeepenings developed in the ice flux simulation, with the ripples failing to channelise flow in the across-shelf direction but instead directing it to be more strongly in the longitudinal direction. This mutes the feedback between ripple geometry and melt seen for 1-D plume flow.

The results of these chapters suggest that seasonal variations in subglacial discharge are not able to cause large changes in ice geometry, acting on their own. However, the simulations were run in a relatively low-melt regime and changes might be more significant in a high-melt case. Variations in ice flux produce more noticeable changes to the ice thickness than variations in subglacial discharge. It appears unlikely that these mechanisms on their own could give rise to transverse channels of the sort observed by Bindschadler, Vaughan, et al. (2011), as they are unable to channelise the plume flow. However, they may be involved in the formation of basal terraces like those observed by Dutrieux, Stewart, et al. (2014). It is also possible that small amplitude ice thickness variations may perturb the stress state, leading to crevasse formation (as proposed by Vaughan et al., 2012). Whilst the ripples have small amplitude, they may be the first points to fail if the ice approaches the threshold for failure.

Finally, Chapter 5 presented a new approach to capturing the evolution of internal reflectors/isochrones in a vertically integrated glacier model. An evolution equation was derived for a Taylor series expansion of the ice pseudo-age in z, suitable for application with vertically integrated ice flow models. Proof-of-concept results were given for a 1-D steady state, periodic time-dependent linear perturbations (both from Chapter 2), and nonlinear simulations (from Chapter 3). These showed that variations in subglacial discharge would have only very small effects on the internal reflectors, as they do not directly alter the ice velocity. However, changes to the ice flux could produce detectable perturbations. This suggests that the origin of ripples on the base of an ice shelf can be determined by whether similar ripples are present in the internal reflectors.

6.2 Avenues for Future Research

The modelling work presented in this thesis could interestingly be extended to account for additional effects not considered here. Though it appears unlikely that these seasonal variations could cause channelisation, it has not been ruled out that this could occur in a regime with stronger melting. Numerical instabilities prevented such a simulation from being run, but it could be worth pursuing in future via a modified numerical approach. It might also be interesting to explore interactions between varying subglacial discharge and ice flux, to see if these forcings would tend to cancel each other out, as speculated in § 3.6. For completeness, the effects of the three equation melt parameterisation and a halocline and/or thermocline in the ambient ocean conditions could be explored. The latter is particularly interesting, as it would alter the steady-state shape of the ice shelf. It would also be possible to use the present nonlinear code to consider oscillating thermocline depth, which Holland (2017) noted caused significant changes to ice shelf melt rate even when occurring over a short period (e.g., with seasonal frequency). The simulations in which ice flux varied did not account for movement of the grounding line, which would alter ice evolution by changing where melting and stretching can begin to occur. As such, it would be interesting to run a simulation which includes grounding line motion. This can be done by coupling a grounded ice sheet and floating ice shelf model, with the domain of each stretching as necessary to reach the instantaneous grounding line location, as described by Schoof (2007).

If seasonal variability does not give rise to the transverse channels observed by (Bindschadler, Vaughan, et al., 2011), (Sergienko, 2013) suggested a spontaneous process due to transverse ice slope arising from stress at the side-walls of the ice shelf, which remains a possibility. It is also possible that the channels form from periodically spaced crevasses in the ice shelf base. Periodic crevasse spacing corresponding to time-scales other than one year has been observed by (McGrath, Steffen, Scambos, et al., 2012) and (Luckman et al., 2012). If the PIIS channels do form from crevasses then the annual spacing would just be a coincidence.

A plume was observed to undergo a possible hydraulic jump in Chapter 3. This could be interesting to explore in more detail on a macro scale (e.g. with a shock-capturing numerical scheme) and on the micro scale to determine if such jumps enhance mixing under the ice. It would not be necessary simulate a plume across the entire length of the ice shelf for this purpose; a small region featuring a discontinuity in the ice slope would be sufficient.

The horizontally-integrated plume model presented in Chapter 4 offers ample opportunity for further development. One immediately apparent step would be to solve for a plume in which the transverse shape is allowed to vary in x. This could be done by calculating the shape factors at each location using the local basal slope. However, this relies on the assumption that the plume is in an asymptotic state in order to calculate the shape coefficients. As such, it would be useful to consider the fundamental fluid mechanics at play throughout the plume in the hopes of deriving parameterisations for the shape coefficients which would hold in the transient regime as well (e.g., expressing them as functions of dimensionless numbers).

Even without these improvements, the horizontally integrated model was found to agree remarkably well with an existing 3-D ocean simulation of an ice shelf cavity. The conditions of that simulation (e.g., transverse variations in the ice shelf slope) could not be reproduced exactly in the horizontally-integrated model, so it would be worthwhile to explicitly consider the effect of transverse variability to provide a better comparison. It may be possible to reformulate the horizontally-integrated model so that it can account for ice shelf slope in the transverse direction. Given that the plume model is able to calculate melt rates that are nonuniform across the width of the ice shelf it could be useful to develop a horizontally-integrated ice shelf model which can respond with the thickness becoming nonuniform in the transverse direction as well.

There has recently been interest in developing simple parameterisations with which to calculate the melt rate under ice shelves in continental-scale ice models for Antarctica (e.g. Lazeroms et al., 2018). It may be possible to adapt the horizontally-integrated model for this purpose by formulating it with non-uniform cavity widths so it can handle non-idealised geometries. As the horizontally-integrated model assumes outflow at the upper y-boundary, it is unable to capture the boundary current which typically forms within ice shelf cavities. One way to address this could be to split the cavity into two coupled horizontally-integrated plumes which would be solved simultaneously. One of these would be equivalent to the existing model. However, the other would have an impermeable upper y-boundary and a lower inflow y-boundary set to receive the transverse outflow values of the first plume.

As speculated upon in § 5.3, the vertically-integrated model developed for the evolution of internal reflectors may have uses for data assimilation and inverse modelling. Initially it might provide an additional data source against which to compare estimates of instantaneous ice velocity based on thickness and direct measurements from the surface. Formulating such an inverse model would be trivial for the 1-D case using equation (5.3) and should not be overly difficult for the 2-D case. While significantly more challenging, it may also be possible to use the time-dependent form of the model to deduce past motion of ice from an instantaneous present day measurement of the internal reflectors.

Appendices

A

ISOFT: A Coupled Ice Shelf/Plume Code

Contents

In order to run the nonlinear simulations described in Chapters 3 and 4, a new piece of software was written and released under the GNU General Public License, version 3. This software, called ISOFT (Ice Shelf/Ocean Fluid and Thermodynamics), attempts to provide an object oriented, extensible framework with which to model glacial flow using modern Fortran (MacMackin, 2018a). Though developed for ice shelves, it could in principle be modified to simulated grounded ice dynamics as well.

This appendix provides an overview of the structure of ISOFT and an explanation of the design choices made, in the hope that it might be useful in others' work. It is limited to a discussion of code architecture, with numerical methods already having been described in § 3.1. A number of design patterns were consciously used when developing ISOFT. Design patterns, popularised for use in software development by Gamma et al. (1994), attempt to provide a standard approach to solving commonly-arising types of problems. The names of these are indicated in the text by small-caps. An understanding of object oriented programming techniques in general and object oriented features in Fortran, in particular, will be useful when reading these notes; see, for example, Rouson et al. (2014). Familiarity with Universal Modelling Language (UML) diagrams will also be helpful (e.g. Rouson et al., 2014, Appendix B). Note that, in the UML diagrams in this appendix, names of derived types are shown in camel case, as is the convention for class names in most object oriented languages. However, as Fortran is case-insensitive, the decision was made to use underscore separation within the code.

In essence, the purpose of ISOFT is to integrate equation (3.1) forward in time to simulate the evolution of an ice shelf. To do this, the basal melt rate must be calculated by solving plume equations (3.6) or (4.5). ISOFT could easily be modified to make the plume equations time-evolving, although running such a model would require a very short time-step and thus be computationally expensive. As much as practical, ISOFT was kept agnostic as to whether it was handling a 1-D or a 2-D representation of an ice shelf/plume. However, the current implementation does explicitly assume a 1-D system in a number of instances and would thus need to be modified to handle 2-D problems.

The 1-D simulations were sufficiently fast that they could be run in serial. Multithreading could easily be implemented in many parts of the code where arithmetic is performed on arrays. Indeed, most of these cases are simple enough that a compiler may be able to parallelise them automatically. More sophisticated approaches involving message passing would likely be necessary to make 2-D simulations practical, but this would be far more difficult to implement and would likely require substantial refactoring of the code. In particular, the nonlinear solvers discussed in § A.3 would likely need to be replaced.

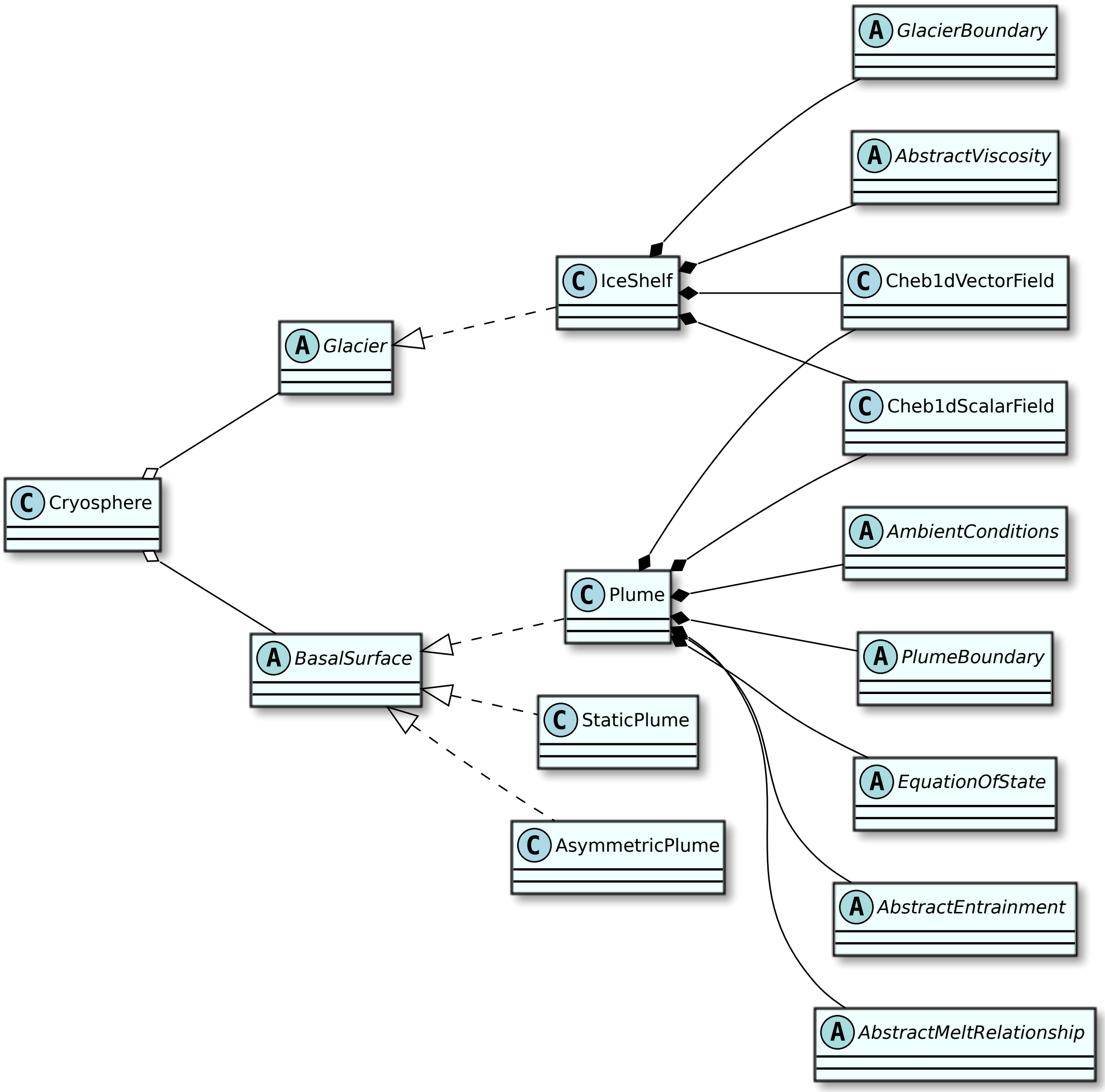

Figure A.1: A UML class diagram illustrating the relationships between the key derived types used in ISOFT. Components and methods of the types are not shown for reasons of space. A "C" next to a type name indicates that it is a concrete implementation of a class, while an "A" indicates an abstract class.

A.1 Representing the a Couple Ice Shelf/Plume

ISOFT uses a large number of *derived types* (equivalent to *classes* in other object oriented languages) in order to model the full glacial system (see figure A.1). The system as a whole is contained within a `cryosphere` type, with methods for saving/loading data to/from the disk as HDF5 files and for integrating forward in time. The `cryosphere` (figure A.2a) contains objects of abstract classes `basal_surface` (figure A.2b) and `glacier` (figure A.2c), the latter representing a glacier

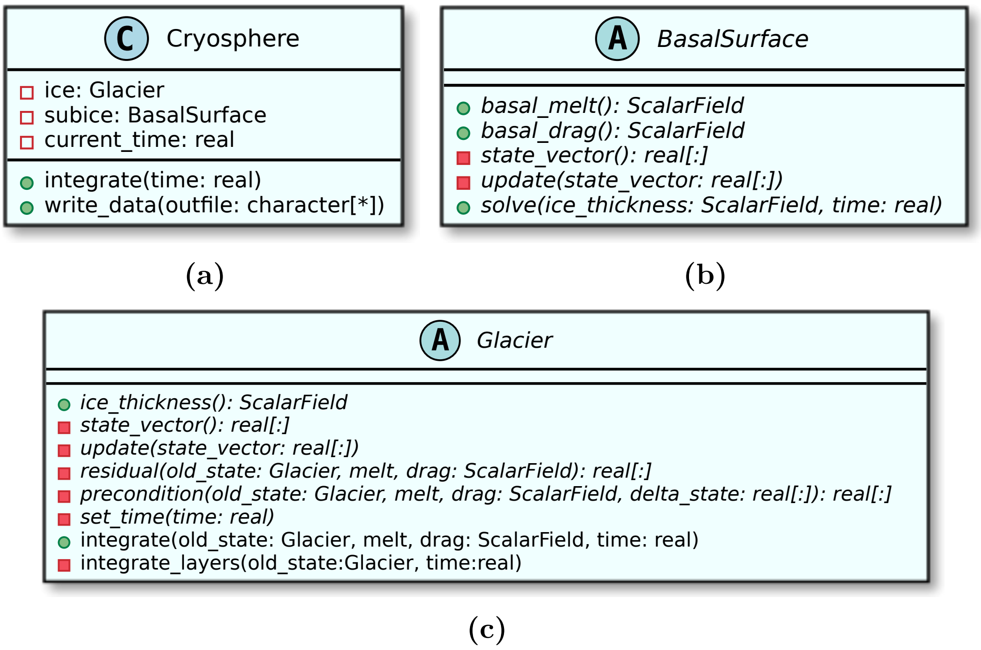

Figure A.2: UML class diagrams for the cryosphere (a), basal surface (b), and glacier (c) derived types, providing a simplified description of the methods associated with each. Red squares indicate private components while green circles indicate public ones which may be accessed in modules other than the one defining the class. Open symbols indicate data components while filled ones indicate methods.

and the former representing whatever is underneath it. Objects of these types have their own methods for reading and writing data, integration, and accessing useful information. Both are general enough to allow ISOFT to model either floating or grounded ice.

The only concrete existing implementation of the `glacier` class is the `ice_shelf` type. As its name suggests, this models the behaviour of an ice shelf. While the implementation of the continuity equation is agnostic towards whether the model is 1-D or 2-D, at present the ice momentum equation is explicitly 1-D. Ideally this will be fixed in the future. The `ice_shelf` type may optionally feature a Lagrangian tracer, assumed to indicate the age of the ice as would be measured from internal reflectors (as described in Chapter 5). There is stub for a grounded `ice_sheet` type, but its methods have not been implemented.

A few implementations of the `basal_surface` class are available. The most commonly used of these is the `plume` type, modelling the 1-D subglacial plume used for simulations in Chapter 3. In principle this can model a second velocity component, but such a model is physically unstable. There is also the `static_plume` type, which does not evolve from the state with which it is initialised or has loaded from saved data. This is useful if a simulation is to be performed with a fixed melt rate. The `asymmetric_plume` provides an implementation of the horizontally-integrated model described in Chapter 4. Various parameters describing the transverse profile of this plume are provided through the associated `plume_shape` derived type. Finally, a `ground` type exists as a stub, which could be fully implemented in future to provide a basal surface with frictional information for a grounded ice sheet.

All of these implementations contain *field types* (see § A.2) for each variable describing their state. They also contain objects representing the boundary conditions and choices of parameterisations, described in more detail in § A.4. This is illustrated in Figure A.3, showing the state of the objects at the beginning of a representative simulation. The `cryosphere` class is a PUPPETEER pattern which, as described by Rouson et al. (2014), coordinates interactions between various other classes (`glacier` and `basal_surface`, in this case) without them needing to directly interact with each other. Thus, interdependencies between different modules of code are simplified. For each time-step, the following sequence of steps occurs, as illustrated in figure A.4:

1. The `cryosphere` first gets the ice thickness from the `glacier`.

2. This information is sent to the `basal_surface` object, with which it can solve for its state at the current time using the QLM solver.

3. The `cryosphere` gets the current melt rate and/or friction parameters from the `basal_surface`.

4. This information is sent to the `glacier` object, where it is used to integrate its state forward in time with NITSOL.

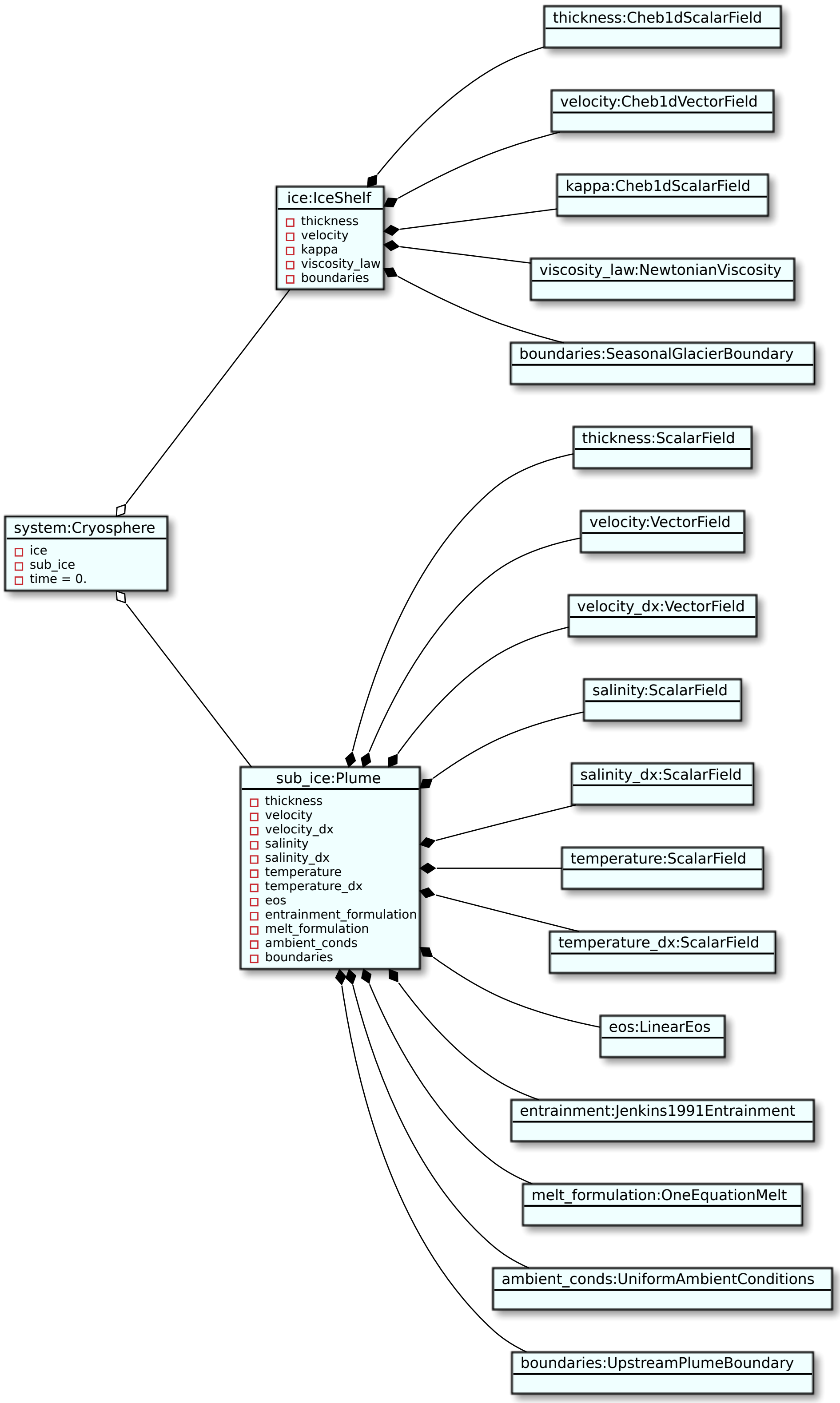

Figure A.3: A UML object diagram displaying the state of simulation `ifNeJeDa` immediately after it has been initialised. Not all components are shown in each object for reasons of space.

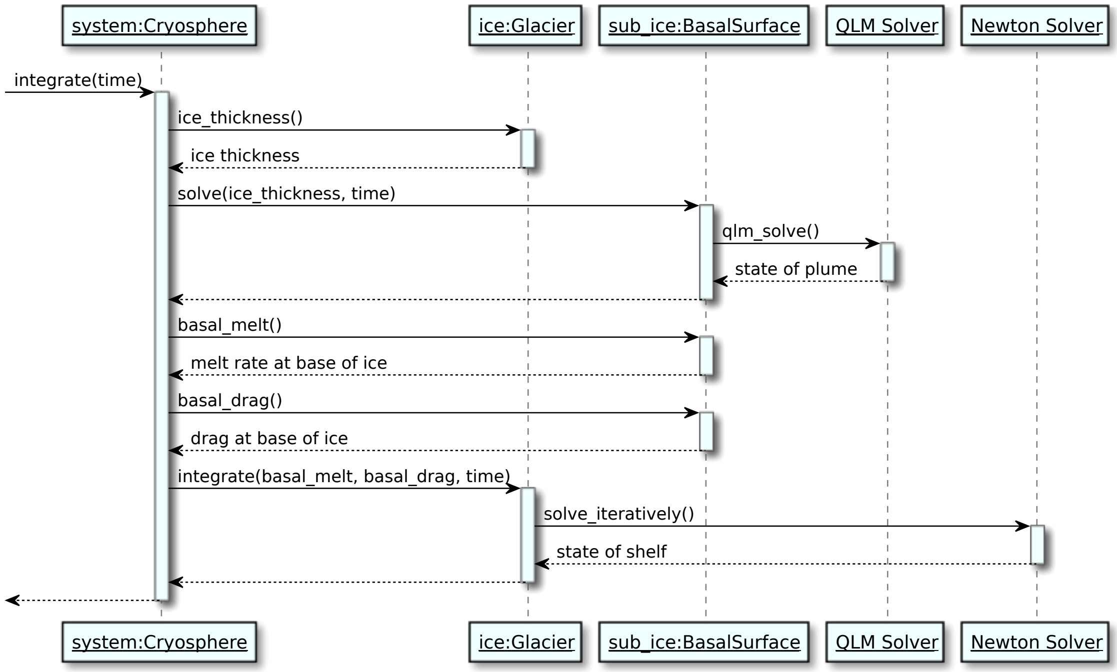

Figure A.4: A UML sequence diagram illustrating the operations involved in each time step of ISOFT. Some of the argument lists have been simplified for reasons of space.

A.2 Discretisation

Spatial derivatives of the variables describing the state of the ice shelf and plume are frequently needed. Multiple approaches exist to discretise these variables and compute their gradients (e.g. finite difference, finite element, pseudospectral, etc.) and the desire was to avoid restricting ISOFT to a particular one. To this end, the Abstract Calculus design pattern, described by Rouson et al. (2014, Chapter 6), was adopted. This design pattern attempts to resolve the disconnect between high-level mathematical notation and the low-level representation of data and operators in code. A hierarchy of derived types was written representing mathematical fields of both scalar and vector quantities (see figure A.5). These fields overloaded all of the standard arithmetic and intrinsic mathematical functions, as well as offering methods for various differential operators. Calculations involving these field types could then be written to be agnostic with regards to field geometry or discretisation technique. In order to send field data to external libraries of numerical methods, such as NITSOL, methods were also provided to return them

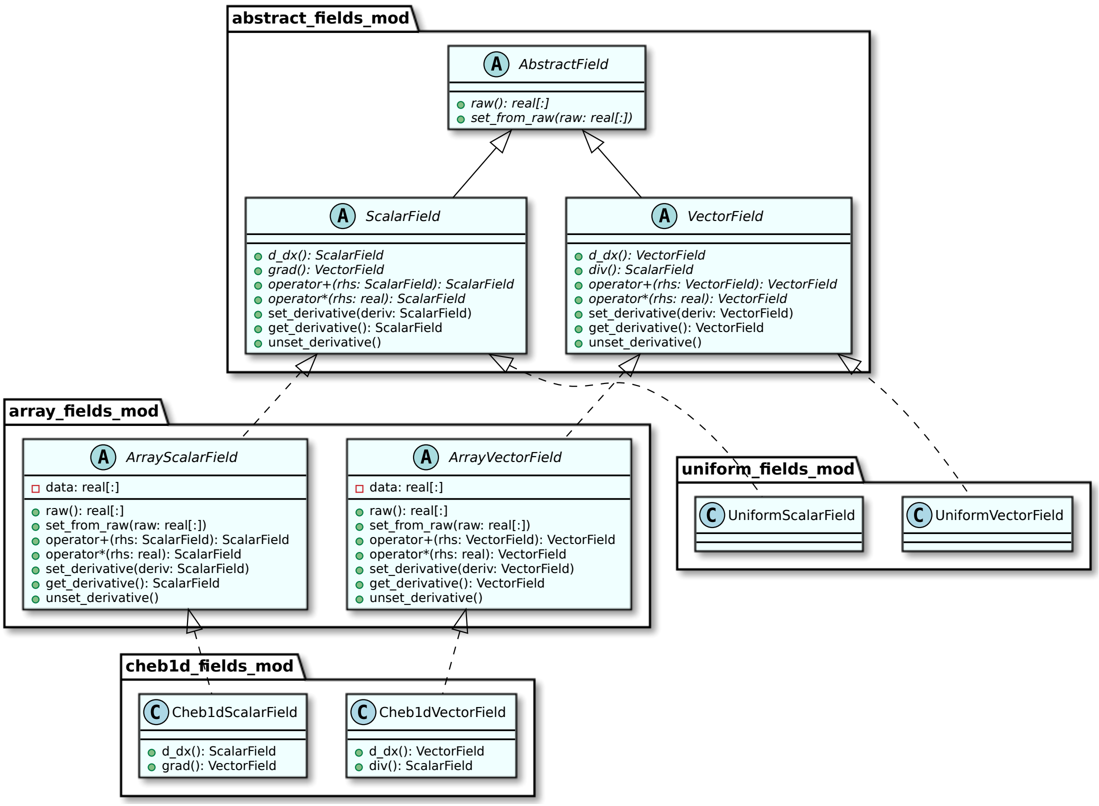

Figure A.5: A UML class diagram for the field types, showing a few notable methods. The uniform field types implement all inherited abstract methods, but these are not shown for reasons of space.

as an array of double precision values.

Properties such as geometry and discretisation are specified within the concrete implementations of the field types. As shown in figure A.5, two groups of these concrete field types exist. The first is the `cheb1d_scalar_field`/`cheb1d_vector_field`, which offers a 1-D field on a Chebyshev grid. The Chebyshev pseudo-spectral method, described in § 3.1.1, is used to calculate derivatives, with Fast Fourier Transforms performed using the FFTW3 library (Frigo and Johnson, 2005). These were subtypes of the abstract classes `array_scalar_field`/`array_vector_field`. The `array` field types provide standard implementations of arithmetic and mathematical functions, leaving only those methods involving grid-layout or calculus to be implemented by concrete type-descendents. This allows easier creation of new field types with reduced code duplication. The other pair of concrete field types are `uniform_scalar_field`/`uniform_vector_field` which, as the names suggest, are uniform throughout all space. These were written to allow some optimisation for cases where a variable proves to be uniform.

The hope was that ISOFT could remain agnostic about which concrete type of field is being used. However, bugs in the version of the `gfortran` compiler used (v6.2.0) made this impossible and in many situations the `cheb1d` implementations are explicitly specified. As a result of this (and some lazy code design) ISOFT has come to depend on using those particular implementations in a number of areas, particularly around preconditioning (see § A.3). However, relatively minor refactoring should allow this issue to be resolved in future.

Despite the conceptual elegance of the Abstract Calculus design, a number of practical issues mean it was likely a mistake to use it so extensively within ISOFT. First is the problem of compiler bugs, mentioned earlier. One of these resulted in memory leaks when a dynamically-allocated field object was returned from a function call. A workaround using an Object Pool was ultimately found. The Object Pool pattern passes pointers to preallocated objects, rather than creating new ones, and releases them back to the pool once they are no longer being used (Grand, 2002, Chapter 5). This avoided memory leaks but required frequent calls to book-keeping functions which ensured objects were released to the pool at the appropriate time. These calls eliminated much of the elegance of Abstract Calculus. Furthermore, overloading the arithmetic operators introduced overhead and likely prevented the compiler from making many optimisations. With hindsight, a better approach would have been to store the data in standard Fortran arrays and have calculus functions provided by a set of derived types according to the Strategy pattern (discussed in § A.4).

However, one situation in which using the field types proved useful was when implementing automatic differentiation (Neidinger, 2010). This works by applying the chain rule to the arithmetic operations and elementary mathematical functions applied to data in order to calculate the derivative of the result with respect to one or more pieces of the data used to produce it. The simpler of the two approaches to doing this is to overload the arithmetic operators and elementary functions to propagate the derivative using the chain rule.[1] Consider ordered pairs of the form $\langle u, u' \rangle$, where u is some value u' is a differential associated with that value. Then:

$$\begin{aligned}\langle u, u' \rangle + \langle v, v' \rangle &= \langle u + v, u' + v' \rangle,\\ \langle u, u' \rangle \times \langle v, v' \rangle &= \langle uv, u'v + uv' \rangle,\\ \sin\langle u, u' \rangle &= \langle \sin u, u' \cos u \rangle,\\ &\vdots\end{aligned}$$

with all other arithmetic and mathematical functions similarly overloaded. As the field types already provide overloading of these operators and routines, adding automatic differentiation required less effort to implement than would otherwise have been necessary.

Automatic differentiation was provided as an optional feature, which the abstract field types support but which subtypes are not required to implement; if the feature is not implemented in a subtype then trying to use the default implementation in the abstract class will result in a run-time error. Methods are provided with which one field can be used to set the derivative values for another. If the derivative for a field has been set then it will be propagated through all subsequent mathematical operations involving that field. Otherwise, no automatic differentiation occurs. The derivative value of the result can be retrieved with a getter method. Automatic differentiation is turned off with a method which clears the derivative information. The `array` fields and their subtypes provide automatic differentiation, but the `uniform` fields do not.

These field types were sufficiently general that they could be used in a number of settings other than ISOFT. As such, they were written as a separate library called FACTUAL (Fortran Abstract Calculus Types, Usable and Aesthetic Library). This is distributed with ISOFT but can also be downloaded on its own.

[1] The other technique, known as *source transformation*, automatically rewrites the entire code prior to compilation so that propagation of the derivative is performed inline.

A.3 Nonlinear Solvers

A.3.1 Ice Shelf Solver: NITSOL

As described in § 3.1.2, when integrating the ice shelf the nonlinear solver NITSOL (Pernice and Walker, 1998) was used. This is a legacy package written in FORTRAN77. ISOFT contains an explicit interface to the main NITSOL subroutine so that arguments can be checked by the compiler when it is invoked. NITSOL takes as an argument a subroutine which receives the current estimate of the state of the system and returns the corresponding residual according to equation (3.18) or (3.22), depending on whether solving for the ice thickness or velocity. The state of the system and the residual are both represented as 1-D arrays of real values. When the state array is received by the residual subroutine it is used to update the value of a field type (see § A.2). Operations are performed using the field type to calculate a residual field. A 1-D array containing the data of the residual field is then extracted and returned by the subroutine.

For NITSOL to converge it required a preconditioner which inverts the Jacobian operator $\mathcal{D}_x A \equiv \partial A/\partial x + A\Delta_x$ (where Δ_x is the differential operator in the x-direction). NITSOL receives the preconditioner as an additional subroutine which takes as an argument an array to be preconditioned and returns the result of that preconditioning as an array. Similarly to the calculation of the residual, the preconditioner subroutine converts the array to a field type, performs the preconditioning, and then converts back to an array. As described in § 3.1.2, the operator can be inverted by solving a tridiagonal matrix approximating the Jacobian using finite-difference discretisation. A derived type called a `jacobian_block` (figure A.6a) was written to encapsulate this process, reinitialised every time a new value of A is needed by the operator. This derived type is also able to represent two variations on the $\mathcal{D}_x$ operator: $\alpha + \mathcal{D}_x X$, where α is a scalar; and $\mathcal{D}_x A\Delta_x$. In addition to inverting the operator on a field, `jacobian_block` objects can apply the forward operator to fields.

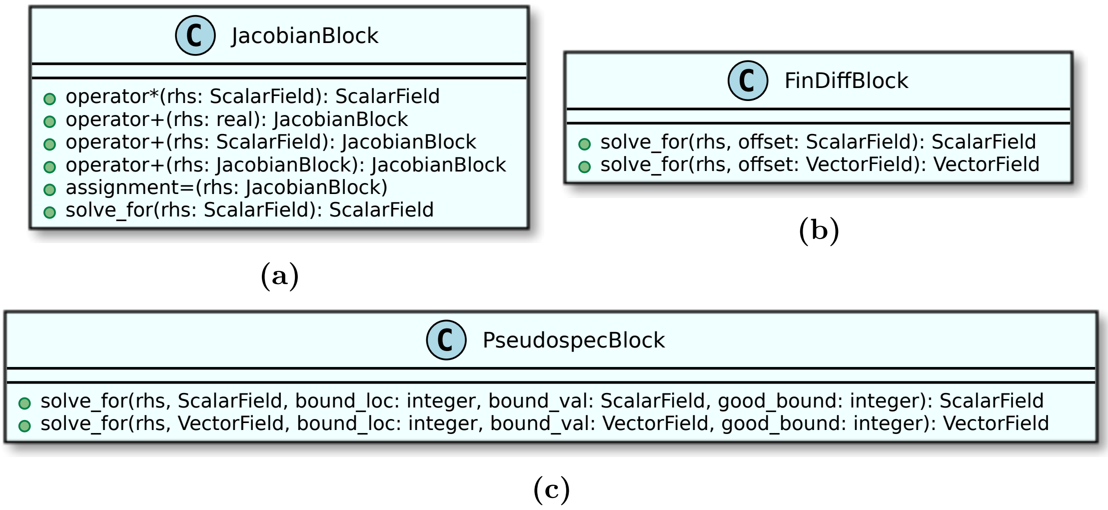

Figure A.6: UML class diagrams for the various derived types used in preconditioning nonlinear solvers. They have conceptually-similar interfaces, but differences exist due to the somewhat ad-hoc way in which they were developed.

A.3.2 Plume Solver: QLM

The plume is solved using the quasi-linearisation method (QLM), as described in § 3.1.3. As the QLM is an obscure algorithm, a custom implementation was written in modern Fortran for ISOFT. It takes as arguments functions representing the linear and nonlinear portions of the nonlinear system of ODEs being solved. It also requires a function which computes the product of the Jacobian of the nonlinear operator with an arbitrary state vector and, optionally, a preconditioner function. All of these operate on and return arrays of real data. The QLM requires solving a linear system at each iteration and this is done using a slightly modified version of the GMRES implementation in NITSOL. The modification allows the GMRES solver to use an initial guess of the solution to the linear system, rather than assume a good initial guess to be zero (as made sense in the context of NITSOL). An explicit interface was written to this FORTRAN77 implementation, along with a wrapper which makes many of the arguments optional, automatically creates the necessary work arrays, and allows for less verbose definitions of the linear system.

Much as when solving for the state of the ice shelf, the linear and nonlinear plume operators take 1-D arrays of real values as arguments. They then use a method of the `plume` class to update the various fields representing the plume variables from this array. The necessary mathematics is performed using these fields and the results converted back to 1-D arrays which are then returned to the QLM solver. The preconditioner works by inverting the linear operator of the plume, taking the anti-derivative of each variable. A derived type called the `pseudospec_block` (figure A.6c) was written to apply this to field types, reversing the Chebyshev differentiation algorithm described on page 84. A similar derived type called `fin_diff_block` (figure A.6b) was also written which performs the same operation using a tridiagonal matrix representing a finite-difference approach to differentiation. However, the much greater accuracy and comparable computational cost of the `pseudospectral_block` made it the better choice.

As mentioned in § 3.1.3, it was found that, to get the level of accuracy needed for the plume solver to converge, the product of the Jacobian could not simply be evaluated using a finite difference approximation. Instead, the automatic differentiation feature of the field types described in § A.2 was used. The vector to be multiplied by the Jacobian is used to provide derivative values for the plume variables. The nonlinear operator is then applied for the current plume state, with the overloaded operators of the field types applying the chain rule at each step to propagate the derivative. The derivative of the operator result will then be the product of the Jacobian and the initial vector.

A.4 Parameterisations and Boundary Conditions

One of the goals of ISOFT is to allow choices of parameterisations to easily be changed. This is achieved using the Strategy pattern (Rouson et al., 2014, Chapter 7), which provides a common abstract interface to accomplish some task, with subtypes implementing different strategies to do so. In ISOFT, the methods in the abstract types were generally given a large number of arguments, to ensure sufficient information is available for all potential parameterisations. Parameter and coefficient values can be specified for each parameterisation when initialising its object.

The only parameterisation for the ice shelf is viscosity (figure A.7). The general interface is provided by the `abstract_viscosity` type. It's subtypes are

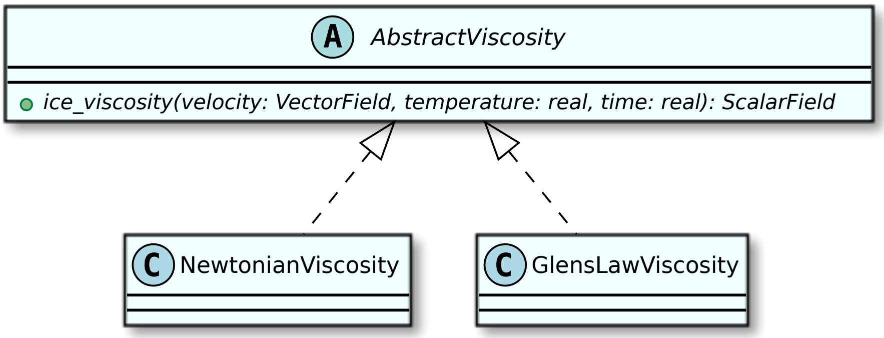

Figure A.7: A UML class diagram for the viscosity type. Subtypes implement all inherited abstract methods, but this is not shown for reasons of space.

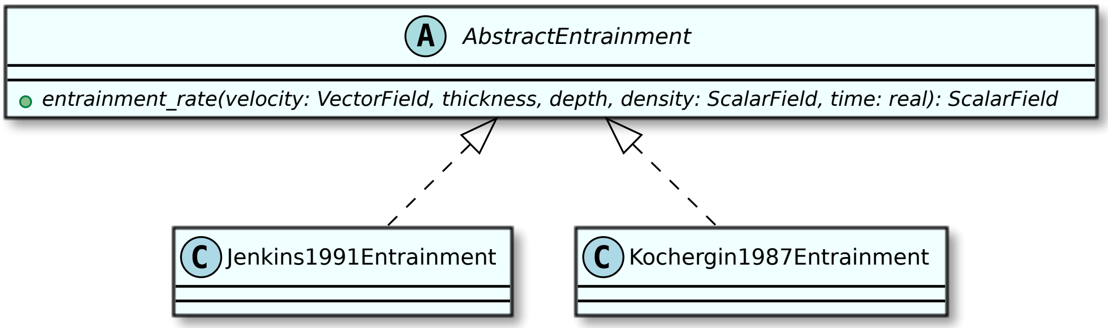

Figure A.8: A UML class diagram for the entrainment type. Subtypes implement the inherited abstract method, but this is not shown for reasons of space.

`newtonian_viscosity`, which returns a `uniform_field` in all cases, and `glens_law_viscosity` which calculates the viscosity from the ice velocity as described in equation (1.3). Currently Glen's law is only implemented for the 1-D case, as attempting to implement it for higher dimensions resulted in a compiler bug.

The plume contains a few parameterisations. The subtypes of `abstract_entrainment` calculate an entrainment rate for the plume (figure A.8). These are `jenkins1991_entrainment` and `kochergin1987_entrainment`, implementing equations (1.11) and (1.12), respectively. The `abstract_melt_relationship` (figure A.9) provides an interface for calculating the melt rate of the ice, in addition to the heat and salt fluxes resulting from melting. The one equation approximation of equation (3.11) was implemented as `one_equation_melt`. A variation of this was implemented as `ave_one_equation_melt`, implementing the horizontally-averaged version of the one equation formulation found in equation (4.8). The subtype

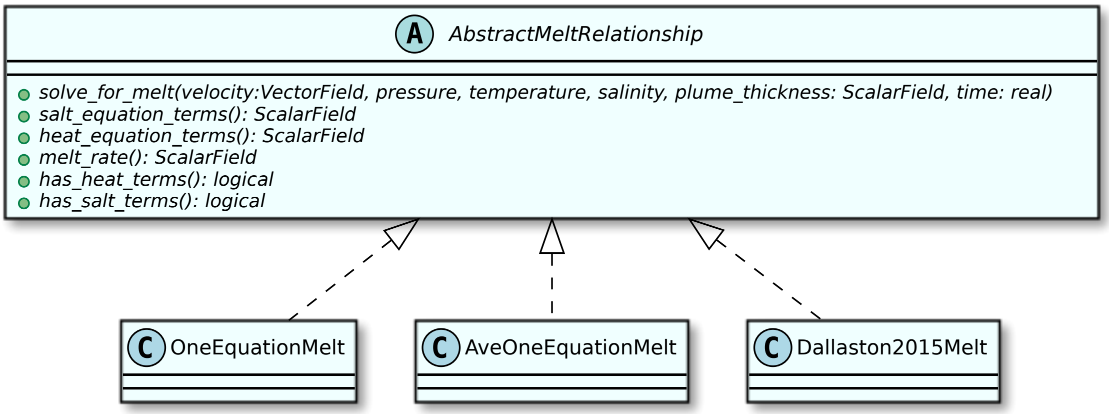

Figure A.9: A UML class diagram for the melt type. Subtypes implement the inherited abstract method, but this is not shown for reasons of space.

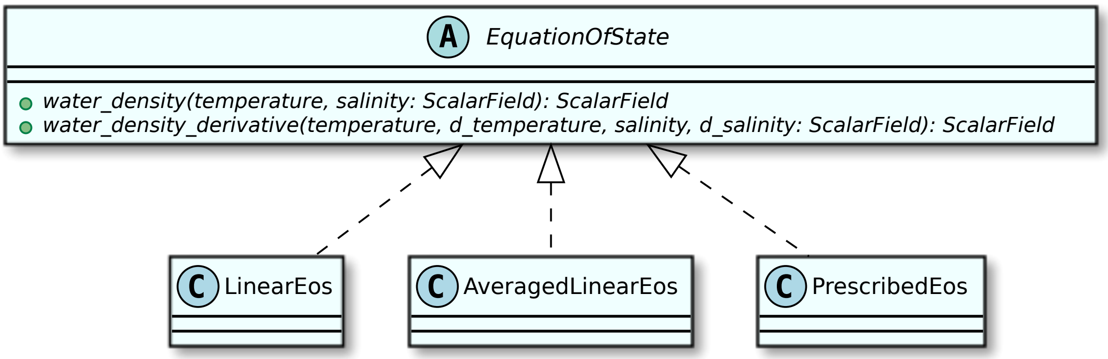

Figure A.10: A UML class diagram for the equation of state type. Subtypes implement all inherited abstract methods, but this is not shown for reasons of space.

`dallaston2015_melt` provides a way to convert from the scaling choices used in § 2.1.1 to those used in ISOFT, which was useful for writing unit tests. The three equation formulation of melting, found in equation (1.17), has not yet been implemented but it would not be difficult to do so. Finally, the abstract type `equation_of_state` sets out the interface for calculating the density of water from salinity and temperature (figure A.10). Subtype `linear_eos` implements the linearised equation of state in equation (1.10). The related `averaged_linear_eos` provides additional methods methods for calculating $\overline{\rho}$ and $\tilde{\rho}$, as defined in equations 4.6 and 4.7. Last, the subtype `prescribed_eos` calculates the density assuming no dependence on temperature and using a prescribed salinity profile; this is also useful in unit tests.

A similar approach was taken for boundary conditions and ambient ocean properties. The types `glacier_boundary` (figure A.11) and `plume_boundary` (figure A.12) provide interfaces for identifying the types of boundary conditions at different locations and determining the appropriate values. The default implementations effectively do not specify boundary conditions and the methods must be overridden to be useful. The interface provided by `plume_boundary` is quite different from that provided by `glacier_bound`. The latter should ideally be refactored to be closer to the more usable interface provided by the former. The subtypes for `glacier_boundary` are `dallaston2015_glacier_boundary`, which provides time-independent boundary conditions like those described in equations (3.34) and (3.35), and `seasonal_glacier_boundary`, which modifies these conditions according to equations (3.40) or (3.48) to allow seasonal oscillations in ice flux.

The first subtype of `plume_boundary` is `simple_plume_boundary`, which implements boundary conditions of the type described in equations (3.34) and (3.36). Closely related to this is `dallaston2015_seasonal_boundary`, which modifies the boundary conditions according to equation (3.37). The type which was ultimately used in all simulations was `upstream_plume_boundary`. This takes a user-provided function which specifies the inflow value of each plume variable and then, assuming no diffusion, integrates the plume a small distance upstream along the current basal draft of the ice shelf using `rksuite` (Brankin and Gladwell, 1994). This allows the plume solver itself to avoid handling narrow boundary layers where the plume salinity and temperature change rapidly. Outflow conditions are again defined according to equation (3.36). Ambient ocean conditions are described according to the interface defined by the abstract type `ambient_conditions` (figure A.13). At present only one implementation is provided (`uniform_ambient_conditions`), specifying constant ambient salinity and temperature.

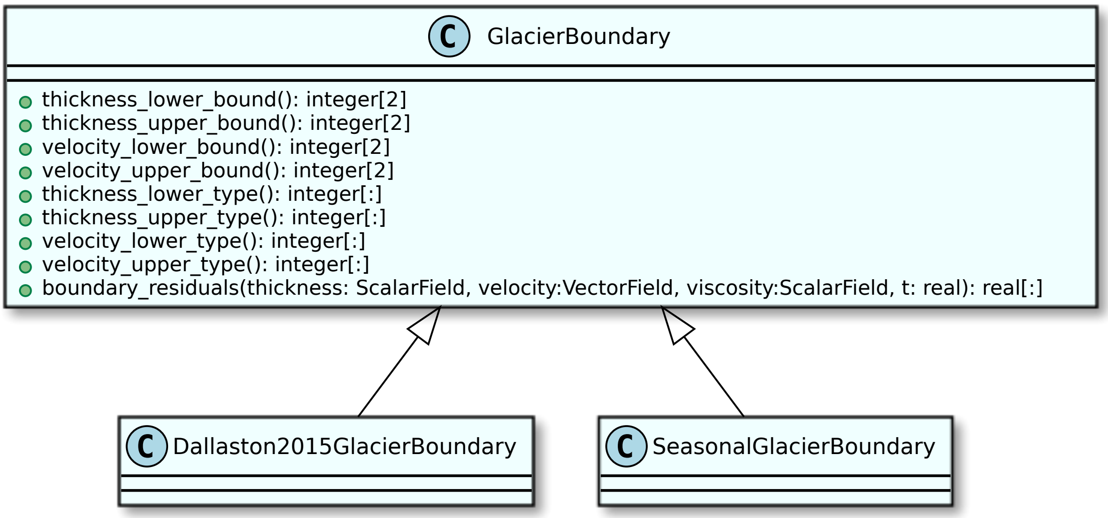

Figure A.11: A UML class diagram for the glacier boundary type. Subtypes implement all inherited abstract methods, but this is not shown for reasons of space.

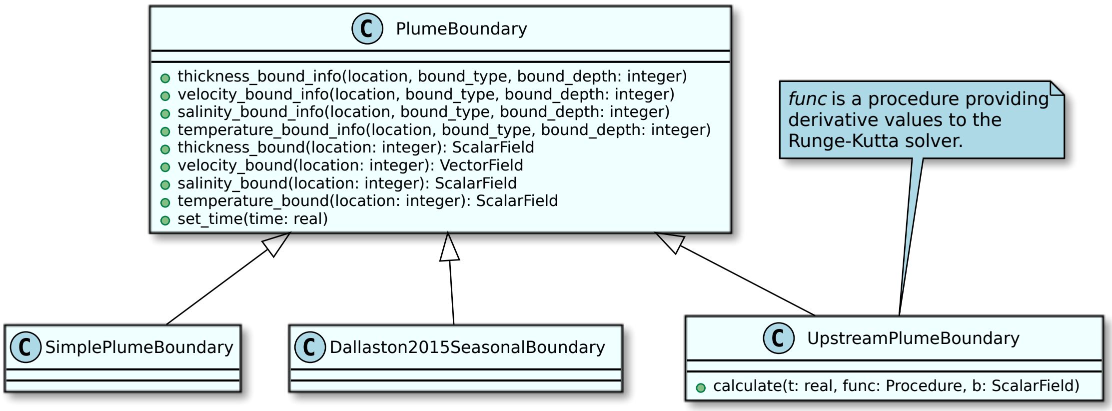

Figure A.12: A UML class diagram for the plume boundary type. Subtypes implement all inherited abstract methods, but this is not shown for reasons of space.

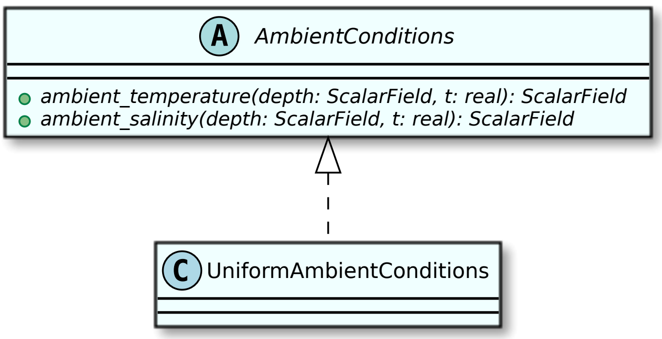

Figure A.13: A UML class diagram of the ambient conditions type. The subtype implements all inherited abstract methods, but this is not shown for reasons of space.

A.5 Unit Tests

Unit tests for ISOFT are run using the pFUnit[2] framework. In addition to tests for ensuring that the shelf and plume solvers converge to the correct solution, described in § 3.1.4, unit tests were written to perform checks on initialisation procedures, setter and getter methods, input and output methods, and all basic mathematics (including automatic differentiation). A few of the parameterisations do not currently have unit tests but these are closely related to implementations which are tested, return trivial results, or are implicitly tested by their use in other parts of the test suite.

A.6 Further Information

In addition to this overview of the ISOFT code, extensive documentation of derived types and individual functions was written within the source itself. The documentation can be extracted to produce HTML documentation using the FORD tool (MacMackin, 2018b) and can be found online[3] or be generated locally after downloading ISOFT. This will provide guidance on how to initialise the various objects needed to run a simulation. The distributed ISOFT code also contains information on how to compile it and an example program using the ISOFT framework.

[2] Available at `http://pfunit.sourceforge.net/`.
[3] See `cmacmackin.github.io/isoft`.

References

Alley, Karen E, Ted A Scambos, et al. (2016). “Impacts of warm water on Antarctic ice shelf stability through basal channel formation”. In: *Nature Geoscience* 9.4, pp. 290–293.

Alley, R.B., S. Anandakrishnan, et al. (2015). “Oceanic forcing of ice-sheet retreat: West Antarctica and more”. In: *Annual Review of Earth and Planetary Sciences* 43, pp. 207–231. DOI: 10.1146/annurev-earth-060614-105344.

Anderson, E. et al. (1999). *LAPACK Users’ Guide*. Third. Philadelphia, PA: Society for Industrial and Applied Mathematics.

Arneborg, L. et al. (2012). “Persistent inflow of warm water onto the central Amundsen shelf”. In: *Nature Geoscience* 5.12, pp. 876–880. DOI: 10.1038/ngeo1644.

Asay-Davis, Xylar S et al. (2016). “Experimental design for three interrelated marine ice sheet and ocean model intercomparison projects: MISMIP v. 3 (MISMIP+), ISOMIP v. 2 (ISOMIP+) and MISOMIP v. 1 (MISOMIP1)”. In: *Geoscientific Model Development* 9, pp. 2471–2497.

Assmann, K. M. et al. (2013). “Variability of Circumpolar Deep Water transport onto the Amundsen Sea Continental shelf through a shelf break trough”. In: *Journal of Geophysical Research: Oceans* 118.12, pp. 6603–6620. DOI: 10.1002/2013JC008871.

Bartholomew, I. et al. (2010). “Seasonal evolution of subglacial drainage and acceleration in a Greenland outlet glacier”. In: *Nature Geoscience* 3.6, pp. 408–411. DOI: 10.1038/ngeo863.

Bindschadler, R., D.G. Vaughan, and P. Vornberger (2011). “Variability of basal melt beneath the Pine Island Glacier ice shelf, West Antarctica”. In: *Journal of Glaciology* 57.204, pp. 581–595. DOI: 10.3189/002214311797409802.

Bindschadler, R.A., S. Nowicki, et al. (2013). “Ice-sheet model sensitivities to environmental forcing and their use in projecting future sea level (the SeaRISE project)”. In: *Journal of Glaciology* 59.214, pp. 195–224. DOI: 10.3189/2013JoG12J125.

Bintanja, R. et al. (2013). “Important role for ocean warming and increased ice-shelf melt in Antarctic sea-ice expansion”. In: *Nature Geoscience* 6.5, pp. 376–379. DOI: 10.1038/ngeo1767.

Bombosch, A. and A. Jenkins (1995). “Modeling the formation and deposition of frazil ice beneath Filchner- Ronne Ice Shelf”. In: *Journal of Geophysical Research* 100.C4, pp. 6983–6992. DOI: 10.1029/94JC03224.

Brankin, RW and I Gladwell (1994). *rksuite 90: software for ODE IVPs*. Tech. rep. NAG Tech. Report, TR6/94, 1994, also ACM Trans. Math. Softw., to appear.(Software available in ode on netlib and in the NAG Fortran 90 library.)

Brent, R.P. (1973). *Algorithms for Minimization Without Derivatives*. Prentice-Hall series in automatic computation. Prentice-Hall.

Budd, W.F., B. Coutts, and R.C. Warner (1998). “Modelling the Antarctic and Northern Hemisphere ice-sheet changes with global climate through the glacial cycle”. In: *Annals of Glaciology* 27, pp. 153–160.
Carter, S.P. and H.A. Fricker (2012). “The supply of subglacial meltwater to the grounding line of the Siple Coast, West Antarctica”. In: *Annals of Glaciology* 53.60, pp. 267–280. DOI: 10.3189/2012AoG60A119.
Catania, G. A. et al. (2006). “Evidence for floatation or near floatation in the mouth of Kamb Ice Stream, West Antarctica, prior to stagnation”. In: *Journal of Geophysical Research: Earth Surface* 111.F1. DOI: 10.1029/2005JF000355. eprint: https://agupubs.onlinelibrary.wiley.com/doi/pdf/10.1029/2005JF000355.
Cooley, J.W. and J.W. Tukey (1965). “An algorithm for the machine calculation of complex fourier series”. In: *Mathematics of Computation* 19.90, pp. 249–259. DOI: 10.1090/S0025-5718-1965-0178586-1.
Costa, Daniel P. et al. (2008). “Upper ocean variability in west Antarctic Peninsula continental shelf waters as measured using instrumented seals”. In: *Deep Sea Research Part II: Topical Studies in Oceanography* 55.3–4. Dynamics of Plankton, Krill, and Predators in Relation to Environmental Features of the Western Antarctic Peninsula and Related Areas: {SO} {GLOBEC} Part {II}, pp. 323–337. DOI: 10.1016/j.dsr2.2007.11.003.
Cuffey, K.M. and W.S.B. Paterson (2010). *The Physics of Glaciers*. Elsevier Science.
Dallaston, M.C., I.J. Hewitt, and A.J. Wells (2015). “Channelization of plumes beneath ice shelves”. In: *Journal of Fluid Mechanics* 785, pp. 109–134. DOI: 10.1017/jfm.2015.609.
Das, Sarah B. et al. (2008). “Fracture Propagation to the Base of the Greenland Ice Sheet During Supraglacial Lake Drainage”. In: *Science* 320.5877, pp. 778–781. DOI: 10.1126/science.1153360. eprint: http://science.sciencemag.org/content/320/5877/778.full.pdf.
De Sturler, E. (1999). “Truncation Strategies for Optimal Krylov Subspace Methods”. In: *SIAM Journal on Numerical Analysis* 36.3, pp. 864–889. DOI: 10.1137/S0036142997315950. eprint: https://doi.org/10.1137/S0036142997315950.
DeConto, R.M. and D. Pollard (2016). “Contribution of Antarctica to past and future sea-level rise”. In: *Nature* 531.7596, pp. 591–597. DOI: 10.1038/nature17145.
Dinniman, Michael S., John M. Klinck, and Eileen E. Hofmann (2012). “Sensitivity of Circumpolar Deep Water Transport and Ice Shelf Basal Melt along the West Antarctic Peninsula to Changes in the Winds”. In: *Journal of Climate* 25.14, pp. 4799–4816. DOI: 10.1175/JCLI-D-11-00307.1.
Dow, Christine F. et al. (2018). “Basal channels drive active surface hydrology and transverse ice shelf fracture”. In: *Science Advances* 4.6. DOI: 10.1126/sciadv.aao7212. eprint: http://advances.sciencemag.org/content/4/6/eaao7212.full.pdf.
Drews, R. (2015). “Evolution of ice-shelf channels in Antarctic ice shelves”. In: *Cryosphere* 9.3, pp. 1169–1181. DOI: 10.5194/tc-9-1169-2015.
Dupont, T.K. and R.B. Alley (2005). “Assessment of the importance of ice-shelf buttressing to ice-sheet flow”. In: *Geophysical Research Letters* 32.4, pp. 1–4. DOI: 10.1029/2004GL022024.
— (2006). “Role of small ice shelves in sea-level rise”. In: *Geophysical Research Letters* 33.9. DOI: 10.1029/2005GL025665.

Dutrieux, P., J. De Rydt, et al. (2014). "Strong sensitivity of Pine Island ice-shelf melting to climatic variability". In: *Science* 343.6167, pp. 174–178. DOI: 10.1126/science.1244341.

Dutrieux, P., C. Stewart, et al. (2014). "Basal terraces on melting ice shelves". In: *Geophysical Research Letters* 41.15, pp. 5506–5513. DOI: 10.1002/2014GL060618.

Dutrieux, P., D.G. Vaughan, et al. (2013). "Pine Island glacier ice shelf melt distributed at kilometre scales". In: *Cryosphere* 7.5, pp. 1543–1555. DOI: 10.5194/tc-7-1543-2013.

Ebert, D.S. et al. (2003). *Texturing & Modeling: A Procedural Approach.* Morgan Kaufmann series in computer graphics and geometric modeling. Morgan Kaufmann.

Eicken, H. et al. (1994). "Textural characteristics and impurity content of meteoric and marine ice in the Ronne Ice Shelf, Antarctica". In: *Journal of Glaciology* 40.135, pp. 386–398.

Ellison, T. H. and J. S. Turner (1959). "Turbulent entrainment in stratified flows". In: *Journal of Fluid Mechanics* 6.3, 423–448. DOI: 10.1017/S0022112059000738.

Foldvik, A. and T. Gammelsrød (1988). "Notes on Southern Ocean hydrography, sea-ice and bottom water formation". In: *Palaeogeography, Palaeoclimatology, Palaeoecology* 67.1-2, pp. 3–17. DOI: 10.1016/0031-0182(88)90119-8.

Fricker, Helen Amanda et al. (2009). "Mapping the grounding zone of the Amery Ice Shelf, East Antarctica using InSAR, MODIS and ICESat". In: *Antarctic Science* 21.5, pp. 515–532. DOI: 10.1017/S095410200999023X.

Frigo, Matteo and Steven G. Johnson (2005). "The Design and Implementation of FFTW3". In: *Proceedings of the IEEE* 93.2. Special issue on "Program Generation, Optimization, and Platform Adaptation", pp. 216–231.

Gagliardini, O. et al. (2010). "Coupling of ice-shelf melting and buttressing is a key process in ice-sheets dynamics". In: *Geophysical Research Letters* 37.14. DOI: 10.1029/2010GL043334.

Gamma, Erich et al. (1994). *Design Patterns: Elements of Reusable Object-Oriented Software.* 1st ed. Addison-Wesley Professional.

Gladish, C.V. et al. (2012). "Ice-shelf basal channels in a coupled ice/ocean model". In: *Journal of Glaciology* 58.212, pp. 1227–1244. DOI: 10.3189/2012JoG12J003.

Glen, JW (1958). "The flow law of ice: A discussion of the assumptions made in glacier theory, their experimental foundations and consequences". In: *Physics of the Movement of Ice: Symposium at Chamonix 1958* 47, pp. 171–183.

Goldberg, D., D.M. Holland, and C. Schoof (2009). "Grounding line movement and ice shelf buttressing in marine ice sheets". In: *Journal of Geophysical Research: Earth Surface* 114.4. DOI: 10.1029/2008JF001227.

Goodman, Jason C. and Raymond T. Pierrehumbert (2003). "Glacial flow of floating marine ice in 'Snowball Earth'". In: *Journal of Geophysical Research: Oceans* 108.C10. DOI: 10.1029/2002JC001471. eprint: https://agupubs.onlinelibrary.wiley.com/doi/pdf/10.1029/2002JC001471.

Gourmelen, N. et al. (2017). "Channelized Melting Drives Thinning Under a Rapidly Melting Antarctic Ice Shelf". In: *Geophysical Research Letters* 44.19, pp. 9796–9804. DOI: 10.1002/2017GL074929.

Grand, Mark (2002). *Patterns in Java: A Catalog of Reusable Design Patterns Illustrated with UML, Volume 1.* 2nd ed. New York: Wiley.

Gudmandsen, P. (1975). "Layer echoes in polar ice sheets". In: *Journal of Glaciology* 15, pp. 95–101.

Gwyther, David E., Eva A. Cougnon, et al. (2016). "Modelling the response of ice shelf basal melting to different ocean cavity environmental regimes". In: *Annals of Glaciology* 57.73, pp. 131–141. DOI: 10.1017/aog.2016.31.

Gwyther, D.E., B.K. Galton-Fenzi, et al. (2015). "The effect of basal friction on melting and freezing in ice shelf-ocean models". In: *Ocean Modelling* 95, pp. 38–52. DOI: 10.1016/j.ocemod.2015.09.004.

Hammer, C.U. (1980). "Acidity of polar ice cores in relation to absolute dating, past volcanism, and radio echoes." In: *Journal of Glaciology* 25.93, pp. 359–372.

Harrison, C. H. (1973). "Radio Echo Sounding of Horizontal Layers in Ice". In: *Journal of Glaciology* 12.66, pp. 383–397. DOI: 10.1017/S0022143000031804.

Hindmarsh, Richard C.A., Gwendolyn J.-M.C. Leysinger Vieli, and Frédéric Parrenin (2009). "A large-scale numerical model for computing isochrone geometry". In: *Annals of Glaciology* 50.51, pp. 130–140. DOI: 10.3189/172756409789097450.

Holland, D.M. and A. Jenkins (1999). "Modeling thermodynamic ice-ocean interactions at the base of an ice shelf". In: *Journal of Physical Oceanography* 29.8 PART 1, pp. 1787–1800.

Holland, D.M., R.H. Thomas, et al. (2008). "Acceleration of Jakobshavn Isbr triggered by warm subsurface ocean waters". In: *Nature Geoscience* 1.10, pp. 659–664. DOI: 10.1038/ngeo316.

Holland, P.R. (2008). "A model of tidally dominated ocean processes near ice shelf grounding lines". In: *Journal of Geophysical Research: Oceans* 113.11. DOI: 10.1029/2007JC004576.

— (2017). "The transient response of ice shelf melting to ocean change". In: *Journal of Physical Oceanography* 47.8, pp. 2101–2114. DOI: 10.1175/JPO-D-17-0071.1.

Holland, P.R. and D.L. Feltham (2006). "The effects of rotation and ice shelf topography on frazil-laden ice shelf water plumes". In: *Journal of Physical Oceanography* 36.12, pp. 2312–2327. DOI: 10.1175/JPO2970.1.

Holland, P.R., D.L. Feltham, and A. Jenkins (2007). "Ice Shelf Water plume flow beneath Filchner-Ronne Ice Shelf, Antarctica". In: *Journal of Geophysical Research: Oceans* 112.5. DOI: 10.1029/2006JC003915.

Holland, P.R., A. Jenkins, and D.M. Holland (2010). "Ice and ocean processes in the Bellingshausen sea, Antarctica". In: *Journal of Geophysical Research: Oceans* 115.5. DOI: 10.1029/2008JC005219.

— (2008). "The response of Ice shelf basal melting to variations in ocean temperature". In: *Journal of Climate* 21.11, pp. 2558–2572. DOI: 10.1175/2007JCLI1909.1.

Hu, A. et al. (2013). "Influence of continental ice retreat on future global climate". In: *Journal of Climate* 26.10, pp. 3087–3111. DOI: 10.1175/JCLI-D-12-00102.1.

Hurford, T.A. and K.M. Brunt (2014). "Antarctic analog for dilational bands on Europa". In: *Earth and Planetary Science Letters* 401, pp. 275–283. DOI: https://doi.org/10.1016/j.epsl.2014.05.015.

Jackson, L.C. et al. (2015). "Global and European climate impacts of a slowdown of the AMOC in a high resolution GCM". In: *Climate Dynamics* 45.11-12, pp. 3299–3316. DOI: 10.1007/s00382-015-2540-2.

Jacobel, Robert W. and Steven M. Hodge (1995). "Radar internal layers from the Greenland Summit". In: *Geophysical Research Letters* 22.5, pp. 587–590. DOI: 10.1029/95GL00110.

Jacobs, S., A. Jenkins, H. Hellmer, et al. (2012). "The Amundsen Sea and the Antarctic ice sheet". In: *Oceanography* 25.3, pp. 154–163. DOI: 10.5670/oceanog.2012.90.

Jacobs, S.S., H.H. Hellmer, and A. Jenkins (1996). "Antarctic Ice Sheet melting in the southeast Pacific". In: *Geophysical Research Letters* 23.9, pp. 957–960. DOI: 10.1029/96GL00723.

Jacobs, S.S., H.H. Helmer, et al. (1992). "Melting of ice shelves and the mass balance of Antarctica". In: *Journal of Glaciology* 38.130, pp. 375–387.

Jacobs, S.S., A. Jenkins, C.F. Giulivi, et al. (2011). "Stronger ocean circulation and increased melting under Pine Island Glacier ice shelf". In: *Nature Geoscience* 4.8, pp. 519–523. DOI: 10.1038/ngeo1188.

James, John and Theo Keith (2006). *Gas Dynamics*. 3rd ed. Prentice Hall.

Jenkins, A. (1991). "A one-dimensional model of ice shelf-ocean interaction". English. In: *Journal of Geophysical Research* 96 (C11), 20671–7.

— (2016). "A simple model of the ice shelf-ocean boundary layer and current". In: *Journal of Physical Oceanography* 46.6, pp. 1785–1803. DOI: 10.1175/JPO-D-15-0194.1.

— (2011). "Convection-driven melting near the grounding lines of ice shelves and tidewater glaciers". In: *Journal of Physical Oceanography* 41.12, pp. 2279–2294. DOI: 10.1175/JPO-D-11-03.1.

Jenkins, A., H.F.J. Corr, et al. (2006). "Interactions between ice and ocean observed with phase-sensitive radar near an Antarctic ice-shelf grounding line". In: *Journal of Glaciology* 52.178, pp. 325–346. DOI: 10.3189/172756506781828502.

Jenkins, A., P. Dutrieux, S. Jacobs, E.J. Steig, et al. (2016). "Decadal Ocean Forcing and Antarctic Ice Sheet Response: Lessons from the Amundsen Sea". In: *Oceanography* 29.

Jenkins, A., P. Dutrieux, S.S. Jacobs, S.D. McPhail, et al. (2010). "Observations beneath Pine Island Glacier in West-Antarctica and implications for its retreat". In: *Nature Geoscience* 3.7, pp. 468–472. DOI: 10.1038/ngeo890.

Jenkins, A., D.M. Holland, et al. (2004). "Seasonal ventilation of the cavity beneath Filchner-Ronne Ice Shelf simulated with an isopycnic coordinate ocean model". In: *Journal of Geophysical Research C: Oceans* 109.1, pages.

Jenkins, A., K.W. Nicholls, and H.F.J. Corr (2010). "Observation and parameterization of ablation at the base of Ronne Ice Ahelf, Antarctica". In: *Journal of Physical Oceanography* 40.10, pp. 2298–2312. DOI: 10.1175/2010JPO4317.1.

Jenkins, Adrian and David Holland (2007). "Melting of floating ice and sea level rise". In: *Geophysical Research Letters* 34.16. DOI: 10.1029/2007GL030784. eprint: https://agupubs.onlinelibrary.wiley.com/doi/pdf/10.1029/2007GL030784.

Jones, Eric, Travis Oliphant, Pearu Peterson, et al. (2001). *SciPy: Open source scientific tools for Python*. [Online; accessed <today>].

Jongma, J.I. et al. (2009). "The effect of dynamic-thermodynamic icebergs on the Southern Ocean climate in a three-dimensional model". In: *Ocean Modelling* 26.1-2, pp. 104–113. DOI: 10.1016/j.ocemod.2008.09.007.

Jordan, James R. et al. (2018). "Ocean-Forced Ice-Shelf Thinning in a Synchronously Coupled Ice-Ocean Model". In: *Journal of Geophysical Research: Oceans* 123.2, pp. 864–882. DOI: 10.1002/2017JC013251. eprint: https://agupubs.onlinelibrary.wiley.com/doi/pdf/10.1002/2017JC013251.

Joughin, Ian et al. (2008). "Seasonal Speedup Along the Western Flank of the Greenland Ice Sheet". In: *Science* 320.5877, pp. 781–783. DOI: 10.1126/science.1153288. eprint: http://science.sciencemag.org/content/320/5877/781.full.pdf.

Jungclaus, Johann H. and Jan O. Backhaus (1994). "Application of a transient reduced gravity plume model to the Denmark Strait Overflow". In: *Journal of Geophysical Research: Oceans* 99.C6, pp. 12375–12396. DOI: 10.1029/94JC00528.

Kader, B.A. and A.M. Yaglom (1972). "Heat and mass transfer laws for fully turbulent wall flows". In: *International Journal of Heat and Mass Transfer* 15.12, pp. 2329–2351. DOI: 10.1016/0017-9310(72)90131-7.

Karlsson, Nanna B. et al. (2014). "Constraining past accumulation in the central Pine Island Glacier basin, West Antarctica, using radio-echo sounding". In: *Journal of Glaciology* 60.221, pp. 553–562. DOI: 10.3189/2014JoG13J180.

Kim, T.W. et al. (2017). "Is Ekman pumping responsible for the seasonal variation of warm circumpolar deep water in the Amundsen Sea?" In: *Continental Shelf Research* 132, pp. 38–48. DOI: https://doi.org/10.1016/j.csr.2016.09.005.

Klinck, John M. et al. (2004). "Water-mass properties and circulation on the west Antarctic Peninsula Continental Shelf in Austral Fall and Winter 2001". In: *Deep Sea Research Part II: Topical Studies in Oceanography* 51.17–19. Integrated Ecosystem Studies of Western Antarctic Peninsula Continental Shelf Waters and Related Southern Ocean Regions, pp. 1925–1946. DOI: 10.1016/j.dsr2.2004.08.001.

Knoll, D.A. and D.E. Keyes (2004). "Jacobian-free Newton-Krylov methods: A survey of approaches and applications". In: *Journal of Computational Physics* 193.2, pp. 357–397. DOI: 10.1016/j.jcp.2003.08.010.

Kochergin, V. P. (1987). "Three-Dimensional Prognostic Models". In: *Three-Dimensional Coastal Ocean Models*. American Geophysical Union, pp. 201–208. DOI: 10.1029/CO004p0201.

Langley, K. et al. (2014). "Complex network of channels beneath an Antarctic ice shelf". In: *Geophysical Research Letters* 41.4, pp. 1209–1215. DOI: 10.1002/2013GL058947.

St-Laurent, P., J. M. Klinck, and M. S. Dinniman (2015). "Impact of local winter cooling on the melt of Pine Island Glacier, Antarctica". In: *Journal of Geophysical Research: Oceans* 120.10, pp. 6718–6732. DOI: 10.1002/2015JC010709. eprint: https://agupubs.onlinelibrary.wiley.com/doi/pdf/10.1002/2015JC010709.

Lazeroms, W.M.J. et al. (2018). "Modelling present-day basal melt rates for Antarctic ice shelves using a parametrization of buoyant meltwater plumes". In: *Cryosphere* 12.1, pp. 49–70. DOI: 10.5194/tc-12-49-2018.

Le Brocq, A.M. et al. (2013). "Evidence from ice shelves for channelized meltwater flow beneath the Antarctic Ice Sheet". In: *Nature Geoscience* 6.11, pp. 945–948. DOI: 10.1038/ngeo1977.

Lewis, E. L. and R. G. Perkin (1986). "Ice pumps and their rates". In: *Journal of Geophysical Research: Oceans* 91.C10, pp. 11756–11762. DOI: 10.1029/JC091iC10p11756.

Leysinger Vieli, G.J.-M.C., R.C.A. Hindmarsh, and M.J. Siegert (2007). "Three-dimensional flow influences on radar layer stratigraphy". In: *Annals of Glaciology* 46, pp. 22–28. DOI: 10.3189/172756407782871729.

Little, Christopher M., Daniel Goldberg, et al. (2012). "On the coupled response to ice-shelf basal melting". In: *Journal of Glaciology* 58.208, pp. 203–215. DOI: 10.3189/2012JoG11J037.

Little, C.M., A. Gnanadesikan, and M. Oppenheimer (2009). "How ice shelf morphology controls basal melting". In: *Journal of Geophysical Research: Oceans* 114.12. DOI: 10.1029/2008JC005197.

Luckman, A. et al. (2012). "Basal crevasses in Larsen C Ice Shelf and implications for their global abundance". In: *Cryosphere* 6.1, pp. 113–123. DOI: 10.5194/tc-6-113-2012.

MacAyeal, Douglas R. (1985). "Evolution of Tidally Triggered Meltwater Plumes Below Ice Shelves". In: *Oceanology of the Antarctic Continental Shelf*. American Geophysical Union, pp. 133–143. DOI: 10.1029/AR043p0133.

MacAyeal, D.R. (1989). "Large-scale ice flow over a viscous basal sediment: theory and application to ice stream B, Antarctica". In: *Journal of Geophysical Research* 94.134, pp. 4071–4087.

MacMackin, Christopher (2018a). *cmacmackin/isoft: Version 0.1.0*. DOI: 10.5281/zenodo.1422482.

— (2018b). *FORD*. DOI: 10.5281/zenodo.1422473.

Magorrian, S.J. and A.J. Wells (2016). "Turbulent plumes from a glacier terminus melting in a stratified ocean". In: *Journal of Geophysical Research: Oceans*. DOI: 10.1002/2015JC011160.

Manabe, S. and R.J. Stouffer (1995). "Simulation of abrupt climate change induced by freshwater input to the North Atlantic Ocean". In: *Nature* 378.6553, pp. 165–167.

Mandelzweig, V. B. and F. Tabakin (2001). " Quasilinearization approach to nonlinear problems in physics with application to nonlinear ODEs". In: *Computer Physics Communications* 141, pp. 268–281. DOI: 10.1016/S0010-4655(01)00415-5.

Manins, P.C. and B.L. Sawford (1979). "A model of katabatic winds." In: *Journal of the Atmospheric Sciences* 36.4, pp. 619–630.

Mankoff, K.D. et al. (2012). "The role of Pine Island Glacier ice shelf basal channels in deep-water upwelling, polynyas and ocean circulation in Pine Island Bay, Antarctica". In: *Annals of Glaciology* 53.60, pp. 123–128. DOI: 10.3189/2012AoG60A062.

Marsh, Oliver J. et al. (2016). "High basal melting forming a channel at the grounding line of Ross Ice Shelf, Antarctica". In: *Geophysical Research Letters* 43.1. 2015GL066612, pp. 250–255. DOI: 10.1002/2015GL066612.

McConnochie, C.D. and R.C. Kerr (2018). "Dissolution of a sloping solid surface by turbulent compositional convection". In: *Journal of Fluid Mechanics* 846, pp. 563–577. DOI: 10.1017/jfm.2018.282.

McGrath, D., K. Steffen, T. Scambos, et al. (2012). "Basal crevasses and associated surface crevassing on the larsen c ice shelf, antarctica, and their role in ice-shelf instability". In: *Annals of Glaciology* 53.60, pp. 10–18. DOI: 10.3189/2012AoG60A005.

McGrath, Daniel, Konrad Steffen, Harihar Rajaram, et al. (2012). "Basal crevasses on the Larsen C Ice Shelf, Antarctica: Implications for meltwater ponding and hydrofracture". In: *Geophysical Research Letters* 39.16. L16504, n/a–n/a. DOI: 10.1029/2012GL052413.

Millgate, T. et al. (2013). "The effect of basal channels on oceanic ice-shelf melting". In: *Journal of Geophysical Research: Oceans* 118.12, pp. 6951–6964. DOI: 10.1002/2013JC009402.

Moré, J. J. et al. (1984). *The MINPACK Project, in Sources and Development of Mathematical Software*. Upper Saddle River, NJ, USA: Prentice-Hall, Inc., pp. 88–111.

Morland, L.W. and E.M. Shoemaker (1982). "Ice shelf balances". In: *Cold Regions Science and Technology* 5.3, pp. 235–251. DOI: 10.1016/0165-232X(82)90017-9.

Mueller, R.D. et al. (2012). "Impact of tide-topography interactions on basal melting of Larsen C Ice Shelf, Antarctica". In: *Journal of Geophysical Research: Oceans* 117.5. DOI: 10.1029/2011JC007263.

Nakayama, Y. et al. (2014). “On the difficulty of modeling Circumpolar Deep Water intrusions onto the Amundsen Sea continental shelf”. In: *Ocean Modelling* 84, pp. 26–34. DOI: 10.1016/j.ocemod.2014.09.007.

Neidinger, R. (2010). “Introduction to Automatic Differentiation and MATLAB Object-Oriented Programming”. In: *SIAM Review* 52.3, pp. 545–563. DOI: 10.1137/080743627. eprint: https://doi.org/10.1137/080743627.

Nereson, N. A. et al. (2000). “The accumulation pattern across Siple Dome, West Antarctica, inferred from radar-detected internal layers”. In: *Journal of Glaciology* 46.152, pp. 75–87. DOI: 10.3189/172756500781833449.

Ng, Felix and Howard Conway (2004). “Fast-flow signature in the stagnated Kamb Ice Stream, West Antarctica”. In: *Geology* 32.6, p. 481. DOI: 10.1130/G20317.1. eprint: /gsw/content_public/journal/geology/32/6/10.1130_g20317.1/3/i0091-7613-32-6-481.pdf.

Nicholls, K.W. and S. Østerhus (2004). “Interannual variability and ventilation timescales in the ocean cavity beneath Filchner-Ronne Ice Shelf, Antarctica”. In: *Journal of Geophysical Research C: Oceans* 109.4, pages. DOI: 10.1029/2003JC002149.

Oerter, H. et al. (1992). “Evidence for basal marine ice in the Filchner-Ronne ice shelf”. In: *Nature* 358.6385, pp. 399–401.

Orszag, Steven A (1980). “Spectral methods for problems in complex geometries”. In: *Journal of Computational Physics* 37.1, pp. 70–92. DOI: 10.1016/0021-9991(80)90005-4.

Parrenin, F., R.C.A. Hindmarsh, and F. Rémy (2006). “Analytical solutions for the effect of topography, accumulation rate and lateral flow divergence on isochrone layer geometry”. In: *Journal of Glaciology* 52.177, pp. 191–202. DOI: 10.3189/172756506781828728.

Parrenin, Frédéric and Richard Hindmarsh (2007). “Influence of a non-uniform velocity field on isochrone geometry along a steady flowline of an ice sheet”. In: *Journal of Glaciology* 53.183, pp. 612–622. DOI: 10.3189/002214307784409298.

Payne, A.J. et al. (2007). “Numerical modeling of ocean-ice interactions under Pine Island Bay’s ice shelf”. In: *Journal of Geophysical Research: Oceans* 112.10. DOI: 10.1029/2006JC003733.

Pedlosky, Joseph (1987). *Geophysical Fluid Dynamics.* 2nd ed. Springer-Verlag.

Pernice, M. and H.F. Walker (1998). “NITSOL: A Newton iterative solver for nonlinear systems”. In: *SIAM Journal on Scientific Computing* 19.1, pp. 302–318.

Press, William H. et al. (2007). *Numerical Recipes 3rd Edition: The Art of Scientific Computing.* 3rd ed. New York, NY, USA: Cambridge University Press.

Prince, P.J. and J.R. Dormand (1981). “High order embedded Runge-Kutta formulae”. In: *Journal of Computational and Applied Mathematics* 7.1, pp. 67–75. DOI: https://doi.org/10.1016/0771-050X(81)90010-3.

Pritchard, H.D. et al. (2012). “Antarctic ice-sheet loss driven by basal melting of ice shelves”. In: *Nature* 484.7395, pp. 502–505. DOI: 10.1038/nature10968.

Reese, R. et al. (2018). “The far reach of ice-shelf thinning in Antarctica”. In: *Nature Climate Change* 8.1, pp. 53–57. DOI: 10.1038/s41558-017-0020-x.

Rignot, E. and S.S. Jacobs (2002). “Rapid bottom melting widespread near antarctic ice sheet grounding lines”. In: *Science* 296.5575, pp. 2020–2023. DOI: 10.1126/science.1070942.

Rignot, E., S. Jacobs, et al. (2013). “Ice-shelf melting around Antarctica”. In: *Science* 341.6143, pp. 266–270. DOI: 10.1126/science.1235798.

Rignot, E. and K. Steffen (2008). “Channelized bottom melting and stability of floating ice shelves”. In: *Geophysical Research Letters* 35.2. DOI: 10.1029/2007GL031765.

Robin, G. De Q., S. Evans, and J. T. Bailey (1969). “Interpretation of Radio Echo Sounding in Polar Ice Sheets”. In: *Philosophical Transactions of the Royal Society of London. Series A, Mathematical and Physical Sciences* 265.1166, pp. 437–505.

Roe, G.H. and R.S. Lindzen (2001). “The mutual interaction between continental-scale ice and atmospheric stationary waves”. In: *Journal of Climate* 14.7, pp. 1450–1465.

Rosier, S.H.R. et al. (2017). “Strong tidal variations in ice flow observed across the entire Ronne Ice Shelf and adjoining ice streams”. In: *Earth System Science Data* 9.2, pp. 849–860. DOI: 10.5194/essd-9-849-2017.

Rouson, D., J. Xia, and X. Xu (2014). *Scientific Software Design: The Object-Oriented Way*. Cambridge University Press.

Schmidtko, Sunke et al. (2014). “Multidecadal warming of Antarctic waters”. In: *Science* 346.6214, pp. 1227–1231. DOI: 10.1126/science.1256117. eprint: http://science.sciencemag.org/content/346/6214/1227.full.pdf.

Schoof, C. (2007). “Ice sheet grounding line dynamics: Steady states, stability, and hysteresis”. In: *Journal of Geophysical Research: Earth Surface* 112.3. DOI: 10.1029/2006JF000664.

— (2012). “Marine ice sheet stability”. In: *Journal of Fluid Mechanics* 698, pp. 62–72. DOI: 10.1017/jfm.2012.43.

Schoof, C. and I. Hewitt (2013). “Ice-sheet dynamics”. In: *Annual Review of Fluid Mechanics* 45, pp. 217–239. DOI: 10.1146/annurev-fluid-011212-140632.

Sergienko, O. V. (2013). “Basal channels on ice shelves”. In: *Journal of Geophysical Research – Earth Surface* 118.3, 1342–1355. DOI: 10.1002/jgrf.20105.

Sergienko, O.V., D.N. Goldberg, and C.M. Little (2013). “Alternative ice shelf equilibria determined by ocean environment”. In: *Journal of Geophysical Research: Earth Surface* 118.2, pp. 970–981. DOI: 10.1002/jgrf.20054.

Shepherd, A., E.R. Ivins, et al. (2012). “A reconciled estimate of ice-sheet mass balance”. In: *Science* 338.6111, pp. 1183–1189. DOI: 10.1126/science.1228102.

Shepherd, A., D. Wingham, and E. Rignot (2004). “Warm ocean is eroding West Antarctic Ice Sheet”. In: *Geophysical Research Letters* 31.23, pp. 1–4. DOI: 10.1029/2004GL021106.

Siegert, Martin J., Richard Hindmarsh, et al. (2004). “Subglacial Lake Ellsworth: A candidate for in situ exploration in West Antarctica”. In: *Geophysical Research Letters* 31.23. DOI: 10.1029/2004GL021477. eprint: https://agupubs.onlinelibrary.wiley.com/doi/pdf/10.1029/2004GL021477.

Siegert, Martin, Neil Ross, et al. (2013). “Late Holocene ice-flow reconfiguration in the Weddell Sea sector of West Antarctica”. In: *Quaternary Science Reviews* 78, pp. 98–107. DOI: https://doi.org/10.1016/j.quascirev.2013.08.003.

Smedsrud, L.H. and A. Jenkins (2004). “Frazil ice formation in an ice shelf water plume”. In: *Journal of Geophysical Research C: Oceans* 109.3, pages.

Smith, D.A. et al. (1999). “Hydrography and circulation of the West Antarctic Peninsula Continental Shelf”. In: *Deep-Sea Research Part I: Oceanographic Research Papers* 46.6, pp. 925–949. DOI: 10.1016/S0967-0637(98)00103-4.

Sole, Andrew et al. (2013). “Winter motion mediates dynamic response of the Greenland Ice Sheet to warmer summers”. In: *Geophysical Research Letters* 40.15, pp. 3940–3944. DOI: 10.1002/grl.50764. eprint: https://agupubs.onlinelibrary.wiley.com/doi/pdf/10.1002/grl.50764.

Stanton, T.P. et al. (2013). “Channelized ice melting in the ocean boundary layer beneath Pine Island Glacier, Antarctica”. In: *Science* 341.6151, pp. 1236–1239. DOI: 10.1126/science.1239373.

Straneo, F. and C. Cenedese (2015). “The dynamics of Greenland’s glacial fjords and their role in climate”. In: *Annual Review of Marine Science* 7, pp. 89–112. DOI: 10.1146/annurev-marine-010213-135133.

Swart, N.C. and J.C. Fyfe (2013). “The influence of recent Antarctic ice sheet retreat on simulated sea ice area trends”. In: *Geophysical Research Letters* 40.16, pp. 4328–4332. DOI: 10.1002/grl.50820.

Swingedouw, D. et al. (2009). “Impact of transient freshwater releases in the Southern Ocean on the AMOC and climate”. In: *Climate Dynamics* 33.2-3, pp. 365–381. DOI: 10.1007/s00382-008-0496-1.

Tedstone, Andrew J. et al. (2013). “Greenland ice sheet motion insensitive to exceptional meltwater forcing”. In: *Proceedings of the National Academy of Sciences* 110.49, pp. 19719–19724. DOI: 10.1073/pnas.1315843110. eprint: http://www.pnas.org/content/110/49/19719.full.pdf.

Thoma, M. et al. (2008). “Modelling Circumpolar Deep Water intrusions on the Amundsen Sea continental shelf, Antarctica”. In: *Geophysical Research Letters* 35.18. DOI: 10.1029/2008GL034939.

Trefethen, L. (2000). *Spectral Methods in MATLAB*. Society for Industrial and Applied Mathematics. DOI: 10.1137/1.9780898719598. eprint: http://epubs.siam.org/doi/pdf/10.1137/1.9780898719598.

Vaughan David G. et al. (1999). “Distortion of isochronous layers in ice revealed by ground-penetrating radar”. In: *Nature* 398, p. 323. DOI: http://dx.doi.org/10.1038/1865310.1038/18653.

Vaughan, D.G. et al. (2012). “Subglacial melt channels and fracture in the floating part of Pine Island Glacier, Antarctica”. In: *Journal of Geophysical Research: Earth Surface* 117.3. DOI: 10.1029/2012JF002360.

Vellinga, M. and R.A. Wood (2002). “Global climatic impacts of a collapse of the atlantic thermohaline circulation”. In: *Climatic Change* 54.3, pp. 251–267. DOI: 10.1023/A:1016168827653.

Waddington, Edwin D. et al. (2007). “Inference of accumulation-rate patterns from deep layers in glaciers and ice sheets”. In: *Journal of Glaciology* 53.183, pp. 694–712. DOI: 10.3189/002214307784409351.

Wåhlin, A.K. et al. (2013). “Variability of warm deep water inflow in a submarine trough on the amundsen sea shelf”. In: *Journal of Physical Oceanography* 43.10, pp. 2054–2070. DOI: 10.1175/JPO-D-12-0157.1.

Walker, D.P., A. Jenkins, et al. (2013). “Oceanographic observations at the shelf break of the Amundsen Sea, Antarctica”. In: *Journal of Geophysical Research: Oceans* 118.6, pp. 2906–2918. DOI: 10.1002/jgrc.20212.

Walker, R.T., T.K. Dupont, et al. (2008). “Effects of basal-melting distribution on the retreat of ice-shelf grounding lines”. In: *Geophysical Research Letters* 35.17. DOI: 10.1029/2008GL034947.

Walker, R.T., D.M. Holland, et al. (2013). “Efficient flowline simulations of ice shelf-ocean interactions: Sensitivity studies with a fully coupled model”. In: *Journal of Physical Oceanography* 43.10, pp. 2200–2210. DOI: 10.1175/JPO-D-13-037.1.

Webber Benjamin G. M. et al. (2017). "Mechanisms driving variability in the ocean forcing of Pine Island Glacier". In: *Nature Communications* 8, p. 14507. DOI: http://dx.doi.org/10.1038/ncomms1450710.1038/ncomms14507.

Weertman, J. (1974). "Stability of the Junction of an Ice Sheet and an Ice Shelf". In: *Journal of Glaciology* 13.67, pp. 3–11. DOI: 10.3198/1974JoG13-67-3-11.

Weijer, W. et al. (2012). "Response of the Atlantic Ocean circulation to Greenland Ice Sheet melting in a strongly-eddying ocean model". In: *Geophysical Research Letters* 39.9. DOI: 10.1029/2012GL051611.

Williams G. D. et al. (2016). "The suppression of Antarctic bottom water formation by melting ice shelves in Prydz Bay". In: *Nature Communications* 7, p. 12577. DOI: http://dx.doi.org/10.1038/ncomms1257710.1038/ncomms12577.

Wilson, N., F. Straneo, and P. Heimbach (2017). "Submarine melt rates and mass balance for Greenland's remaining ice tongues". In: *The Cryosphere Discussions* 2017, pp. 1–17. DOI: 10.5194/tc-2017-99.

Woods, A.W. (1992). "Melting and dissolving". In: *Journal of Fluid Mechanics* 239, pp. 429–448. DOI: 10.1017/S0022112092004476.

Zwally, H.J. et al. (2002). "Surface melt-induced acceleration of Greenland ice-sheet flow". In: *Science* 297.5579, pp. 218–222. DOI: 10.1126/science.1072708.